VOLTAGE TUNABLE RADIO FREQUENCY MICROELECTROMECHANICAL RESONATORS AND FILTERS

A Dissertation

Presented to the Faculty of the Graduate School

of Cornell University

in Partial Fulfillment of the Requirements for the Degree of

Doctor of Philosophy

by

Hengky Chandrahalim

August 2009

VOLTAGE TUNABLE RADIO FREQUENCY
MICROELECTROMECHANICAL RESONATORS AND FILTERS

Hengky Chandrahalim, Ph.D.
Cornell University 2009

Advanced radio technology demands for low power consumption and compact architecture that operate at the global range of frequency standards. Using discrete components based on traditional surface acoustic wave (SAW) or thin film bulk acoustic resonator (TFBAR) technology to manufacture quad-band and 7-band radios presently requires an enormous number of power-hungry and large-size filters fabricated on different substrates. On the other hand, employment of Micro Electromechanical Systems (MEMS) technology to create radio front-ends facilitates reductions in size, weight, cost, and power in radio communications.

Several research groups from academia and industry have recently demonstrated electrostatically and ferroelectrically transduced microelectromechanical resonators and filters that operate at high frequency and exhibit low insertion loss as potential substitutes for conventional quartz and ceramic devices. However, the modern radio architecture today also requires the ability to discern bandwidths between 0.1 MHz and 5 MHz. This requires frequency-agile intermediate-frequency filters, generating a strong demand for narrow-bandwidth channel-select filters with very high quality factors (Q), which can be formed using high-Q MEMS resonators. This dissertation presents the state of the art transduction mechanisms of MEMS resonators and filters with key innovations in DC voltage tuning schemes, packaging technology and system integration.

Electrically coupled, high-Q, tunable channel-select ladder filters comprised

of dielectrically transduced thickness shear mode resonators are presented using integrated circuit compatible bulk micromachining technology. The ladder filter consists of shunt and series resonators operating in the half-wave thickness shear vibration mode. Each constituent resonator of the filter can be excited at above 810 MHz resonant frequency with Q of $7,800$ in air and a motional impedance (R_X) of 59 Ω. The ladder filter demonstrates a center frequency tuning range of 8 MHz at 817 MHz and an adjustable bandwidth from 600 kHz to 2.8 MHz, while maintaining an insertion loss < 4 dB, stop-band rejection > 30 dB and pass-band ripple < 2 dB. By having a tunability feature, radio frequency (RF) MEMS filters can accommodate various signal waveforms with bandwidth range of 0.1 MHz and 5 MHz. In addition, errors due to fabrication can be compensated and capacitive loading in receiver architecture can be minimized.

Multi-frequency and multi-band filters on-chip has motivated the design and fabrication of a center frequency and bandwidth tunable RF MEMS filter using a series-coupled array of dielectrically-transduced square-extensional contour mode resonators. The proposed digital tuning scheme provides channel-agility and bandwidth granularity for analog spectral processors and RF spectrum analyzers. A 512 MHz overtone square-extensional mode resonator is demonstrated with a Q of $1,800$ in air and R_X of 3.1 kΩ. An array of four such resonators is coupled mechanically to form a channel-select filter with 1.4 MHz bandwidth at 509 MHz center frequency. By switching the DC-biasing scheme, the filter is split into narrower high and low sub-bands, each 700 kHz wide.

Despite of the advances in device performance, packaging technology for MEMS resonators and filters remains a critical challenge. Because of the extreme sensitivity to environment, MEMS resonators and filters need a good vacuum encapsulation technology. The promising on-chip applications also require a CMOS

compatible packaging process. The first successful combination of a dielectrically-transduced 200 MHz width-extensional contour mode resonator with the epi-silicon encapsulation process is demonstrated. The fabricated encapsulated-resonator exhibits a resonant frequency of 207 MHz and a Q of $6,400$. The high $f \times Q$ (1.2×10^{12} Hz) makes this encapsulated resonator an excellent candidate for applications in local oscillators for RF front-ends and frequency references.

Dielectric transduction is not only limited to solid dielectric transduction. Lateral contour-mode resonators in which the transduction gaps are filled with a liquid dielectric having much higher permittivity than air are presented. Aqueous transduction is more efficient than air-gap transduction and has a higher frequency tuning range compared to solid dielectric transduction. A 42 MHz poly-SiGe disk resonator with de-ionized (DI) water confined to the electrode gaps is demonstrated. The resonator has a measured Q of $3,800$, R_X of 3.9 kΩ and 3% series frequency tuning range.

Ferroelectric materials like lead zirconate titanate (PZT) is of interest because it offers a large electromechanical coupling coefficient ($k_t{}^2$) and electric field dependent permittivity and modulus of elasticity. In this effort, PZT transduced resonators with the same lateral dimensions are designed and fabricated with and without a silicon device layer to explore the insertion loss, linearity, tunability and Q trade-offs between the two types of resonators. A novel air-bridge fabrication technology is developed to minimize the pad capacitances and enables the frequency excitation of PZT transduced resonators above 1.8 GHz.

PZT transduced fully-differential filters are designed by mechanically coupling two high-overtone width-extensional mode resonators. The fully-differential filter configuration cancels the feed-through capacitance and improves the stop-band floor of the filter. The demonstrated electric field tuning provides channel-agility

and bandwidth adjustability for incorporation of analog spectral processors in state of the art radio receiver architectures. The filter demonstrates a center frequency tuning range of 7 MHz at 260 MHz and an adjustable bandwidth from 3 MHz to 6.3 MHz, while maintaining a maximum frequency shift due to hysteresis effects below 0.14% and a stop-band rejection floor of −60 dB. In order to improve immunity to hysteresis and realize the narrow bandwidth channel-select filter, the PZT transduced fully-differential filters are integrated with silicon device layer. A 206.3 MHz high-overtone width-extensional filter is demonstrated with 653 kHz bandwidth, −25 dB insertion loss and −62 dB stop-band rejection in air. Uncompensated temperature coefficient of frequency (TCF) of −16 ppm/°C and third-order input intercept point (IIP_3) of +29 dBm are demonstrated by the filter.

The monolithic integration of RF components has long been a goal of researchers and will enable not only more compact and lower cost systems but previously unachievable signal processing functions. This dissertation provides the first experimental demonstration of monolithically integrated piezoelectric RF MEMS switches with contour mode filters. PZT thin films are utilized to enable both low-voltage switch operation and filter tunability. This research leverages previous work using PZT actuators for low-voltage, wide-band switches and PZT transduced silicon resonators. The two device technologies are combined using a hybrid fabrication process that combines the key components of each device fabrication into a single unified process using silicon-on-insulator (SOI) substrates. The voltage tunable and switchable filter array provides a drop-in solution for frequency-agile channel selectivity required in tranceiver front-ends.

BIOGRAPHICAL SKETCH

Hengky Chandrahalim was born and brought up in Parakan, Central Java, Indonesia. He studied at Loyola High School in Semarang, Indonesia. After graduating from high school, he moved to Columbus, Ohio, to attend the Ohio State University. He completed his undergraduate education with the degree of Bachelors of Science in Electrical and Computer Engineering in 2000. After finishing his undergraduate degree, he spent three years working as an integrated circuit design engineer at Integrated Circuit Systems, Inc. in San Jose, California.

In 2003, he joined the Master of Engineering program in electrical and computer engineering at Cornell University in Ithaca, New York. He worked under supervision of Professor Amit Lal in designing on-chip PZT actuation circuits for micro-atomizers. Soon after receiving his master's degree he decided to further pursue a doctoral degree in electrical and computer engineering at Cornell University. He then worked under the guidance of Professor Sunil A. Bhave and Professor Amit Lal in the field of radio frequency microelectromechanical systems.

To my beloved family

ACKNOWLEDGEMENTS

The successful completion of this thesis relies upon innumerable contributions from people throughout the multiple phases my life. I am forever in debt to many individuals who provided me with friendship and companionship whom I cannot acknowledge by their names here.

First and foremost, I would like to express my deepest appreciation to my research advisor, Professor Sunil A. Bhave, for his continuous advice, support and friendship during my graduate years. He has been a very understanding advisor, wonderful friend and genuine source of guidance to me during the last five years at Cornell. I thank him for strongly coupling me into multifarious aspects of research and teaching. I have always been impressed with his resourcefulness in the technical area. His understanding and benevolence to students are always the supreme virtues to me. I am thankful to my research co-advisor Professor Amit Lal who first introduced me to MEMS and supported my early research at Cornell. His futuristic engineering wisdom always enlightens me of bountiful research possibilities in MEMS area. I really appreciate his valuable feedback from time to time throughout my Ph.D. years. I am also grateful to Professor Ephrahim Garcia for serving as members of my dissertation committee, reviewing this manuscript and providing constructive critique and advice, and to Professor Clifford R. Pollock and Professor Tsuhan Chen for their enlightening discussions and encouragement.

I would like to thank Professor Paul L. McEuen and his group for supporting our experiments with nanotubes and graphene in his laboratory. Special thanks for Arend van der Zande, Zhaohui Zhong and Scott Bunch who assisted me to grow the carbon nanotubes and deposited graphene on our devices.

I am indebted to many former and current members of *Oxide*MEMS and *Sonic*MEMS laboratories. I would like to particularly thank Shankar Radhakrishnan, who thought me most of my micro-fabrication skills, Serhan Ardanuç, who is always willing to share his technical wisdom in acoustics and MEMS in general, Dana Weinstein for deriving the electrical equivalent model of thickness shear mode resonator, Lih Feng Cheow for running extensive simulations on the ladder filter, Chen Chen for providing spontaneous entertainments to the group , Venkata Siva Prasad Pulla, Steven Tin and Norimasa Yoshimizu for plenty of helpful technical and non-technical discussions. I ought to thank all the *Oxide*MEMS and *Sonic*MEMS members whose companionship made my life in Phillips Hall more exciting and stimulating - Dana Weinstein, Chen Chen, Eugene Hwang, Suresh Sridaran, Tiffany Cheng, Susmita Bhandari, Laura Fegely, David Hutchison, Wenzhe Zhou, Muhammet Kürşad Araz, Kwame Amponsah, Serhan Ardanuç, Alper Bozkurt, Venkata Siva Prasad Pulla, Abhishek Ramkumar, Janet Shen, Steven Tin, Norimasa Yoshimizu, Xi Chen, Rajesh Duggirala, Hang Guo, Hui Li, Pietro Toscano, Shankar Radhakrishnan and Shyi-Herng Kan.

My time spent at Cornell was made special through the social and academic interactions with my fellow students. I am very fortunate to have these people as friends. In no particular order, I wish to thank Wei Min Chan, Tchefor Tumasang Ndukum, Manoj Pandey, Song Peng, Christianto Liu, Georgios Lilis, Onimisi Ojeba, Khye Suian Wei, Udayan Ganguly, Shriram Shivaraman, Sasikanth Manipatruni, Jaegoo Lee, Alex Tuohung Hou, Rajeev Kumar Dokania, Xiao Wang, Haining Wang, Navin Mallavarpu, Ali Gokirmak, An-swol Hu, Kwok Loon Chan, Jonathan Aaron Winter, Keith Lyon, Justin Seo, Raymond Hyun Chull Kim, Yunju Sun and Joon Young Kwak.

I thank all the past and present members of the Cornell Badminton Club, for the camaraderie and thrill I enjoyed on the courts of Helen Newman Hall. My life in Ithaca will not be the same without all of you: Professor Anil Netravali, who is the faculty advisor to the club, Xiaoshi Jin, Siew Ann Cheong, Chuan Lee, Archit Lal, Shengfeng Shen and I-Ho Chang, Ram Narayan, Mike Hsu, Chula Watugala, Winson Lin, Zhongtao Fu, Yuping Zhou, Seung Jin Oh, Peeyush Bhargava, Charlie Chuan-Che Wang and Nai-Ying Chang, Ivan Han, Suntao Wang, Xujie Zhang, Jian Zhang, Yong Sheng Khoo, Sebastien Lavoue, Peng Zhao, Quan Zhang, Venkat Krishnan and Shrut Kirti.

I also cannot forget the administrative support of present and former ECE department staff including Sue Bulkley, Lisa Gould, Sally Bird, Cheryl Francis, Dorothy Palladino, Linda Struzinsky and Daniel Richter. Special thanks to Jamie Dal Cero, who helped me a lot with the "shipping business" and always made sure I got prompt reimbursement for expenses during business travels and to Scott Coldren, who is our department manager of student services for his kind assistance in writing departmental letters, and for reminding us with all the important deadlines throughout the Ph.D. years.

I feel grateful to my former colleagues at ICS, who remain good friends until now. This includes Teck Chuan Ng, Eugene Chin, Kah Suan Seah, Deanna Luu, Vince Tat, Bruce Lo, Kristen Chen, Toai Nguyen, Pouran Asadipour, Allen Su, David Chiu, Tacettin (Taji) Isik, Michel Charbonnier and Chau Nguyen. Special thanks to Hoang Tran, who was my team manager for being a very understanding and supportive manager, and to Linda Wheeler, who gave me the opportunity to handle the duty of an integrated circuit design engineer despite of my lacking of relevant experience at that time.

I am fortunate to meet friends from MEMS community in various conferences and had wonderful discussions with them. Their comments, critiques and suggestions are very beneficial for my research and in writing this manuscript. In no prticular order, I would like to thank Jonathan Hammond, Jagan Rao, Bongsang Kim, Maryam Ziaie-Moayyed, Yang Lin, Cheng Jie Zuo, Gavin Ho, Gianluca Piazza, Phil Stephanou, Tomohiro Ishikawa, Chiung Cheng Lo, Chuan-Yu Shao, Shih-Wei Lee, Franklin Chiang, Gaurav Shah, Jon Lovseth, Wen-Lung Huang, Jan Kuypers, Sheng-Shian Li and Yu-Wei Lin.

The fabrication of solid dielectrically transduced devices was made possible through kind assistances of Rob Ilic, Meredith Metzler, Vince Genova, Phil Infante, Garry J. Bordonaro, Michael Skvarla, Jerry Drumheller and the rest of the staff of the Cornell Nanoscale Science and Technology Facility. Special thanks to Rob Illic for his help in the clean room especially during odd hours, and to Meredith Metzler and Vince Genova who developed and characterized the etch recipe for hafnia. I am grateful for the support of Cornell Center for Materials Research and Center for Nanoscale Systems staff. Special thanks to Dr. Jonathan Shu, who assisted me with RF testing before our testing facility in Phillips Hall was ready, and to Mick Thomas, who has been always helpful with FIB.

Thanks to all Analog Spectral Processors (ASP) team members whose expertise has greatly helped me in completing this thesis. I would like to especially thank Professor Roger T. Howe and Professor Thomas W. Kenny at Stanford University for providing constructive comments and suggestions with the encapsulated resonators. Thanks to Kuan-Lin Chen and Shasha Wang at Stanford University who worked on the packaging process our dielectrically transduced contour-mode resonators.

I would also like to thank the outstanding researchers and scientists with whom I have collaborated on various projects. Special thanks to Dr. Ronald Polcawich and Jeff Pulskamp at U.S. Army Research Laboratories for their assistance in fabricating PZT transduced devices, to Dr. Emmanuel Quévy for providing poly-SiGe samples, to Dr. Jennifer Sigman, Dr. Jon Ihlefeld and Dr. Paul Clem at Sandia National Laboratories for their assistance in fabricating ferroelectrically transduced devices, to Dr. Graham Cameron at Mayo Clinic, who assisted ASP program with device verification, to Dr. Christian Rembe and Sebastian Boedecker at Polytec, who helped with optical characterization of our resonators, to Dr. Kushal Bhattacharjee at RF Micro Devices, Inc. and Dr. Robert Potter at Rockwell Collins, Inc. for technical discussions, help, and encouragement.

Most of all, I would like to thank my parents for their love and support and to my sister Yulia that I love very much. I would like to thank Imelda Friska who has assisted me tremendously by providing many useful illustrations to complete this dissertation, and to Candra Alisiswanto a great friend who has always been there for me.

This research was funded by the DARPA ASP program, by Cornell Center for Nanoscale Systems (an NSF/Industry/University Research Center), by a grant from RF Micro Devices, Inc., and by a grant from the Charles Stark Draper Laboratory, Inc.

TABLE OF CONTENTS

Biographical Sketch . . . iii
Dedication . . . iv
Acknowledgements . . . v
Table of Contents . . . x
List of Tables . . . xiii
List of Figures . . . xiv

1 RF MEMS and the New Paradigms in Modern Wireless Communications 1
1.1 Analog Spectral Processors . . . 7
1.2 Previous Electromechanical Resonators . . . 10
1.2.1 Quartz Crystal Resonators . . . 10
1.2.2 Surface Acoustic Wave Resonators . . . 13
1.2.3 Bulk Acoustic Wave and FBAR Resonators . . . 15
1.2.4 Contour-Mode Resonators . . . 17
1.3 Contributions of this Dissertation . . . 22
1.4 Dissertation Organization . . . 22

2 High-Q MEMS Thickness Shear Resonators and Analog Voltage Tunable Electrically-coupled Channel-Select RF Filters 24
2.1 Introduction . . . 24
2.2 Quarter-wave Thickness Shear Resonator . . . 26
2.2.1 Electrical Equivalent Impedances of a Quarter-wave TSM Resonator . . . 27
2.2.2 Fabrication Process . . . 31
2.2.3 Measurement Results . . . 33
2.3 Half-wave Thickness Shear Resonator . . . 36
2.3.1 Motional Impedance of a Half-wave TSM Resonator . . . 37
2.3.2 Fabrication Process . . . 39
2.3.3 Measurement Results . . . 39
2.4 Electrically Coupled RF MEMS Ladder Filters . . . 41
2.5 RF MEMS Channel-select Filters with Tunable Center Frequency and Bandwidth . . . 45
2.5.1 Orthogonal Frequency Tuning . . . 46
2.5.2 Pole-Zero Seperation Tuning . . . 47
2.5.3 Filter Tuning Algorithm . . . 49
2.5.4 Fabrication Process . . . 49
2.5.5 Measurement Results . . . 51
2.6 Conclusion . . . 56

3 High-overtone Square-extensional Resonators and Digitally Programmable Mechanically-coupled Frequency-agile Filters 58
3.1 Introduction . . . 58
3.2 High-overtone Square-extensional Mode Resonator . . . 59
3.2.1 Effective mass, Damping ratio and Effective spring constant 61
3.2.2 Electromechanical Coupling Constant . . . 63
3.2.3 Electrical Equivalent Impedances of a High-overtone Square-extensional Resonator . . . 64
3.3 Digitally Programmable Filters . . . 65
3.4 Fabrication Process . . . 70
3.5 Calibration and De-embedding Techniques . . . 74
3.6 Characterization of a High-overtone Square-extensional Mode Resonator . . . 74
3.7 Characterization of a Digitally Programmable Filter . . . 76
3.8 Conclusion . . . 77

4 Vacuum-encapsulated CMOS-compatible Packaging Technology for Contour-mode Resonators 81
4.1 Introduction . . . 81
4.2 Width-extensional Mode Resonator . . . 82
4.3 Epitaxy-silicon Microshell Packaging . . . 83
4.4 Fabrication Process . . . 85
4.5 Measurement Results . . . 87
4.6 Conclusion . . . 91

5 Aqueous Transduction of Contour-Mode RF MEMS Resonators 92
5.1 Introduction . . . 92
5.2 Aqueous Transduction of a Contour-mode Poly-SiGe Disk Resonator 93
5.2.1 Measurement of a Poly-Sige Disk Resonator in Air . . . 94
5.2.2 Measurement of Poly-Sige Disk Resonators with DI Water . 97
5.2.3 Series Frequency Tuning of Poly-Sige Disk Resonators . . . 100
5.3 Conclusion . . . 101

6 PZT Transduced Voltage Tunable Resonators 103
6.1 Introduction . . . 103
6.2 Length Extensional Mode Resonator . . . 104
6.2.1 Effective mass, Damping ratio and Effective spring constant 106
6.2.2 Electromechanical Coupling Constant . . . 108
6.2.3 Electrical Equivalent Impedances of a PZT Transduced LEM Resonator . . . 109
6.3 Fabrication Process . . . 110
6.4 Measurement Results . . . 113
6.4.1 Resonance Frequency, Motional Impedance, and Quality Factor . . . 113

6.4.2 DC Voltage Tuning . . . 115
6.4.3 Linearity . . . 116
6.4.4 Hysteresis . . . 117
6.5 High-overtone Width-extensional Mode Resonators . . . 117
6.6 Air-bridge Fabrication Process . . . 119
6.7 Measurement Results . . . 122
6.8 Conclusion . . . 124

7 PZT Transduced Mechanically-coupled Frequency-agile Filters 126
7.1 Introduction . . . 126
7.2 PZT-only Mechanically-coupled Filters . . . 127
7.2.1 Fully-differential High-overtone Width-extensional Filters . . 127
7.2.2 Measurement Results . . . 129
7.3 PZT-on-silicon Mechanically-coupled Filters . . . 133
7.3.1 Measurement Results . . . 135
7.4 Conclusion . . . 139

8 Monolithically Integrated Piezo-MEMS Switches and Contour-mode Filters 141
8.1 Introduction . . . 141
8.2 Design of Integrated PZT transduced Switches and Filters . . . 143
8.3 Fabrication Process . . . 146
8.4 Measurement Results . . . 147
8.4.1 Frequency Domain Measurement . . . 147
8.4.2 Time Domain Measurement . . . 150
8.5 Conclusion . . . 151

9 Future Research Directions 152
9.1 Solid Dielectrically Transduced Devices . . . 152
9.1.1 Transduction Efficiency . . . 152
9.1.2 On-chip Fully-differential Configuration . . . 152
9.1.3 Long-term Stability . . . 153
9.1.4 Post-MEMS CMOS Integrated Systems . . . 154
9.2 Liquid Dielectrically Transduced Devices . . . 156
9.3 PZT Transduced Devices . . . 158
9.3.1 High-Q SHF PZT Transduced Resonators . . . 158
9.3.2 Monolithically-integrated PZT Based Microsystems . . . 159

A Fabrication Process of Thickness Shear Resonators and Filters 160

B Calibration and De-embedding Techniques 166

Bibliography 168

LIST OF TABLES

1.1 Quartz crystal mode of vibration and frequency range 11
1.2 Quartz crystal cut and frequency range 12

2.1 The measured characteristics of electrically coupled TSM filters . . 43

3.1 Design parameters of the high-overtone square-extensional resonator 67
3.2 Design parameters and measured data of the high-overtone square-extensional resonator 76
3.3 Performance summary of the digitally programmable filter 80

6.1 The measured characteristics of PZT-on-silicon resonators 114
6.2 The measured characteristics of PZT-only resonators 114
6.3 The measured characteristics of PZT-on-silicon resonator with different bias voltages 116
6.4 The measured characteristics of PZT-only resonator with different bias voltages 116
6.5 The measured characteristics of high-overtone WEM resonators with different silicon thicknesses 125

7.1 The measured frequency response of a PZT transduced high-overtone WEM filter 132
7.2 The measured frequency response of a PZT-on-silicon high-overtone WEM filter 137

LIST OF FIGURES

1.1 Schematic illustrating the Hybrid Insect MEMS (HIMEMS). 2
1.2 Super-heterodyne Radio Architecture. 3
1.3 Mechanically-coupled resonant gate transistors (RGT) (a) Device geometry, (b) Microphotogrpah of a device with cantilever length of 240 μm, (c) Frequency response of a mechanically-coupled RGT with f_C of of 22 kHz and BW of 300 Hz, and (d) Frequency response of a mechanically-coupled RGT with f_C of of 132 kHz and BW of 1 kHz. 5
1.4 Receiver architecture of Analog Signal Processors. 9
1.5 Quartz crystal resonators: (a) Flexural/Length-extensional resonator, (b) Face-shear resonator, (c) Thickness-shear resonator, (d) Packaged quartz crystal resonator. 12
1.6 A typical SAW device consists of two sets of interdigital transducers. The input transducer converts electric field energy into mechanical wave energy, and the output transducer senses the propagated surface waves and converts the mechanical energy back into an electric field. 13
1.7 Packaged SAW resonators and filters with various frequency ranges. 14
1.8 Cross-section of bulk acoustic wave (BAW) resonators: (a) Solidly mounted resonators (SMR), (b) Membrane bulk acoustic wave resonator (FBAR). 16
1.9 Air-gap contour-mode resonators: (a) A radial-contour mode disk resonator, (b) A polysilicon hollow-disk ring resonator, (c) An extensional wine-glass-mode resonator, (d) A nanocrystalline diamond disk resonator, (e) A square-extensional mode resonator, and (f) A Poly-SiGe contour-mode disk resonator. 18
1.10 Piezoelectrically transduced contour-mode resonators: (a) An AlN transduced ring-shaped contour-mode resonator, (b) An AlN transduced square-ring-shaped contour-mode resonator, and (c) A ZnO on silicon contour-mode resonator, (d) A ZnO-on-nanocrystalline diamond resonator, and (e) An AlN transduced mechanically-coupled contour-mode filter. 21

2.1 X-displacement contour plot from Ansys simulation of the symmetric quarter-wave thickness shear mode. 27
2.2 The schematic of an unreleased thickness shear bar. 28
2.3 2-D cross-section schematic of the conversion of transverse electrostatic stress in the silicon nitride thin film to thickness shear mode in the half-length (A-A' in Figure 2) bar resonator. 29
2.4 Fabrication process flow of quarter-wave thickness shear mode resonators. 32
2.5 SEM of a silicon nitride-on-silicon unreleased bar resonator. 33

2.6 Measured transmission of the thickness shear mode of the unreleased resonator in air. 34
2.7 A partially released quarter-wave thickness shear mode resonator. . 34
2.8 Measured transmission of the partially released shear mode resonator in air. 35
2.9 ANSYS contour plot of the symmetric half-wave thickness shear mode. 36
2.10 Schematic of a fully released half-wave thickness shear bar resonator. 37
2.11 ANSYS simulation of length (L) vs resonant frequency (f_C) of the 3.2 μm thick half-wave shear mode resonator. 38
2.12 (a) SEM of a hafnium dioxide-on-silicon fully released bar resonator. (b) SEM of the 30 nm hafnium dioxide layer on the top of the silicon resonator. 39
2.13 Measured transmission response of a half-wave TSM resonator in air. 40
2.14 (a) Electrically coupled ladder filter configuration. (b) Bandpass frequency response of the ladder filter. 41
2.15 SEM of an array of ladder configuration electrically coupled thickness shear filters. 42
2.16 Measured transmission response showing two 650 kHz channel-select filters. 44
2.17 Measured filter transmission response over a wide frequency range. 44
2.18 The distorted bandpass response of the filter due to fabrication tolerances. 45
2.19 Longitudinal cross-section of a deflected half-wave thickness shear mode resonator due to the orthogonal biasing configuration. 47
2.20 Electrical equivalent circuit of a dielectrically transduced MEMS resonator. 48
2.21 (a) The 3-D model of tunable ladder filter. (b) The device cross-section with isolated resonator and substrate for applying independent tuning voltages. 50
2.22 Microphotograph of tunable ladder filter with a gold wirebond bridge. 51
2.23 (a) The uncalibrated frequency characteristic of the resonator. (b) The measured frequency characteristic of the resonator after Cascade substrate calibration. 52
2.24 (a) Measured frequency characteristic of the resonator after SOI calibration. (b) Measured series resonance tuning for $V_S = 5$ V and $V_S =$ (i) 12 V, (ii) 8 V, and (iii) 5 V. (c) Resonant frequency tuning vs. substrate voltage. 53
2.25 (a,b,c) Measured transmission response demonstrating pole-zero separation of a thickness shear mode resonator as DC bias V_P increases from 5 V to 10 V. (d) Measured pole-zero separation vs. DC bias voltage of the resonator. 54

2.26 (a) Measured transfer function of ladder filter with no tuning. (b) Measured transmission of ladder filter with f_C tuning from 817 MHz to 809 MHz with (i) no tuning, and (ii) series resonator: $V_P = 5$ V, $V_S = 15$ V; shunt resonator: $V_P = 5$ V, $V_S = 12$ V. (c) Measured transmission of ladder filter with BW tuning from 0.6 MHz to 2.8 MHz with (i) no tuning, (ii) series resonator: $V_P = 12$ V, $V_S = 12$ V; shunt resonator: $V_P = 13$ V, $V_S = 16$ V. (d) Measured transfer function of ladder filter with BW tuning from 0.6 MHz to 1.4 MHz and f_C tuning from 817 MHz to 811 MHz with (i) no tuning, and (ii) series resonator: $V_P = 10$ V, $V_S = 19$ V; shunt resonator: $V_P = 9$ V, $V_S = 17$ V. 55

3.1 (a) Schematic of a 2-port high-overtone square-extensional mode resonator. (b) Cross-section of the device showing various layers that are deposited to build the resonator. (c) ANSYS mode shape of a high-overtone square-extensional resonator. 60

3.2 Electrical equivalent circuit of a dielectrically transduced high-overtone square-extensional resonator. 65

3.3 Simulated performance of a 500 MHz high-overtone square-extensional resonator. 66

3.4 Schematic of a digitally programmable filter composed of four series mechanically-coupled checkered-electrode resonators. Each resonator has individually addressable RF + DC lines. The silicon device layer is an RF ground to prevent substrate losses. 68

3.5 Four vibration modes of a 4-pole filter consisting of overtone square-extensional mode resonators. 69

3.6 Simulated performance of a digitally programmable filter composed of four series mechanically-coupled checkered-electrode resonators. (a) Simulated 4-pole frequency response of the filter. (b) Simulated lower sub-band filter response. The biasing scheme forces the left two resonators to vibrate out of phase and sums the out-of-phase motional current of the right two resonators. (c) Simulated higher sub-band filter response. The biasing scheme forces the left two resonators to vibrate in phase and sums the in-phase motional current of the right two resonators. 71

3.7 Fabrication process flow of high-overtone square-extensional mode resonators and digitally programmable filters. 72

3.8 SEM image of a high-overtone 2-D square-extensional mode resonator with checkered electrodes for transduction. The resonator consists of a 55 nm SiN transducer sandwiched between poly electrodes and 2.75 μm thick silicon device layer. An oxide pedestal layer is implemented to elevate the RF signal lines off the ground plane. Pt/Au metal traces and pads are introduced to improve RF signal integrity and reduce noise during probing. 73

3.9 SEM image of a digitally programmable filter composed of four series mechanically-coupled checkered-electrode resonators. Each resonator has individually addressable $RF + DC$ lines. The silicon device layer is an RF ground to prevent substrate losses. All RF paths are metalized, routed on an elevated oxide bridge to reduce capacitance and de-embedded to the edge of DRIE trench. 73
3.10 (a) Testing configuration for a 2-port high-overtone square-extensional mode resonator. (b) Measured series resonance response of a 2-port high-overtone square-extensional mode resonator in air at room temperature and pressure. 75
3.11 Performance of a 50 Ω terminated filter with three different bias configurations in air. (a) Measured 4-pole frequency response of the filter. (b) Measured lower sub-band filter response. The biasing scheme forces the left two resonators to vibrate out of phase and sums the out-of-phase motional current of the right two resonators. (c) Measured higher sub-band filter response. The biasing scheme forces the left two resonators to vibrate in phase and sums the in-phase motional current of the right two resonators. 78
3.12 Transmission response of the filter with three different bias configurations after termination using the PNA's pole-Z conversion function. The attenuated modes are clearly visible in the transmission response of the lower sub-band filter. The filter stop-band floor is high because electrical resistance in the ground plane leads to large capacitive feedthrough between drive and sense ports. 79

4.1 (a) Schematic diagram of the dielectrically transduced, width-extensional mode resonator. (b) ANSYS contour plot of the width-extensional bar mode shape. 83
4.2 Epi-silicon microshell encapsulation process for dielectrically transduced resonators. Vertical epi-vias to the poly electrodes provide RF input/output while the vias to the silicon device layer provide a micro RF-cage providing a shielded micro-environment. 84
4.3 SEM of the fabricated resonator. The zoomed-in picture on the right shows the thin poly electrode on top of the resonator bar. The zoomed-in picture on the left shows the electrical contact between the epi-silicon and the device layer. 86
4.4 Transmission response using the 2-port measurement. Capacitive feedthrough masks the electromechanical resonance, resulting in a sharp dip at the target frequency. 87
4.5 (a) Schematic of the pseudo-differential measurement setup, and (b) The equivalent circuit of pseudo-differential measurement to cancel the capacitive feedthrough current. 89

4.6 Transmission responses of the simple 2-port measurement and pseudo-differential measurement. It is clearly shown that the resonance peak matches the sharp dip shown in the 2-port measurement. . . . 90

5.1 SEM image of a poly-SiGe disk resonator: (a) Cross-section of the resonator showing the 60 nm lateral air-gap (b) Close-up of anchor, and (c) Top view. 95
5.2 (a) Transmission measurement setup, and (b) Transmission response in air. 96
5.3 (a) Schematic illustrating the experiment. The water wicks the 60 nm gap and is left under the structure. (b) Photograph of water droplet placed on resonator and then moved to the edge. (c) Measured transmission response after water drop is rolled away from the resonator: Q of 430 at 36 MHz. 97
5.4 (a) Schematic of water droplet rolled across the resonator; wicking the transducer gap but minimizing the water left underneath the resonator. (b) Transmission response: Q of $3,800$ at 42 MHz with $R_X = 3.9$ kΩ. 99
5.5 Transmission response of a resonator with repeated rolls of the DI water droplet. 100
5.6 (a) 0.1% center frequency tuning of the air-gap transduced disk resonator before anchor failure. (b) In DI water, the resonator center frequency is tuned up to 3%, before the onset of electrolysis. 101

6.1 A 3-D schematic of PZT-on-Silicon length-extensional mode resonator. 104
6.2 An ANSYS mode shape of a length-extensional mode resonator. . . 105
6.3 The cross-section of a length-extensional mode resonator. 106
6.4 Electrical equivalent circuit of a PZT transduced LEM resonator. . 109
6.5 Fabrication process-flow for PZT-on-silicon and PZT-only resonators.111
6.6 (a) SEM of a released PZT-only resonator. (b) SEM of a released PZT-on-silicon resonator. The isotropic pit due to the XeF_2 etch can be seen in the background. 112
6.7 Measured transmission response of PZT-only and PZT-on-silicon resonators with the exact same lateral dimensions in air at room temperature and pressure. 113

6.8 (a) Measured transmission of a 190 μm x 40 μm PZT transduced resonator on 10 μm silicon with different bias voltages in air at room temperature and pressure. 0.2% frequency tuning capability is observed due to DC bias dependent Young's modulus and density of PZT thin film. (b) Measured transmission of a 90 μm x 20 μm PZT-Only resonator with five different bias voltages in air at room temperature and pressure. 5.1% frequency tuning capability is observed due to DC bias dependent Young's modulus and density of PZT thin film. 115
6.9 Measured IIP_3 of (a) a 90 x 20 μm^2 PZT-only, and (b) a 190 x 40 μm^2 PZT on 10 μm silicon resonator with 0 V DC bias in air at room temperature. 117
6.10 (a) Measured hysteresis effect in the relative permittivity of a PZT thin film. (b) A PZT-on-silicon resonator shows imperceptible hysteresis, while a PZT-Only resonator shows a maximum of 0.17% center frequency (f_C) shift. 118
6.11 (a) Schematic of a PZT-only high-overtone width-extensional mode resonator. (b) Schematic of a PZT-on-silicon high-overtone width-extensional mode resonator. (c) ANSYS mode shape of a high-overtone width-extensional mode resonator. 120
6.12 Air-bridge process cross-section of PZT-only and PZT-on-silicon high-overtone width-extensional mode resonators fabricated on the same wafer. 121
6.13 SEM of the fabricated high-overtone width-extensional mode resonator. The zoom-in picture shows the air-bridge routing that isolates the resonator from the bonding-pads. 123
6.14 (a) Measured transmission response of PZT-only and PZT on 3 μm, 5 μm and 10 μm silicon resonators with the exact same lateral dimensions in air at room temperature and pressure. All measurements were performed using termination impedances (R_L) of 50 Ω. (b) A plot of silicon thickness (t_{Si}) vs the calculated, simulated and measured resonance frequency (f_C). 124

7.1 (a) ANSYS modal analysis showing in-phase and out-of-phase mode of vibrations of a mechanically-coupled high-overtone width extensional filter. (b) SEM image of a PZT transduced high-overtone mechanically-coupled width-extensional filter with differential electrodes. 128
7.2 Testing configuration for a 2-pole mechanically-coupled high-overtone fully-differential filter. 129
7.3 Measured transmission of a PZT transduced 2-pole high-overtone WEM filter with electric field tuning. Input and output terminals were terminated with 50 Ω termination impedances (R_L) for all measurements. 131

7.4 Measured third-order input intercept point (Δ_f = 400 kHz) of the filter demonstrates IIP_3 of +21 dBm. 131
7.5 Measured frequency shifts in PZT transduced high-overtone width extensional filter due hysteresis effect in PZT. A maximum frequency shift of 0.14% was recorded. 133
7.6 (a) Schematic of a mechanically-coupled PZT-on-silicon filter. (b) SEM image of a PZT-on-silicon high-overtone mechanically-coupled width-extensional filter with differential electrodes. 134
7.7 Measured transmission of a PZT-on-silicon 2-pole high-overtone WEM filter with electric field tuning. Input and output terminals were terminated with 50 Ω termination impedances (R_L) for all measurements. 136
7.8 Measured third-order input intercept point (Δ_f = 400 kHz) of the filter demonstrates IIP_3 of +29 dBm. 138
7.9 Measured frequency shifts in PZT-on-silicon high-overtone width extensional filter due hysteresis effect in PZT. An imperceptible frequency shift of 0.013% was recorded. 139

8.1 SEM image of an integrated single pole dual throw (SP2T) PZT-MEMS switch and two PZT transduced width-extensional contour-mode filters. 143
8.2 (a) SEM image of the air-bridge used for switch operation, and (b) reduced large pad capacitances in the filters. 144
8.3 (a) SEM image of the width-extensional contour-mode filter. (b) Anti-symmetric and symmetric ANSYS mode shapes of a fundamental width-extensional mode filter. 145
8.4 (a) S_{21} data at 0 V and 7 V for the PZT-MEMS switch co-fabricated with the PZT transduced width-extensional contour-mode filters. (b) S_{21} response of an integrated SP2T switch and filter with the switch in the Off-state (0 V), (c) S_{21} response for the left switch and filter with the switch On (7 V) and with 10 V V_{DC} applied to the filter, and (d) S_{21} response for the right switch and filter. . . . 148
8.5 S_{21} response for a stand-alone PZT transduced contour-mode filter and an integrated PZT transduced switch + contour-mode filter with the DC bias at 10 V for both devices. The switch increases insertion loss (IL) by 0.4 dB. 149
8.6 Time domain measurements of the switch + filter highlighting the 7 V switching actuation pulses and the ring-up response of the filter with the switch in the On-state. 151

9.1 Estimated values of motional resistance (R_X) versus DC bias voltage for different dielectric materials. 153

9.2 (a) Pseudo-differential measurement setup to characterize the vacuum-encapsulated resonator. (b) On-chip fully-differential configuration to eliminate parasitic capacitances. 154
9.3 Open-loop long-term stability measurement of a silicon nitride transduced vacuum-encapsulated resonator. (a) Measured quality factor as a function of time, and (b) Measured frequency as a function of time. 155
9.4 (a) Hybrid-integration of a super-regenerative CMOS-MEMS transceiver. (b) Post-MEMS CMOS monolithically integrated system. 155
9.5 (a) Four fundamental fluidic operations considered essential to build digital microfluidic circuits, which can be used for lab-on-a-chip or micro total analysis system all by electrowetting. (b) Lateral photographs of light-driven motion of an olive oil droplet. (c) Top-view of a liquid droplet moving along a liquophilic microstripe. The array of Ti-resistors (shown in light gray) beneath the liquophilic stripes locally heat the droplet thereby modifying the surface tension and propelling the liquid toward the colder regions of the device surface. The dark gray stripes represent the leads and contacts (Au) for the heating resistors. (d) Time shots of droplets moving on ratchet-tracks. 157
9.6 (a) ANSYS modal analysis of a high-overtone thickness-mode resonator. (b) Measured frequency response of a 50 Ω terminated PZT transduced high-overtone thickness-mode resonator in air at room temperature and pressure. 158
9.7 Applications within the radio frequency spectrum. 159

B.1 SOT de-embedding (a) schematic (b) equivalent circuit to cancel pad capacitance and sheet resistance without canceling out any parasitic elements inherent to the resonators and filters. 167

CHAPTER 1

RF MEMS AND THE NEW PARADIGMS IN MODERN WIRELESS COMMUNICATIONS

Wireless communication systems have evolved rapidly with the advancements of radio engineering during the recent years. Since the first broadcast of the human voice was transmitted through the air on Christmas Eve of 1906 by Reginald Fessenden, there has been a surge of research activities in wireless telegraphy. Applications in this area have grown tremendously, allowing ubiquitous communication among people and devices. Cellular phones, wireless networks, wireless internet, sensor networks, and wireless entertainments are just to name a few. Apart from commercial applications, the wireless radio frequency (RF) communication has seen futuristic targets desired by armed forces. There is a growing military interest in developing a handheld radio operating from 20 MHz to 6 GHz with the ability to discern bandwidths between 0.1 MHz and 5 MHz.

The recent progress in Bio Micro Electro Mechanical Systems (Bio-MEMS) also has created a space for ultra low-power wireless transceivers. The U.S. Defense Advanced Research Projects Agency (DARPA) has been trying to develop tightly coupled machine-insect interfaces by placing micro-mechanical systems inside the insects during the early stages of metamorphosis as shown in Figure 1.1. The ultimate goal of this research project is to develop insect cyborgs, which could carry one or more sensors, such as a microphone or a gas sensor, to relay back information gathered from the target destination. The goal of the MEMS, inside the insects, will be to control the locomotion by obtaining motion trajectories from global positioning system (GPS) coordinates. The shrinkage in dimensions and reduction in power consumption have been the commonly recognized challenges in any integrated systems. An ultra low-power on-chip GPS radio system is necessary

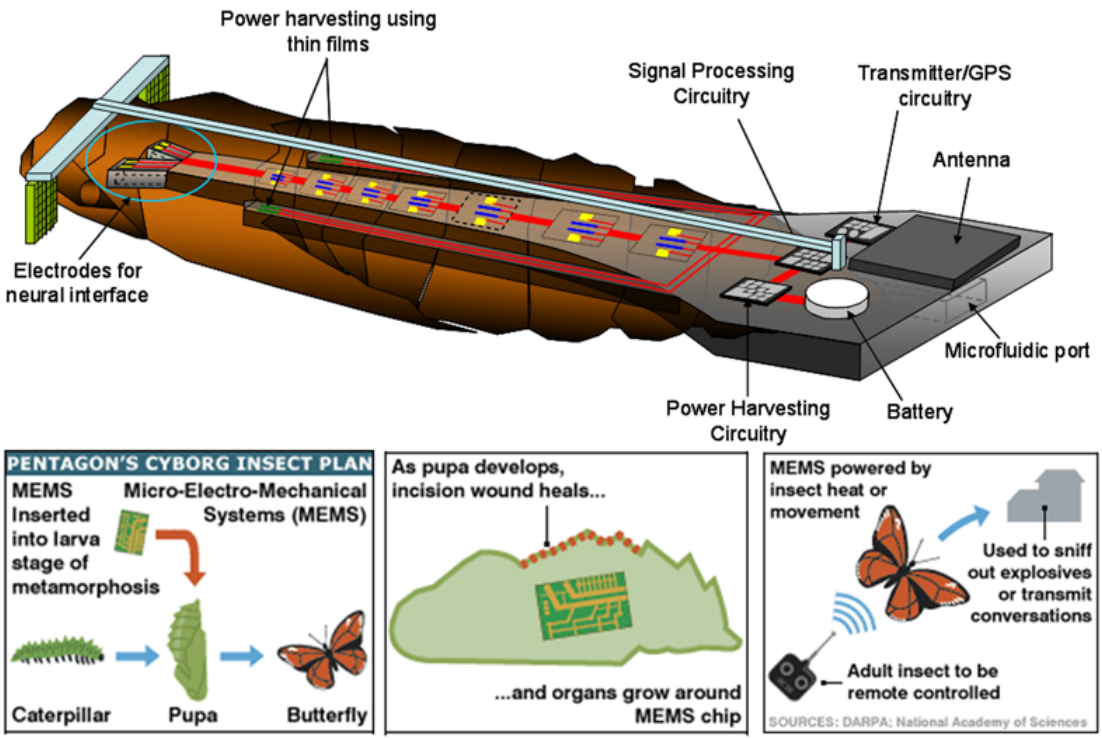

Figure 1.1: Schematic illustrating the Hybrid Insect MEMS (HIMEMS).

in these integrated microsystems on insect because the tiny insects must be able to lift and carry the implanted microsystems including the power source to electrify the embedded electronics.

Almost all wireless devices use a transceiver to receive and transmit information. A significant amount of research has been focused on smart system architectures or other circuit-level innovations to improve the performance of radio transceivers [1–4]. However, the conventional super-heterodyne radio architecture has been commonly recognized to realize wireless transceivers today because of its reliable performance [5]. Figure 1.2 introduces the typical super-heterodyne radio architecture. The scaling law in integrated circuits over years has benefited wireless gadgets in reducing the area consumed by the active components. Unfortunately, not all the functionality in the transceiver can be implemented using transistors, especially the channel-select filtering at RF front end. As a matter of fact, presently

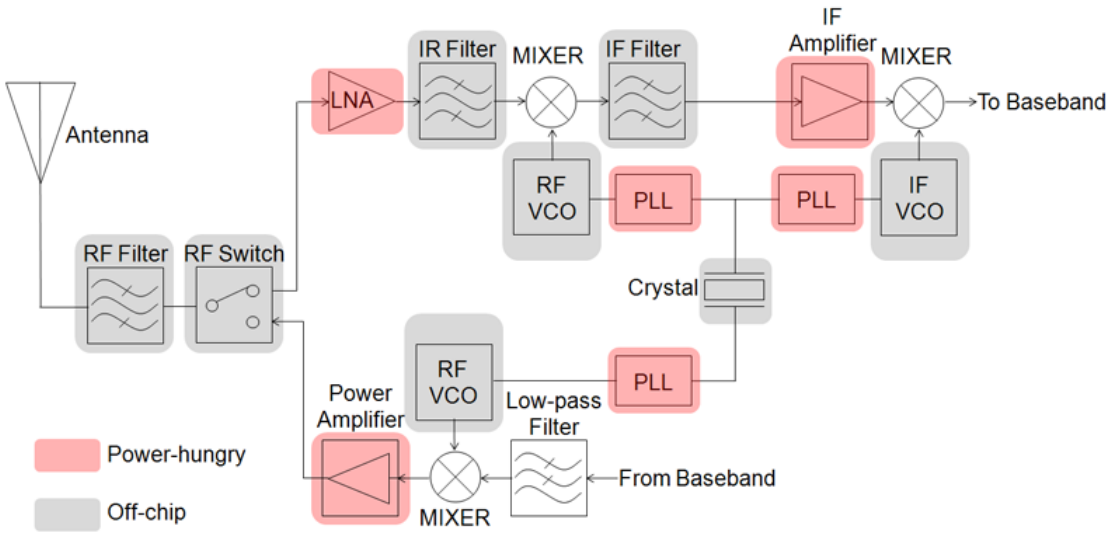

Figure 1.2: Super-heterodyne Radio Architecture.

most radio transceivers depend on a large number of discrete frequency-selection components, such as RF band-pass filters, intermediate-frequency (IF) channel-selection filters, RF voltage-controlled oscillators (VCOs) and quartz crystal oscillators to perform the necessary analog signal processing as shown in Figure 1.2. These off-chip devices occupy a large portion of transceiver architecture, expensive in terms of price and the active electronics required to interface with them consume considerable amount of power.

The recent development in utilizing integrated circuit (IC) compatible lithography to micromachine mechanical structures has created an emerging field called Micro Electro Mechanical Systems (MEMS). This new field allows a new way of viewing electrical circuits and mechanical structures as an integrated system that can perform multiple of functions, including actuation, sensing and signal processing. The novel technology to fabricate microscale mechanical parts integrated with electronics has resulted vibrant research in this area. Earlier research works in MEMS since 1980s have been geared toward micro-sensors. A high-sensitivity capacitive pressure transducer with active processing circuit on the chip was demon-

strated [6]. The electrostatically resonated microbridge was fabricated and its vibration was detected capacitively using an integrated NMOS circuit [7]. Two novel processes for fabricating silicon piezoresistive pressure sensors were reported [8]. A surface micromachined capacitive accelerometer was designed and fabricated with on-chip detection circuitry [9].

The history of micromachining high quality factor (Q) vibrating structure was dated back in 1965, when Nathanson and Wickstrom from Westinghouse Research Laboratories fabricated mechanically resonating cantilevers over a semiconductor surface [10]. The further development of these devices resulted an electrostatically excited tuning fork that employs field effect transistor to read the output [11]. A bandpass filter response was excited by mechanically coupling two adjacent resonant gate transistors (RGT). Two adjacent RGT's were fabricated with a coupling spring near the clamped end. Input electrodes were patterned underneath the first RGT to excite it electrostatically. The vibrations of the first RGT are mechanically transmitted to the second RGT via the coupling web, causing the second RGT to vibrate. The motional output current is detected by the electrodes underneath the second RGT. Figure 1.3 (a) and (b) show the schematic and microphotograph of a 2-pole mechanically-coupled resonant gate transistors fabricated by H. C. Nathanson *et al*. Frequency response of the filter exhibits center frequency (f_C) of 22 kHz and filter bandwidth (BW) of 300 Hz as shown in Figure 1.3 (c). In this work Nathanson *et al* was able to demonstrate a mechanically-coupled RGT filter with maximum f_C of 132 kHz and BW of 1 kHz as shown in Figure 1.3 (d).

The research in resonant gate transistors at that time encountered several technical barriers and did not proceed any further. The most severe technical problems that researchers encountered thereupon were reproducibility and predictability of resonant frequencies, temperature stability and potential limitations on lifetime

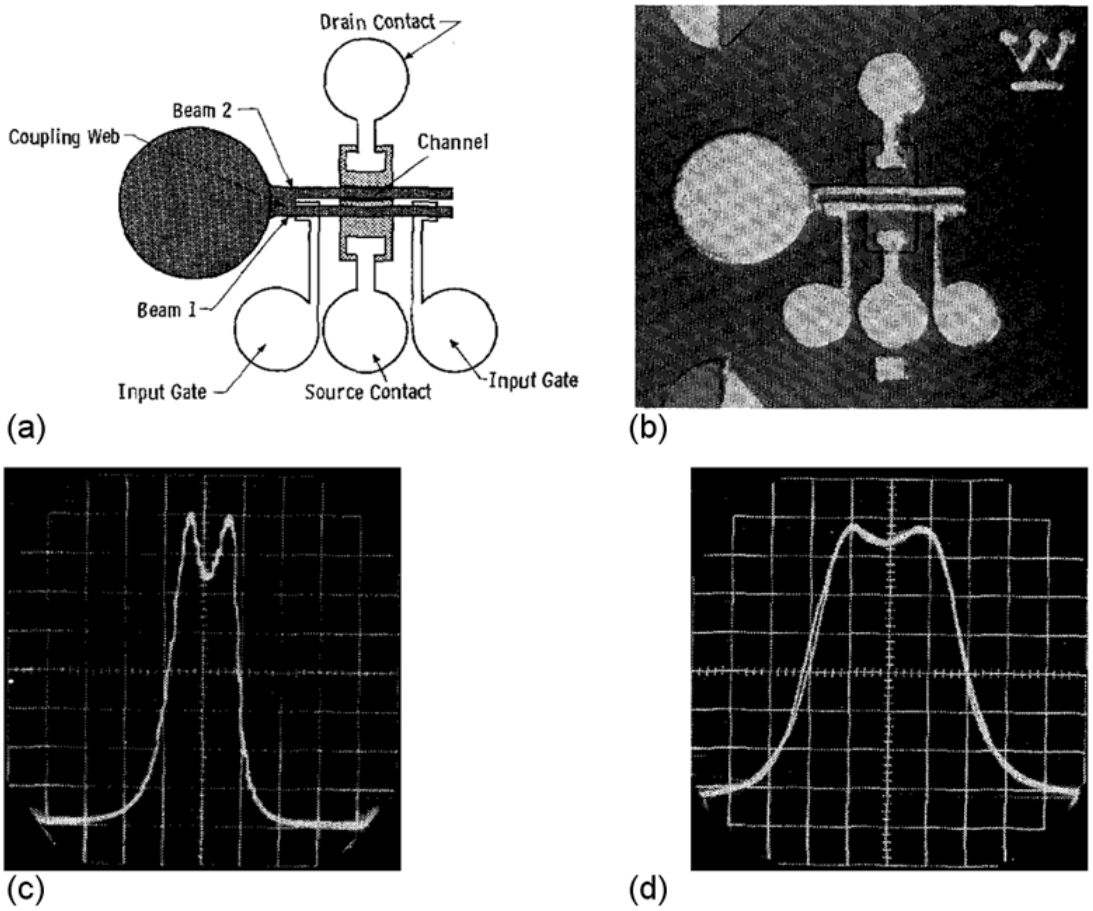

Figure 1.3: Mechanically-coupled resonant gate transistors (RGT) (a) Device geometry, (b) Microphotogrpah of a device with cantilever length of 240 μm, (c) Frequency response of a mechanically-coupled RGT with f_C of of 22 kHz and BW of 300 Hz, and (d) Frequency response of a mechanically-coupled RGT with f_C of of 132 kHz and BW of 1 kHz.

due to fatigue [12]. Surface micromachining started to gain back the attention since Howe and Muller successfully demonstrated the resonant-microbridge vapor sensor [7]. The advancement in surface micromachining in the recent years has attracted a number of scientists to investigate more reliable, stable and reproducible micromechanical resonators and filters. Interdigitated finger (comb) structures were demonstrated to be effective for exciting electrostatically the resonance of polysilicon microstructures parallel to the plane of the substrate [13]. Resonance was observed visually, with frequencies ranging from 18 kHz to 80 kHz and quality factors from 20 to 130. Microelectromechanical filters based on coupled, lateral microresonators were succesfully fabricated [14]. This class of device has potential signal-proceessing applications for filters which require narrow bandwidth (high-Q), good signal-to-noise ratio (SNR) and stable temperature and aging characteristics. The filter has a measured center frequency of 18.7 kHz and a bandwidth of 1.2 kHz in atmospheric pressure. Further research in surface micromachining of polysilicon has resulted the MEMS based monolithic high-Q oscillator, fabricated via a combined CMOS plus surface micromachining technology [15].

Early experiments at AT&T Bell Laboratories in etching bulk silicon have been developed to become another popular process of micromachining beside surface micromachining. Bulk micromachining is a fabrication technique to build mechanical structures by starting with a bulk silicon wafer, and then etching away unwanted parts, and being left with the desired mechanical devices. Bulk micromachining has been adopted strongly by MEMS community and became another prominent method to realize microelectromechanical resonators and filters. Bulk micromachining was used to back-etched a silicon wafer and released thin film bulk acoustic resonators (FBARS) with measured Q's of over 1000 and resonant frequencies (f_C) as low as 1.5 GHz and as high as 7.5 GHz [16]. The availability of high quality

single crystalline silicon device on insulator (SOI) wafers in combination with bulk micromachining technique has motivated several research groups to investigate the performance of SOI based MEMS resonators. Single-crystal silicon (SCS) capacitive resonators with operating frequencies in the high frequency ($3-30$ MHz) and very high frequency ($30-300$ MHz) range were successfully fabricated and characterized [17]. A bulk acoustic mode silicon micromechanical resonator with the first eigen frequency at 12 MHz and the Q of $180,000$ was demonstrated [18]. By using a low-noise preamplifier, a high spectral purity oscillator constructed using the same resonator was reported with phase noise less than -115 dBc/Hz at 1 kHz offset from the carrier.

The demand for ultra low-power, light weight and highly integrated System-on-Chip (SoC) solutions has been placing accumulating pressure on the conventional RF circuit technology to reduce the number of off-chip and bulky passive components including the power-hungry electronic circuitry. On the other hand, the recent progress and development in micromachining through surface and bulk micromachining processes have promised innovative solutions to integrate RF electronics and MEMS technology. The "demand" factor from one research field and "availability" factor from another research area have strongly bridge the engagement between RF and MEMS as a new promising integrated technology to answer many of the unsolved problems in wireless communications.

1.1 Analog Spectral Processors

Wireless communications and microprocessing have greatly motivated the research of RF MEMS resonators and filters today. As the communication industry moves towards quad-band and 7-band technology, there is a growing demand for light-weight, low-power consumption and compact cellular phones that operate at the global range of frequency standards. Using traditional surface acoustic wave (SAW)

technology for these quad-band and 7-band radios, $10-15$ large and power-hungry filters fabricated on different substrates are required. On the other hand, filter banks composed of high-Q micromechanical resonators can be fabricated on-chip in silicon, reducing size, weight, cost, and power in radio communications. This fact has driven several research groups to target their investigation to fit the performance of MEMS resonators or filters for a certain industry standard transceiver architecture or for a particularly allocated frequency spectrum and bandwidth [19–21].

Apart from commercial motivation, there is a growing Military interest in developing a handheld radio operating from 20 MHz to 6 GHz. This high performance radio is expected to aid battlefield communication by enabling a cognitive system that can find less-crowded frequencies to operate. In order to realize this class of radio, we need to constitute a compact, low-power handheld device that combines a spectrum analyzer and a truly powerful communication device. The spectrum analyzer would scan the frequency spectrum all the way from 20 MHz to 6 GHz to find empty spots channels that are receiving less use. Such a wide-band spectral processor would help soldiers switch channels quickly to avoid enemy jamming measures at military-use frequencies, while also enhancing military and civilian communications at other frequencies. The simplified receiver architecture of the Analog Signal Processors (ASP) is shown in Figure 1.4.

In contrast to the traditional super heterodyne receiver architecture, this receiver architecture requires the existence of high performance tunable filters to discern signals with dynamic waveforms and bandwidths between 0.1 MHz and 5 MHz. This requires frequency-agile RF filters, generating a strong demand for narrow-bandwidth channel-select filters with very high quality factors, which can be formed using high-Q MEMS resonators.

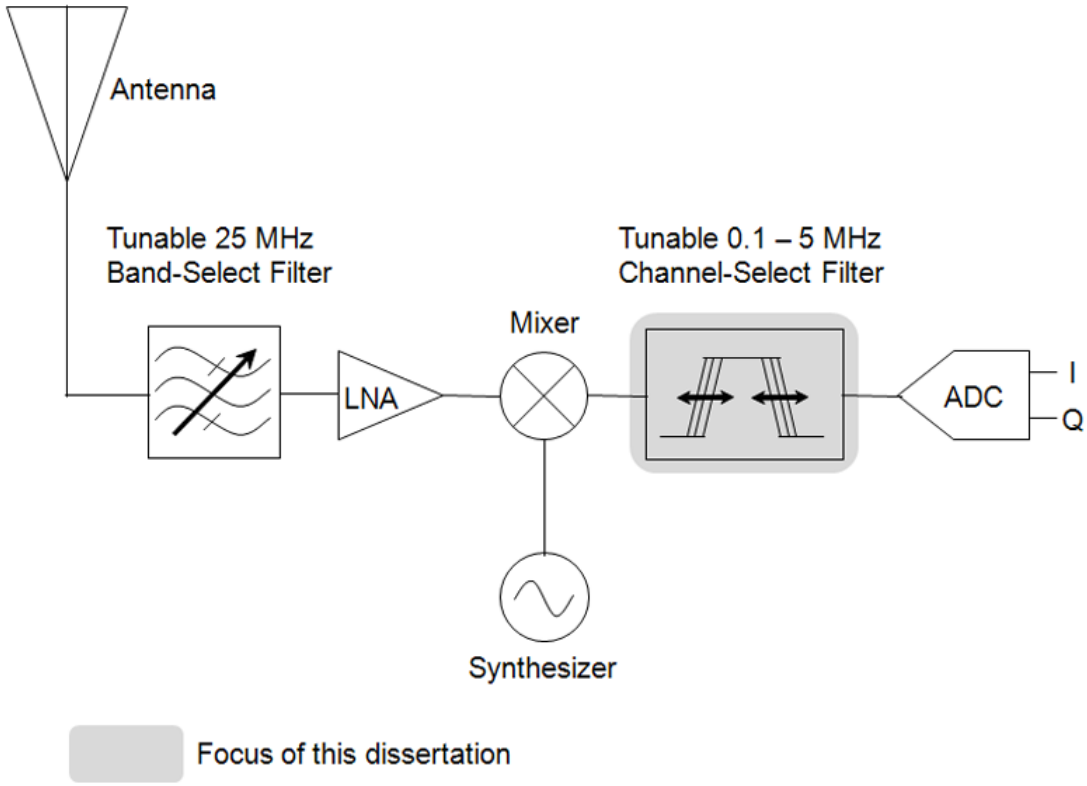

Figure 1.4: Receiver architecture of Analog Signal Processors.

The focus of this dissertation is to investigate different transducer materials, transduction mechanisms and device designs to realize these frequency tunable radio frequency channel-select filters using the currently available micro-fabrication technology.

1.2 Previous Electromechanical Resonators

A resonator is the basic building block for filters and oscillators in radio architecture. A resonator array can be electrically coupled in a ladder or lattice configuration to form a band-pass filter [22]. In mechanical domain, an array of mechanical resonator can be mechanically coupled with coupling springs to excite a band-pass filter response [23]. High-Q constituent resonators are the essential ingredients for designing narrow-bandwidth band-pass filters. In electrical engineering world, the resonator tank can be realized with electrical components such as inductor (L) and capacitor (C). However, filter designers will find the practical Q for $L-C$ filter is very limited to achieve the channel-select filtering requirement for radio front-end. A vast amount of research efforts have been done to produce resonators with high quality factors. At this point, it is informative to review high-Q resonators that people have designed and fabricated over the years.

1.2.1 Quartz Crystal Resonators

Piezoelectricity has found various applications since it was discovered by Curie brothers in 1880. Early research on exploiting piezoelectric properties of quartz crystal for resonator application was done by Professor Walter Cady in 1921. He developed the first quartz crystal resonator and proposed to use quartz crystals to constitute a filter [24]. Even though there are a variety of materials that exhibit

Table 1.1: Quartz crystal mode of vibration and frequency range

Mode	Frequency Range
Flexural	0.4 - 100 kHz
Extensional	40 kHz - 15 MHz
Shear	0.1 - 200 MHz

piezoelectric effect, however, quartz has become a primary choice to construct narrow bandwidth filter because it is well known to have an excellent long term stability, superior temperature coefficient of frequency (TCF) and high quality factor.

Frequency of operation of quartz crystal resonators is determined by the mode of vibrations. Low-frequency of operation is normally attained by exciting flexural or length-extensional mode of vibrations. A typical low-frequency quartz crystal construction is shown in Figure 1.5 (a) and (b) [22]. The resonance frequency for this class of resonator is determined primarily by the blank length and width dimensions. The blank is supported by headed wires attached at nodal points so as not to dampen the mechanical resonance. These wires are then attached to posts in the crystal base. Higher-frequency crystals are of the thickness shear type, where the resonance frequency is determined by the blank thickness as shown in Figure 1.5 (c). The common packaging of quartz crystal resonator is shown in Figure 1.5 (d). Depending on the frequency of operation the length dimension of a packaged quartz crystal resonator may range from $1.3 - 6.4$ cm. The frequency ranges of typically used modes for quartz crystals are summarized in Table 1.1 [25].

During manufacturing process quartz bar must be cut according to a specific orientation with respect to the crystallographic axes of the quartz. A particular cut will define the optimum frequency of operation, frequency drift over time,

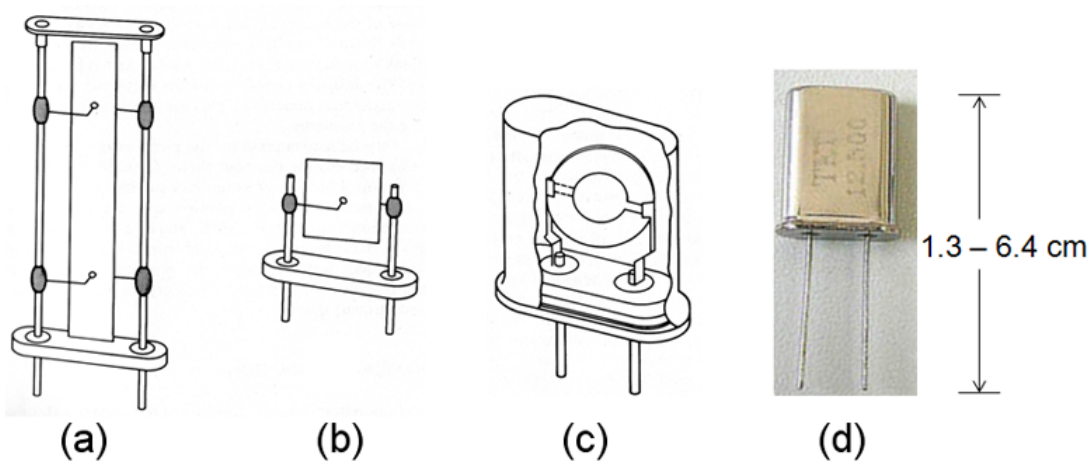

Figure 1.5: Quartz crystal resonators: (a) Flexural/Length-extensional resonator, (b) Face-shear resonator, (c) Thickness-shear resonator, (d) Packaged quartz crystal resonator.

Table 1.2: Quartz crystal cut and frequency range

Cut	Frequency Range (kHz)
X	40 - 20,000
Y	1,000 - 20,000
AT	500 - 200,000
BT	1,000 - 75,000
GT	100 - 550

quality factor, and temperature coefficient of frequency of the resonator. Some of the more common crystal cuts used are summarized, along with frequency ranges, in Table 1.2 [26, 27].

Quartz crystal resonators have been the prima donna for frequency reference and electromechanical signal processing in wireless communications since 1930s due to their superior quality factor, frequency and temperature stability up to very high frequency (VHF) range of operation. However, as the demand in ultra high frequency (UHF) filtering increases, a new class of device is necessary to

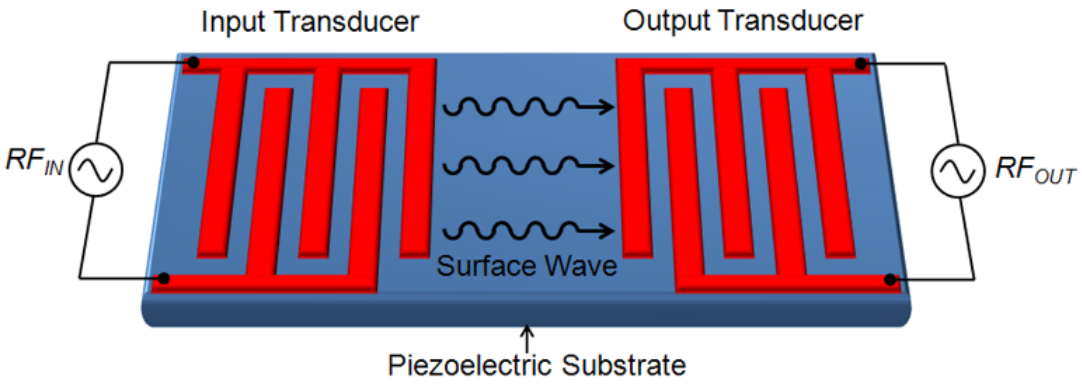

Figure 1.6: A typical SAW device consists of two sets of interdigital transducers. The input transducer converts electric field energy into mechanical wave energy, and the output transducer senses the propagated surface waves and converts the mechanical energy back into an electric field.

extend the frequency domain coverage of quartz crystal resonators.

1.2.2 Surface Acoustic Wave Resonators

The existence of surface acoustic wave (SAW) was first discovered by Lord Rayleigh in 1885 [28]. However, engineering community has not given too much attention until White and Voltmer from University of California, at Berkeley initiated the use of interdigital transducer (IDT) on piezoelectric substrates to excite SAW [29]. The schematic of a SAW resonator is illustrated in Figure 1.6. As a varying electric field is applied to the input transducer, the piezoelectric effect of the substrate induces mechanical displacements. The strongest coupling to surface waves happens when the transducer period matches with the SAW wavelength. The transmitted surface waves across the substrate are detected by the output transducer and converted into electrical output signal. SAW devices normally are fabricated on piezoelectric materials such as quartz, gallium arsenide (GaAs), lithium niobate ($LiNbO_3$) or lithium tantalate ($LiTaO_3$).

SAW devices operate well up to 2.5 GHz frequency range [30]. They are widely

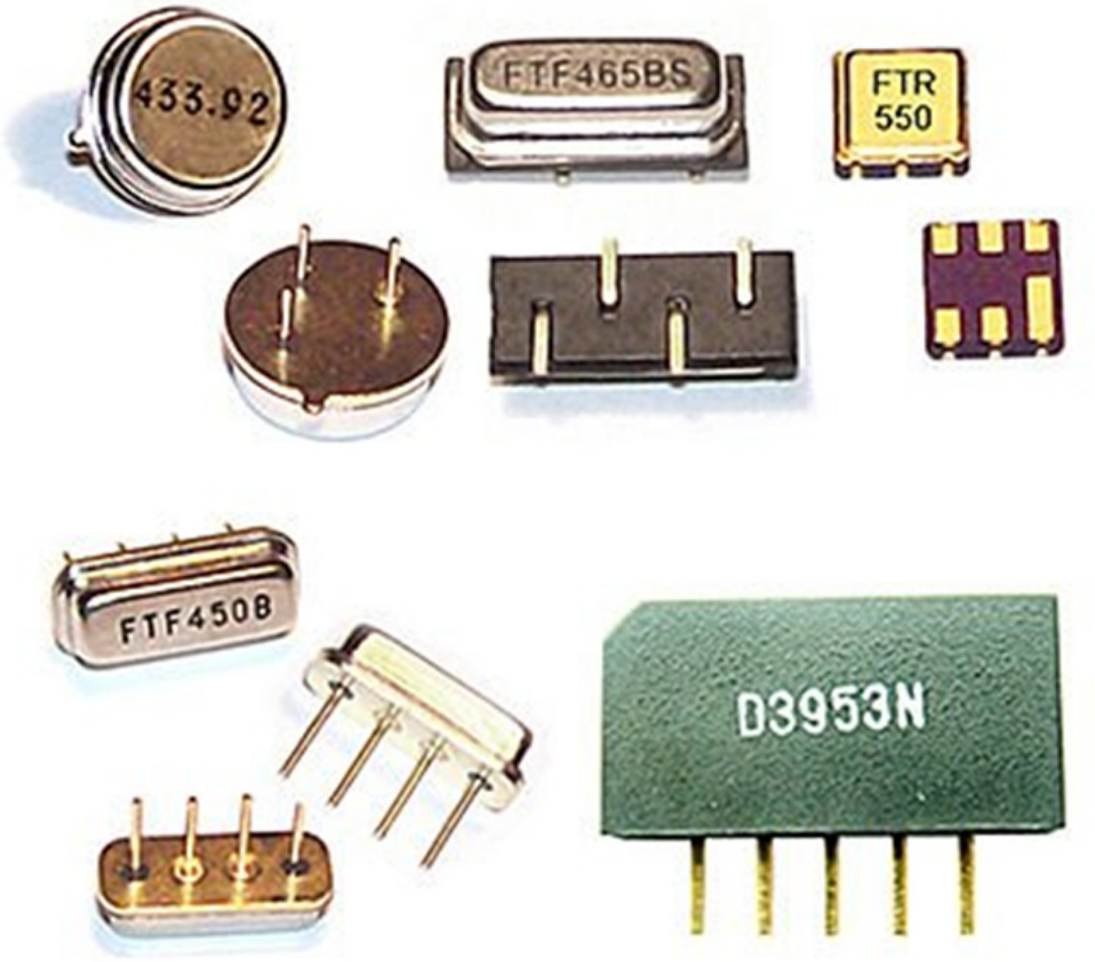

Figure 1.7: Packaged SAW resonators and filters with various frequency ranges.

used for UHF filtering in communication industry [31]. The commonly packaged SAW resonators and filters are shown in Figure 1.7. Despite of the ability to perform excellent filtering at UHF range and ubiquitously used in today's wireless gadgets, SAW devices suffer from poor power handling and frequency shifting due to changes in temperature [32]. The accumulating pressure for miniaturized RF components in wireless communication with superior performance and minimum cost has fueled research activity in development of more integrated, silicon integrated circuit (IC) compatible, micro/nanoscale solutions for signal processing.

1.2.3 Bulk Acoustic Wave and FBAR Resonators

Bulk acoustic wave (BAW) and thin film bulk acoustic resonators (FBAR) have been dominating the wireless market hand in hand since early 1990s. BAW [33–39] and FBAR [40–42] possess lucrative features such as smaller dimensions, higher frequency of operation, better power handling and temperature coefficient compared to SAW devices. They can also be fabricated with traditional IC fabrication process. These two technologies today capture the market for US-PCS duplexers and transmit filters which are needed between the power amplifier and antenna in mobile phone applications [38]. Unlike SAW resonators, both BAW and FBAR devices are transduced by exciting the standing bulk acoustic waves across the thickness of an acoustically isolated piezoelectric thin-film. Aluminum nitride (AlN) and zinc oxide (ZnO) are the commonly used piezoelectric transducer materials for BAW or FBAR devices.

BAW resonators or commonly recognized as solidly mounted resonators (SMR) are normally fabricated on the a stack of acoustic mirror to achieve acoustic isolation from the substrate as shown in Figure 1.8 (a). The more straightforward way to build a bulk acoustic standing wave resonator is by fabricating a membrane BAW or FBAR as shown in Figure 1.8 (b) [36]. The SMR configuration has the advantage of the better mechanical robustness and the simpler process control. Wafer-handling, dicing and packaging of SMR are considerably easy as compared to FBAR. However, the acoustic behavior of FBAR is easier to model and fabrication efforts to accurately deposit the mirror layers can be eradicated.

SMR and FBAR have been conquering wireless market for nearly two decades for their excellent performance in filtering and processing signals at UHF range. The drawback of bulk acoustic wave resonators is they only have single frequency of operation for each deposited layer of transducer. Research efforts have been done

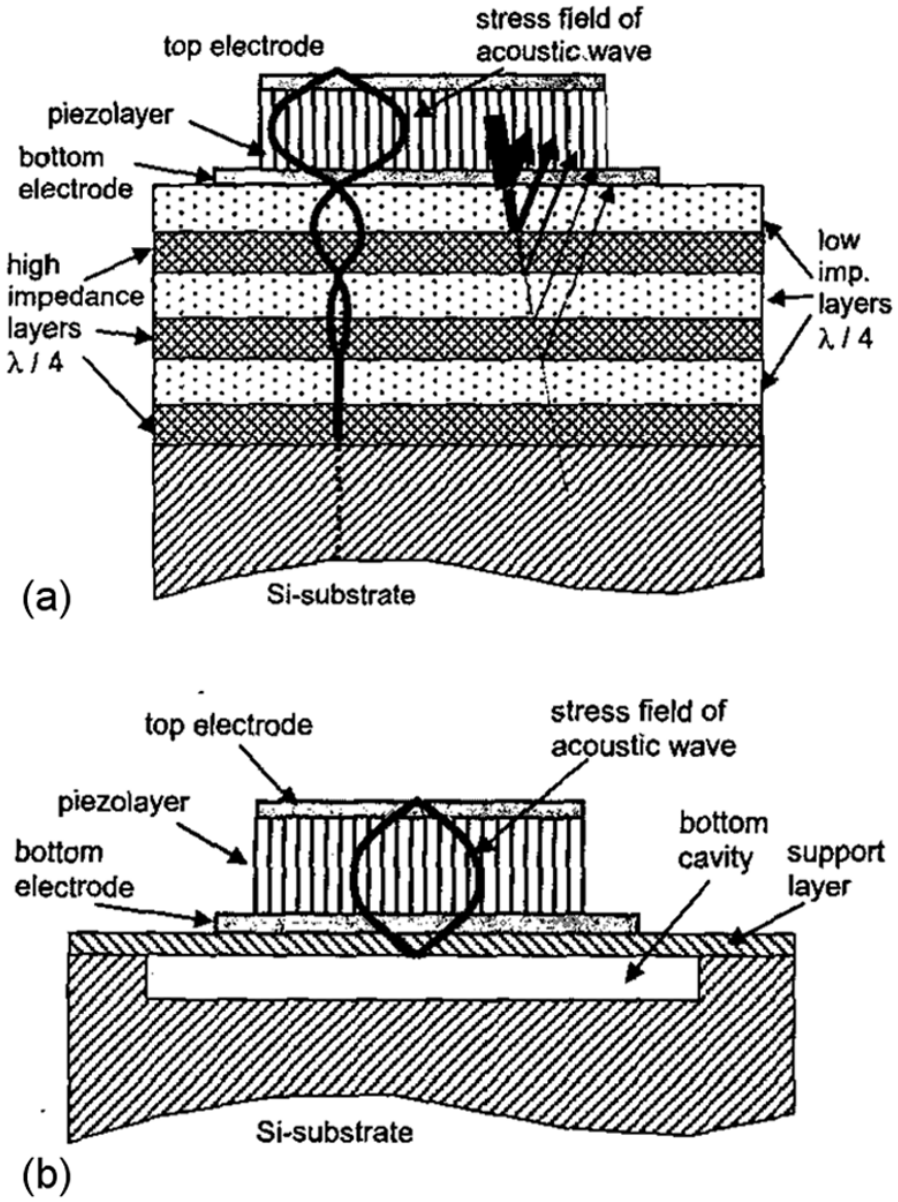

Figure 1.8: Cross-section of bulk acoustic wave (BAW) resonators: (a) Solidly mounted resonators (SMR), (b) Membrane bulk acoustic wave resonator (FBAR).

to introduce frequency tuning in FBAR [43]. However, the recent demand for integrated ultra low-power multi-frequency signal processors on a single chip has motivated researchers to investigate a new generation of devices with alternative modes of vibrations.

1.2.4 Contour-Mode Resonators

Contour mode resonators and filters are of interest because their frequency of operation is determined by the lateral dimensions. Thus, this class of resonators has a large frequency design space that enables the next generation of integrated analog signal processors on a single chip. A resonance frequency above UHF range can be attained by properly scaling the lateral dimensions and excite the device at high-overtone modes of vibrations.

Air-Gap Electrostatically Transduced Resonators

The recent advancement in surface micromachining has facilitated the rapid development of MEMS contour-mode resonators. Since the comb-drive era [13–15], the air-gap surface micromachined electrostatic resonators have aggressively evolved to catch the performance of SAW, BAW and FBAR resonators. A fabrication process has been demonstrated that combines polysilicon surface micromachining, metal electroplating, and a sidewall sacrificial-spacer technique, to achieve high-aspect-ratio, submicron, lateral capacitive gaps between a micromechanical structure and its metal electrodes, without the need for advanced lithographic and etching technology [44]. Using similar fabrication process, radial-contour mode disk resonators were fabricated and reported a resonance frequency as high as 829 MHz and with Q as high as $23,000$ at 193 MHz [45]. A vibrating polysilicon micromechanical "hollow-disk" ring resonator has been demonstrated in several vi-

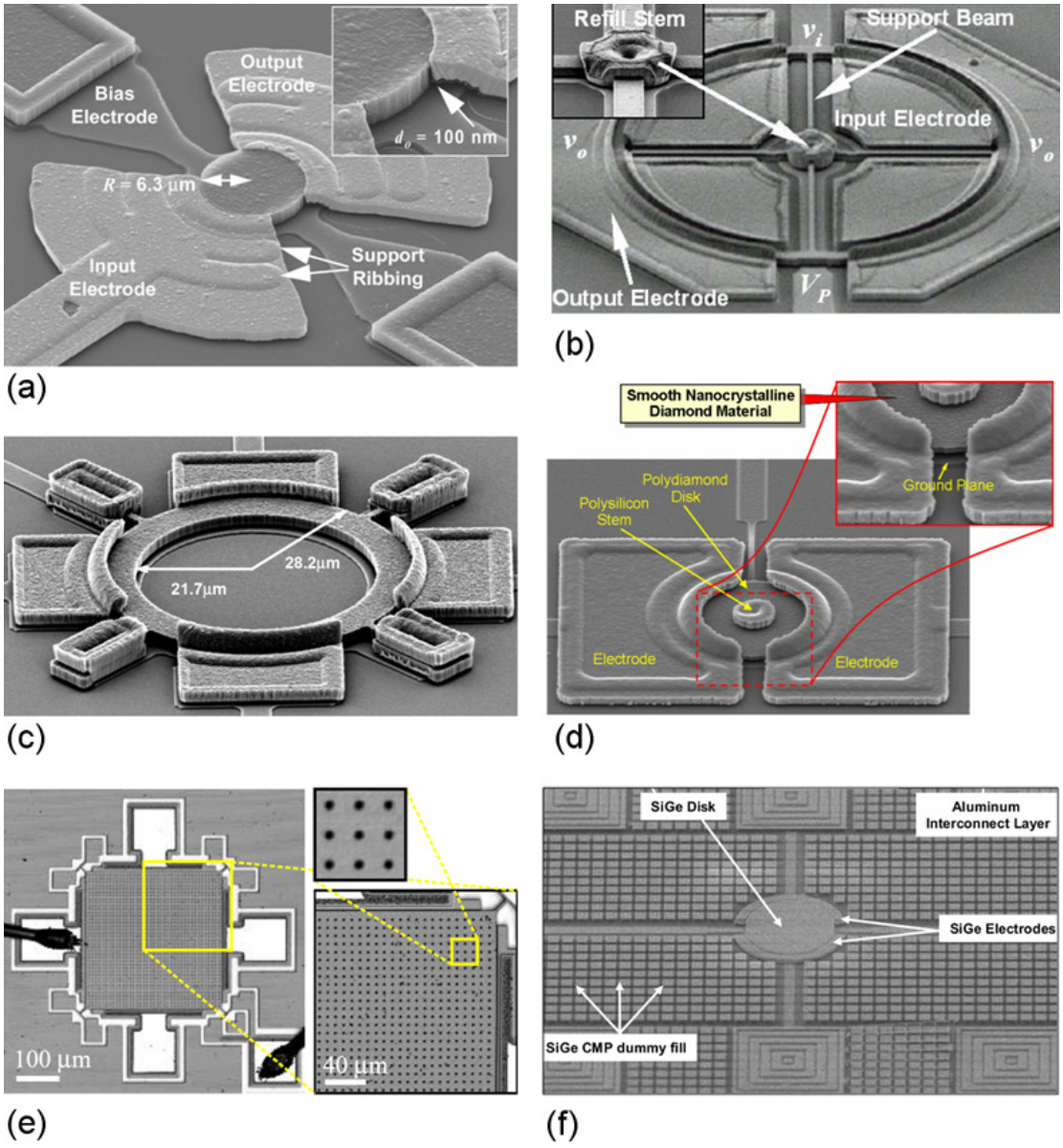

Figure 1.9: Air-gap contour-mode resonators: (a) A radial-contour mode disk resonator, (b) A polysilicon hollow-disk ring resonator, (c) An extensional wine-glass-mode resonator, (d) A nanocrystalline diamond disk resonator, (e) A square-extensional mode resonator, and (f) A Poly-SiGe contour-mode disk resonator.

bration modes spanning frequencies from HF (24.4 MHz), to VHF (72.1 MHz), to UHF (1.169 GHz), with Qs as high as $67,519$, $48,048$, and $5,846$, respectively [46]. Vibrating polysilicon micromechanical ring resonators, using a unique extensional wine-glass-mode shape to achieve lower impedance, have been designed and characterized at frequencies as high as 1.2 GHz with a Q of $3,700$, and 1.52 GHz with a Q of $2,800$ [47]. The first CVD nanocrystalline diamond micromechanical disk resonator with material-mismatched stem has been demonstrated with a recorded resonance frequency of 1.51 GHz with a Q of $11,555$ [48]. A micromechanical 13.1 MHz 2-D plate bulk acoustic mode (BAW) silicon resonator was reported with Q of $130,000$ [49]. Investigations to integrate air-gap contour-mode resonators with SiGe BiCMOS electronics based process have also been performed [50]. Figure 1.9 illustrated several of the previously fabricated air-gap contour-mode resonators.

Despite of the high frequency and high-Q that air-gap electrostatically transduced resonators perform, they suffer from a relatively large motional impedance (R_X), due to reduced transducer area [51] and inefficient electrostatic transduction (compared to lateral d_{31} piezoelectric transduction [52, 53]).

Piezoelectrically Transduced Resonators

Piezoelectric materials such as aluminum nitride or quartz offer larger electromechanical coupling coefficients that facilitate an efficient electromechanical transduction. In order to accommodate multiple-frequency resonators on a single chip with low motional impedance, a number of research teams have explored the development of piezoelectrically transduced contour-mode MEMS resonators and filters. Rectangular plates and rings resonators with an aluminum nitride layer as a transducer sandwiched between the bottom platinum electrode and top aluminum electrode have been fabricated and characterized up to frequency of 236 MHz. These devices were electrically cascaded to form a low insertion-loss (IL) bandpass filter

at 93 MHz [54]. The next generation devices were fabricated and exhibit frequency from 19 to 656 MHz [55]. Zinc oxide transduced contour-mode resonators have been developed and reported f_C of 90 MHz, maximum Q of $3,400$ and R_X of 600 Ω [56]. Piezoelectric on nano-crystalline diamond composite contour-mode resonators were fabricated. These resonators benefit from the large elastic modulus of the nano-crystalline diamond to boost the resonance frequency up to 1.2 GHz [57]. Contour-mode resonators can be mechanically-coupled to realize a bandpass filter. The development of narrow bandwidth, post-CMOS compatible aluminum nitride transduced MEMS filters operating in the VHF and UHF bands have been reported [58]. Figure 1.10 illustrated several of the previously fabricated piezoelectrically transduced contour-mode resonators.

The state of the art piezoelectrically transduced contour-mode resonator has been experimentally measured at frequency of 8.5 GHz [59]. Even though AlN transduced devices are able to attain super high frequency (SHF) range, however, they do not exhibit any frequency tuning capability.

Dielectrically Transduced Resonators

Internal dielectric transduction enhances both the force density of the actuator as well as the sense capacitance [60]. It has been previously proposed and experimentally verified using an aluminum nitride FBAR resonator in non-linear electrostatic mode [61]. Bhave *et al* successfully demonstrated a 121 MHz 3^{rd} harmonic lateral bar resonator with internal electrostatic actuation and sensing of the mechanical motion, by depositing silicon nitride on the top surface of a silicon bar. In this dissertation we will explore more on dielectrically transduced high-Q RF MEMS resonators and investigate the device design for voltage tunable filters.

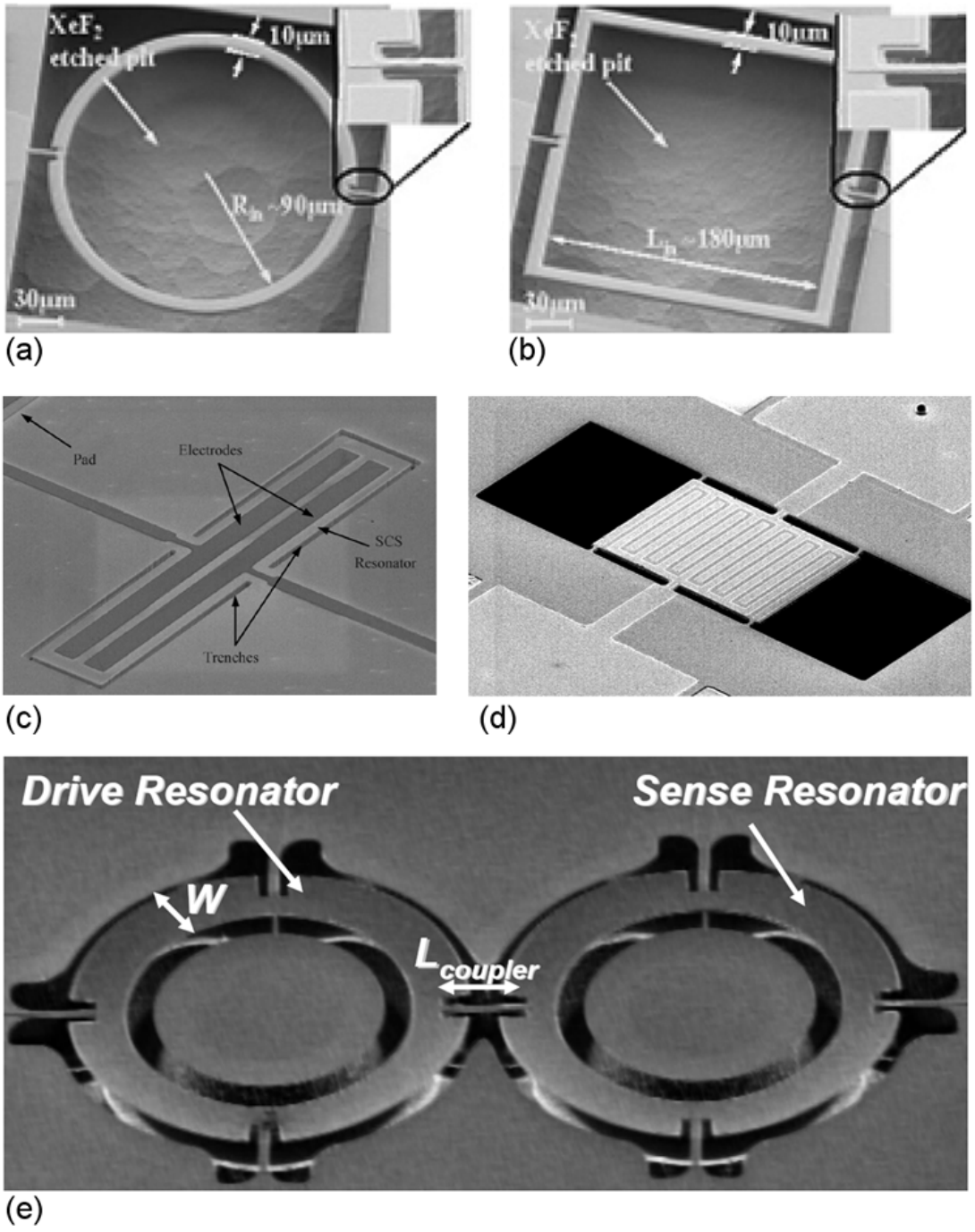

Figure 1.10: Piezoelectrically transduced contour-mode resonators: (a) An AlN transduced ring-shaped contour-mode resonator, (b) An AlN transduced square-ring-shaped contour-mode resonator, and (c) A ZnO on silicon contour-mode resonator, (d) A ZnO-on-nanocrystalline diamond resonator, and (e) An AlN transduced mechanically-coupled contour-mode filter.

1.3 Contributions of this Dissertation

This thesis identifies crucial key features in RF MEMS field that have never been addressed before such as analog and digital frequency and bandwidth tuning of MEMS resonators and filters. The properties of high permittivity solid dielectric transducers such as silicon nitride and hafnia are exploited to demonstrate high-Q MEMS resonators and voltage tunable filter. This thesis also introduces a liquid dielectric to enhance the transduction efficiency and enable the voltage tuning of contour-mode resonators. A novel packaging technology for dielectrically transduced contour-mode resonators and filters that enables the post-MEMS CMOS integrated process is reported.

The properties of ferroelectric materials such as lead zirconate titanate (PZT) are examined and utilized to realize center frequency and bandwidth tunable resonators and filters. The monolithic integration of RF components on-chip has long been a goal of researchers and will enable not only more compact and lower cost systems but previously unachievable signal processing functions. This dissertation successfully demonstrated for the first time monolithically integrated piezoelectric MEMS RF switches with contour-mode filters.

1.4 Dissertation Organization

Chapter 2 demonstrates the design, fabrication and characterization of high-Q thickness shear mode resonators and analog voltage tunable filters. Chapter 3 presents the performances of high-overtone square extensional resonator and digitally programmable filter. Chapter 4 provides an overview of a wafer level packaging technology for MEMS contour-mode resonators. Chapter 5 discusses the aqueous transduction of contour-mode resonators. Chapter 6 explores the study

on PZT transduced resonators. Chapter 7 exploits the properties of PZT transduced resonators to realize voltage tunable bandpass filters. Chapter 8 presents the monolithically integrated PZT MEMS switches and contour-mode filters. Chapter 9 looks ahead on research possibilities that can be performed in the near future based on results that have been accomplished in this thesis.

Appendices of this dissertation will cover the fabrication technologies for thickness shear mode resonators and filters and the calibration and de-embedding methods to characterize RF MEMS resonators and filters.

CHAPTER 2

HIGH-Q MEMS THICKNESS SHEAR RESONATORS AND ANALOG VOLTAGE TUNABLE ELECTRICALLY-COUPLED CHANNEL-SELECT RF FILTERS

2.1 Introduction

A great number of applications in cellular transceivers and sensor networks have mobilized the growth of on-chip, high-Q MEMS resonators and filters to substitute the present off-chip SAW, ceramic and quartz resonators in direct conversion transceivers. Multi-band, multi-standard radio receivers have narrow channels and are susceptible to nearby strong interferers. Channel-select filtering requires small bandwidth, superior stopband rejection, and excellent shape factor to filter out undesired frequencies. MEMS resonators with high-Q, high resonant frequency, and low R_X can be coupled electrically in a ladder configuration to form a channel-select filter that operates at radio frequency.

Radio receivers require a large array of channel-select filters connected in parallel that causes the input capacitance of the filter array to load individual filters and worsening their stop-band rejection. For reconfigurable radios the front-end filters must also handle encoded waveforms with different bandwidth specifications. A filter that facilitates dynamic tuning of filter center frequency and bandwidth will not only overcome fabrication tolerances and performance degradation due to thermal drift, but will also reduce capacitive loading at the filter input, enable handling of multiple waveforms, and substantially decrease the number of filters in next-generation receivers.

The desired filter characteristics are defined by the MEMS resonators as the building blocks of the filter. Minimum insertion loss can be satisfied by decreasing

R_X, while the resonators' Q determines the shape factor. Air-gap electrostatically transduced MEMS resonators have $Q > 10,000$ but are limited by their large motional impedance ($R_X > 10$ kΩ) [48]. In lieu, piezoelectric FBARs have small motional impedance ($R_X > 10\ \Omega$) but relatively low Q ($2,000$) [41].

The thickness shear mode resonator is a suitable nominee to construct a MEMS filter for a number of reasons. Its high-Q mode has been demonstrated successfully in quartz resonators. Furthermore, it has a high frequency and low motional impedance. The thickness shear mode resonator also presents a frequency tuning capability which is useful for compensation of frequency shift due to fabrication errors. Dielectric transduction is accomplished here by sandwiching a thin film high-κ dielectric material between the silicon bar resonator and polysilicon electrodes. This enhances both the force density of the actuator as well as the sense capacitance, thereby improving the resonator's motional impedance by a factor of κ^2 [60].

High frequency resonators were fabricated by reducing the air gap and increasing the transducer area of bulk-mode bar resonators [62]. In spite of their high frequency, the huge R_X of these resonators will produce a high insertion loss filter. An effort to decrease R_X by filling the air gap of a wine-glass disk resonator with silicon nitride is presented in [63], resulting in a resonant frequency of 165 MHz with a Q of $21,400$ and an R_X of 8.5 kΩ. Alternatively, contour-mode aluminum nitride piezoelectric resonators with 656 MHz resonant frequency and an R_X of 170 Ω have been reported. However, the ladder filter comprised of these low-Q piezoelectric resonators exhibited a 20 dB shape factor of 2.7 [55].

This Chapter will first discuss the quarter-wave thickness shear mode (TSM) silicon bar resonator. The silicon bar resonator is capable to reach 723 MHz resonant frequency with a Q of $4,400$ and an R_X of 2.4 kΩ using silicon nitride dielectric

transduction. Furthermore, the superior Q half-wave thickness shear mode of a fully-released bar resonator will be demonstrated. The motional impedance of the half-wave thickness shear bar resonator is significantly reduced by substituting silicon nitride ($\kappa \sim 9$) with hafnium dioxide ($\kappa \sim 28$), reducing dielectric thickness, and increasing the electrode area. The high-Q and low R_X of this resonator facilitate the design of high quality channel-select filters. High performance MEMS resonators can be coupled electrically to form a bandpass filter that operates at radio frequency. The discussion will turn into the design and performance of electrically coupled thickness shear filters. Electrically coupled channel-select filters with 814 MHz center frequency, 600 kHz bandwidth, -4 dB insertion loss (IL) and < 1 dB pass-band ripple will be demonstrated. The next section of this Chapter will present the design of a reconfigurable ladder filter using RF MEMS resonators with voltage-tunable series and parallel resonance frequencies. We will introduce a voltage biasing scheme capable of independently tuning the series resonance and pole-zero separation of the filter's constituent resonators [64]. Coupled with orthogonal frequency tuning, we can construct the filter with desired pass-band characteristic in real time. Finally, this Chapter will be concluded with a concise summary.

2.2 Quarter-wave Thickness Shear Resonator

The quarter-wave thickness shear mode (TSM) bar resonator is excited in a very similar way to quartz resonators. The asymmetric thickness shear mode is common in quartz resonators, excited by the application of an AC signal across electrodes on opposing faces of a quartz crystal [65]. In contrast to the quartz thickness shear mode, the electrode configuration of the dielectrically transduced silicon bar induces a symmetric mode, as shown in Figure 2.1.

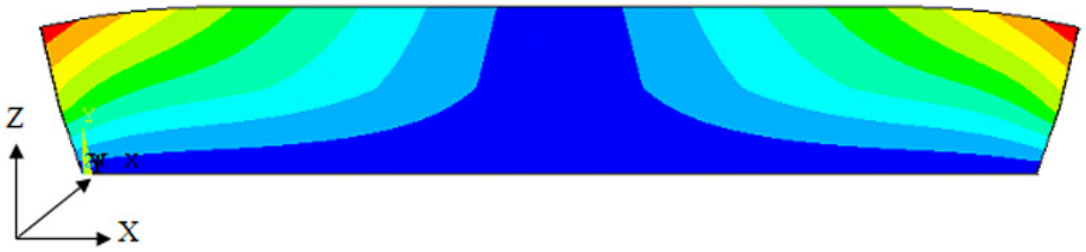

Figure 2.1: X-displacement contour plot from Ansys simulation of the symmetric quarter-wave thickness shear mode.

2.2.1 Electrical Equivalent Impedances of a Quarter-wave TSM Resonator

A one-dimensional thickness shear mode is derived for an unreleased silicon bar transduced by a thin dielectric film. The film, deposited on top of the bar, is sandwiched between the silicon bar and conducting top electrodes as shown in Figure 2.2. The bottom face of the bar is fixed to an effectively infinite oxide layer, imposing a zero-displacement boundary condition at the base of the bar. In this configuration, the silicon bar is biased to a DC voltage V_{DC} while a small alternating voltage v_{AC} is applied to the top electrode. The voltage drop across the electrode-bar parallel plate capacitor induces a normal force on the dielectric film, transferring to a lateral strain in the dielectric. Though the strain is in fact uniform in both lateral directions, we consider a long narrow bar, approximating a one dimensional model of the strain. This strain is distributed between the film and silicon bar, inducing a quarter-wave thickness shear resonant mode. The lateral displacement u_x for the one-dimensional thickness shear mode is given by

$$u_x(x,z,t) = Ax \sin\left(\omega \left(\sqrt{\frac{\rho}{G}}\right)_{Si} z\right) e^{j\omega t} \tag{2.1}$$

for the quarter-wave thickness shear resonant frequency of

$$\omega = \frac{\pi}{2b}\left(\sqrt{\frac{\rho}{G}}\right)_{Si} \tag{2.2}$$

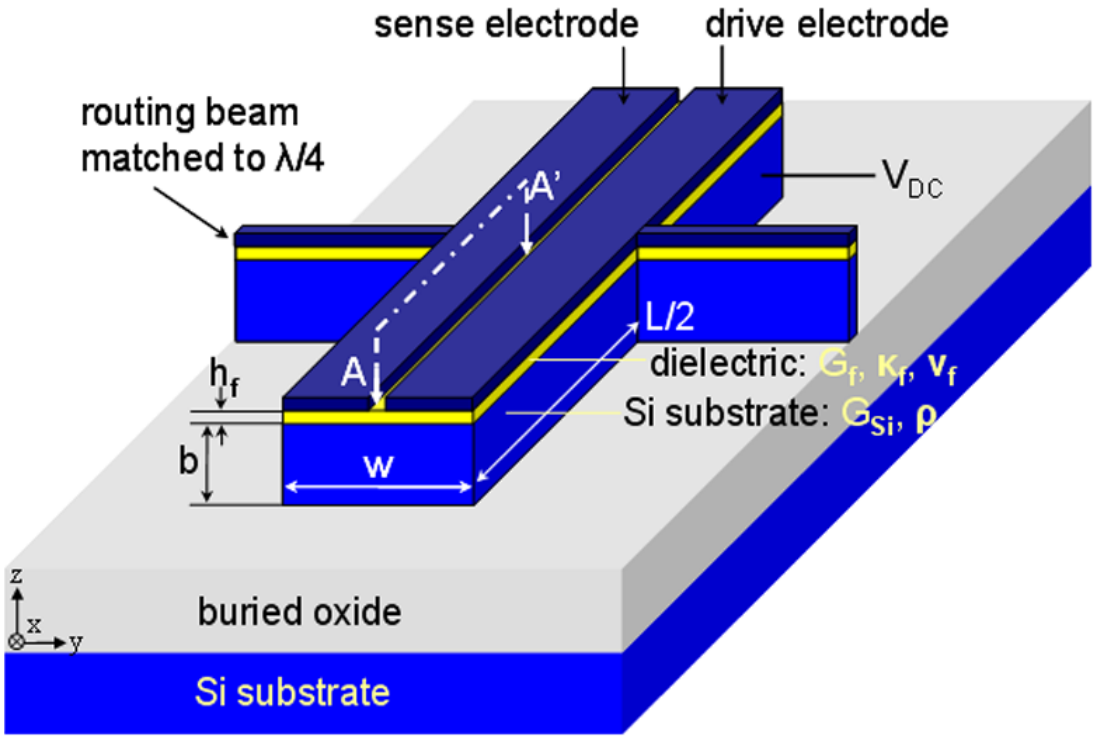

Figure 2.2: The schematic of an unreleased thickness shear bar.

A voltage $V_{DC} + v_{AC}$ applied across the dielectric film generates a normal force

$$f_z \approx -V_{DC}\frac{\kappa_f \epsilon_0 wL}{2{h_f}^2} v_{AC} \tag{2.3}$$

for a bar of width w and length L, where κ_f and h_f are the relative permittivity and thickness of the dielectric film, respectively. Here, we make the approximation that $v_{AC} << V_{DC}$. The factor of 2 in the denominator arises from a configuration in which the drive electrode covers half the width of the bar, and the sense electrode occupies the other half. The laterally transferred strain in the film is

$$\epsilon_{x,f} = \nu_f \epsilon_z = \frac{\nu_f f_z}{E_f wL} \tag{2.4}$$

and the lateral stress in the film is

$$\sigma_0 = {E_f}^* \epsilon_{x,f} = \frac{\nu_f f_z}{(1-\nu_f)\, wL} \tag{2.5}$$

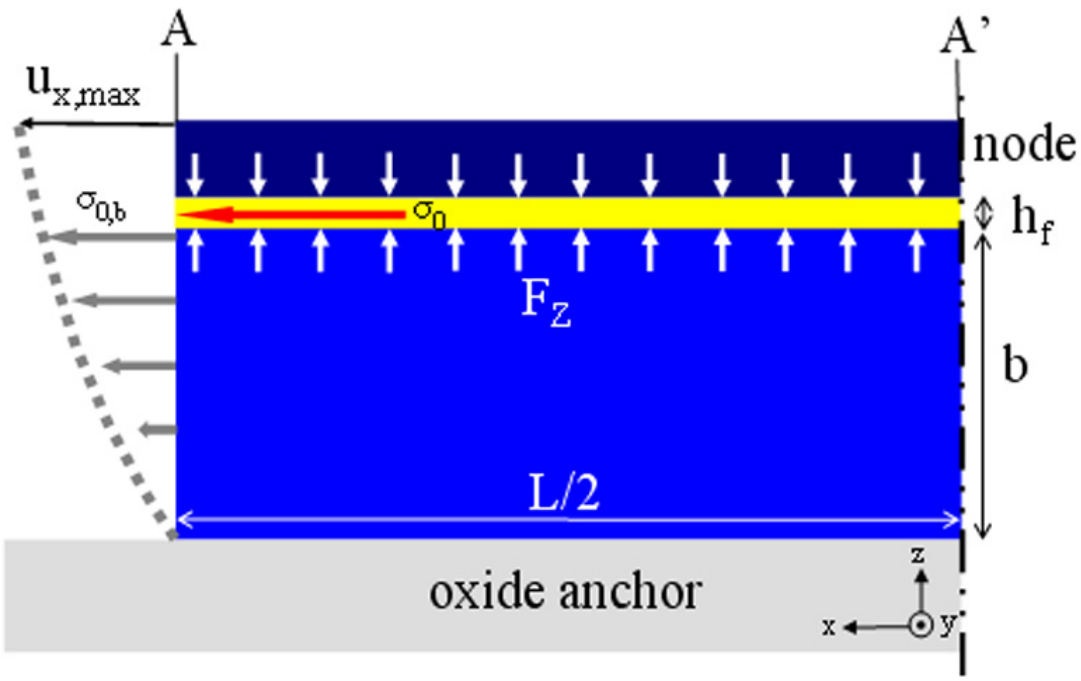

Figure 2.3: 2-D cross-section schematic of the conversion of transverse electrostatic stress in the silicon nitride thin film to thickness shear mode in the half-length (A-A' in Figure 2) bar resonator.

where $E_f{}^*$ is the axial Young's modulus of the dielectric film. This initial lateral stress σ_0 functions like an effective residual stress in the film, consequently distributing itself in both film and bulk silicon, as illustrated in Figure 2.3. We assume that the electrode's thickness is negligible with respect to the thickness of the silicon bar resonator. The one-dimensional approximation holds true for resonators with $L >> w, b$. The shear stress in the silicon is approximated to be distributed linearly through the bar due to the displacement boundary condition imposed by the oxide anchor. This yields a maximum shear stress in the silicon of

$$\sigma_{0,b} = \frac{G_{Si} h_f}{G_f h_f + \frac{1}{2} G_{Si} b} \sigma_0 \approx \frac{2h_f}{b} \sigma_0 \tag{2.6}$$

in the approximation that $h_f << b$. The maximum displacement of the bar can then be approximated as

$$u_{x,max} = \frac{b}{G_{Si}}\sigma_{0,b} = \frac{\nu_f \kappa_f \epsilon_0 V_{DC} v_{AC}}{(1-\nu_f)\, G_{Si} h_f} \tag{2.7}$$

With the first-order determination of the quarter-wave thickness shear mode, we calculate the motional impedance R_X, inductance L_X, and capacitance C_X of the resonator. The change in the sensed capacitance over time is approximated as

$$\frac{\partial C}{\partial t} \approx \frac{Q\omega\kappa_f\epsilon_0 wL}{2{h_f}^2}\Delta h_{max} \tag{2.8}$$

The quality factor Q is introduced here to account for effective displacement amplification at resonance. The film is laterally expanded and contracted as the bar resonates, causing the thickness of the film to change with a Poisson efficiency factor. The maximum change in the film thickness is given by

$$\Delta h_{max} = \nu_f u_{x,max} \tag{2.9}$$

The output current is

$$I_{Out} = V_{DC}\frac{\partial C}{\partial t} = \frac{Q\pi\left(\nu_f\kappa_f\epsilon_0 V_{DC}\right)^2}{4\left(1-\nu_f\right)\sqrt{G_{Si}\rho}}\frac{wL}{{h_f}^3 b} v_{AC} \tag{2.10}$$

giving a motional impedance of

$$R_X = \frac{v_{AC}}{I_{Out}} = \frac{4\sqrt{G_{Si}\rho}}{Q\pi}\frac{(1-\nu_f)}{\left(\nu_f\kappa_f\epsilon_0 V_{DC}\right)^2}\frac{{h_f}^3 b}{wL} \tag{2.11}$$

The effective mass for the thickness shear mode is

$$M_{Eff} = \frac{\rho w}{L^2}\int\int x^2 \sin^2\left(\omega\sqrt{\frac{\rho}{G_{Si}}}z\right)dxdz = \frac{1}{6}\rho wLb \tag{2.12}$$

and the effective spring constant is

$$K_{Eff} = M_{Eff}\omega^2 = \frac{\pi^2}{24}\frac{G_{Si}wL}{b} \tag{2.13}$$

From equations 2.11 to 2.13, for

$$R_X = \frac{\sqrt{K_{Eff} M_{Eff}}}{Q\eta^2} \tag{2.14}$$

The electromechanical coupling constant η is given by

$$\eta^2 \approx \frac{\left(\pi w L \nu_f \kappa_f \epsilon_0 V_{DC}\right)^2}{24\left(1-\nu_f\right) {h_f}^3 b} \tag{2.15}$$

The motional capacitance C_X is

$$C_X = \frac{\eta^2}{K_{Eff}} = \frac{\left(\nu_f \kappa_f \epsilon_0 V_{DC}\right)^2}{\left(1-\nu_f\right) G_{Si}} \frac{wL}{{h_f}^3} \tag{2.16}$$

and the motional inductance L_X is

$$L_X = \frac{M_{Eff}}{\eta^2} = \frac{4\left(1-\nu_f\right)\rho}{\pi^2\left(\nu_f \kappa_f \epsilon_0 V_{DC}\right)^2} \frac{b^2 {h_f}^3}{wL} \tag{2.17}$$

2.2.2 Fabrication Process

A 68 nm low stress silicon nitride thin film is first deposited by LPCVD at 850°C on an n-type low resistivity silicon on insulator (SOI) wafer with a 1.8 μm thick single crystal silicon (SCS) device layer. The silicon nitride is patterned to open contact holes to bias the silicon resonator as shown in Figure 2.4 (a). A 120 nm layer of n-doped polysilicon is then deposited by LPCVD at 620°C, annealed at 1,000°C for 40 minutes, and patterned to form the electrodes as shown in Figure 2.4 (b). This is followed by a deep reactive ion etch (DRIE) step to define the resonator into the silicon device layer as shown in Figure 2.4 (c). The unreleased SEM image of a quarter-wave thickness shear mode resonator is shown in Figure 2.5. Appendix A will discuss a detail fabrication process flow for thickness shear mode resonators.

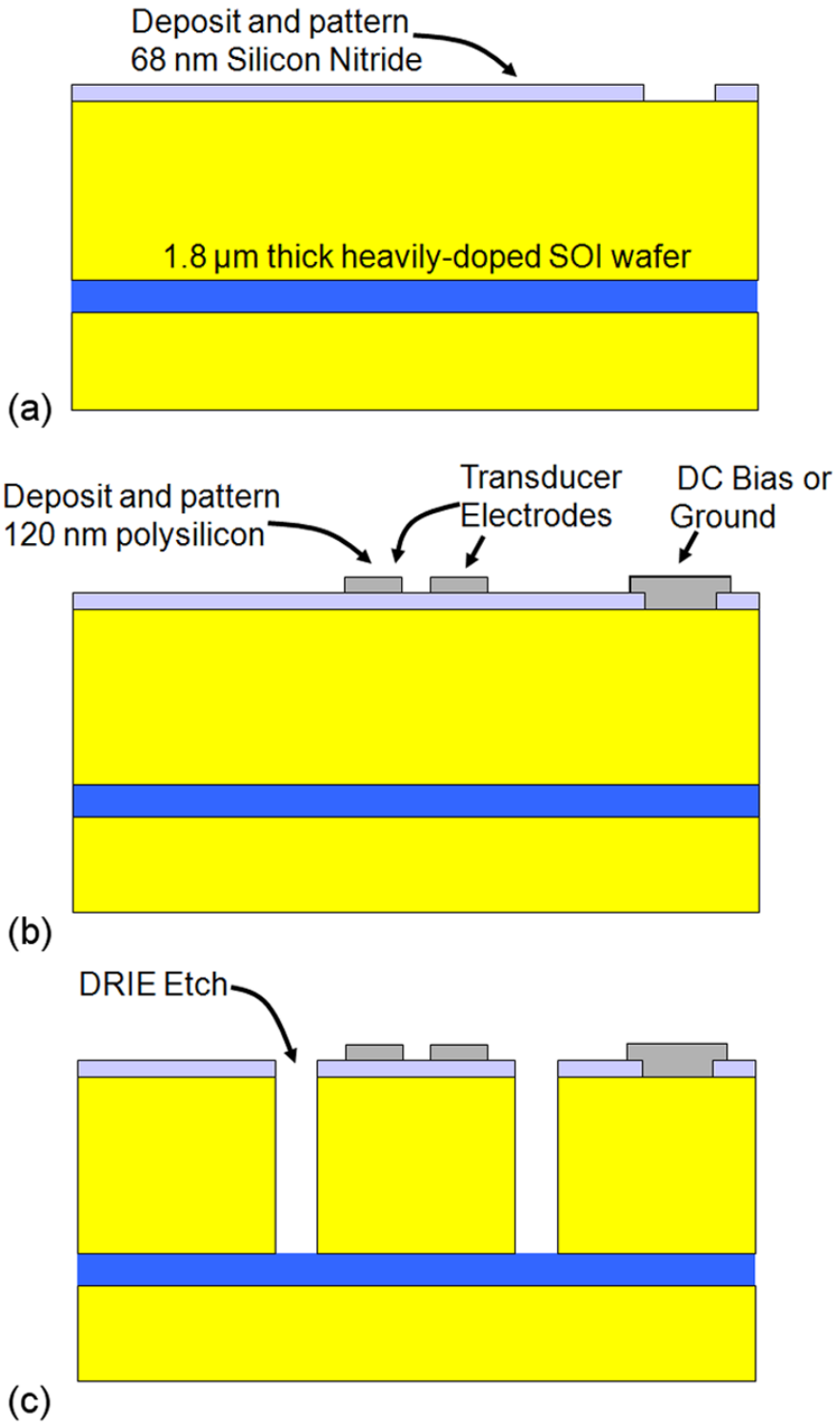

Figure 2.4: Fabrication process flow of quarter-wave thickness shear mode resonators.

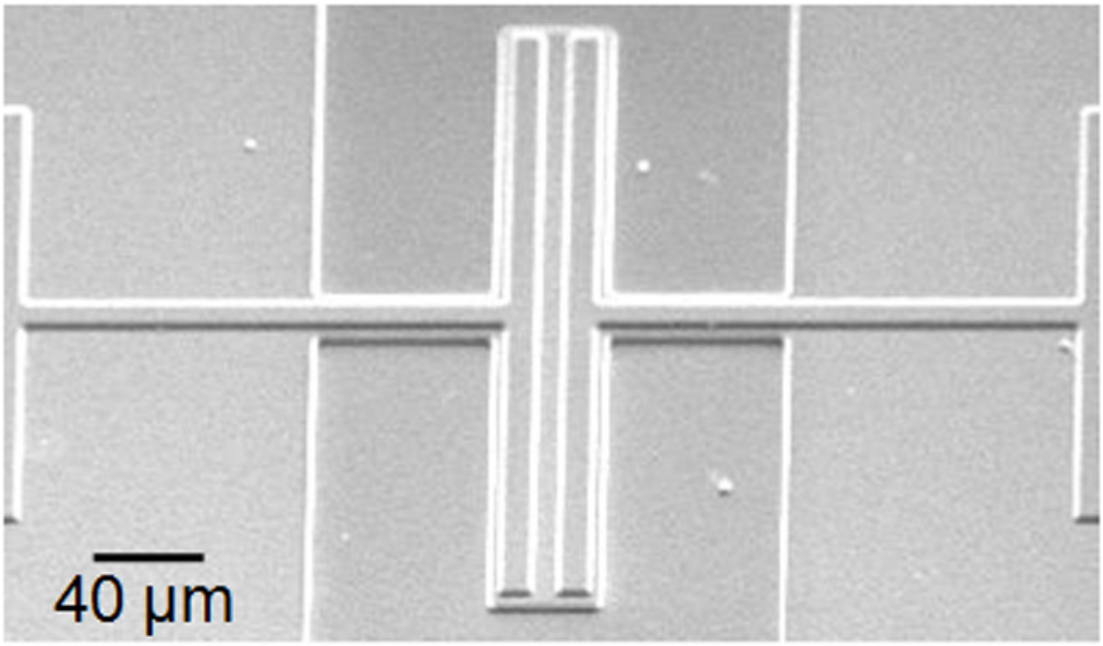

Figure 2.5: SEM of a silicon nitride-on-silicon unreleased bar resonator.

2.2.3 Measurement Results

An unreleased 80 μm long by 40 μm wide bar resonator was characterized using a Desert Cryo microwave probe station. The resonator body was grounded and a *DC* bias was applied to both the drive and sense electrodes with bias-Ts from MiniCircuits. Transmission measurements were performed using an Agilent 8753ES Network Analyzer and the quality factor and insertion loss were extracted from the measured data. The motional impedance of the resonator was determined from the insertion loss data after adjusting for the attenuation losses at the drive pad. The quarter-wave thickness shear vibration mode of the unreleased silicon resonator was measured with a resonant frequency of 713 MHz, an R_X of 10.5 kΩ and Q of $1,517$. Transmission response of the measured device is shown in Figure 2.6.

It has previously been shown that quality factor improves with reduced anchor area. By performing a timed etch of the buried oxide in HF as shown in Figure 2.7,

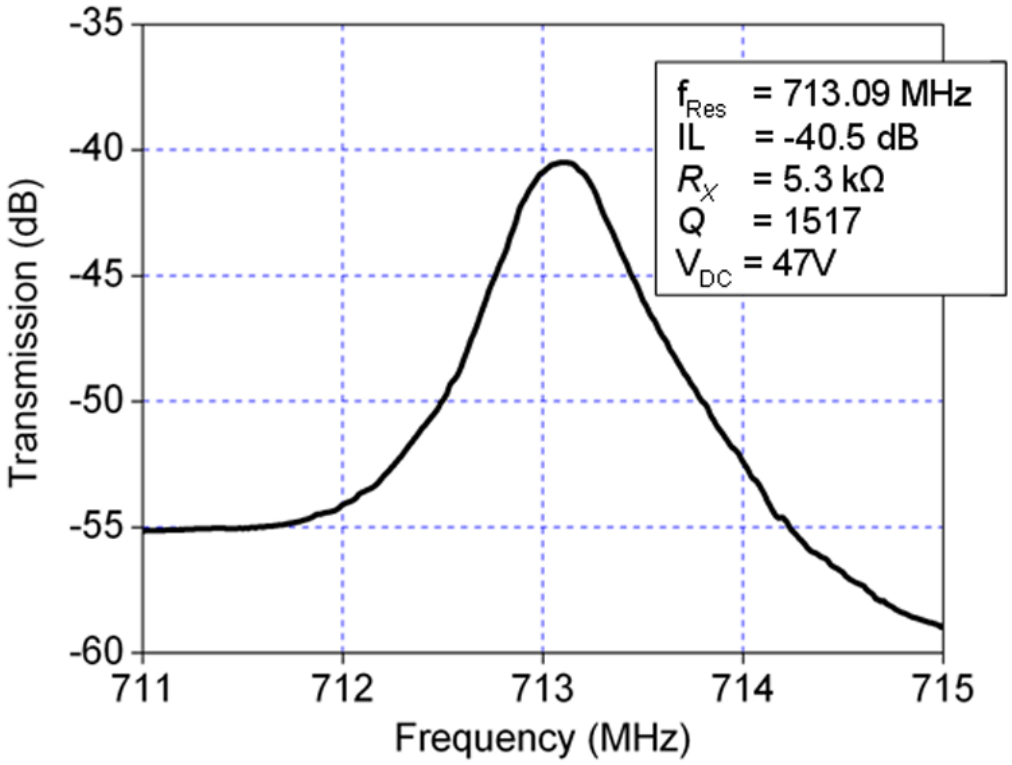

Figure 2.6: Measured transmission of the thickness shear mode of the unreleased resonator in air.

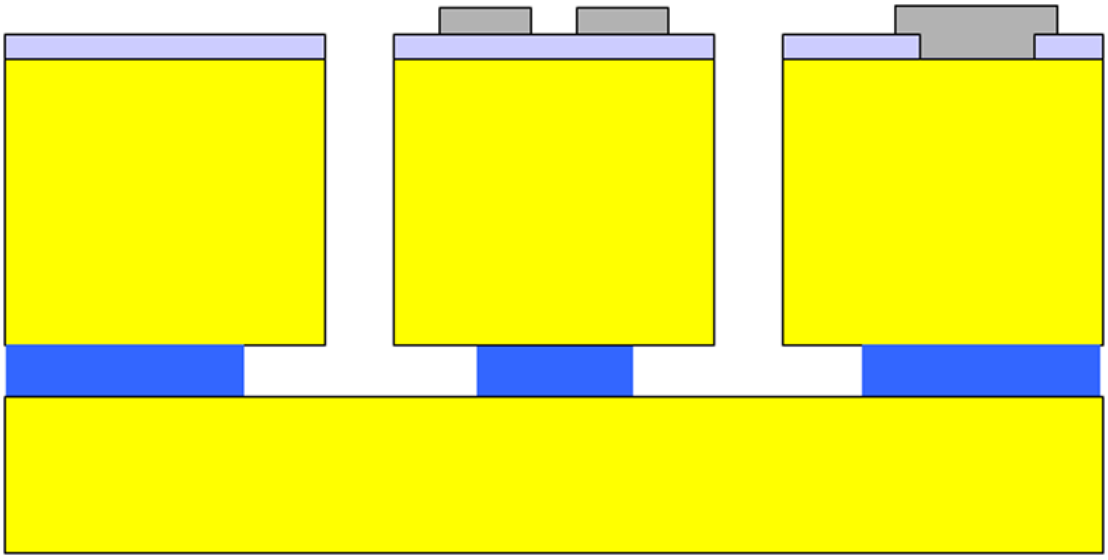

Figure 2.7: A partially released quarter-wave thickness shear mode resonator.

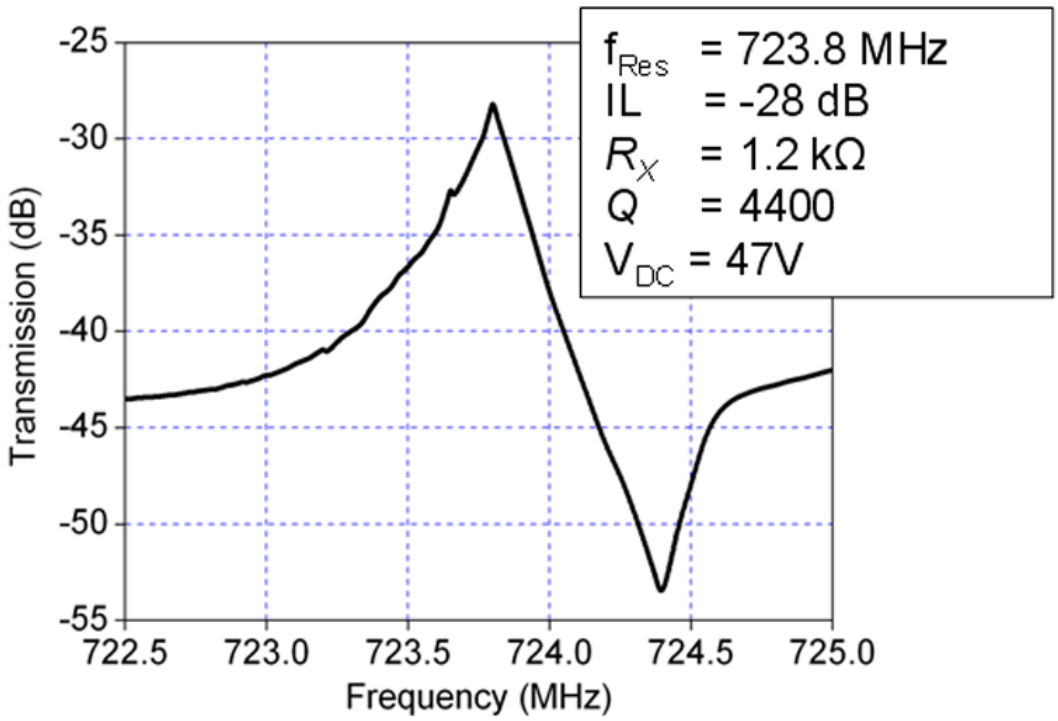

Figure 2.8: Measured transmission of the partially released shear mode resonator in air.

the overall contact area between the oxide and bottom surface of the resonator was reduced to approximately 30 μm x 5 μm. This partially released bar had a resonant frequency of 723 MHz, R_X of 2.4 kΩ and Q of 4, 400 in air. Transmission response of the measured device is shown in Figure 2.8. The large acoustic mismatch of the air gap reduces leakage of the shear standing wave into the anchor, thereby decreasing the quarter wavelength of the vibration mode. This explains the increased resonant frequency of the partially released bar relative to the unreleased bar.

The electromechanical coupling factor of the quarter-wave TSM resonator (${k_t}^2$) was measured using

$$ {k_t}^2 = \frac{f_S}{f_P} - 1 \approx \frac{C_X}{C_{ft}} \tag{2.18} $$

where f_S and f_P are the series and parallel resonances of the device and C_{ft} is the feedthrough capacitance between input and output ports. The resonator exhibits

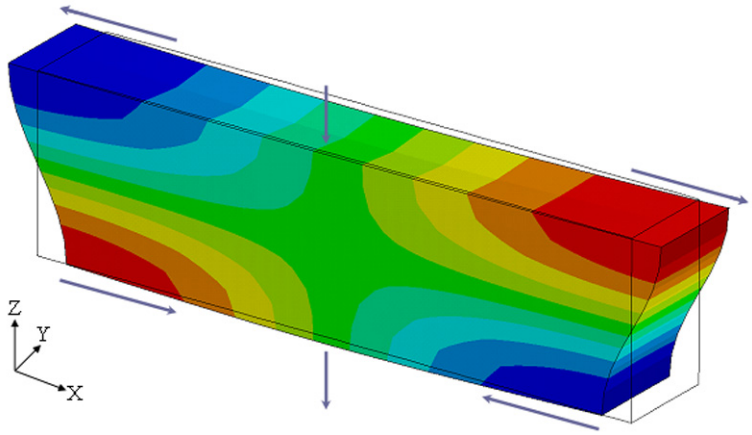

Figure 2.9: ANSYS contour plot of the symmetric half-wave thickness shear mode.

$k_t{}^2$ of 0.03. This value is comparable to the coupling factor of quartz crystals [51].

Although a quarter-wave thickness shear mode resonator using dielectric transduction can achieve a high resonant frequency with low motional impedance, however, the relatively inadequate quality factor of the resonator constrains us from coupling the resonators to build a MEMS filter with a good shape factor. Hence, an attempt to enhance the quality factor of the resonator was done by exciting a half-wave thickness shear mode in the fully released silicon bar.

2.3 Half-wave Thickness Shear Resonator

The half-wave thickness shear bar resonator is excited in the same way as the quarter-wave thickness shear bar resonator. The electrode configuration of the dielectrically transduced silicon bar induces the symmetric half-wave thickness shear mode, as shown in Figure 2.9. This mode causes the tether suspension at the nodal plane to move along the Z-axis, as indicated by the down arrows.

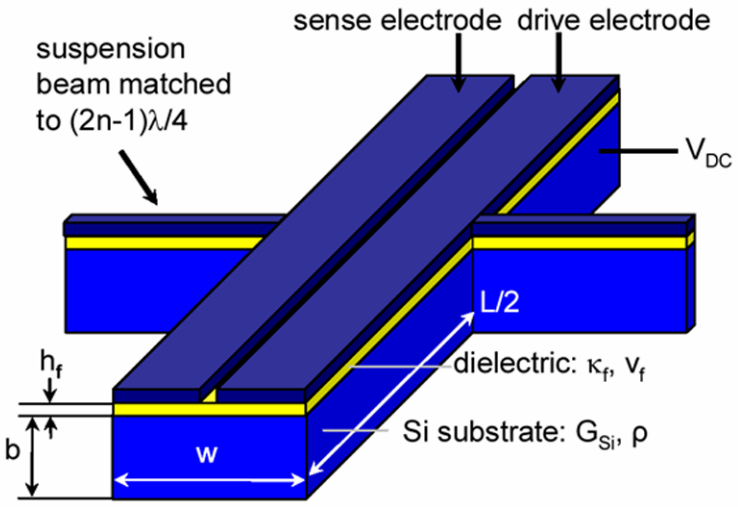

Figure 2.10: Schematic of a fully released half-wave thickness shear bar resonator.

2.3.1 Motional Impedance of a Half-wave TSM Resonator

A one-dimensional quarter-wave thickness shear mode model was derived for an unreleased silicon bar transduced by a thin dielectric film in the previous section. In order to excite the half-wave thickness shear mode, the oxide layer of the SOI wafer is fully etched, leaving a free displacement boundary condition on the bottom face of the bar. The schematic of a fully released bar resonator is shown in Figure 2.10.

The resonant frequency of the half-wave thickness shear mode resonator is two times of its quarter-wave counter part. Therefore, the first-order motional impedance of the half-wave thickness shear bar resonator is also twice of the quarter-wave thickness shear mode resonator's motional impedance. The motional impedance of the half-wave thickness shear bar resonator at resonant is given by

$$R_X = \frac{8\sqrt{G_{Si}\rho}}{Q\pi} \frac{(1-\nu_f)}{(\nu_f \kappa_f \epsilon_0 V_{DC})^2} \frac{{h_f}^3 b}{wL} \tag{2.19}$$

Pure half-wave thickness shear mode resonance of a bar depends only on thickness b, with frequency

$$f_C = \frac{1}{2b}\sqrt{\frac{G_{Si}}{\rho_{Si}}} \tag{2.20}$$

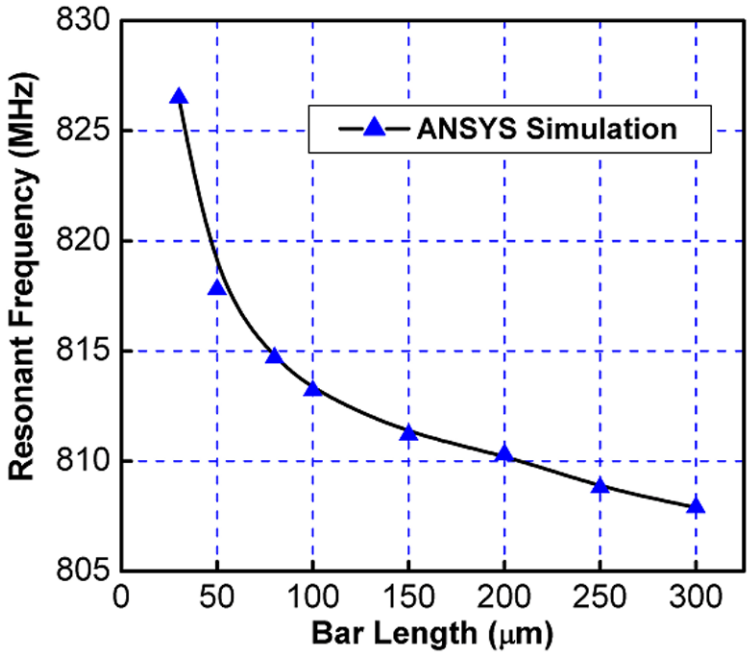

Figure 2.11: ANSYS simulation of length (L) vs resonant frequency (f_C) of the 3.2 μm thick half-wave shear mode resonator.

where G_{Si} and ρ_{Si} are the shear modulus and mass density of the silicon resonator, respectively. In reality, the resonator exhibits a small-amplitude flexure mode coupled to the shear mode. This coupling can be observed in the ANSYS modal analysis in Figure 2.9. The Southwell-Dunkerley formula [66] approximates the combined shear-flexure frequency as

$$\frac{1}{{f_{Total}}^2} = \frac{1}{{f_{Shear}}^2} + \frac{1}{{f_{Flexure}}^2} \tag{2.21}$$

Therefore, the silicon bar's lateral dimensions affect the resonant frequency, giving layout design flexibility covering a 30 MHz range below 840 MHz. Figure 2.11 shows the bar's simulated resonant frequency as a function of the bar length. The pure shear mode resonant frequency of the bar is 844 MHz. This property is exploited to fabricate multiple frequency resonators and filters on the same chip.

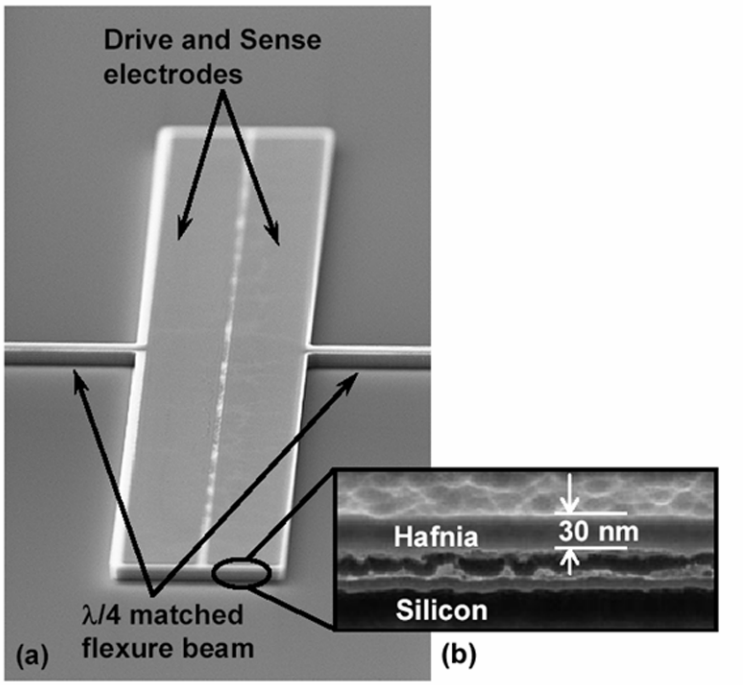

Figure 2.12: (a) SEM of a hafnium dioxide-on-silicon fully released bar resonator. (b) SEM of the 30 nm hafnium dioxide layer on the top of the silicon resonator.

2.3.2 Fabrication Process

The resonator is fabricated in a 4-mask SOI process similar to the fabrication process explained in the previous section. The silicon nitride layer is replaced with a 30 nm hafnium dioxide film ($\kappa \sim 28$, and acoustic velocity (V_A) $\sim 8,500$ m/s) on a low resistivity SOI wafer with a 3.2 μm thick SCS device layer. An SEM of the resonator is shown in Figure 2.12 (a). A high-resolution SEM revealing the 30 nm hafnium dioxide layer is shown in Figure 2.12 (b).

2.3.3 Measurement Results

A 100 μm x 40 μm bar resonator was tested in a Desert Cryo microwave probe station at room temperature and pressure. In order to simplify the microwave frequency measurement, the resonator device layer was grounded and both drive and sense electrodes were biased to 5 V using bias-Ts. SLOT (short-load-open-

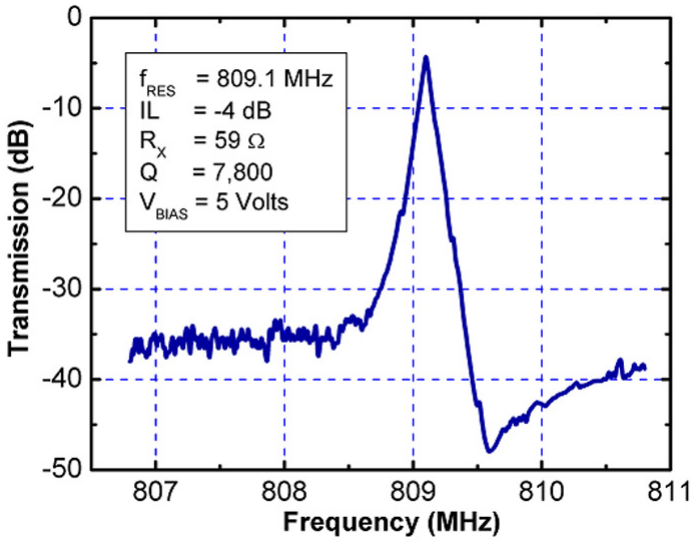

Figure 2.13: Measured transmission response of a half-wave TSM resonator in air.

through) characterization and transmission measurements were performed using an Agilent 8720ES network analyzer and the Q and insertion loss were determined from the measured S_{21} response. As expected, the motional impedance decreases with area of the resonator. In addition, the cubic dependence of R_X on dielectric film thickness h_f and its inverse square dependence on dielectric constant κ_f improve motional impedance to values close to 50 Ω. The half-wave thickness shear mode of the released silicon resonator was measured with a resonant frequency of 809 MHz, a Q of $7,800$ and an R_X of 59 Ω in air. Transmission response of the measured device is shown in Figure 2.13. The calculated f x Q product of the resonator is 6.2 x 10^{12} Hz. MEMS resonators with the performance shown by the half-wave thickness shear mode resonator can be coupled electrically to form a channel-select RF MEMS filter that has both excellent shape factor and low insertion loss.

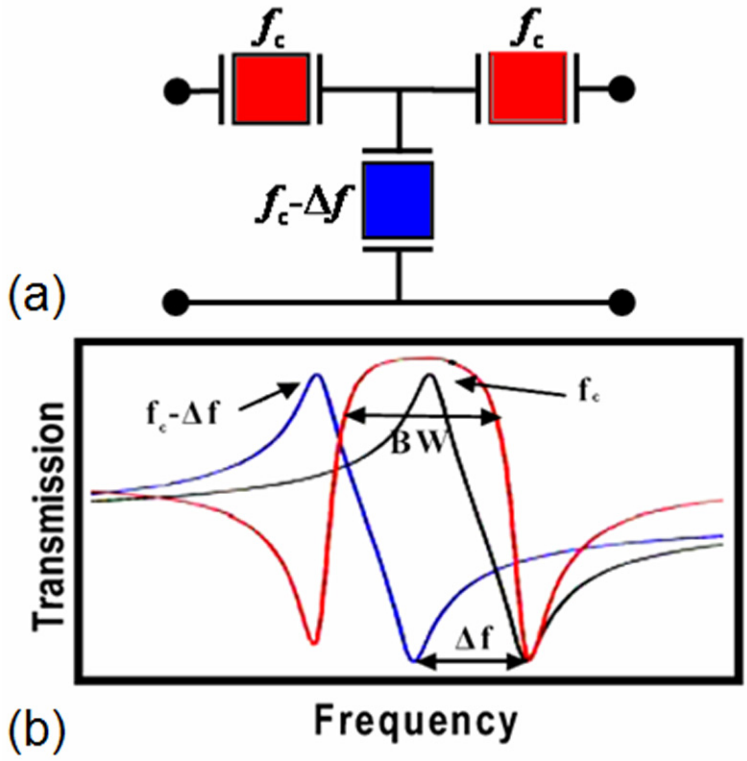

Figure 2.14: (a) Electrically coupled ladder filter configuration. (b) Bandpass frequency response of the ladder filter.

2.4 Electrically Coupled RF MEMS Ladder Filters

Electrical coupling is achieved by routing the electrical signal from successive resonators in a ladder configuration. The design flexibility afforded by the frequency dependence on lateral dimensions enables the design of series and parallel resonators of the ladder without the need for additional mass-loading or electro-etching steps to reduce the shunt resonator frequency [32, 54]. The ladder filter configuration and its bandpass frequency response are shown in Figure 2.14 (a) and (b) respectively.

Five electrically coupled ladder filters were designed with 1 MHz separation in center frequency and 3 dB bandwidth of $\sim$ 600 kHz. Figure 2.15 shows an SEM of two ladder filters. The series resonators are 280 μm x 100 μm and the shunt

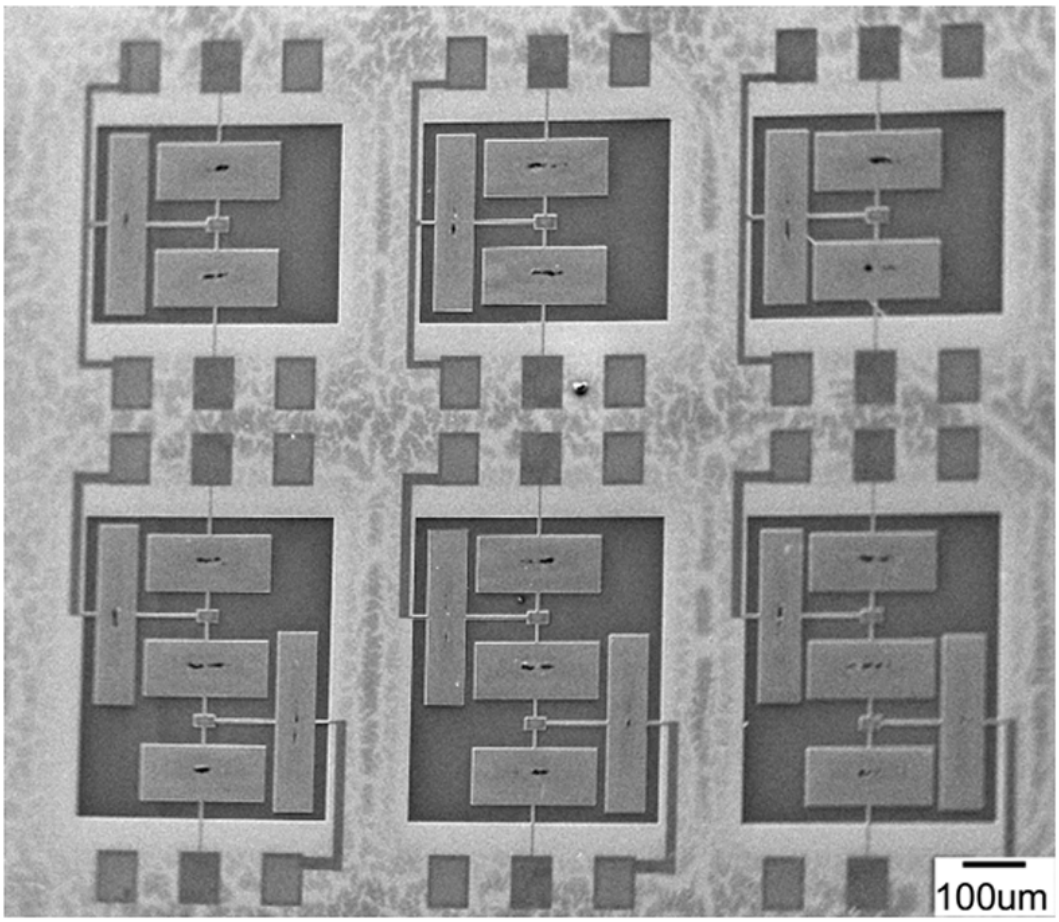

Figure 2.15: SEM of an array of ladder configuration electrically coupled thickness shear filters.

Table 2.1: The measured characteristics of electrically coupled TSM filters

	Ladder filter 1	Ladder filter 2
IL	-3.5 dB	-4 dB
3dB BW	630 kHz	680 kHz
f_c	813.6 MHz	814.5 MHz
Ripple	< 1 dB	< 1.1 dB
Stop Band Rejection	-24 dB	-25.2 dB
20dB Shape Factor	1.43	1.5
R_L	712 Ω	750 Ω

resonators are 300 μm x 100 μm. Figure 2.16 provides the frequency response of the filters and Table 2.1 summarizes the filters performance in air with termination resistance R_L. In order to verify that there are no spurious responses in the vicinity of the filter passband region, frequency was swept over a wide range. The wide spectrum swept of the channel-select filters in search of spurious responses is shown in Figure 2.17.

Pole-zero alignment in an electrically coupled ladder filter is a very critical factor to acquire the desired bandpass response. Fabrication errors can reallocate the pole and zero of the filter, hence the bandpass response of the filter may be distorted as shown in Figure 2.18. In order to overcome this problem a reconfigurable ladder filter using high performance MEMS resonators that can dynamically tune the pole and zero of the filter is necessary.

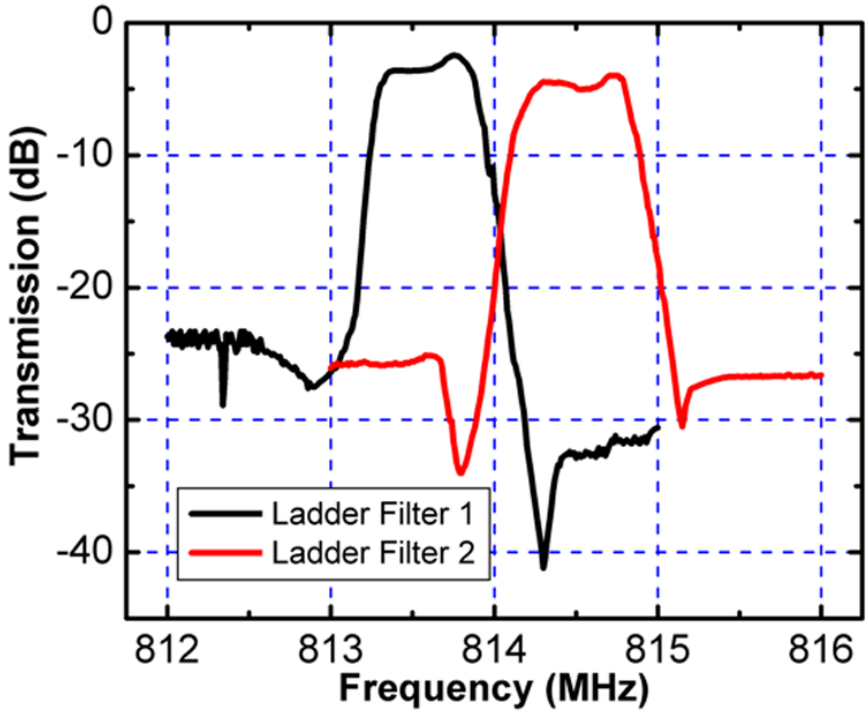

Figure 2.16: Measured transmission response showing two 650 kHz channel-select filters.

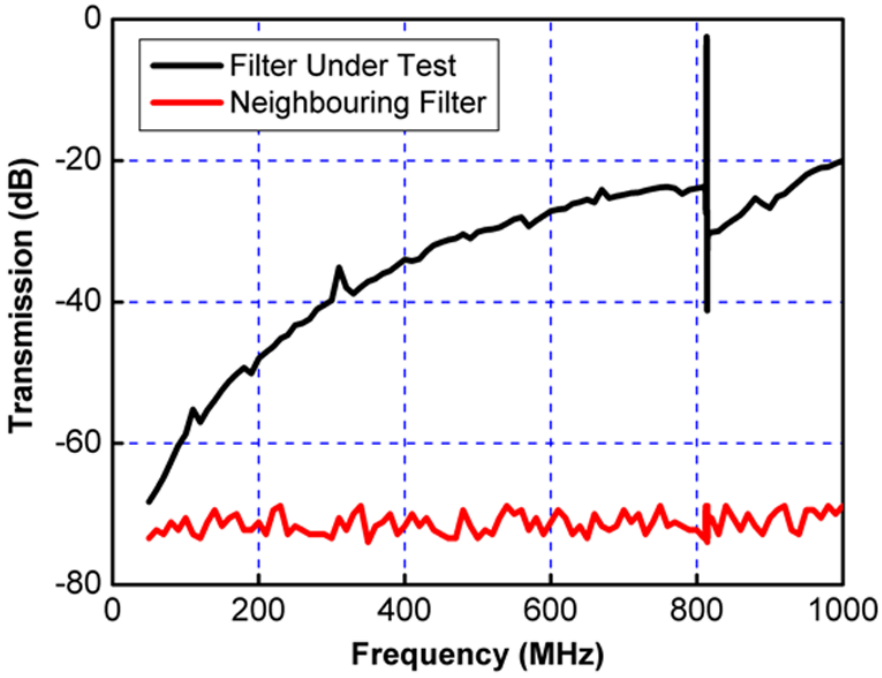

Figure 2.17: Measured filter transmission response over a wide frequency range.

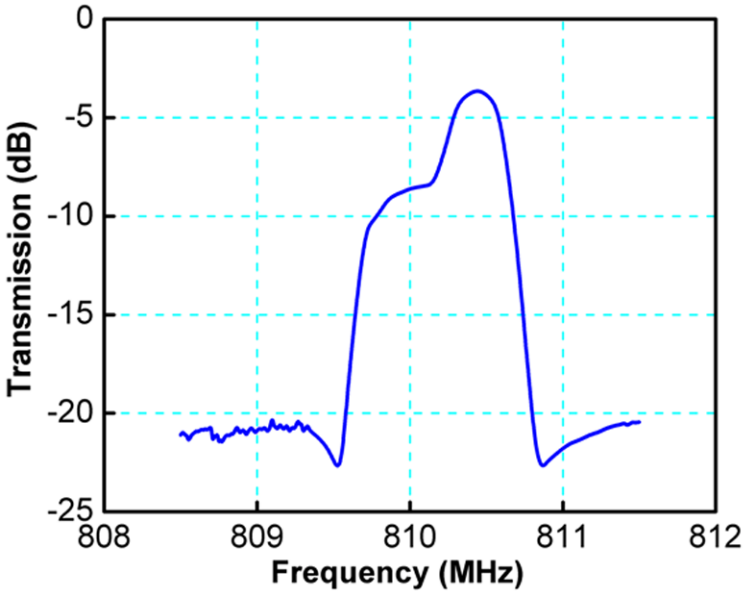

Figure 2.18: The distorted bandpass response of the filter due to fabrication tolerances.

2.5 RF MEMS Channel-select Filters with Tunable Center Frequency and Bandwidth

Low frequency filters comprised of electrostatically-coupled resonators have been demonstrated with 10x bandwidth tunability [67]. However, it is challenging to implement electrostatic coupling springs at GHz frequencies even with 100 nm air-gaps. Galayko *et al* presented a tunable bandwidth filter using clamped-clamped beam resonators in a ladder configuration [68]. The first transmission zero (and hence filter bandwidth) was tuned by controlling the series resonance frequency of the shunt resonator, though large parasitic capacitance prevented implementation and tunability of the second transmission zero of the filter.

In a typical ladder filter configuration, the parallel resonance frequency of the shunt resonator (ω_P), which defines the filter center frequency f_C, is matched to the series resonance frequency of the series resonators (ω_S). Filter bandwidth

(BW) is determined by notches on either side of the pass-band and is 2x the pole-zero separation of the series and shunt resonators. The key to tunable ladder filters is the ability to change f_C and to dynamically tune the pole-zero separation (ω_P - ω_S) of the resonators. In the previous section we have demonstrated high performance channel-select ladder filters with 600 kHz bandwidth, 25 dB stop-band rejection, excellent shape factor, and low insertion loss (IL) using dielectrically-transduced thickness shear mode resonators. In this section, we introduce a voltage biasing scheme capable of independently tuning the series resonance and pole-zero separation of the filter's constituent resonators. Coupled with orthogonal frequency tuning, we can configure the filter with desired pass-band characteristic in real time.

2.5.1 Orthogonal Frequency Tuning

The series resonance of low frequency resonators can be tuned by electrostatic spring tuning. However, the stiffness of high frequency resonators is quite large (a 1 GHz bulk-mode resonator has a stiffness on the order of 1 MN/m in the resonant direction) and would require considerable electrostatic force to tune the stiffness and the series resonance frequency.

In contrast, orthogonal frequency tuning deforms the resonator in a direction perpendicular to the direction of vibration. The resonators are generally less stiff in the orthogonal direction and can be deformed with substantially less force. The symmetric half-wave thickness shear mode resonator exhibits a small-amplitude flexure mode coupled to the shear mode as discussed in the previous section. The Southwell-Dunkerley formula approximates the combined shear-flexure frequency is given by equation 2.21. When a polarization voltage V_P is applied to the resonator and a voltage V_S is applied to the substrate, the tuning voltage V_P - V_S generates an electrostatic force that deflects the structure towards the substrate, as illustrated

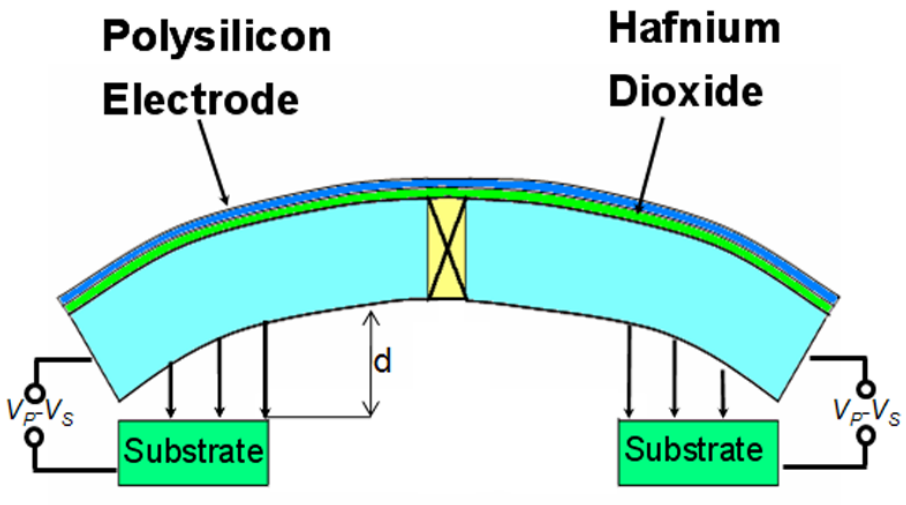

Figure 2.19: Longitudinal cross-section of a deflected half-wave thickness shear mode resonator due to the orthogonal biasing configuration.

in Figure 2.19. Bending the structure will soften the flexural mode stiffness, hence the series resonance frequency will be reduced.

2.5.2 Pole-Zero Seperation Tuning

A dielectrically transduced MEMS resonator can be represented by an electrical equivalent series LCR circuit in parallel with a feedthrough capacitance C_{ft}, as shown in Figure 2.20. For a given transduction efficiency $\eta \equiv V_P \, \partial C/\partial X$, $R_X = b/\eta^2$, $C_X = \eta^2/K$ and $L_X = M/\eta^2$, where b, K and M denote the damping constant, effective spring stiffness and effective mass of the resonator. The feedthrough capacitance in a two-port resonator originates from electric field coupling from the input electrode to the output electrode and is a function of electrode geometry. The series resonance frequency is given by

$$\omega_S = \frac{1}{\sqrt{L_X C_X}} = \sqrt{\frac{K}{M}} \tag{2.22}$$

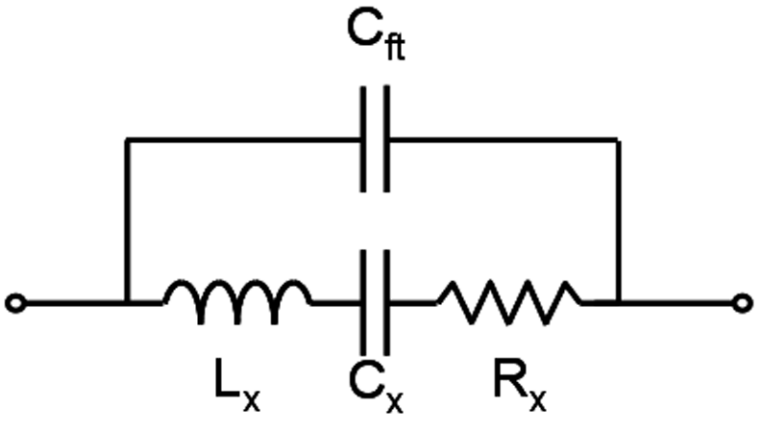

Figure 2.20: Electrical equivalent circuit of a dielectrically transduced MEMS resonator.

An expression for the parallel resonance frequency is obtained through a first-order Taylor's expansion

$$\omega_P = \frac{1}{\sqrt{L_X \frac{C_X C_{ft}}{C_X + C_{ft}}}} = \omega_S \sqrt{1 + \frac{C_X}{C_{ft}}} \approx \omega_S \left(1 + \frac{C_X}{2C_{ft}}\right) \tag{2.23}$$

$$\omega_P - \omega_S \approx \omega_S \frac{C_X}{C_{ft}} \tag{2.24}$$

$$\frac{\Delta\left(\omega_P - \omega_S\right)}{\Delta\omega_S} \approx \frac{C_X}{C_{ft}} \tag{2.25}$$

For electrostatic transduction, the ratio of C_X to C_{ft} is very small ($10^{-4} - 10^{-2}$). Therefore, the separation between the series and parallel resonances is largely independent of the series resonance frequency shifts due to changes in the spring constant K. The pole-zero separation can be modeled as a function of structure bias voltage V_P.

$$\omega_P - \omega_S = \left(\frac{\epsilon^2 A^2}{2d^4 C_{ft}\sqrt{KM}}\right) {V_P}^2 \tag{2.26}$$

In other words, the parallel resonance frequency is simply a voltage-controlled offset from the series resonance frequency.

2.5.3 Filter Tuning Algorithm

A ladder filter consists of a shunt resonator and two series resonators. For minimum insertion loss and pass-band ripple, the parallel resonance frequency of the shunt resonator is matched to the series resonance frequency of the series resonators. Ladder filters can be cascaded to provide higher stop-band rejection at the expense of insertion loss. To achieve the desired center frequency and bandwidth, we use the following filter synthesis method:

1. Fix V_P and change V_S for the series and shunt resonators such that the desired series resonance frequencies are obtained (orthogonal frequency tuning).

2. Tune V_P - V_S separately for each resonator to obtain the desired pole-zero offset. Since V_P - V_S remains constant, the bending of the resonators does not change so the series resonance frequency remains fixed.

2.5.4 Fabrication Process

Filter T-sections consisting of one shunt and two series resonators shown in Figure 2.21 (a) were fabricated on an SOI wafer with a 3 μm heavily doped device layer and 0.5 μm buried oxide. The resonators are 310 μm (and 300 μm) x 100 μm x 3.1 μm released silicon bars with 20 nm of hafnium dioxide and 50 nm of polysilicon layers on top for dielectric transduction. Orthogonal frequency tuning was achieved by applying a substrate bias voltage to bend the resonators in the vertical direction. A back-side etch was added to the previous fabrication process to create substrate islands for independent tuning of the resonators. A front-side trench etch allowed isolated DC bias voltages to be applied to the resonators as shown in Figure 2.21 (b). Process limitations prevented polysilicon connections between the series and shunt resonators, so a small gold bondwire was implemented

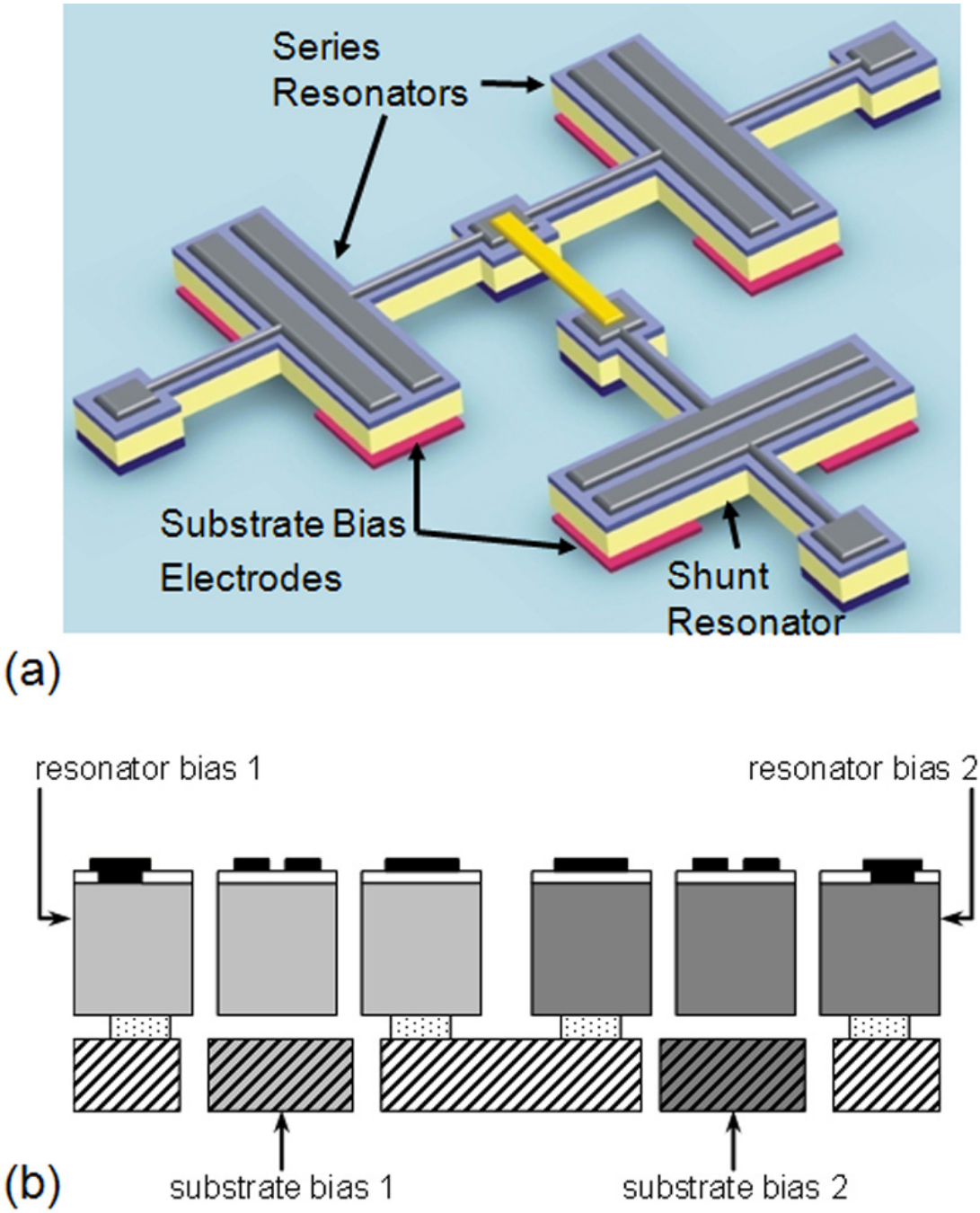

Figure 2.21: (a) The 3-D model of tunable ladder filter. (b) The device cross-section with isolated resonator and substrate for applying independent tuning voltages.

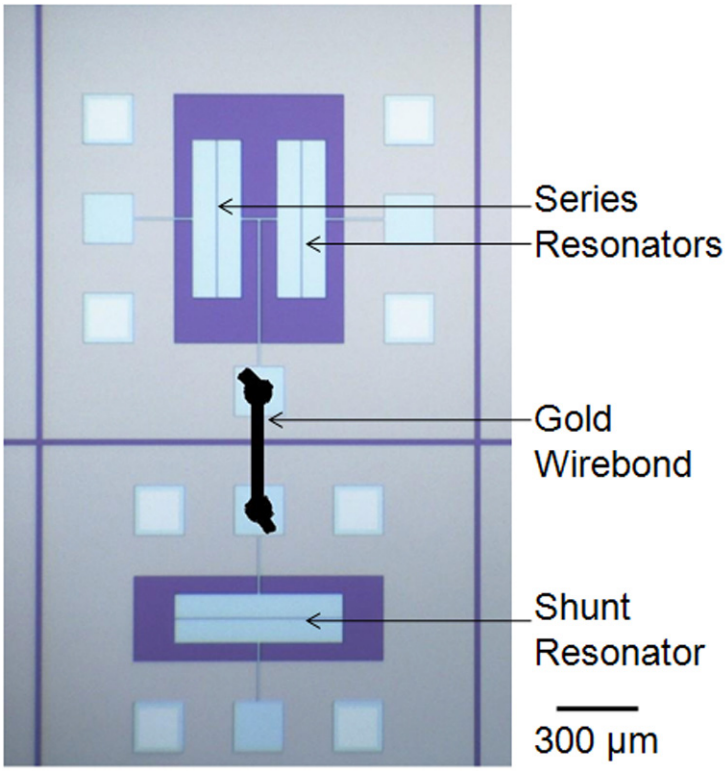

Figure 2.22: Microphotograph of tunable ladder filter with a gold wirebond bridge.

as seen in Figure 2.22. Care must be taken to ensure that the wirebond does not damage the oxide under the pads and short the devices.

2.5.5 Measurement Results

Due to parasitics feedthrough, several calibrations are compulsory to extract the mechanical properties of the filter. The resonators and filters were characterized using a Desert Cryo microwave probe station. The resonator proof-mass was grounded and a DC bias V_P was applied to both the drive and sense electrodes with MiniCircuits bias-Ts. Quality factor characterization and S_{21} transmission measurements were performed using an Agilent 8722ES Network Analyzer with 32 averaging steps. The resonators and filters were terminated with 50 Ω and 500 Ω impedances, respectively. The uncalibrated frequency characteristic of the res-

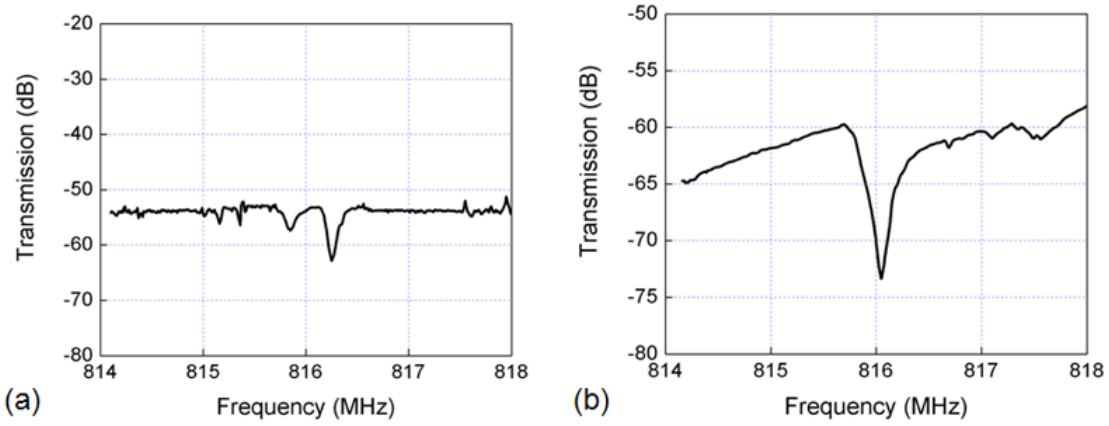

Figure 2.23: (a) The uncalibrated frequency characteristic of the resonator. (b) The measured frequency characteristic of the resonator after Cascade substrate calibration.

onator is shown in Figure 2.23 (a). Cascade substrate calibration cancels the cables and probes capacitances. The measured frequency characteristic of the resonator after Cascade substrate calibration is shown in Figure 2.23 (b). In addition, SOI substrate calibration is also necessary to minimize the effect of pad capacitance, electrical resistance of electrodes and nominal capacitance ($V_P = 0$). The measured frequency response of the resonator after SOI substrate calibration is shown in Figure 2.24 (a). Measurement results demonstrating orthogonal frequency tuning are shown in Figure 2.24 (b) and (c). Keeping V_P constant at 5 V and varying the substrate bias V_S from 5 V to 17 V, we can tune the series resonance frequency of a single resonator from 816 MHz to 802 MHz, while maintaining a quality factor $Q > 7,000$. The parallel and series resonance separation does not change during orthogonal frequency tuning.

Figure 2.25 shows that the pole-zero separation of the resonator varies from 0.6 MHz to 1.6 MHz when V_P is changed from 5 V to 12 V. The substrate bias V_P was held at V_P during this measurement to prevent orthogonal forces acting on the resonator.

A bias voltage $V_P = 5$ V yields a pass-band with $f_C = 817.2$ MHz, 0.6 MHz

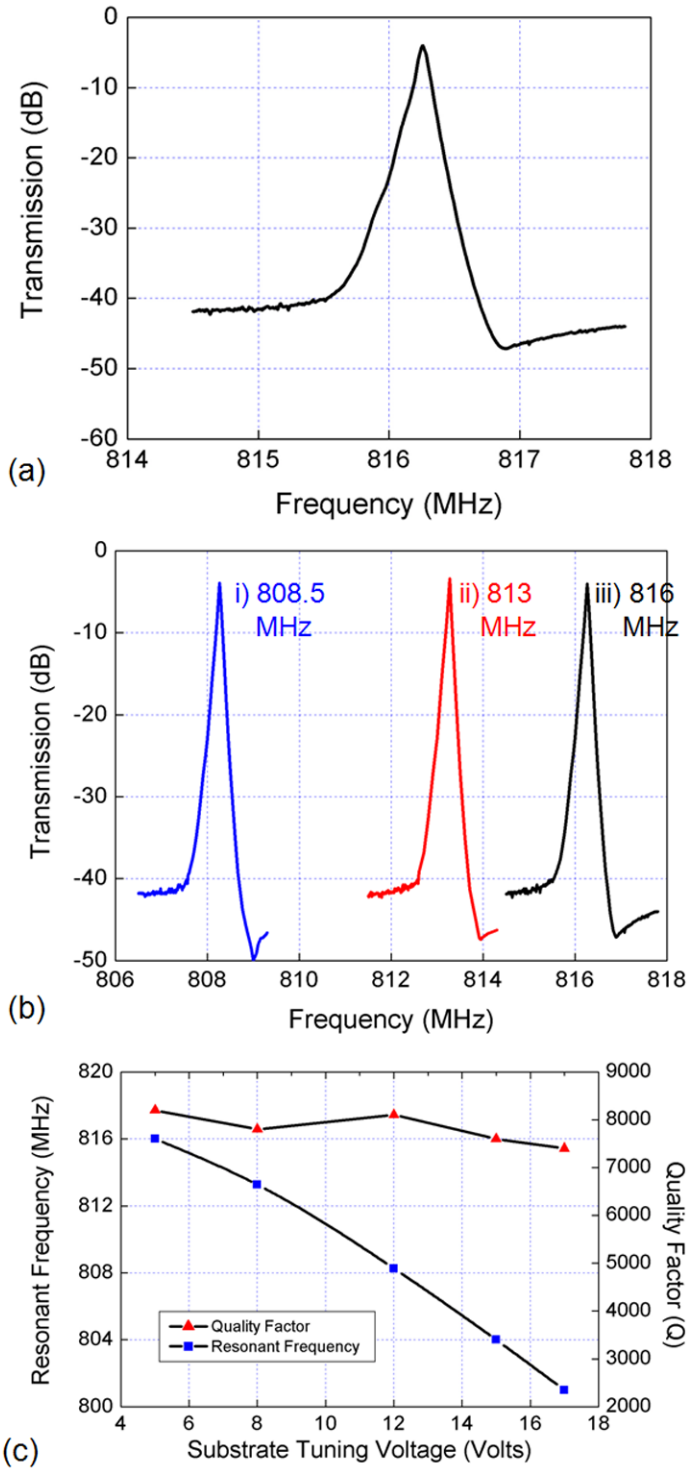

Figure 2.24: (a) Measured frequency characteristic of the resonator after SOI calibration. (b) Measured series resonance tuning for $V_S = 5$ V and $V_S =$ (i) 12 V, (ii) 8 V, and (iii) 5 V. (c) Resonant frequency tuning vs. substrate voltage.

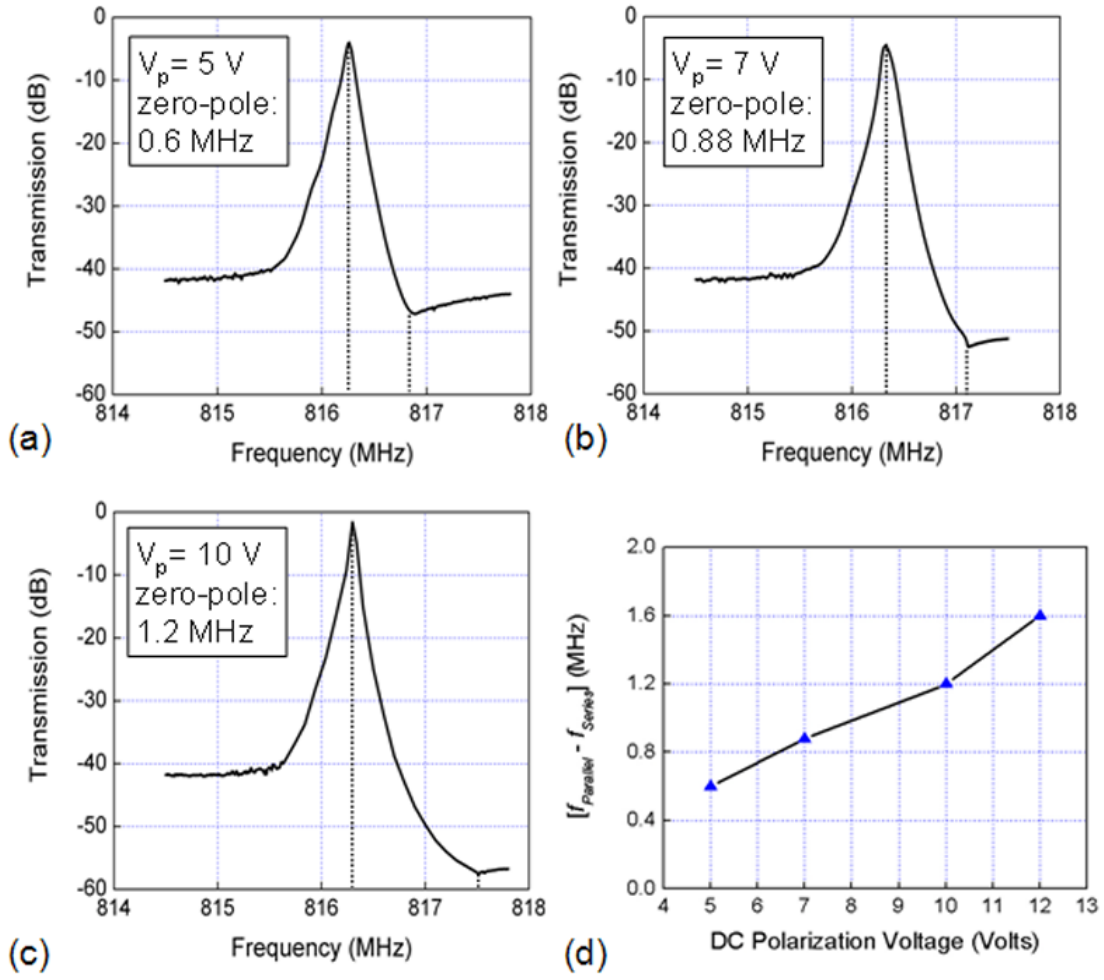

Figure 2.25: (a,b,c) Measured transmission response demonstrating pole-zero separation of a thickness shear mode resonator as *DC* bias V_P increases from 5 V to 10 V. (d) Measured pole-zero separation vs. *DC* bias voltage of the resonator.

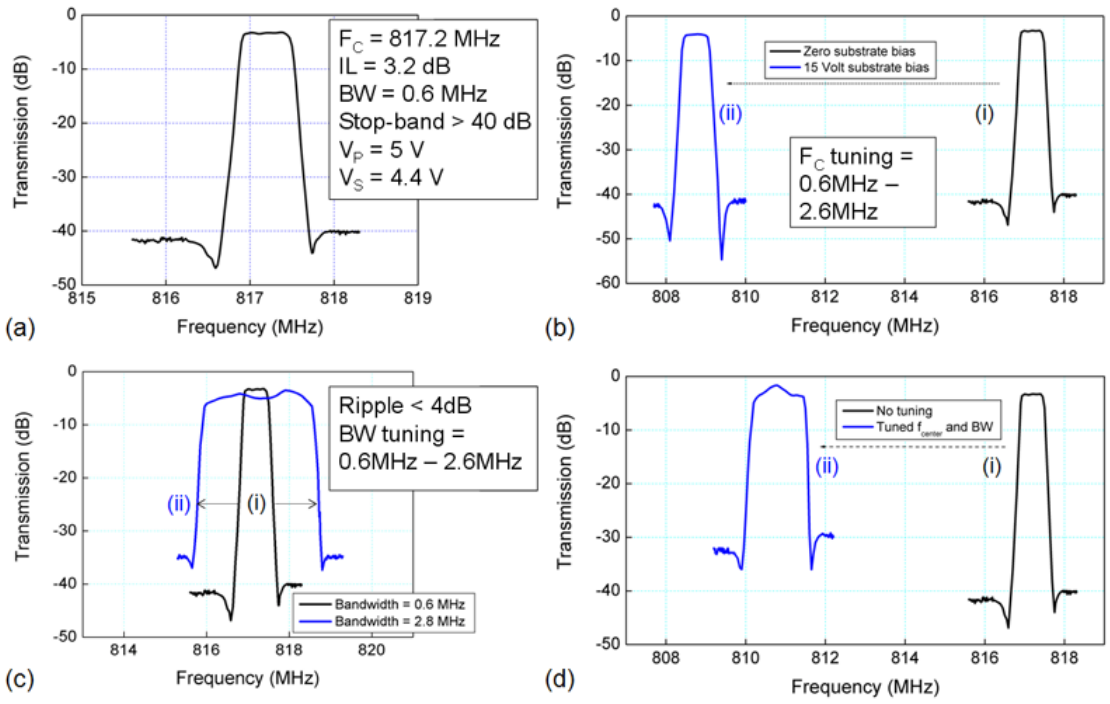

Figure 2.26: (a) Measured transfer function of ladder filter with no tuning. (b) Measured transmission of ladder filter with f_C tuning from 817 MHz to 809 MHz with (i) no tuning, and (ii) series resonator: $V_P = 5$ V, $V_S = 15$ V; shunt resonator: $V_P = 5$ V, $V_S = 12$ V. (c) Measured transmission of ladder filter with BW tuning from 0.6 MHz to 2.8 MHz with (i) no tuning, (ii) series resonator: $V_P = 12$ V, $V_S = 12$ V; shunt resonator: $V_P = 13$ V, $V_S = 16$ V. (d) Measured transfer function of ladder filter with BW tuning from 0.6 MHz to 1.4 MHz and f_C tuning from 817 MHz to 811 MHz with (i) no tuning, and (ii) series resonator: $V_P = 10$ V, $V_S = 19$ V; shunt resonator: $V_P = 9$ V, $V_S = 17$ V.

bandwidth, and IL of 3.2 dB as demonstrated in Figure 2.26 (a). Applying $V_S = 12$ V and 15 V to the shunt and series resonators respectively, the center frequency is tuned from 817 MHz to 809 MHz without degradation in IL (3.5 dB) and shape factor (1.3), as shown in Figure 2.26 (b). Figure 2.26 (c) shows the bandwidth tuning from 0.6 MHz to 2.8 MHz while maintaining a constant center frequency at 817.2 MHz. Finally, a combination of bandwidth and center frequency tuning is shown in Figure 2.26 (d). A pass-band with $f_C = 811$ MHz and 1.4 MHz bandwidth is obtained.

2.6 Conclusion

Thickness shear mode resonators that inherit the high resonant frequency and high-Q from Quartz resonators have been successfully fabricated using integrated circuit compatible process in SOI wafers. The partially released quarter-wave thickness shear bar resonator's f x Q product of 3.2 x 10^{12} Hz is within a factor of five of the f x Q product for quartz resonators. Quarter-wave thickness shear mode resonators using silicon nitride thin film as a dielectric transducer achieve high frequencies with greatly improved motional impedance. The lateral electrode design causes a Poisson ratio inefficiency in the transfer of vertical strain into lateral strain. However, this transfer is necessary to induce a shear resonance. Furthermore, this configuration allows for a large electrode area, significantly decreasing the resonator's motional impedance.

In addition, half-wave thickness shear mode resonators with frequencies greater than 800 MHz and $Q > 7,000$ have been fabricated. Dielectric transduction by a high-κ hafnium dioxide thin film reduces the motional impedance of the resonators more than 40 times relative to the previously design quarter-wave thickness shear mode resonator. Their 59 Ω motional impedance is the lowest reported to date for any silicon-based electrostatic VHF MEMS resonator design. An array of ladder filters with 600 kHz bandwidth, < 4 dB insertion loss, and < 1 dB pass-band ripple has been demonstrated.

Voltage tunability is more versatile than one-time modifications like laser trimming and mass loading, and enables us to overcome process tolerance and temperature variation frequency shifts. The frequency dependence of the thickness shear mode resonators on lateral dimensions provides the ability to fabricate resonators of various frequencies on a single chip. We have demonstrated bandwidth and center frequency tunability in an RF MEMS filter with $IL < 4$ dB and stop-band

rejection $>$ 30 dB. With process tolerance and temperature variation frequency shifts of ± 1.2 MHz and -14 ppm/°C, respectively, this tuning capability not only overcomes these variations, but also enables channel agility and adaptability in multi-mode radio receivers.

CHAPTER 3

HIGH-OVERTONE SQUARE-EXTENSIONAL RESONATORS AND DIGITALLY PROGRAMMABLE MECHANICALLY-COUPLED FREQUENCY-AGILE FILTERS

3.1 Introduction

Multi-band, multi-standard radio receivers such as next generation 7-band cellular phones and the Joint Tactical Radio System (JTRS) require a large array of channel-select filters connected in parallel. The input capacitance of the filter array will 'load' individual filters, deteriorating their stop-band rejection. Therefore, such frequency agile radios need multi-octave tunable band-select radio frequency (RF) filters and bandwidth tunable channel-select intermediate frequency (IF) filters with good shape factor and excellent stop-band rejection. An RF filter with dynamically tunable bandwidth will enable handling of multiple waveforms, eliminate out-of-channel interferers, and substantially decrease the number of filters in next-generation receivers.

Dielectrically-transduced thickness shear-mode resonators with analog voltage tunable center frequency and bandwidth are suitable candidates for channel-select RF filters [69]. The resonators require a back-side etch of the SOI substrate to pattern orthogonal frequency tuning electrodes and eliminate parasitic pad capacitance and resistive ground loops. However, such back-side processing is not compatible with the high-vacuum, ultra-clean epi-Silicon encapsulation technology [70] necessary for field deployment of these filters. Contour-mode MEMS resonators with $Q > 5,000$, low motional impedance (R_X), compatibility with epi-Silicon encapsulation and CAD-defined resonance frequencies from 10 MHz - 1 GHz are excellent candidates for designing channel-select filter arrays [71]. But unlike

thickness shear mode resonators, the frequency expressions for contour modes and flexural vibration modes do not directly couple. It is therefore difficult to perform orthogonal frequency tuning of contour-mode resonators. Since extensional mode resonators cannot be tuned at device-level (without excessive heating [72] or using liquid dielectric [73]), we implemented a tunable filter using a novel DC-biasing strategy in mechanically-coupled resonator array. This method does not require any frequency off-set between constituent resonators. As a result, lithography challenges are minimized, spatial distortion is greatly reduced and spurs in filter transmission are attenuated [74].

3.2 High-overtone Square-extensional Mode Resonator

MEMS resonators vibrating in a bulk-mode have superior linearity and high quality factors [75, 76]. Significant reductions in motional impedance of MEMS resonators have been achieved by mechanically coupling and exciting a parallel array of corner-coupled polysilicon square plate resonators [77]. By strongly coupling identical resonators in two dimensions a larger area can be acquired to further reduce the motional impedance. In addition, two-dimensional modal excitation causes less mode dispersion by averaging out the stochastic resonator characteristics [78]. The bulk-extensional mode resonance of a square resonator depends on L, with frequency of operation (f_C) given by:

$$f_C = \frac{n}{2L}\sqrt{\frac{E}{\rho}} \tag{3.1}$$

where n is the overtone order, E is the effective elastic modulus for two-dimensional expansion, ρ is the effective density and L is the length of the resonator. Higher frequency overtone modes are selectively excited by patterning electrodes in checkerboard configuration on top of the resonator using dielectric transduction [79]. The

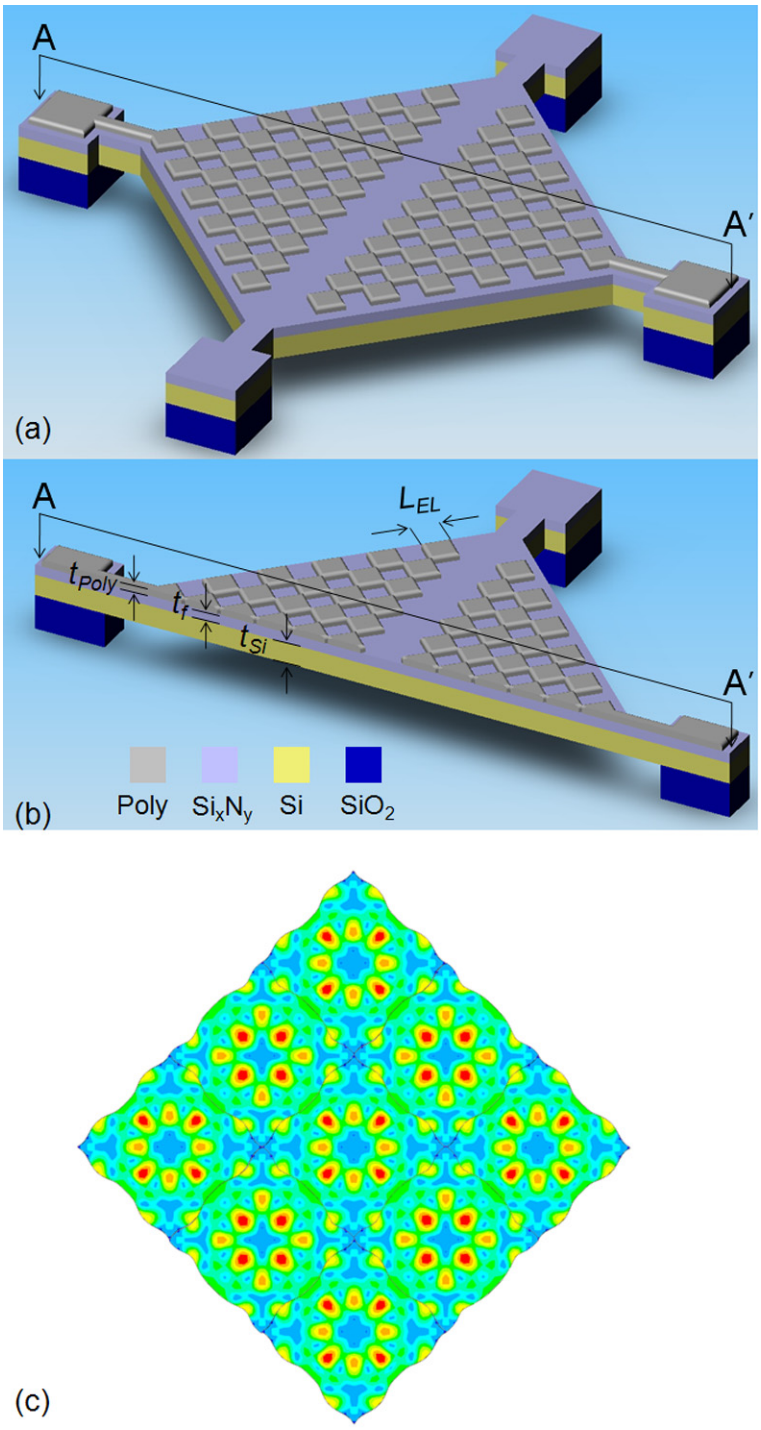

Figure 3.1: (a) Schematic of a 2-port high-overtone square-extensional mode resonator. (b) Cross-section of the device showing various layers that are deposited to build the resonator. (c) ANSYS mode shape of a high-overtone square-extensional resonator.

schematic of a 2-port dielectrically transduced high-overtone square-extensional mode resonator is illustrated Figure 3.1 (a) and (b). The resonator is modeled and simulated using finite element method in ANSYS. The ANSYS modal analysis of a high-overtone square-extensional resonator is shown in Figure 3.1 (c).

The 50 nm thin film silicon nitride film deposited on top of the resonator is sandwiched between the 2.75 μm thick silicon device layer and the 100 nm thick conducting top electrodes. A 50 V DC bias is superimposed to the AC signal at both input and output ports using bias-Ts and the silicon device layer is connected to RF ground. This time-varying voltage causes a squeezing force on the dielectric thin film. Due to the Poisson effect, the dielectric layer experiences a lateral strain. As the strain distributes through the resonator, the overtone square-extensional mode is excited.

3.2.1 Effective mass, Damping ratio and Effective spring constant

The overtone square-extensional resonator can be treated as a parallel two-dimensional array of mechanically-coupled smaller square-extensional resonators with length L_{EL} as shown in Figure 3.1 (a). The wave equation for a two-dimensional vibrating square-extensional mode resonator including the damping factor and external forces is

$$\begin{aligned} \rho t_{Eff}\frac{\partial^2 u}{\partial t^2}(x,y,t) - bt_{Eff}\frac{\partial}{\partial t}\left(\frac{\partial^2 u}{\partial x^2}(x,y,t) + \frac{\partial^2 u}{\partial y^2}(x,y,t)\right) & \\ -Et_{Eff}\left(\frac{\partial^2 u}{\partial x^2}(x,y,t) + \frac{\partial^2 u}{\partial y^2}(x,y,t)\right) &= \frac{\partial f}{\partial t}(x,y,t) \end{aligned} \tag{3.2}$$

By the method of separation of variables, we assume equation 3.2 has solutions of the form

$$u(x,y,t) = g(t)\left(\sin\left(\frac{n\pi}{L_{EL}}x\right) + \sin\left(\frac{n\pi}{L_{EL}}y\right)\right) \tag{3.3}$$

Substituting 3.3 into 3.2 gives

$$\begin{aligned} &\rho t_{Eff}\left(\sin\left(\tfrac{n\pi}{L_{EL}}x\right) + \sin\left(\tfrac{n\pi}{L_{EL}}y\right)\right)\tfrac{\partial^2 g(t)}{\partial t^2} \\ &+bt_{Eff}\left(\tfrac{n\pi}{L_{EL}}\right)^2\left(\sin\left(\tfrac{n\pi}{L_{EL}}x\right) + \sin\left(\tfrac{n\pi}{L_{EL}}y\right)\right)\tfrac{\partial g(t)}{\partial t} \\ &+Et_{Eff}\left(\tfrac{n\pi}{L_{EL}}\right)^2\left(\sin\left(\tfrac{n\pi}{L_{EL}}x\right) + \sin\left(\tfrac{n\pi}{L_{EL}}y\right)\right)g(t) \quad = \quad \tfrac{\partial f}{\partial t}(x,y,t) \end{aligned} \tag{3.4}$$

Multiply 3.4 by $\sin\left(\frac{n\pi}{L_{EL}}x\right) + \sin\left(\frac{n\pi}{L_{EL}}y\right)$ and integrate over the area yields

$$\begin{aligned} &\int_{-L/2}^{L/2}\int_{-L/2}^{L/2}\rho t_{Eff}\left(\sin\left(\tfrac{n\pi}{L_{EL}}x\right) + \sin\left(\tfrac{n\pi}{L_{EL}}y\right)\right)^2\tfrac{\partial^2 g(t)}{\partial t^2} \\ &+bt_{Eff}\left(\tfrac{n\pi}{L_{EL}}\right)^2\left(\sin\left(\tfrac{n\pi}{L_{EL}}x\right) + \sin\left(\tfrac{n\pi}{L_{EL}}y\right)\right)^2\tfrac{\partial g(t)}{\partial t} \\ &+Et_{Eff}\left(\tfrac{n\pi}{L_{EL}}\right)^2\left(\sin\left(\tfrac{n\pi}{L_{EL}}x\right) + \sin\left(\tfrac{n\pi}{L_{EL}}y\right)\right)^2 g(t)dxdy \quad = \quad F(t) \end{aligned} \tag{3.5}$$

where $F(t)$ is

$$\int_{-L/2}^{L/2}\int_{-L/2}^{L/2}\frac{\partial f}{\partial t}(x,y,t)\left(\sin\left(\frac{n\pi}{L_{EL}}x\right) + \sin\left(\frac{n\pi}{L_{EL}}y\right)\right)dxdy \tag{3.6}$$

Equation 3.5 can be simplified as

$$\rho t_{Eff}{L_{EL}}^2\frac{\partial^2 g(t)}{\partial t^2} + bt_{Eff}\left(\frac{n\pi}{L_{EL}}\right)^2{L_{EL}}^2\frac{\partial g(t)}{\partial t} + Et_{Eff}\left(\frac{n\pi}{L_{EL}}\right)^2{L_{EL}}^2 g(t) = F(t) \tag{3.7}$$

From equation 3.7, we can recognize the effective mass, damping ratio and effective spring constant of a square-extensional resonator with length L_{EL} are given by

$$M_{Eff} = \rho\ t_{Eff}{L_{EL}}^2 \tag{3.8}$$

$$\zeta = b\ t_{Eff} \left(\frac{n\pi}{L_{EL}}\right)^2 {L_{EL}}^2 = b\ t_{Eff}\ (n\pi)^2 \tag{3.9}$$

$$K_{Eff} = E\ t_{Eff} \left(\frac{n\pi}{L_{EL}}\right)^2 {L_{EL}}^2 = E\ t_{Eff}\ (n\pi)^2 \tag{3.10}$$

3.2.2 Electromechanical Coupling Constant

A voltage $V_{DC} + v_{AC}$ applied across the dielectric film generates a normal force

$$f_Z \approx V_{DC} \frac{\epsilon_f {L_{EL}}^2}{{t_f}^2} v_{AC} \tag{3.11}$$

Here, we make the approximation that $v_{AC} \ll V_{DC}$. The laterally transferred strain in the film is

$$\epsilon_{x,f} = \epsilon_{y,f} = \frac{\nu_f f_Z}{E_f {L_{EL}}^2} \tag{3.12}$$

and the lateral stress in the film is

$$\sigma_{x,f} = \sigma_{y,f} = \frac{\nu_f}{(1-\nu_f){L_{EL}}^2} \frac{\epsilon_f {L_{EL}}^2}{{t_f}^2} V_{DC} v_{AC} \tag{3.13}$$

This initial lateral stress $\sigma_{x,f}$ acts like an effective residual stress in the film and consequently distributing itself across the thickness of dielectric thin film and bulk silicon. The distributed lateral strain in the structure is approximated as

$$\epsilon_x = \epsilon_y = \frac{t_f \sigma_{x,f}}{E_f t_f + \frac{1}{2} E_{Si} t_{Si}} \tag{3.14}$$

This yields the distributed lateral stress in the bulk silicon

$$\sigma_{x,Si} = \sigma_{y,Si} = \frac{t_f E_{Si} \sigma_{x,f}}{E_f t_f + \frac{1}{2} E_{Si} t_{Si}} \tag{3.15}$$

Assuming the thickness of the structure is dominated by the bulk silicon ($t_f \ll t_{Si}$), we have a lateral force

$$F_{x,f} = F_{y,f} = \frac{2t_f}{t_{Si}} \frac{\nu_f}{(1-\nu_f)} \frac{\epsilon_f}{{t_f}^2} t_{Si} L_{EL} V_{DC} v_{AC} \tag{3.16}$$

The efficiency of electromechanical transduction is indicated by the electromechanical coupling constant η.

$$\eta = \frac{F_{x,f}}{v_{AC}} = \frac{F_{y,f}}{v_{AC}} \tag{3.17}$$

From 3.16 and 3.17, we recognize the transduction electromechanical coupling constant

$$\eta = \frac{2L_{EL}}{t_f}\frac{\nu_f}{(1-\nu_f)}\epsilon_f V_{DC} \tag{3.18}$$

3.2.3 Electrical Equivalent Impedances of a High-overtone Square-extensional Resonator

The effective mass, damping ratio and effective spring constant can be related in to electrical circuit parameters. By substituting $\frac{\partial g(t)}{\partial t}$ in 3.7 by $\frac{i(t)}{\eta}$, we obtain

$$\frac{M_{Eff}}{\eta}\frac{\partial i(t)}{\partial t} + \frac{\zeta}{\eta}i(t) + \frac{K_{Eff}}{\eta}\int i(t)dt = F(t) \tag{3.19}$$

or

$$\frac{M_{Eff}}{\eta^2}\frac{\partial i(t)}{\partial t} + \frac{\zeta}{\eta^2}i(t) + \frac{K_{Eff}}{\eta^2}\int i(t)dt = v(t) \tag{3.20}$$

From 3.20 we can define the motional resistance, capacitance and inductance of the resonator in Figure 3.2. The feedthrough capacitance in a two-port resonator originates from electric field coupling from the input electrode to the output. The small signal electrical equivalent impedances a resonator consist of j number of smaller square-extensional resonators vibrating in fundamental mode ($n = 1$) connected in parallel are

$$R_X = \frac{\sqrt{K_{Eff}M_{Eff}}}{Q\eta^2} = \frac{\pi}{4jQ}\left(\frac{(1-\nu_f)}{\nu_f}\right)^2 \frac{{t_f}^2 t_{Eff}}{L_{EL}}\frac{\rho E}{{\epsilon_f}^2}\frac{1}{{V_{DC}}^2} \tag{3.21}$$

$$C_X = \frac{\eta^2}{K_{Eff}} = \frac{4j}{\pi^2}\left(\frac{\nu_f}{(1-\nu_f)}\right)^2 \frac{{\epsilon_f}^2}{E}\frac{{L_{EL}}^2}{{t_f}^2 t_{Eff}}{V_{DC}}^2 \tag{3.22}$$

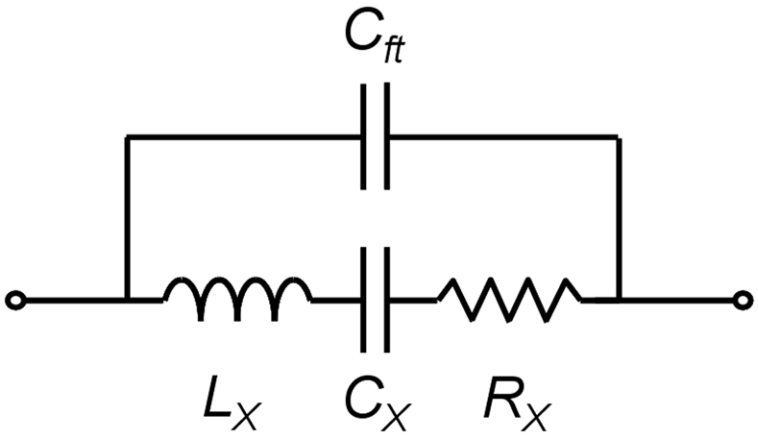

Figure 3.2: Electrical equivalent circuit of a dielectrically transduced high-overtone square-extensional resonator.

$$L_X = \frac{M_{Eff}}{\eta^2} = \frac{1}{4j}\left(\frac{(1-\nu_f)}{\nu_f}\right)^2 \frac{\rho}{{\epsilon_f}^2} {t_f}^2 t_{Eff} \frac{1}{{V_{DC}}^2} \tag{3.23}$$

The high-overtone square-extensional resonator is designed using the RLC electrical equivalent circuit models and simulated in Agilent Advanced Design System (ADS) software. The resonator design parameters are summarized in Table 3.1 and the simulation result is shown in Figure 3.3.

3.3 Digitally Programmable Filters

Electrically-coupled filters using AlN overtone-mode resonators have been recently demonstrated with narrow-bandwidth and low IL [80]. However, the electrical losses in the shunt capacitors and the patterned ground-plane degrade the shape-factor of the filter. These losses are more severe in electrically-coupled differential lattice configurations. Mechanically-coupled devices demand smaller area since the coupling spring is small. Furthermore, they do not suffer from energy losses since the coupling spring is made of crystalline material. In multi-pole mechanically-coupled filters the resonators are coupled using quarter-wavelength suspensions with stiffness ks at low-velocity nodes. The quarter-wavelength springs

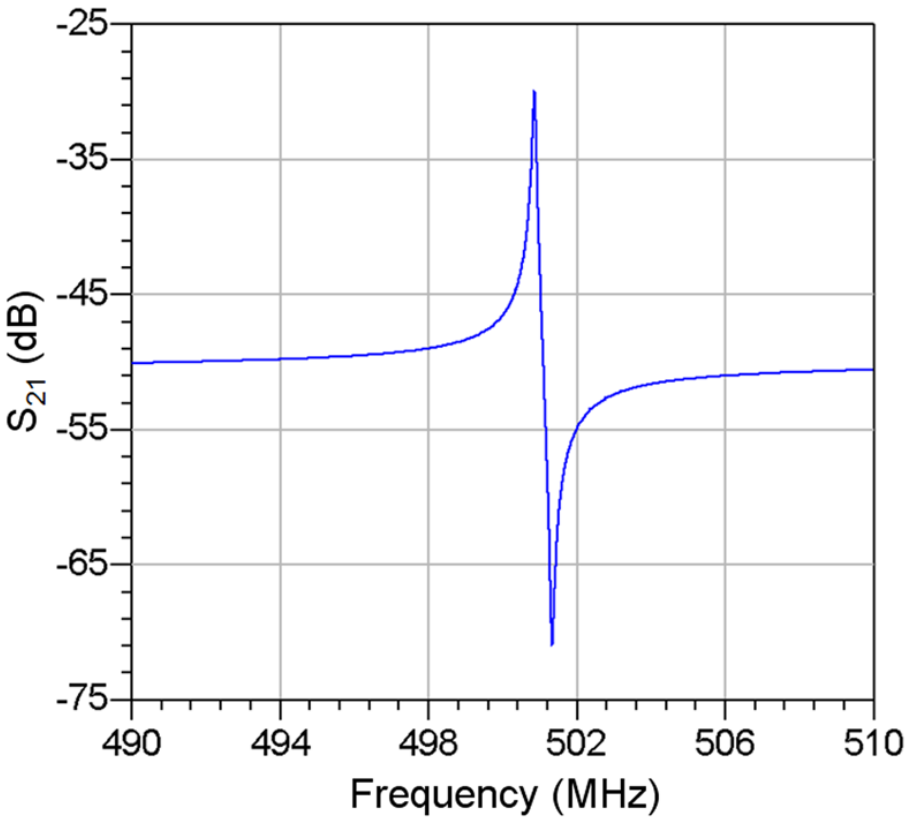

Figure 3.3: Simulated performance of a 500 MHz high-overtone square-extensional resonator.

Table 3.1: Design parameters of the high-overtone square-extensional resonator

Parameter	Value	Unit
L_{EL}	8.5	μm
t_f	50	nm
t_{Si}	2.75	μm
t_{Poly}	80	nm
n	1	—
j	72	—
Q	$2,000$	—
R_X	3.3	kΩ
L_X	5.36	mH
C_X	18.8	aF
R_L	50	Ω
f_C	500	MHz

minimize mass-loading of the resonators and low-velocity coupling enables narrow-bandwidth filter design with standard lithography tools. However, as we scale to radio frequencies K_{Eff} and M_{Eff} of overtone mode resonators scale with the overtone order, minimizing filter distortion due to mass-loading and simplifying narrow-bandwidth filter design with coupled resonators at maximum-velocity locations. The schematic mechanically coupled four-pole filter consisting of overtone square-extensional resonators is shown in Figure 3.4. The four vibration modes of the filter are [21]:

$$f_{C1} = \frac{1}{2\pi}\sqrt{\frac{K_{Eff}}{M_{Eff}}} \tag{3.24}$$

$$f_{C2} = \frac{1}{2\pi}\sqrt{\frac{K_{Eff} + K_S}{M_{Eff}}} \tag{3.25}$$

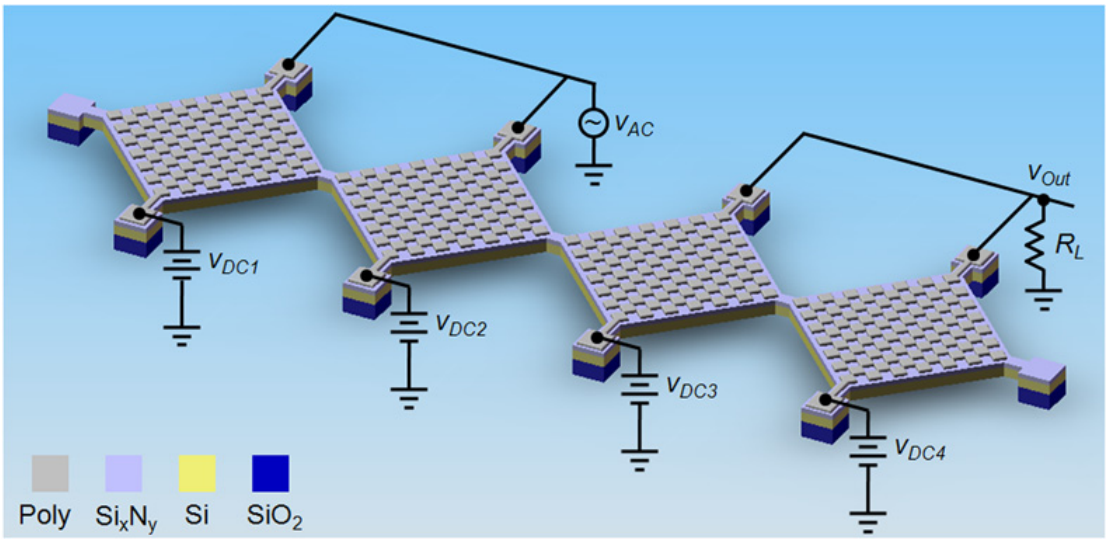

Figure 3.4: Schematic of a digitally programmable filter composed of four series mechanically-coupled checkered-electrode resonators. Each resonator has individually addressable $RF + DC$ lines. The silicon device layer is an RF ground to prevent substrate losses.

$$f_{C3} = \frac{1}{2\pi}\sqrt{\frac{K_{Eff} + 2K_S}{M_{Eff}}} \tag{3.26}$$

$$f_{C4} = \frac{1}{2\pi}\sqrt{\frac{K_{Eff} + 3K_S}{M_{Eff}}} \tag{3.27}$$

The four vibration modes of a 4-pole filter composed by four mechanically coupled overtone square-extensional resonators are shown in Figure 3.5. Only the first and last resonators of multi-pole mechanically-coupled filters need to be electrostatically transduced. The intermediate resonators are mechanically coupled and DC biasing is not an absolute requirement. We retain individual control of the DC bias (V_{DC}) for each resonator and exploit this property to implement digitally-tunable bandwidth channel-select filters. The programmable filter is configured as follows:

1. $[DC_1 = +V_{DC}, DC_2 = DC_3 = \text{OFF}, DC_4 = +V_{DC}]$ - excites all four vibration modes and enables 4-port filter response.

2. $[DC_1 = DC_3 = +V_{DC}, DC_2 = DC_4 = -V_{DC}]$ - excites the first two resonators

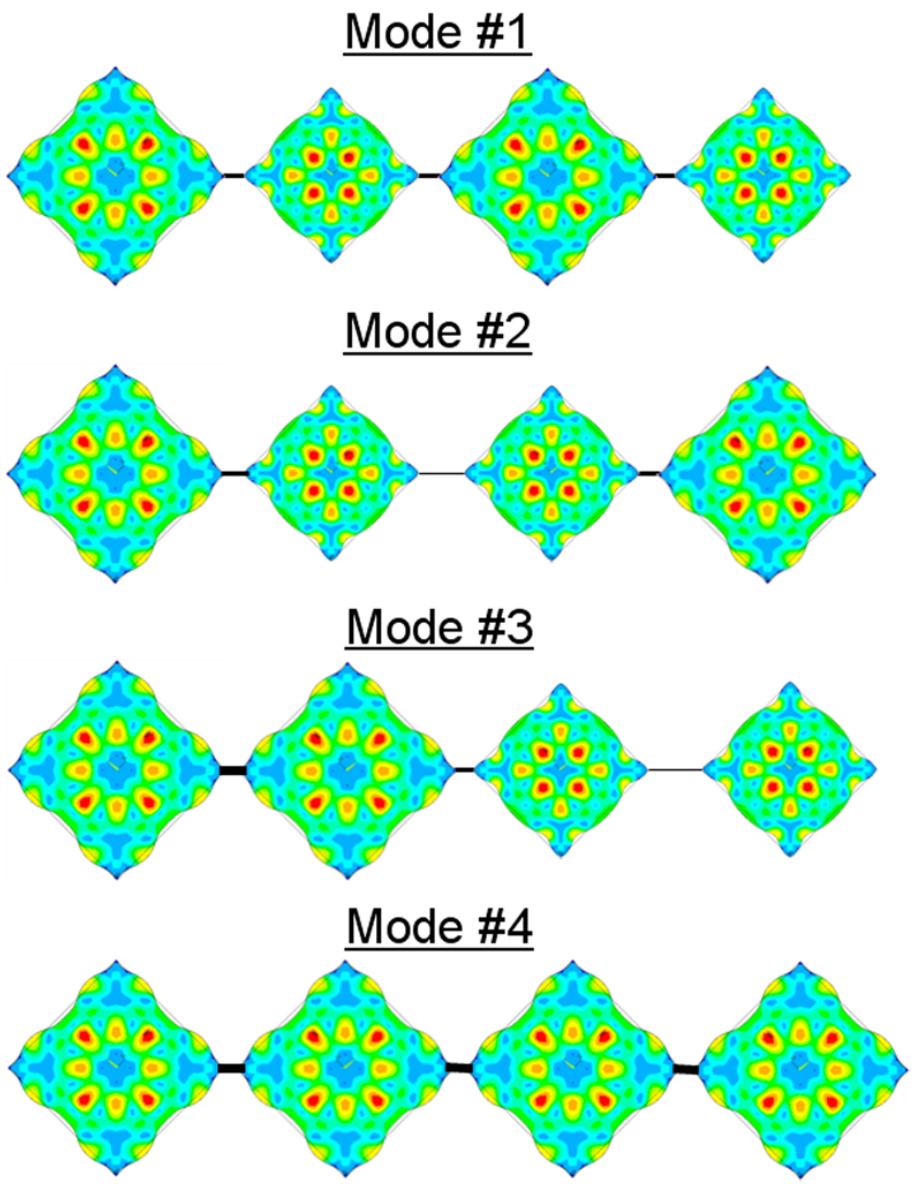

Figure 3.5: Four vibration modes of a 4-pole filter consisting of overtone square-extensional mode resonators.

out-of-phase. The system still has four vibration modes, however the DC bias configuration attenuates the excitation of modes #3 and #4. In addition, the DC bias configuration of the last two resonators sums the out-of-phase motion of the resonators while nulling in-phase modes (and motional currents). The configuration results in a 2-pole lower sub-band filter.

3. $[DC_1 = DC_2 = DC_3 = DC_4 = +V_{DC}]$ - excites the first two resonators in-phase. This leads to exact inverse of the above configuration and results in a 2-pole higher sub-band filter.

The filter is modeled as a network of mechanically coupled mass-spring-damper and simulated in MATHEMATICA. The simulation results demonstrate the filter frequency response with digitally programmable center frequency and bandwidth as shown in Figure 3.6.

3.4 Fabrication Process

The fabrication process of the high-overtone square-extensional resonators and digitally programmable filters is summarized in Figure 3.7. A 1 μm thick undoped oxide is initially deposited by plasma-enhanced chemical vapor deposition (PECVD) on an n-type low resistivity SOI wafer with 2.75 μm thick single-crystal silicon (SCS) device layer. The oxide layer is patterned using fluorine based reactive ion etcher as shown in Figure 3.7 (a). This oxide pedestal is patterned everywhere under the signal pad to reduce the pad capacitance. Next, a 55 nm layer of low-stress silicon nitride thin film is deposited by low-pressure chemical vapor deposition (LPCVD) at 850°C. A 75 nm layer of n-doped polysilicon is then deposited by LPCVD at 620°C, annealed at 1000°C for 40 minutes, and patterned to form the top electrodes as shown in Figure 3.7 (c). This is followed by a deep reactive ion etch (DRIE) step to define the resonators and filters into the silicon

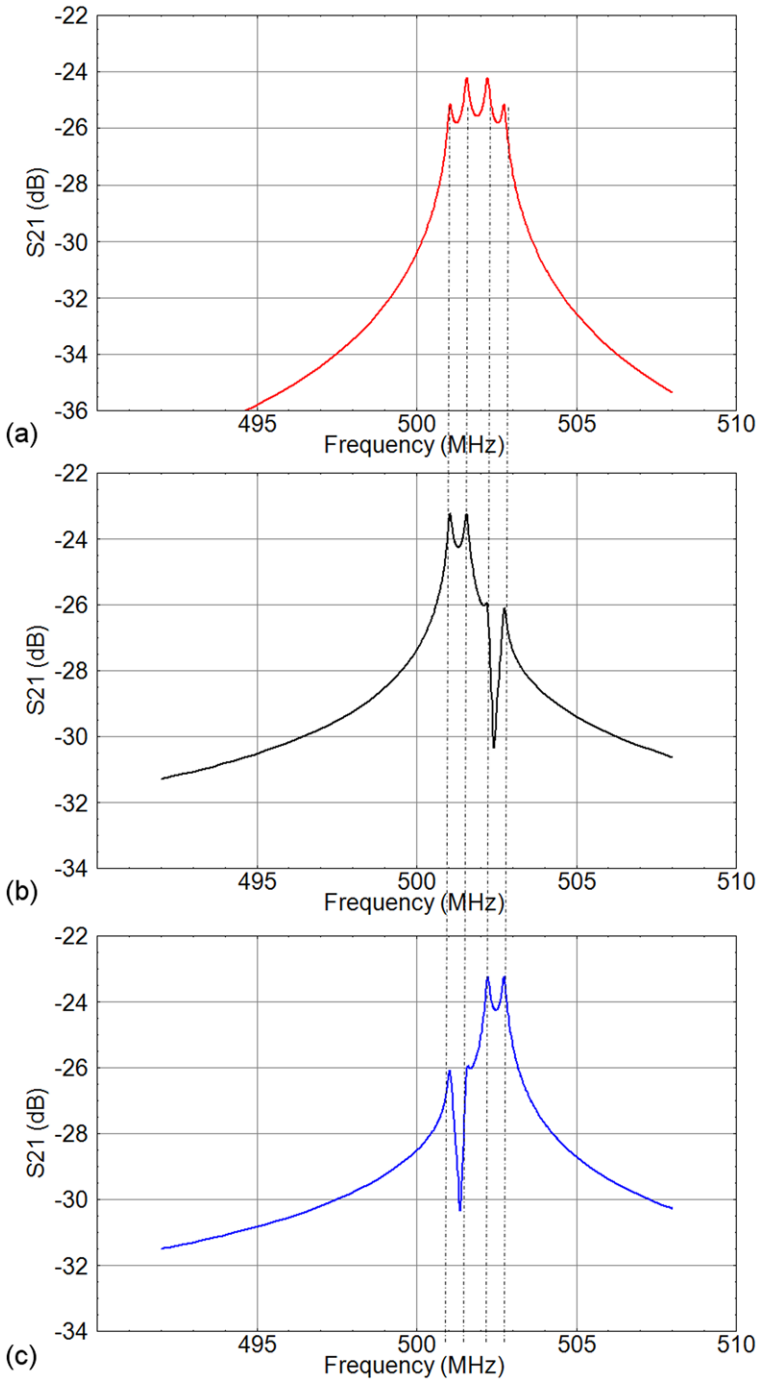

Figure 3.6: Simulated performance of a digitally programmable filter composed of four series mechanically-coupled checkered-electrode resonators. (a) Simulated 4-pole frequency response of the filter. (b) Simulated lower sub-band filter response. The biasing scheme forces the left two resonators to vibrate out of phase and sums the out-of-phase motional current of the right two resonators. (c) Simulated higher sub-band filter response. The biasing scheme forces the left two resonators to vibrate in phase and sums the in-phase motional current of the right two resonators.

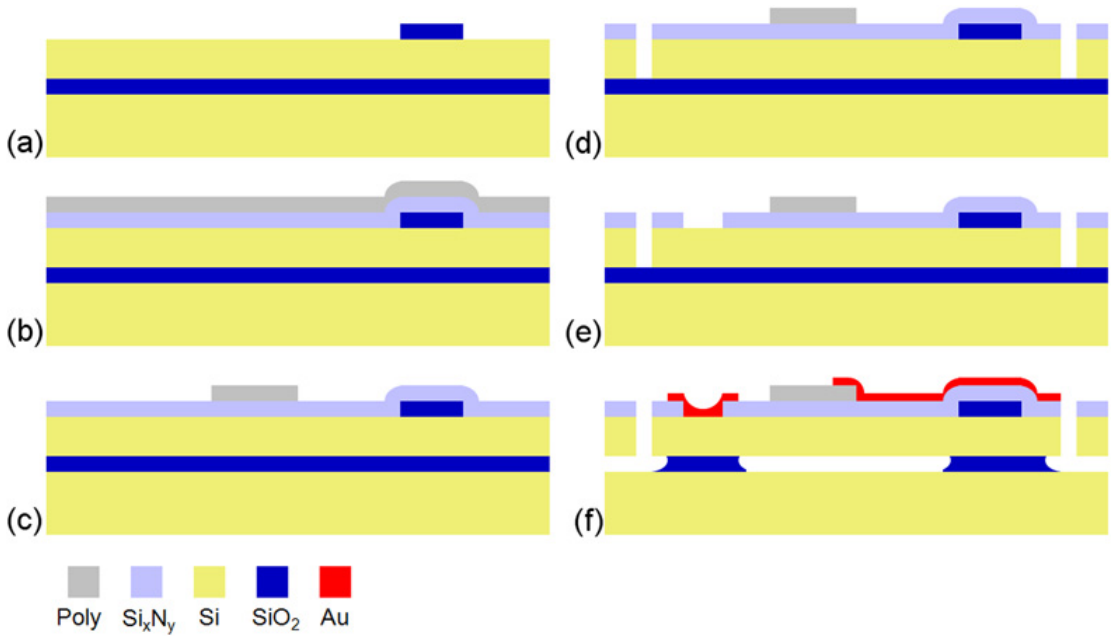

Figure 3.7: Fabrication process flow of high-overtone square-extensional mode resonators and digitally programmable filters.

device layer. The silicon nitride is patterned to open contact holes to bias the resonators and filters. Partial metal routing is done by evaporating and patterning 80 nm layer of Pt/Au. Finally, the devices are released by performing a timed-etch of the buried oxide in hydrofluoric acid (HF) as shown in Figure 3.7 (f). The key innovations of this process include implementation of a pedestal oxide underneath each signal pad to minimize the pad capacitance and employment of partial metal routing to improve electrical conductivity. The Pt/Au layer is used to carry electrical input signals from input pads to the degenerately-doped polysilicon electrodes on the devices and to deliver the output signals from the devices to output pads. The released SEM images of a high-overtone square-extensional resonator and a 4-pole digitally programmable filter are shown in Figure 3.8 and 3.9 respectively.

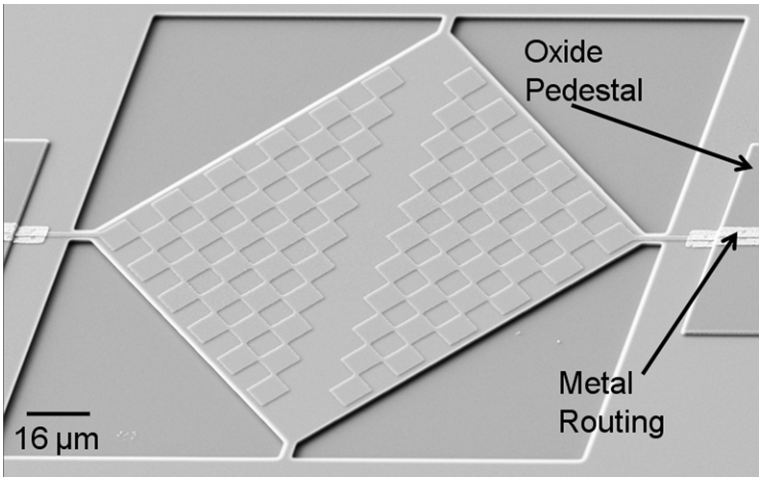

Figure 3.8: SEM image of a high-overtone 2-D square-extensional mode resonator with checkered electrodes for transduction. The resonator consists of a 55 nm SiN transducer sandwiched between poly electrodes and 2.75 μm thick silicon device layer. An oxide pedestal layer is implemented to elevate the RF signal lines off the ground plane. Pt/Au metal traces and pads are introduced to improve RF signal integrity and reduce noise during probing.

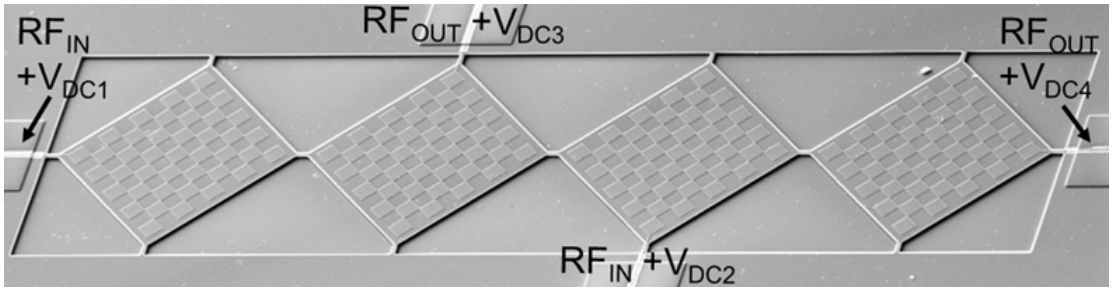

Figure 3.9: SEM image of a digitally programmable filter composed of four series mechanically-coupled checkered-electrode resonators. Each resonator has individually addressable RF + DC lines. The silicon device layer is an RF ground to prevent substrate losses. All RF paths are metalized, routed on an elevated oxide bridge to reduce capacitance and de-embedded to the edge of DRIE trench.

3.5 Calibration and De-embedding Techniques

The resonators and filters are characterized in a Cascade RF probe station in a 2-port configuration using high-performance RF coaxial wires, GSG probes and bias-Ts. In order to characterize the 4-pole filters, additional in-phase and out-of-phase power-splitters are necessary. Parasitics up to the probe tips are first cancelled with Short-Open-Load-Thru (SOLT) RF measurements on a standard calibration substrate. De-embedding is then performed with Cascade WinCal software, using Short-Open-Thru (SOT) structures fabricated on-chip, but separate from the resonators [81]. Appendix B will discuss in more detail the calibration and de-embedding techniques to measure the high-overtone square-extensional mode resonators and the digitally programmable filters.

3.6 Characterization of a High-overtone Square-extensional Mode Resonator

The 2-port high-overtone square-extensional mode resonator is characterized using the measurement setup illustrated in Figure 3.10 (a). DC voltage is superimposed to the AC signal using Bias-Ts to introduce resonance at both input and output ports while the silicon device layer is connected to ground. Agilent E8364B PNA microwave vector network analyzer is used to measure the transmission and quality factor of the resonator. The measured frequency response of a high-overtone square-extensional mode resonator in air at room temperature and pressure has a resonance frequency of 512 MHz, motional impedance (R_X) of 3.1 kΩ and Q of $1,800$ as demonstrated in Figure 3.10 (b). For comparative study, the designed and measured data for the resonator are summarized and tabulated in Table 3.2.

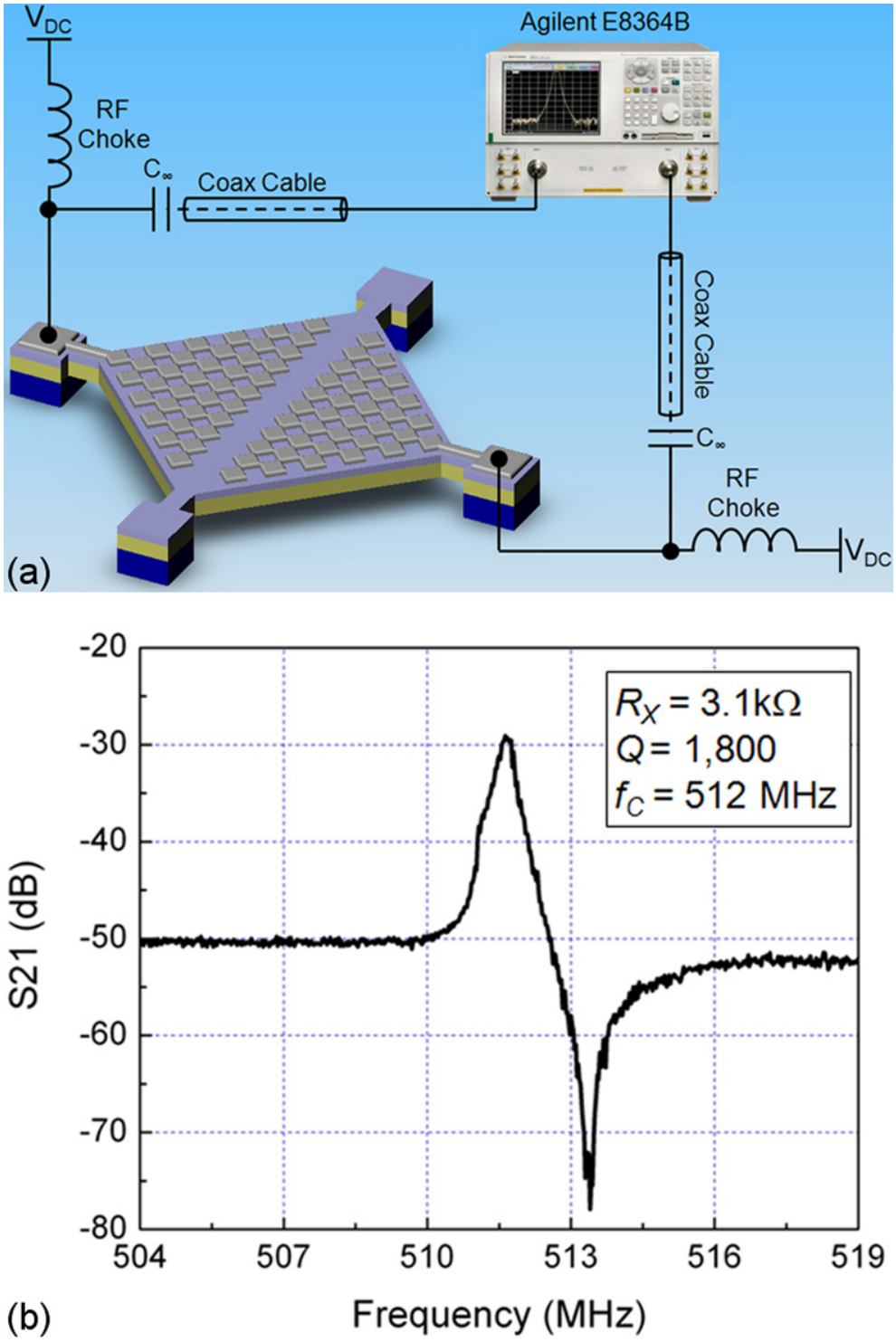

Figure 3.10: (a) Testing configuration for a 2-port high-overtone square-extensional mode resonator. (b) Measured series resonance response of a 2-port high-overtone square-extensional mode resonator in air at room temperature and pressure.

Table 3.2: Design parameters and measured data of the high-overtone square-extensional resonator

Parameter	Designed Value	Measured Value	Unit
L_{EL}	8.5	8.5	μm
t_f	50	50	nm
t_{Si}	2.75	2.75	μm
t_{Poly}	80	80	nm
n	1	1	—
j	72	72	—
Q	$2,000$	$1,800$	—
R_X	3.3	3.1	kΩ
R_L	50	50	Ω
f_C	500	512	MHz

3.7 Characterization of a Digitally Programmable Filter

The 4-pole digitally programmable filter is characterized in 2-port configuration according to the measurement setup illustrated in Figure 3.4. In order to retain individual control of each transducer and reduce RF losses to the substrate, the silicon device layer is maintained at an RF ground and each RF I/O port has a superimposed independent DC supply. Calibration and de-embedding procedures to eliminate excessive probe-pad and substrate parasitics is again performed prior to all RF measurements. The power-splitters and bias-Ts ($DC = GND$) for RF_{IN} and RF_{OUT} signals are included during de-embedding process. The programmable filter is configured and characterized as follows:

1. [$V_{DC1} = 50$ V, $V_{DC2} = V_{DC3} = 0$ V, $V_{DC4} = 50$ V] - enables a 4-pole filter with

1.4 MHz bandwidth at 508.7 MHz center frequency.

2. [$V_{DC1} = V_{DC3} = 40$ V, $V_{DC2} = V_{DC4} = -40$ V] - preferentially excites and senses the first two vibration modes which results in a 720 kHz bandwidth lower sub-band filter.

3. [$V_{DC1} = V_{DC2} = V_{DC3} = V_{DC4} = 40$ V] - preferentially excites and senses the last two vibration modes which results in a 660 kHz bandwidth higher sub-band filter.

The 50 Ω terminated frequency response of the filter for each case of bias voltage configuration measured in air at room temperature and pressure is presented in Figure 3.11. In order to maximize the power transfer from input to output, the termination impedance of the filter is adjusted. Figure 3.12 and Table 3.3 summarize the filter response of each configuration with adjusted termination impedance. The DC bias for the sub-band filters was reduced to 40 V to compensate for increased transducer area and ensure all filters have the same impedance for characterization.

3.8 Conclusion

In this work we demonstrated the design, modeling, simulation, fabrication and characterization of high-overtone square-extensional resonators and digitally programmable filters. The center frequency and filter bandwidth are digitally tunable by controlling the DC bias voltages of individual resonators in a series coupled array. Using tri-state polarization voltage control ($-V_{DC}$, GND, $+V_{DC}$), the programmable filter provides bandwidth granularity for next generation frequency-agile radios. Although square-extensional and other contour-mode MEMS resonators are excellent candidates for designing channel-select filter arrays, they cannot be tuned significantly at the device level. By using the system-level digital-

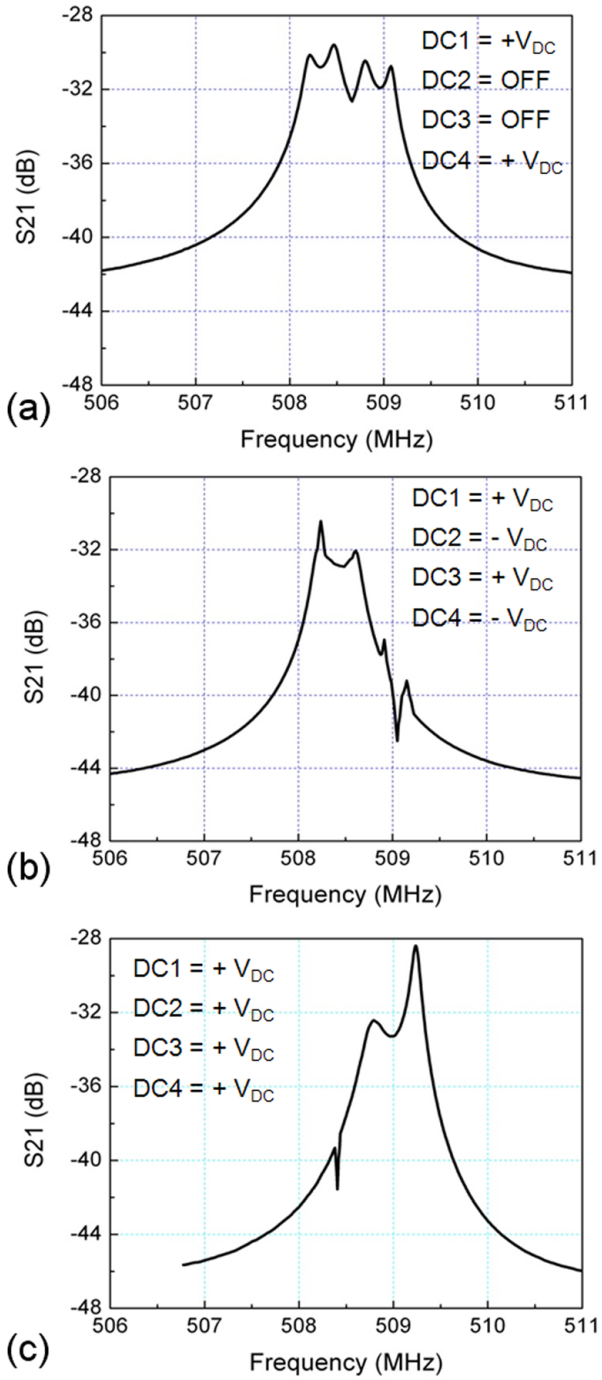

Figure 3.11: Performance of a 50 Ω terminated filter with three different bias configurations in air. (a) Measured 4-pole frequency response of the filter. (b) Measured lower sub-band filter response. The biasing scheme forces the left two resonators to vibrate out of phase and sums the out-of-phase motional current of the right two resonators. (c) Measured higher sub-band filter response. The biasing scheme forces the left two resonators to vibrate in phase and sums the in-phase motional current of the right two resonators.

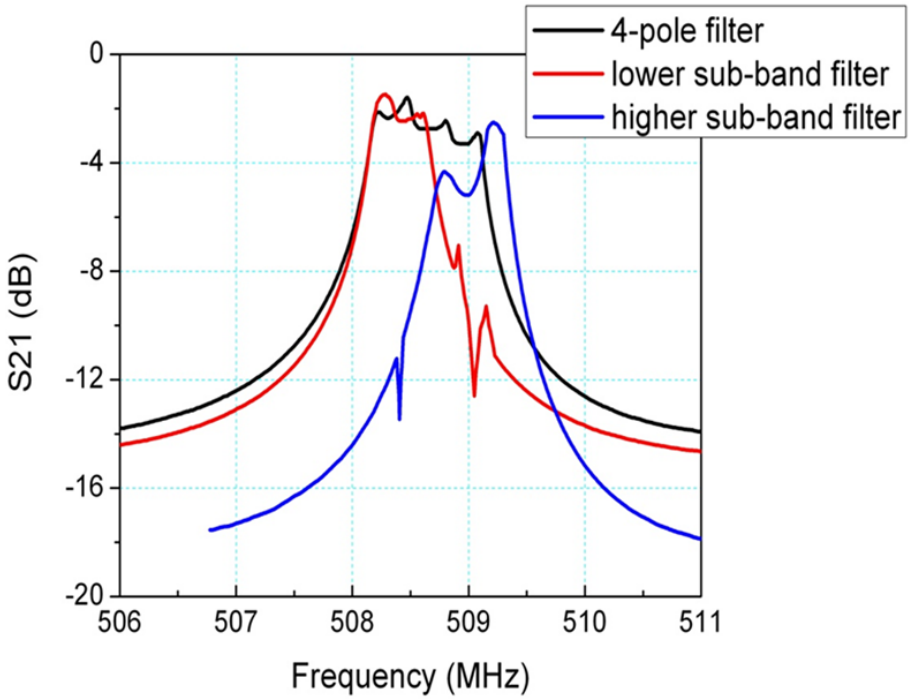

Figure 3.12: Transmission response of the filter with three different bias configurations after termination using the PNA's pole-Z conversion function. The attenuated modes are clearly visible in the transmission response of the lower sub-band filter. The filter stop-band floor is high because electrical resistance in the ground plane leads to large capacitive feedthrough between drive and sense ports.

Table 3.3: Performance summary of the digitally programmable filter

Parameter	4-pole filter	Lower sub-band filter	Higher sub-band filter
IL	-2.4 dB	-2 dB	-3.1 dB
$3dB\ BW$	1.4 MHz	720 kHz	660 kHz
f_C	508.7 MHz	508.3 MHz	509.1 MHz
Ripple	< 2 dB	< 1 dB	< 3 dB
Stop Band Rejection	-14 dB	-14 dB	-20 dB
V_{DC}	50 V	40 V and -40 V	40 V
R_L	4.1 kΩ	2.8 kΩ	2.9 kΩ

tuning scheme we have demonstrated a 4-pole filter consisting of four overtone square-extensional mode resonators at 509 MHz with 1.4 MHz bandwidth. By switching the DC polarization voltage of the individual resonators, the filter is split into narrower high and low sub-bands, each approximately 700 kHz wide. Due to limitations of the SOI fabrication process and resistive losses through the device layer, we were limited to four resonators and each $RF\ I/O$ port had a superimposed independent DC supply. However, this can be easily resolved by switching to a surface-micromachining process [82]. Adding more resonators to the array will provide finer bandwidth granularity, however the maximum possible bandwidth is still limited by the coupling efficiency of the transducer.

CHAPTER 4

VACUUM-ENCAPSULATED CMOS-COMPATIBLE PACKAGING TECHNOLOGY FOR CONTOUR-MODE RESONATORS

4.1 Introduction

Wireless communication has greatly impacted our daily lives since the first radio system was invented. Applications, such as cellular phones, satellite television, GPS navigation, and wireless internet networks, are driving the development of RF components in the direction of being smaller, more inexpensive and requiring less power, and thus this topic has been one of the hottest research areas. MEMS resonators have great potential for replacing conventional resonators used in portable wireless applications because of their merits of small size, high quality factor (Q), and low power consumption [83]. There is also great interest in using coupled micro-resonators as band-pass filters and exciting results have been demonstrated in Chapter 2 and Chapter 3 of this dissertation.

Despite the advances in device performance, packaging for MEMS resonators remains a critical challenge. Because of their extreme sensitivity to the environment, MEMS resonators need vacuum encapsulation to enable real applications and post-MEMS CMOS integration. The promising on-chip application also requires a CMOS compatible packaging process. Due to the stringent RF requirements, the electrical properties and hermeticity of the packaging are also very important.

This Chapter presents the design, fabrication, packaging design, and measurement of a dielectrically transduced, width-extensional mode resonator encapsulated in an epitaxial-grown silicon package. The major challenges of merging two technologies into a promising solution of a high frequency MEMS-based device will also be discussed.

4.2 Width-extensional Mode Resonator

Dielectrically-transduced silicon bar resonators vibrating in the bulk-mode have superior linearity and high quality factors [60, 79]. The width-extensional mode resonance of a bar resonator depends on the width, W, with frequency (f_C) given by

$$f_C = \frac{n}{W}\sqrt{\frac{E}{\rho}} \tag{4.1}$$

where n is the mode number (n = 1, 3, ...), and E and ρ are the effective elastic modulus for 2-D expansion and the density of silicon, respectively. The width-extensional mode is excited by patterning electrodes in plate configuration on top of the resonator using dielectric transduction, as shown in Figure 4.1 (a). The main resonator bar consists of three layers - a 100 nm polysilicon electrode layer, a 100 nm silicon nitride transducer layer, and a 3 μm single-crystal silicon resonator layer. As shown in Figure 4.1, the input and output electrodes are patterned on polysilicon and the silicon nitride layer is used as a high-κ dielectric to enhance the transduction (compared to an air-gap). The quarter-wavelength anchoring scheme is designed to minimize mass-loading of the resonator. A DC bias is superimposed on a small AC voltage using a Bias-T and applied to the drive electrode, while the silicon device layer is connected to RF ground. This time-varying voltage causes a squeezing force on the dielectric thin film. Due to the Poisson effect, the dielectric layer experiences a lateral strain. Since the silicon nitride layer is structurally integrated with the silicon bar, the lateral strain is transferred from the dielectric film to the silicon resonator layer. As the strain distributes through the resonator, the width-extensional mode is excited and the motional current is sensed through the sense electrode. The ANSYS fundamental mode shape of the width-extensional resonator is shown in Figure 4.1 (b).

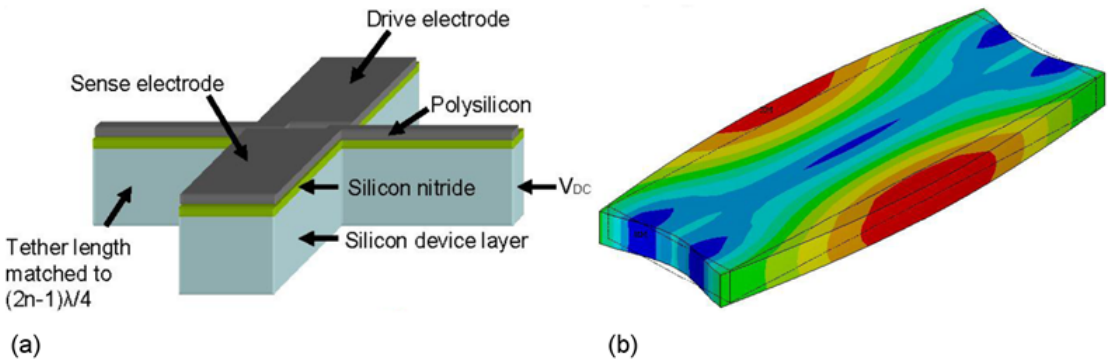

Figure 4.1: (a) Schematic diagram of the dielectrically transduced, width-extensional mode resonator. (b) ANSYS contour plot of the width-extensional bar mode shape.

4.3 Epitaxy-silicon Microshell Packaging

The fabrication process is the fusion of two technologies developed at Cornell and Stanford [60, 84]. The wafer-level encapsulation packaging developed at Stanford University has the advantage of a small foot-print, superior long-term stability, and CMOS compatibility [85–87]. The epitaxial-grown silicon allows CMOS circuitry to be built on top of the package to be integrated with the MEMS device packaged inside.

Previously, there have been accelerometers and resonators working at 1.2 - 1.4 MHz or below, encapsulated in this packaging. However, there has not been an attempt to encapsulate devices with resonant frequencies higher than 20 MHz using this silicon package. A thorough study of the electrical performance of the packaging was investigated [88]. The paper indicates that the silicon vertical interconnect has less than 1 dB attenuation up to 6 GHz, which extends the utility of this packaging for intermediate frequency to high frequency resonator applications.

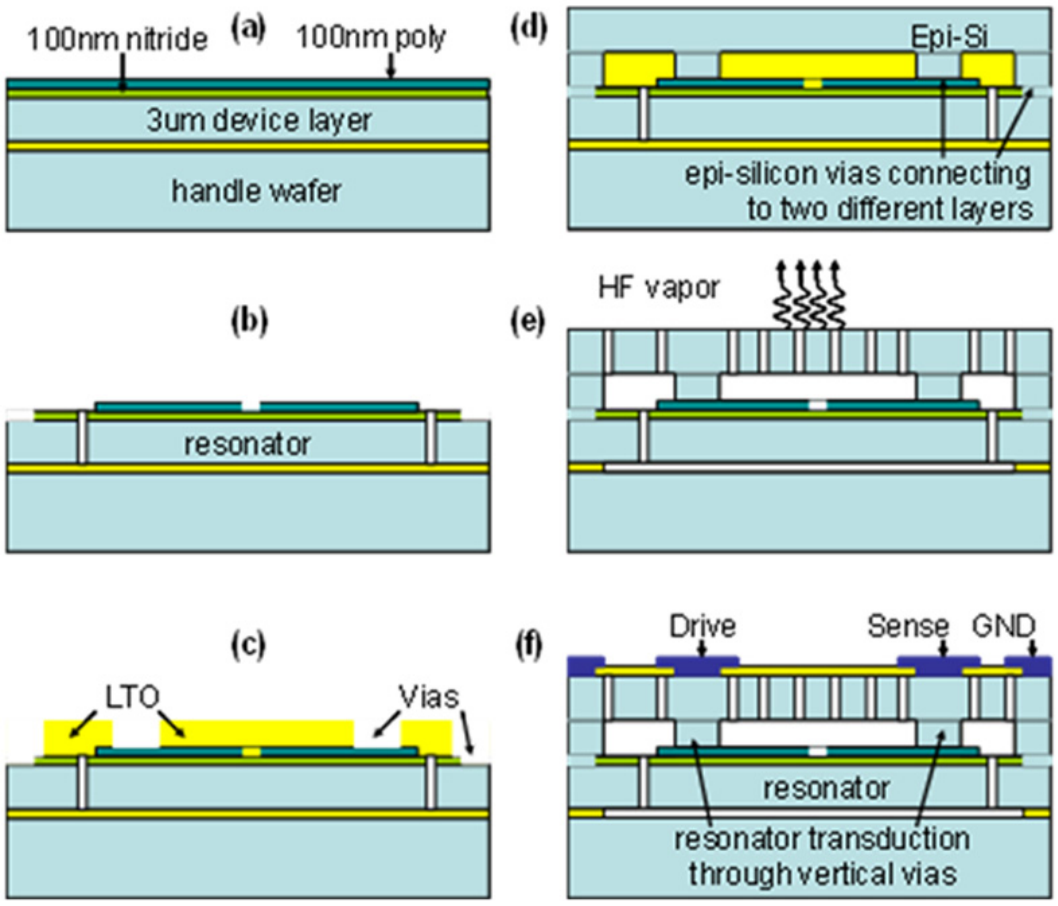

Figure 4.2: Epi-silicon microshell encapsulation process for dielectrically transduced resonators. Vertical epi-vias to the poly electrodes provide RF input/output while the vias to the silicon device layer provide a micro RF-cage providing a shielded micro-environment.

4.4 Fabrication Process

As shown in Figure 4.2, the fabrication begins with a silicon-on-insulator (SOI) wafer with a device layer of 3 μm. A stack of 100 nm stoichiometric silicon nitride and 100 nm heavily doped n+ polysilicon was deposited using low pressure chemical vapor deposition (LPCVD). The polysilicon layer was patterned to create electrodes. Part of the silicon nitride layer was etched to create electrical contact to the device layer, as shown in Figure 4.2 (b). The resonator was then patterned and etched through the nitride/silicon stack using deep reactive ion etching (DRIE). Low temperature oxide (LTO) was deposited as the sacrificial layer to create a cavity on top of the resonator. The LTO was then patterned and etched to create electrical contacts.

The main challenge is in creating low-loss vertical interconnects making contact to two different layers of the resonator. As shown in Figure 4.2 (d), the LTO was patterned and etched to create an electrical connection to the polysilicon layer as well as the device layer. Due to the thickness variation from the LTO deposition, stopping the etch on two different layers is extremely challenging using an academic-grade plasma etcher (insufficient etching selectivity, non-uniform etching across the wafer, etc.) However, this challenge can be greatly reduced with an industry-grade etcher.

Another challenging issue is the resistivity of the epi-polysilicon interconnects. A lot of characterization was done to ensure the resistivity of the epi-polysilicon was less than 10 mΩ-cm. Highly phosphorus doped epi-silicon was then grown on the top of the wafer to encapsulate the resonators. Vent holes were patterned to open access to the sacrificial LTO. A custom made HF vapor etcher in the Stanford Nanofabrication Facility was used to release the resonator. After releasing, vent holes were again sealed by LTO in a low pressure environment to vacuum-

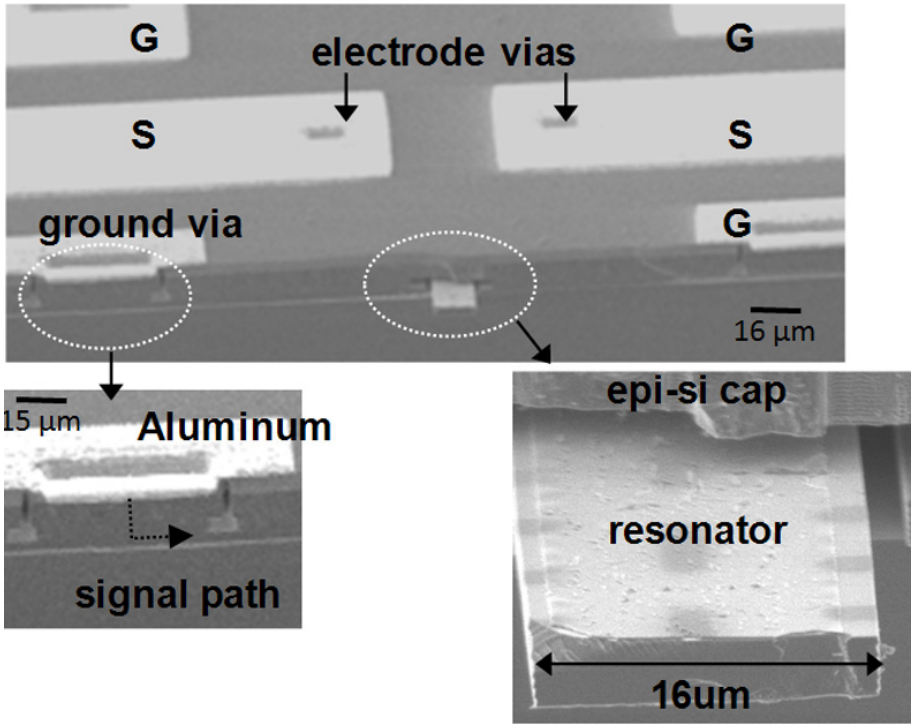

Figure 4.3: SEM of the fabricated resonator. The zoomed-in picture on the right shows the thin poly electrode on top of the resonator bar. The zoomed-in picture on the left shows the electrical contact between the epi-silicon and the device layer.

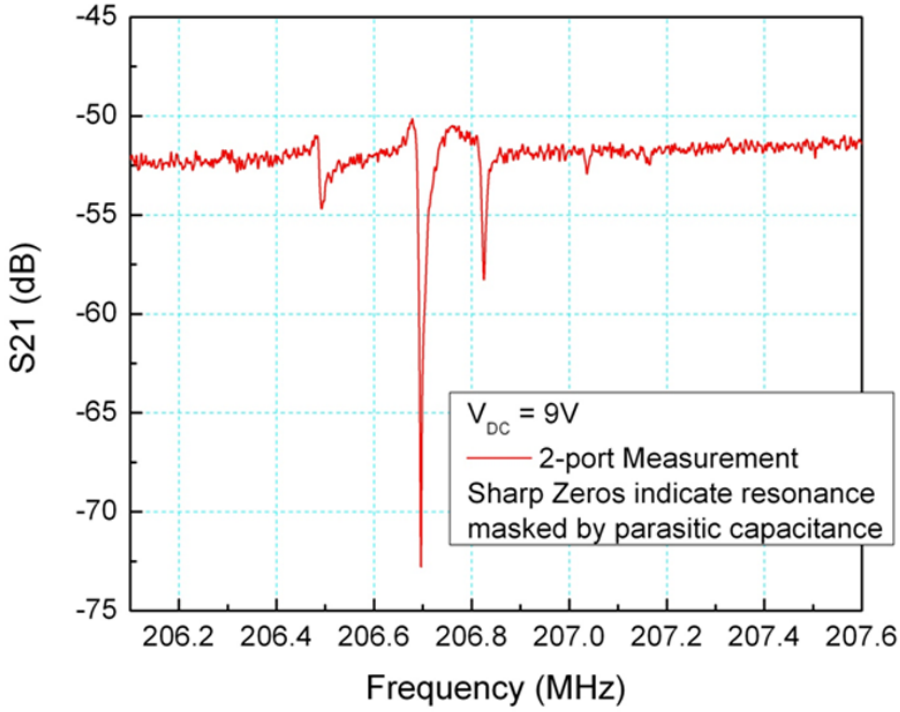

Figure 4.4: Transmission response using the 2-port measurement. Capacitive feedthrough masks the electromechanical resonance, resulting in a sharp dip at the target frequency.

encapsulate the resonators. Finally, an aluminum layer was used for electrical interconnects and bond pads. An SEM picture of a fabricated width-extensional mode resonator is shown in Figure 4.3.

4.5 Measurement Results

As shown in Figure 4.4, a simple two-port measurement gives a clear sharp dip in S_{21}, indicating the electromechanical resonance is masked by the parasitic feedthrough. To overcome the capacitive feedthrough, the resonator was characterized using a differential measurement technique, inspired by [89, 90]. An RF signal from the network analyzer first goes into a splitter to create in-phase and out-of-phase signals, represented by $+RF_{in}$ and $-RF_{in}$, respectively. In order to

induce resonance of the resonator, a DC bias, V_{DC}, was added into $+RF_{in}$ using a Bias-T. Two identical resonators were driven by $+RF_{in}$ and $-RF_{in}$. While $+RF_{in}$ + V_{DC} was driving the resonator, the pure AC signal ($-RF_{in}$) was driving the dummy resonator, with only its parasitic capacitance being driven. The outputs from both structures were then mixed together, where the out-of-phase current from the parasitic capacitance cancels out the parasitic component in the signal from the resonator. The exact differential measurement setup and equivalent electrical circuit used in this work is express in Figure 4.5 . Although it would be ideal to have two identical resonators side-by-side when the differential measurement is conducted, the fabricated wafer only has a similar resonator by its side. Therefore, although the improvement of the signal to noise ratio is already greatly enhanced by using a similar structure as the dummy resonator, the feedthrough cancellation is not yet optimized.

From the SEM picture, one can observe that the vertical interconnect is firmly connected to the device layer, providing electrical ground to the resonator beam. One can also note that the thin ($\sim$ 13 μm) epi-silicon is enough to provide mechanical stability for the low-pressure hermetic packaging. It is important to keep this layer thin because of the electrical requirements [88].

The fabricated resonator was measured using the differential measurement setup explained in the previous section. Figure 4.6 shows the response using feedthrough cancellation on top of the response from the 2-port measurement. The resonant frequency is 207 MHz and the quality factor is $6,400$. This is the highest reported frequency for a MEMS resonator packaged in a microshell. One can also note that there is a -13 dB noise reduction due to the implementation of the differential measurement.

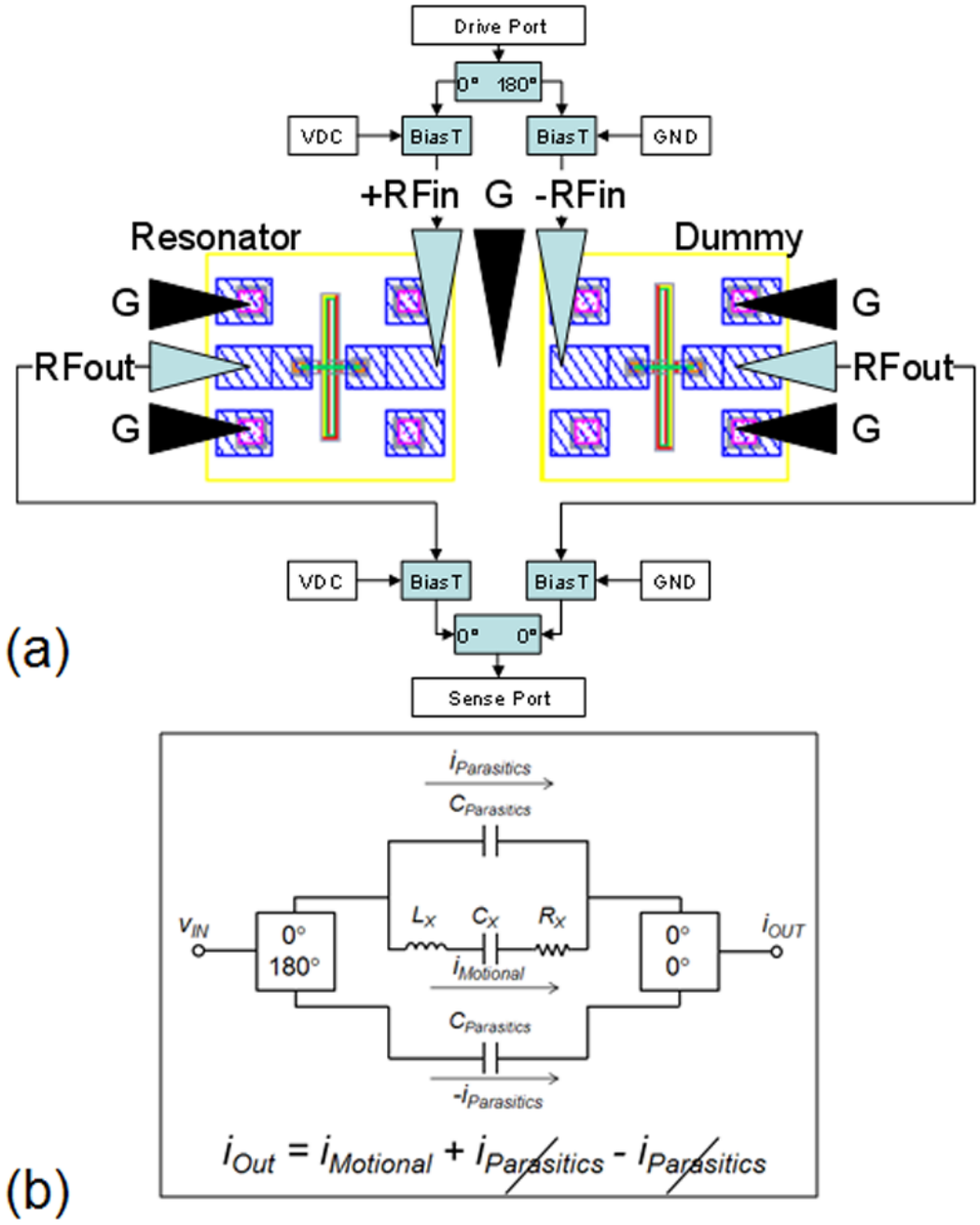

Figure 4.5: (a) Schematic of the pseudo-differential measurement setup, and (b) The equivalent circuit of pseudo-differential measurement to cancel the capacitive feedthrough current.

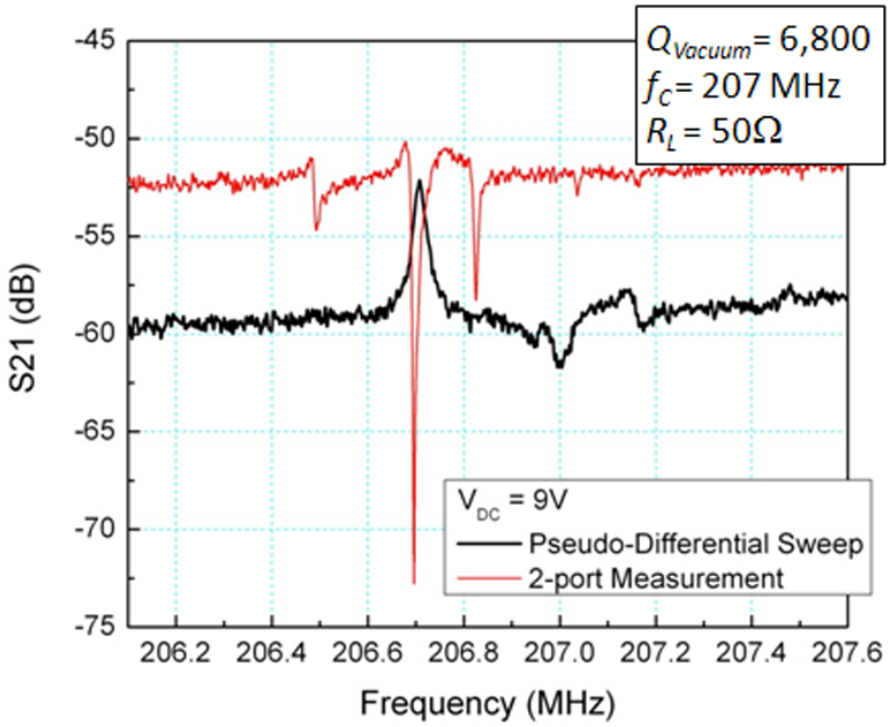

Figure 4.6: Transmission responses of the simple 2-port measurement and pseudo-differential measurement. It is clearly shown that the resonance peak matches the sharp dip shown in the 2-port measurement.

4.6 Conclusion

A fully encapsulated, width-extensional mode resonator was successfully fabricated with an f x Q product of 12 x 10^{11} Hz, making it an excellent candidate for drop-in insertion in local oscillator and RF spectrum analyzer applications. The performance of the epitaxial-silicon packaging is also verified to sufficiently package VHF devices. In the future, we plan to introduce Hafnium dioxide (HfO_2) as the dielectric film to reduce the motional impedance. Furthermore, the length of the width-extensional mode resonator can be increased to enlarge the transduction area. Hence, the motional impedance of the encapsulated resonator could be reduced and alleviate the challenge of impedance matching.

CHAPTER 5

AQUEOUS TRANSDUCTION OF CONTOUR-MODE RF MEMS RESONATORS

5.1 Introduction

The increasingly crowded radio spectrum and the impending arrival of next generation 7-band cellular phones and the joint task force radio system (JTRS) has necessitated front-end filter arrays capable of eliminating both out-of-band and out-of-channel interferers. The filters will require extremely narrow bandwidth, good stop-band rejection and excellent shape factor. Dielectrically-transduced contour-mode MEMS resonators with quality factor $Q > 10,000$, low motional impedance R_X and CAD-defined resonance frequencies from 40 MHz - 2 GHz are excellent candidates for designing channel-select filter arrays [63,71,91]. But unlike thickness shear mode resonators, the frequency expressions for contour modes and flexural vibration modes do not directly couple. It is therefore difficult to perform orthogonal frequency tuning of contour-mode resonators [64].

Electrostatically transduced RF MEMS resonators have very high (Q) which will enable design of narrow-bandwidth channel-select filters with steep shape-factor. However, to date the high (R_X) of these resonators leads to large insertion loss (IL) in the filters when connected directly to 50 Ω RF systems. Therefore, it is essential to minimize the motional impedance, while retaining high quality factors.

In lateral-gap contour-mode resonators, the motional impedance is given by

$$R_X = \frac{\sqrt{K_{Eff} M_{Eff}}}{Q\left(\frac{{V_{DC}}^2 \epsilon^2 A^2}{g^4}\right)} \tag{5.1}$$

where K_{Eff} and M_{Eff} are the effective spring constant and mass of the resonator. R_X can be reduced by decreasing the transducer gap (g), increasing the bias voltage

(V_{DC}), electrode area (A) or dielectric constant (ϵ) of the transducer. This work focuses on increasing the dielectric constant of the transducer, by replacing vacuum or air-gap with DI-water.

The high permittivity of DI water ($\kappa_{Water} = 80.1$) relative to air or vacuum enhances the efficiency of the transducer, thereby enabling operation at low DC bias voltage. Moreover, water has a low acoustic velocity ($1,500$ m/s) compared to silicon, poly-SiGe and poly-SiC. The large acoustic mismatch between water and silicon allows the resonators to achieve a relatively large displacement in lateral direction. In addition, the high-κ dielectric liquid increases the electrostatic force between the electrodes and the resonator, which facilitates a larger electrostatic frequency tuning capability.

Sournart *et al* demonstrated that by using a local oscillator (LO) signal that is faster than the response time of a polar fluid, it is possible to prevent electrode polarization and double-layer formation [92]. Electrostatic actuators and viscosity sensors operating in water have been demonstrated using this technique [93, 94]. In this chapter, we demonstrate that the same approach enhances the performance of contour-mode poly-SiGe disk resonators by constraining DI water to the lateral transducer gaps.

5.2 Aqueous Transduction of a Contour-mode Poly-SiGe Disk Resonator

Lateral dielectrically transduced thickness shear mode resonators with 0.8% tunable center frequency (f_C)have been demonstrated in Chapter 2 of this thesis. However, the frequency of operation of these resonators is limited by the device thickness. Contour-mode air-gap poly-SiGe disk resonators are exceptionally at-

tractive choice for radio frequency filtering because their frequency of operation is defined lithographically. Furthermore, they have low anchor-loss, high-Q in air and can be integrated with CMOS electronics. However, since air is not a very efficient transducer ($\kappa_{Air} = 1$), these devices have high motional impedances and ppm/V tuning range.

5.2.1 Measurement of a Poly-Sige Disk Resonator in Air

In order to verify the feasibility of using DI water for aqueous transduction of MEMS resonators, we used a previously fabricated 50 nm air-gap poly-SiGe contour mode disk resonator shown in Figure 5.1 [95]. Figure 5.2 (a) shows the measurement setup and experimental result of the first radial mode air-gap poly-SiGe resonator. The superimposed LO signal prevents bi-layer formation [92] and enables aqueous transduction. Even though the LO signal might not be necessary on the actuation side since the actuation frequency is considerably high, it is required on the sense side. Care is taken to attenuate harmonics of the LO signal and prevent unintentional actuation of the resonator through non-linear electrostatic force. Before characterizing the resonator, we performed two standard RF calibrations. The first calibration is the Short, Load, Open, and Through (SLOT) substrate calibration up to the probe tips to remove parasitics associated with the cable and probe assembly. The second calibration is the Short, Open, and Through (SOT) de-embedding using Cascade WinCal software to cancel the large pad capacitances. Appendix B will discuss in more detail the calibration and de-embedding techniques for MEMS resonators and filters. The resonator has a transmission response with $Q = 5,300$ and $R_X = 517$ kΩ in air with a 5 V polarization voltage as shown in Figure 5.2 (b).

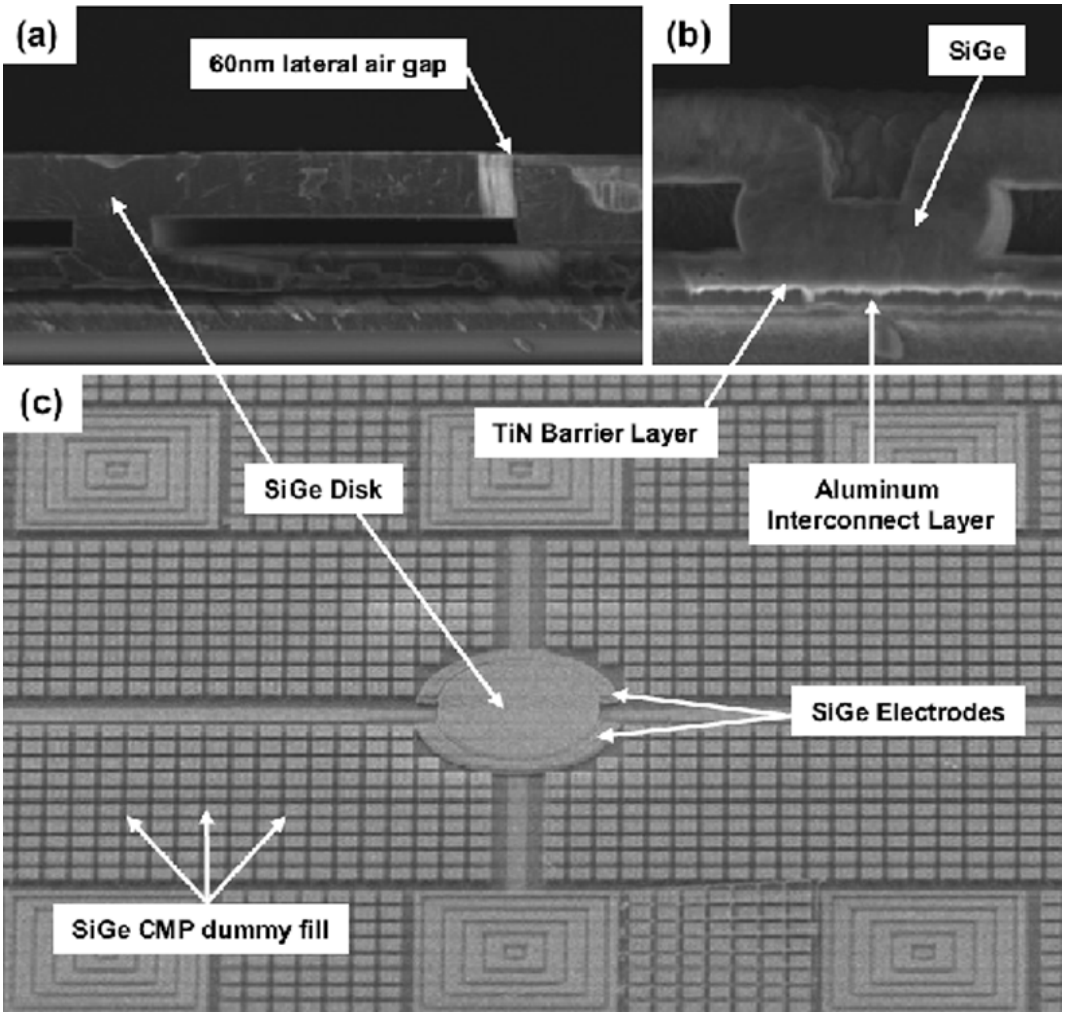

Figure 5.1: SEM image of a poly-SiGe disk resonator: (a) Cross-section of the resonator showing the 60 nm lateral air-gap (b) Close-up of anchor, and (c) Top view.

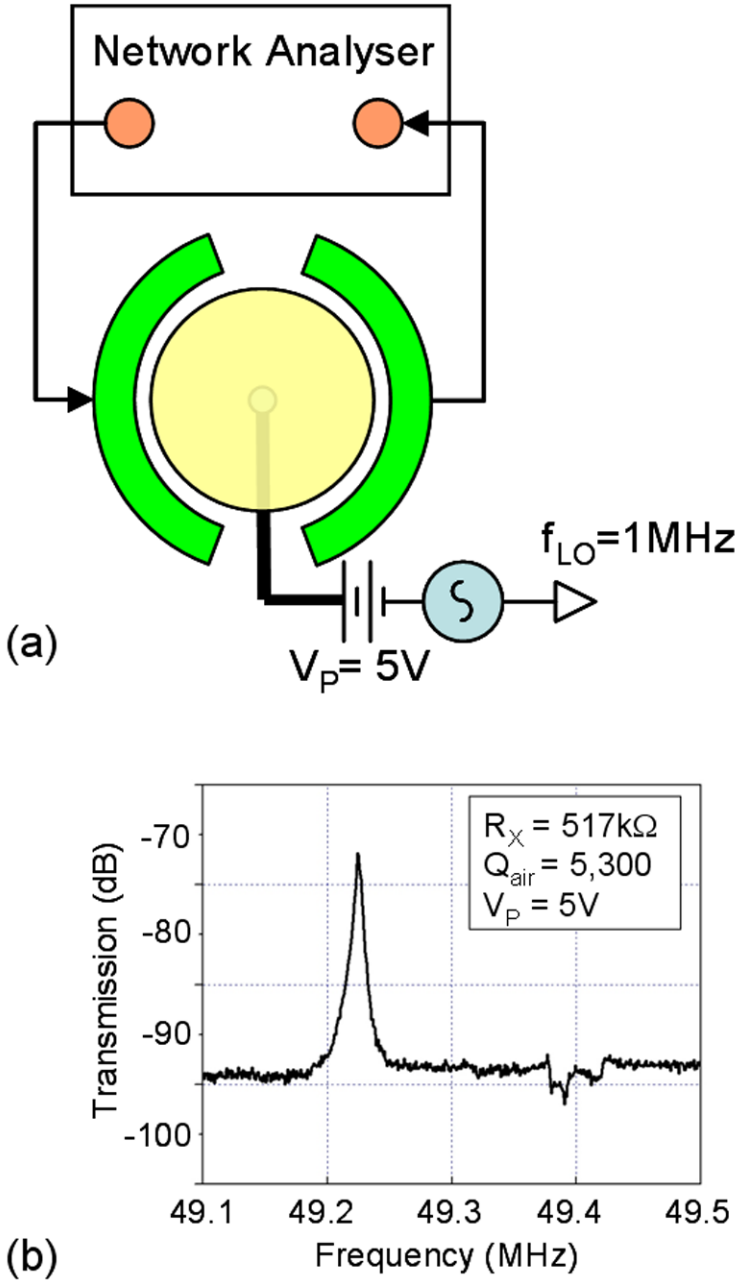

Figure 5.2: (a) Transmission measurement setup, and (b) Transmission response in air.

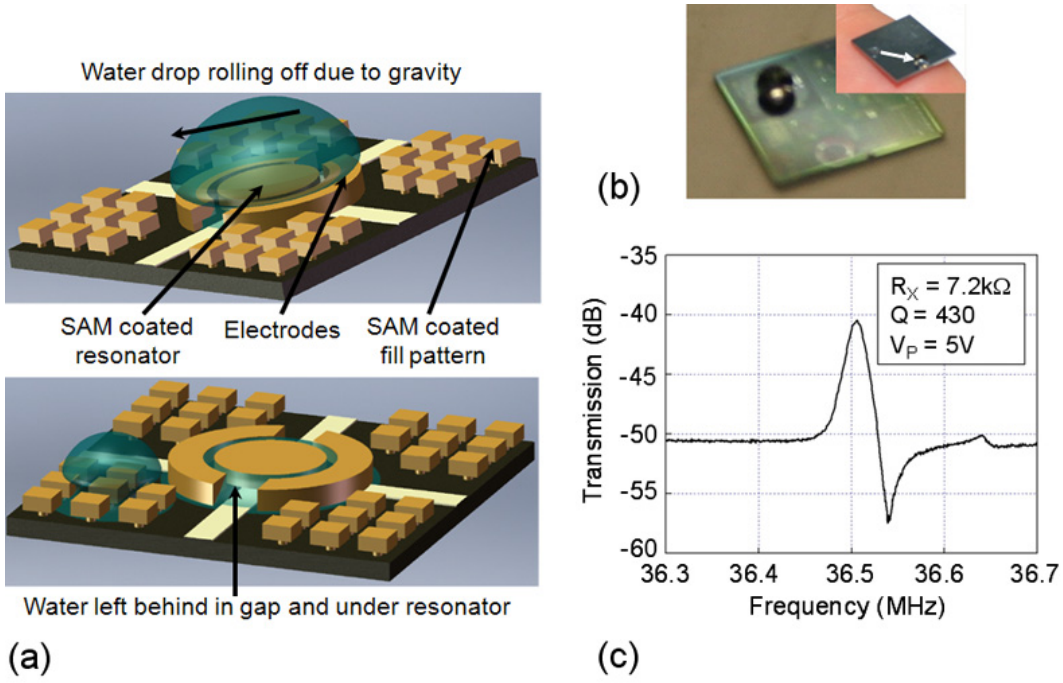

Figure 5.3: (a) Schematic illustrating the experiment. The water wicks the 60 nm gap and is left under the structure. (b) Photograph of water droplet placed on resonator and then moved to the edge. (c) Measured transmission response after water drop is rolled away from the resonator: Q of 430 at 36 MHz.

5.2.2 Measurement of Poly-Sige Disk Resonators with DI Water

In our experiments, we used high resistivity DI water specially acquired to minimize the leakage current down to < 1 μA. Water has high loss tangent at frequencies above 2 GHz [96], which should be sufficient for most RF MEMS application frequencies. The initial trial was to immerse the resonator in a water droplet and measure the transmission response. However, after submerging the resonator under a water droplet, we could not measure a transmission response due to excessive mass-loading and Q losses resulting from viscous drag.

The subsequent attempt was done by coating the resonator with a hydrophobic self-assembled monolayer (SAM) to eliminate mass-loading and viscosity effects of

the water droplet on the resonator. The SAM layer is non-conformal, coating the top surface of the poly-SiGe disk resonator, while leaving the 50 nm transducer gaps hydrophilic. A drop of DI water was placed on the resonator and then the chip was slowly tipped to one side to let the water droplet roll-off the structure as shown in Figure 5.3 (a,b). The DI water 'wicked' the electrostatic transducer gaps and a transmission response with a Q of 430 at 36 MHz was measured due to the reduced mass-loading and viscous damping on top of the resonator (Figure 5.3 (c)).

The Q was low because water got under the resonator through the space between the resonator and the CMP fill-pattern. Even though the gap under the disk was < 2 μm, the water underneath the resonator causes viscous damping and degrade the resonator's quality factor. In order to reduce this effect, the water droplet was initially placed further away from the resonator on the SAM-coated fill pattern. The chip was slowly tipped, ensuring that the water droplet rolled over both the transducer gaps of the resonator as illustrated in Figure 5.4 (a). The short time that the water droplet overlapped the resonator was sufficient to wick the transduction gaps but greatly reduced the chance of water seeping under the resonator.

The hydrophobic SAM-coated CMP fill-pattern enabled the droplet to 'roll' rather than drag along the chip surface. This allowed repetitive measurements with reasonable control over droplet roll-over. The transmission response of the resonator was measured with $Q > 3,500$ and $R_X = 4.2$ kΩ near 42 MHz as shown in Figure 5.4 (b).

As the water droplet is rolled back and forth, the capacitive floor increases and R_X improves as shown in Figure 5.5. This phenomena happened because the water did not entirely 'wick' the transduction gaps during the first-pass. Subsequent rolls

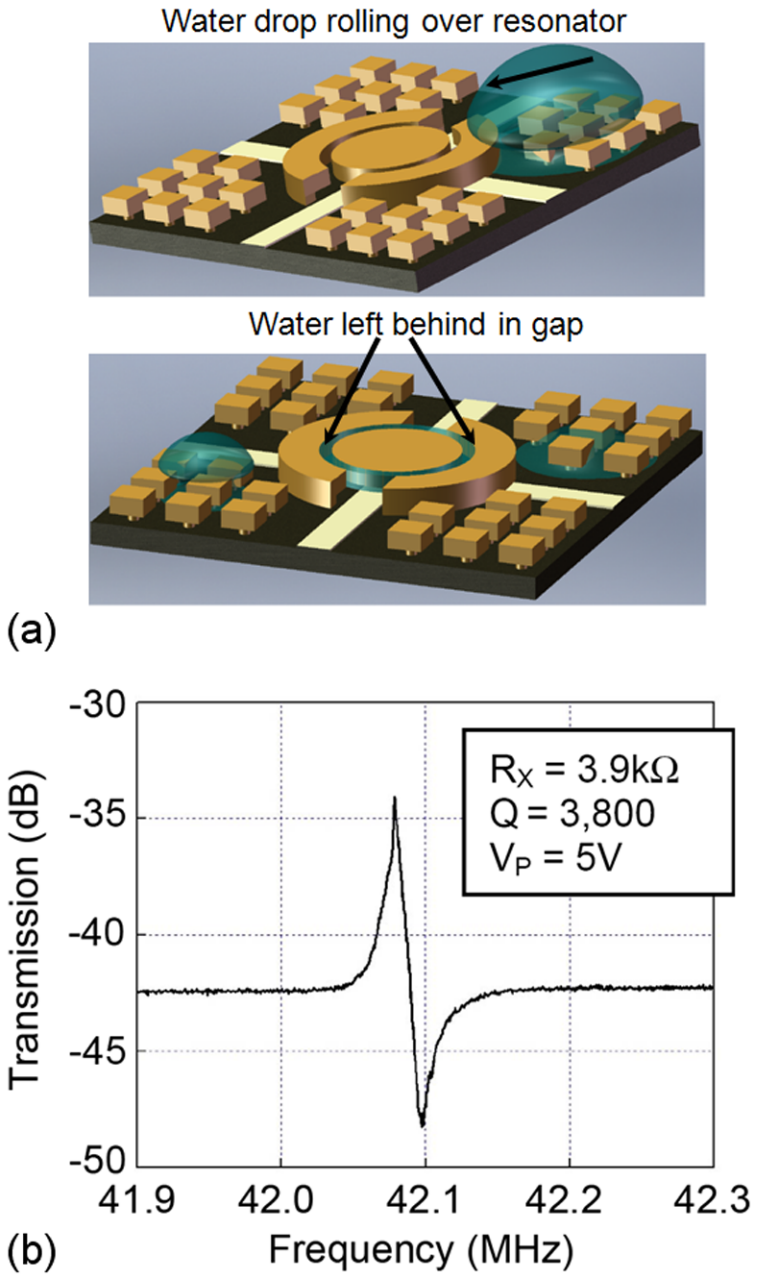

Figure 5.4: (a) Schematic of water droplet rolled across the resonator; wicking the transducer gap but minimizing the water left underneath the resonator. (b) Transmission response: Q of $3,800$ at 42 MHz with $R_X = 3.9$ kΩ.

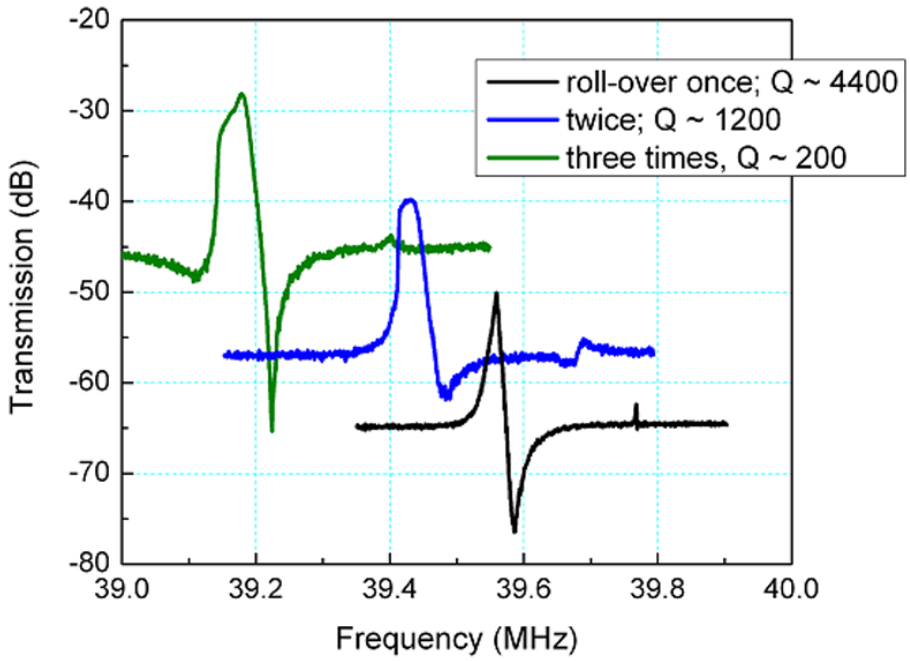

Figure 5.5: Transmission response of a resonator with repeated rolls of the DI water droplet.

allow more DI water to enter the gaps, however, the measured Q dropped from $4,000$ to 200 due to viscous damping as shown in Figure 5.5.

5.2.3 Series Frequency Tuning of Poly-Sige Disk Resonators

Non-linearity in air-gap parallel-plate electrostatic transducers introduces a DC bias-dependent resonant frequency shift. This electrical spring stiffness is given by

$$K_E = \frac{{V_{DC}}^2 C_0}{g^2} \tag{5.2}$$

where C_0 is the nominal capacitance between the electrode area and the resonator body. K_E directly subtracts from the mechanical spring stiffness K_M. The electrical spring constant provides DC-bias controlled, post-fabrication tuning of electrostatically transduced resonators:

$$\frac{\Delta f}{f_{Mech}} = -\frac{1}{2}\frac{{V_{DC}}^2 C_0}{K_M g^2} = -\frac{1}{2}\frac{{V_{DC}}^2 \epsilon A}{K_M g^3} \tag{5.3}$$

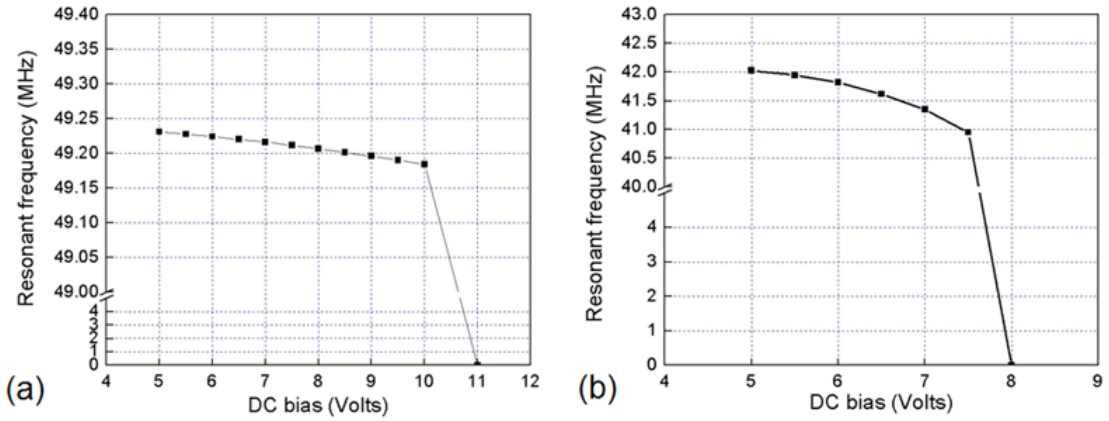

Figure 5.6: (a) 0.1% center frequency tuning of the air-gap transduced disk resonator before anchor failure. (b) In DI water, the resonator center frequency is tuned up to 3%, before the onset of electrolysis.

The tuning range of low frequency (< 10 MHz) bending-mode beam resonators using electrostatic spring softening is on the order of 5 - 10 %. This facilitates resonator designs which not only overcome fabrication tolerances and temperature drift, but also enables frequency-agile filter and oscillator design. However, because tunability relies on the ratio of K_E to K_M, the relatively large effective stiffness of air-gap contour mode resonators limits their tuning range $< 0.05\%$ [97]. Other tuning techniques such as tuning the series capacitance and heating the resonator, de-Q the resonator [43] and cost excessive power consumption [98] respectively. Replacing air in the sub-micron transducer gap with DI water enhanced the electrostatic spring by >50 x and extended the tuning range to 3% - the highest tuning-range reported to date for electrostatically transduced contour-mode resonators as shown in Figure 5.6.

5.3 Conclusion

Aqueous transduction is an excellent alternative to solid-dielectric transduction due to the high permittivity and low acoustic velocity of water. However, the operating

frequency is limited up to 2 GHz as water has a significant loss tangent above that frequency [96]. It also facilitates a large frequency tuning capability. The 3% limit of electrostatic tuning capability was mainly due to electrolysis of water and bubble formation, which suggests that using an alternate low loss-tangent liquid such as dielectric oil [99] will enable high resonant frequency operation and wide tuning range. In addition to RF applications, aqueous transduction can be used for thermal cooling and isolation, single-molecule mass detection in liquid media and frequency-domain dielectric spectroscopy.

CHAPTER 6

PZT TRANSDUCED VOLTAGE TUNABLE RESONATORS

6.1 Introduction

Numerous applications in wireless communications and sensor networks have motivated the development of on-chip, high-Q MEMS resonators and filters to realize portable radios that consume low power and operate at the global range of frequency standards. Dielectrically transduced thickness shear mode and contour-mode resonators have the capability to reach high frequency of operation while maintaining high Q and low motional impedance as presented in Chapter 2 and Chapter 3 of this dissertation. A band-pass filter can be constructed by electrically or mechanically coupling an array of these resonators. However, the inadequate effective coupling efficiency of the dielectrically transduced resonators limits the bandwidth of the filter, creating a demand for transducers with high electromechanical coupling coefficient.

Aluminum Nitride (AlN) is a popular material for fabrication of thin film bulk acoustic wave (BAW) and contour-mode resonators and filters because it possesses a high acoustic velocity, high quality factor and post-CMOS integration capability [54, 100]. However, intermediate frequency applications have driven the investigations for new piezoelectric or/and ferroelectric materials for resonators. At low frequencies, ferroelectrics like lead zirconate titanate (PZT) are better suited as they avoid thick film requirements and reduce the area required for the filters. Furthermore, PZT exhibits larger electromechanical coupling coefficient than AlN, enabling the design of larger % bandwidth filters [101].

A resonator with dynamically tunable center frequency will not only overcome fabrication tolerances and thermal drift, but will also facilitate filter design that

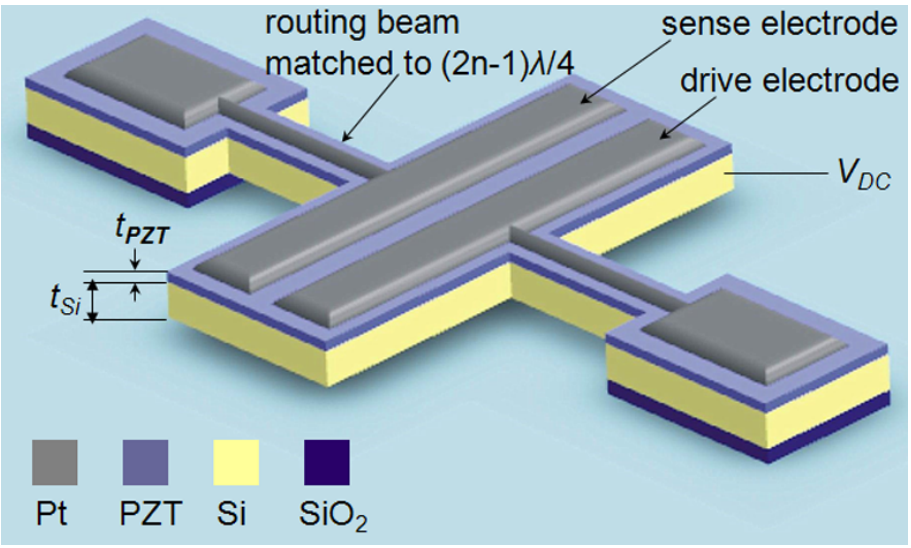

Figure 6.1: A 3-D schematic of PZT-on-Silicon length-extensional mode resonator.

has the ability to discern bandwidths between 0.1 MHz to 5 MHz, enabling a handheld analog spectral processor with voltage dependent dynamic frequency trimming and tuning. PZT has been previously shown to have frequency tuning capabilities [102, 103]. However, PZT-only resonators are well known to have low quality factor ($Q < 300$) [101, 104]. In order to overcome the low quality factor of PZT-only resonators, we developed a new fabrication technology to integrate PZT transduction with single-crystal silicon (SCS) resonators.

6.2 Length Extensional Mode Resonator

Previous results have shown that length-extensional mode (LEM) vibrations can be excited by sandwiching a piezoelectric transducer (AlN, Zinc Oxide, PZT, etc.) between metal electrodes [54,105]. However, due to poor crystallinity and repeatability of the piezoelectric thin-films, several research groups have chosen to use the piezoelectric material for actuation and sensing, while utilizing single-crystal silicon as the resonating structure [52, 106]. The schematic of a PZT transduced length-

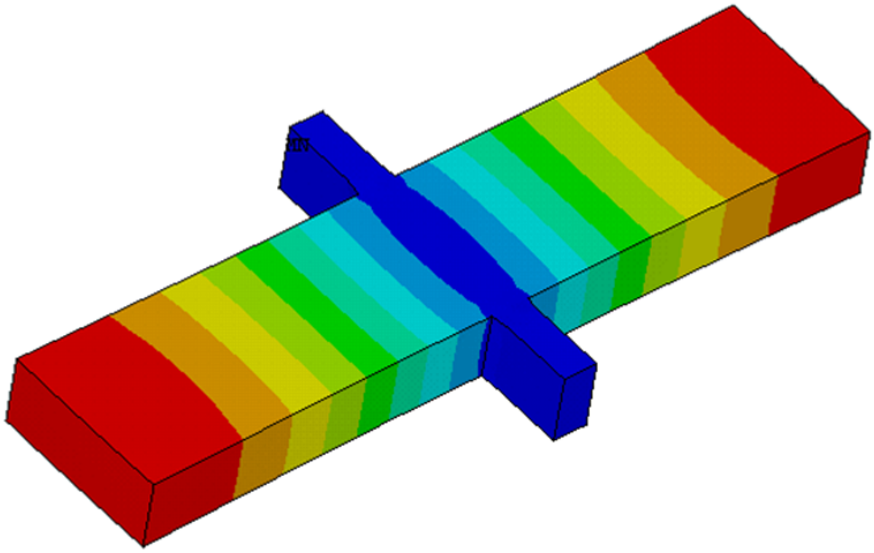

Figure 6.2: An ANSYS mode shape of a length-extensional mode resonator.

extensional mode resonator on single-crystal silicon is presented in Figure 6.1. The ANSYS mode shape of the designed LEM resonator is demonstrated in Figure 6.2. In this effort, PZT transduced resonators were fabricated with and without a 10 μm thick silicon device layer to explore the insertion loss and Q trade-offs between the two types of resonators. The bulk-extensional mode resonance of a length-extensional mode resonator depends on L, with frequency of operation (f_C) given by:

$$f_C = \frac{n}{2L}\sqrt{\frac{E}{\rho}} \tag{6.1}$$

where L is the length of the resonator, E and ρ are effective elastic modulus for 2-D expansion and density of the resonator respectively, and n is the harmonic order. The frequency independent motional impedances of the fundamental mode of PZT transduced length-extensional mode two-port resonators will be derived in the next subsections.

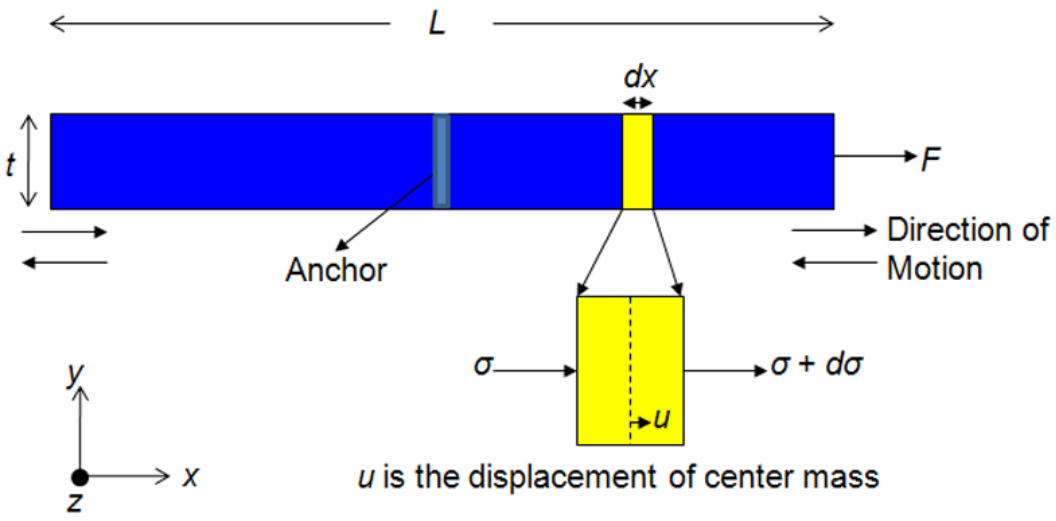

Figure 6.3: The cross-section of a length-extensional mode resonator.

6.2.1 Effective mass, Damping ratio and Effective spring constant

The cross-section of a length-extensional mode resonator with length, L and thickness, t is shown in Figure 6.3. The resonator vibrates in the direction normal to area, A (not shown in the picture).

From Newton's law of motion, the sum of forces that act on the resonator can be expressed as

$$\Sigma F = m\ a \rightarrow (\sigma(x,t) - d\sigma(x,t))\, A - \sigma(x,t)A = \rho A dx \frac{\partial^2 u(x,t)}{\partial t^2} \tag{6.2}$$

Equation 6.2 can be written as

$$A\frac{\partial \sigma(x,t)}{\partial x} = \rho A \frac{\partial^2 u(x,t)}{\partial t^2} \tag{6.3}$$

$$A\frac{\partial E\frac{\partial u(x,t)}{\partial x}}{\partial x} = \rho A \frac{\partial^2 u(x,t)}{\partial t^2} \rightarrow EA\frac{\partial^2 u(x,t)}{\partial x^2} = \rho A \frac{\partial^2 u(x,t)}{\partial t^2} \tag{6.4}$$

where E is the Young's modulus of the structure. The wave equation for a one-dimensional vibrating length-extensional mode resonator including the damping

factor and external forces is

$$\rho A\frac{\partial^2 u}{\partial t^2}(x,t) - bA\frac{\partial}{\partial t}\frac{\partial^2 u}{\partial x^2}(x,t) - EA\frac{\partial^2 u}{\partial x^2}(x,t) = \frac{\partial f}{\partial t}(x,t) \tag{6.5}$$

By the method of separation of variables, we assume equation 6.5 has solutions of the form

$$u(x,t) = g(t)\sin\left(\frac{n\pi}{L}x\right) \tag{6.6}$$

Substituting 6.6 into 6.5 gives

$$\rho A\sin\left(\frac{n\pi}{L}x\right)\frac{\partial^2 g(t)}{\partial t^2} + bA\left(\frac{n\pi}{L}\right)^2\sin\left(\frac{n\pi}{L}x\right)\frac{\partial g(t)}{\partial t} + EA\left(\frac{n\pi}{L}\right)^2\sin\left(\frac{n\pi}{L}x\right)g(t) = \frac{\partial f}{\partial t}(x,t) \tag{6.7}$$

Multiply 6.7 by $\sin\left(\frac{n\pi}{L}x\right)$ and integrate over the length yields

$$\begin{aligned} &\int_{-L/2}^{L/2}\rho A\left(\sin\left(\tfrac{n\pi}{L}x\right)\right)^2\tfrac{\partial^2 g(t)}{\partial t^2} \\ &+bA\left(\tfrac{n\pi}{L}\right)^2\left(\sin\left(\tfrac{n\pi}{L}x\right)\right)^2\tfrac{\partial g(t)}{\partial t} \\ &+EA\left(\tfrac{n\pi}{L}\right)^2\left(\sin\left(\tfrac{n\pi}{L}x\right)\right)^2 g(t)dx \quad = \quad F(t) \end{aligned} \tag{6.8}$$

where $F(t)$ is

$$\int_{-L/2}^{L/2}\frac{\partial f}{\partial t}(x,t)\sin\left(\frac{n\pi}{L}x\right)dx \tag{6.9}$$

Equation 6.8 can be simplified as

$$\frac{\rho AL}{2}\frac{\partial^2 g(t)}{\partial t^2} + \frac{bAL}{2}\left(\frac{n\pi}{L}\right)^2\frac{\partial g(t)}{\partial t} + \frac{EAL}{2}\left(\frac{n\pi}{L}\right)^2 g(t) = F(t) \tag{6.10}$$

From equation 6.10, we can recognize the effective mass, damping ratio and effective spring constant of a length-extensional mode resonator with length L are given by

$$M_{Eff} = \frac{\rho AL}{2} \tag{6.11}$$

$$\zeta = \frac{bAL}{2}\left(\frac{n\pi}{L}\right)^2 = \frac{n^2 bA\pi^2}{2L} \tag{6.12}$$

$$K_{Eff} = \frac{EAL}{2}\left(\frac{n\pi}{L}\right)^2 = \frac{n^2 EA\pi^2}{2L} \tag{6.13}$$

6.2.2 Electromechanical Coupling Constant

The lateral stress, σ in PZT is governed by the constitutive equation

$$\sigma = E\epsilon - e_{31}\frac{v_{AC}}{t} \tag{6.14}$$

where ϵ, e_{31}, E and t are the strain, piezoelectric coefficient, Young's Modulus and thickness of PZT respectively. If the PZT is free to deform, the total stress is zero, and equation 6.14 becomes

$$0 = E\epsilon - e_{31}\frac{v_{AC}}{t} \tag{6.15}$$

and the strain ϵ is

$$\epsilon = \frac{e_{31}}{E}\frac{v_{AC}}{t} \tag{6.16}$$

The piezoelectric force, F_{PZT} due to PZT transduction is

$$F_{PZT} = \epsilon EA = e_{31}A\frac{v_{AC}}{t} \tag{6.17}$$

where the cross sectional area $A = t_{PZT}$ x 2 x W_{PZT} (The width of the resonator bar (W) is approximately 2 x W_{PZT}). By substituting e_{31} with d_{31} x E, equation 6.17 can be written as

$$F_{PZT} = 2\ d_{31}\ E\ W_{PZT}\ v_{AC} \tag{6.18}$$

The efficiency of electromechanical transduction by PZT is indicated by the electromechanical coupling constant η.

$$\eta = \frac{F_{PZT}}{v_{AC}} = 2\ d_{31}\ E\ W_{PZT} \tag{6.19}$$

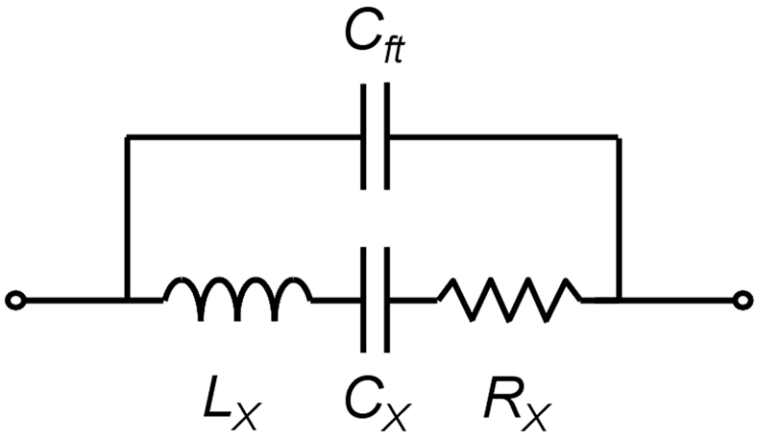

Figure 6.4: Electrical equivalent circuit of a PZT transduced LEM resonator.

6.2.3 Electrical Equivalent Impedances of a PZT Transduced LEM Resonator

The effective mass, damping ratio and effective spring constant can be related in to electrical circuit parameters. By substituting $\frac{\partial g(t)}{\partial t}$ in 6.10 by $\frac{i(t)}{\eta}$, we obtain

$$\frac{M_{Eff}}{\eta}\frac{\partial i(t)}{\partial t} + \frac{\zeta}{\eta}i(t) + \frac{K_{Eff}}{\eta}\int i(t)dt = F(t) \tag{6.20}$$

or

$$\frac{M_{Eff}}{\eta^2}\frac{\partial i(t)}{\partial t} + \frac{\zeta}{\eta^2}i(t) + \frac{K_{Eff}}{\eta^2}\int i(t)dt = v(t) \tag{6.21}$$

From 6.21 we can define the motional resistance, capacitance and inductance of the 2-port PZT-only transduced resonator in Figure 6.4. The feedthrough capacitance in a two-port resonator originates from electric field coupling from the input electrode to the output. The small signal electrical equivalent impedances a PZT Transduced LEM resonator vibrating in fundamental mode ($n = 1$) are

$$R_{X\_PZT-only} = \frac{\sqrt{K_{Eff}M_{Eff}}}{Q\eta^2} = \frac{\pi}{4Q}\frac{{\rho_{PZT}}^{\frac{1}{2}}}{{E_{PZT}}^{\frac{3}{2}}}\frac{t_{PZT}}{W_{PZT}}\frac{1}{{d_{31}}^2} \tag{6.22}$$

$$C_{X\_PZT-only} = \frac{\eta^2}{K_{Eff}} = \frac{4}{\pi^2}\frac{W_{PZT}L}{t_{PZT}}E_{PZT}{d_{31}}^2 \tag{6.23}$$

$$L_{X\_PZT-only} = \frac{M_{Eff}}{\eta^2} = \frac{\rho_{PZT}}{{E_{PZT}}^2}\frac{t_{PZT}L}{W_{PZT}}\frac{1}{4{d_{31}}^2} \tag{6.24}$$

Using the identical line of derivation, the motional resistance, capacitance and inductance of the 2-port PZT-on-silicon transduced resonator are given by

$$R_{X\_PZT-on-silicon} = \frac{\pi}{4Q}\frac{{\rho_{Eff}}^{\frac{1}{2}}{E_{Eff}}^{\frac{1}{2}}}{{E_{PZT}}^2}\frac{(t_{Si}+t_{PZT})}{W_{PZT}}\frac{1}{{d_{31}}^2} \tag{6.25}$$

$$C_{X\_PZT-on-silicon} = \frac{4}{\pi^2}\frac{W_{PZT}L}{(t_{Si}+t_{PZT})}\frac{{E_{PZT}}^2}{E_{Eff}}{d_{31}}^2 \tag{6.26}$$

$$L_{X\_PZT-on-silicon} = \frac{\rho_{Eff}}{{E_{PZT}}^2}\frac{(t_{Si}+t_{PZT})\,L}{W_{PZT}}\frac{1}{4{d_{31}}^2} \tag{6.27}$$

where ρ_{Eff} and E_{Eff} are the effective (PZT + silicon) density and Young's modulus, W_{PZT} is the width of PZT transducer under the input electrode, d_{31} is the transverse piezoelectric coefficient, and ρ_{PZT} and E_{PZT} are the density and Young's modulus of the PZT thin-film.

6.3 Fabrication Process

The device fabrication is largely based on the fabrication sequence outlined by Polcawich *et al* [107]. This process flow is highlighted in Figure 6.5. We started with an SOI wafer with 10 μm thick silicon device layer. We deposited 50 nm SiO_2 to mitigate lattice mismatch issues between the PZT-metal stack and the silicon. Then we successively deposited 100 nm platinum bottom metal, 0.5 μm PZT and another 100 nm platinum top metal. The PZT films were deposited using a chemical solution deposition method modified from reference [108] and using a crystallization temperature of 700°C. We patterned the top metal electrodes and signal pads using lift-off followed by pattern and wet-etch of PZT to open ground pads. The resonator was then defined by anisotropic etching of the PZT, platinum, silicon dioxide, silicon device layer and the buried oxide [109]. A novel technique of dry releasing the devices using a gentle front-side XeF_2 alleviated the need for

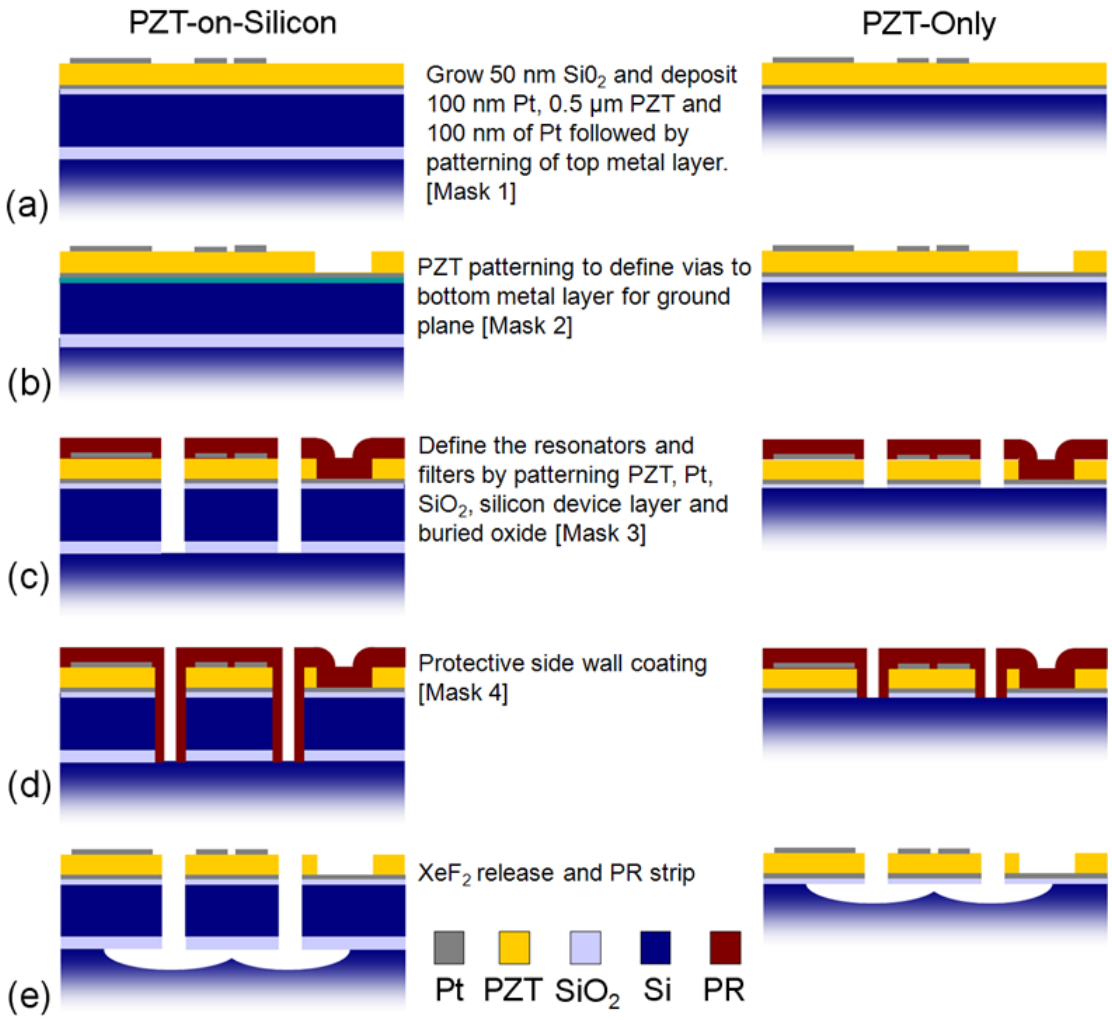

Figure 6.5: Fabrication process-flow for PZT-on-silicon and PZT-only resonators.

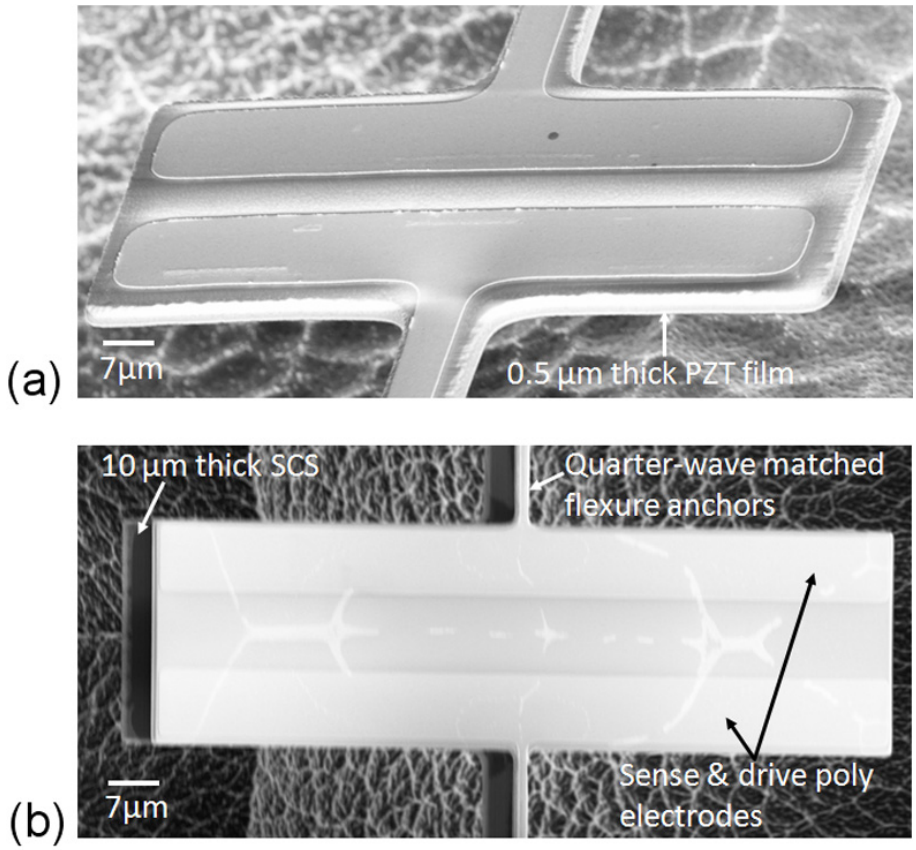

Figure 6.6: (a) SEM of a released PZT-only resonator. (b) SEM of a released PZT-on-silicon resonator. The isotropic pit due to the XeF_2 etch can be seen in the background.

backside DRIE used in [110]. An organic photodefinable layer was developed to provide protection of the resonator while allowing undercutting of the handle wafer silicon using a XeF_2 etch. Finally, the PZT resonators were subjected to electric fields of 200 kV/cm for 10 minutes to align the ferroelectric domains. Figure 6.6 (a) and (b) show PZT-only and PZT-on-silicon bar resonators fabricated in this process.

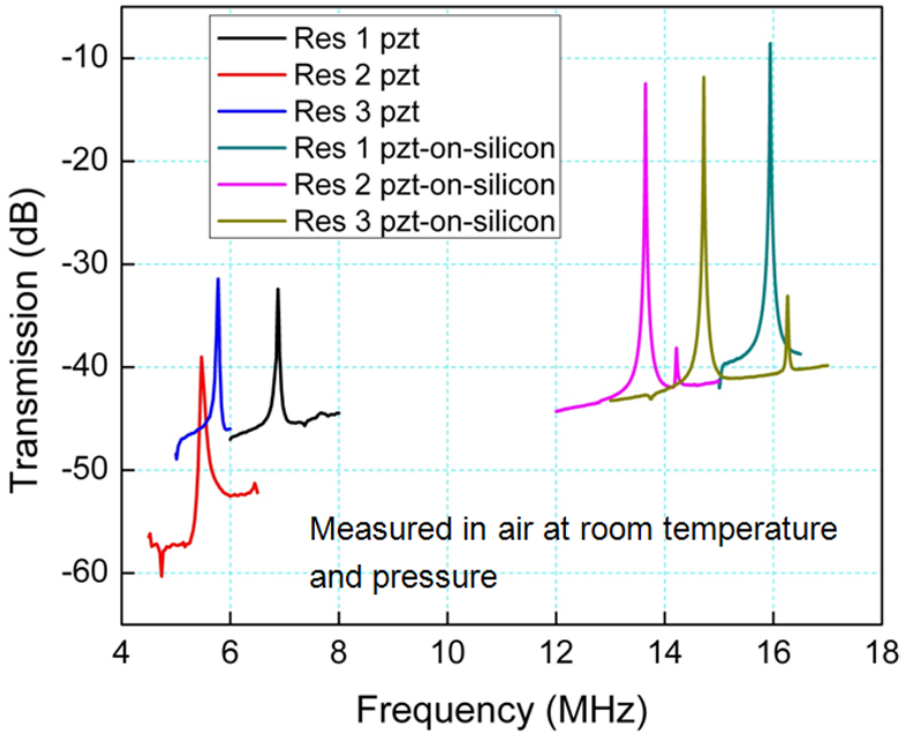

Figure 6.7: Measured transmission response of PZT-only and PZT-on-silicon resonators with the exact same lateral dimensions in air at room temperature and pressure.

6.4 Measurement Results

6.4.1 Resonance Frequency, Motional Impedance, and Quality Factor

The resonators were characterized after performing SOLT calibration followed by SOT de-embedding. The *DC* bias is superimposed to the *AC* signal at both input and output ports using bias-T's for all measurements. Measured transmission response of the PZT-only and PZT-on-silicon resonators with the exact same lateral dimensions in air at room temperature and pressure are shown in Figure 6.7. The PZT-on-silicon resonators exhibit higher Q, higher resonant frequency (f_C) and lower motional impedance (R_X) compared to their PZT-only counterparts.

Table 6.1: The measured characteristics of PZT-on-silicon resonators

Parameter	Res 1	Res 2	Res 3
Dimensions (μm^2)	240 x 40	280 x 60	260 x 60
Q	5,040	3,820	4,224
f_C (MHz)	15.94	13.65	14.72
R_X (Ω)	167	319	290

Table 6.2: The measured characteristics of PZT-only resonators

Parameter	Res 1	Res 2	Res 3
Dimensions (μm^2)	240 x 40	280 x 60	260 x 60
Q	202	91	241
f_C (MHz)	6.88	5.47	5.78
R_X (Ω)	4,078	8,812	3,628

PZT-on-silicon resonators also have higher resonant frequency because the thick silicon device layer that dominates the composite structures causes an increase in the ratio of E_{Eff} to ρ_{Eff}. These measurement results confirm that integrating PZT transduction with single-crystal silicon retains the mechanical energy within the high quality silicon device layer. The improvement in Q (35x) outweighs the increase in t_{Si} (10 μm), resulting in a net decrease in R_X. The performances of PZT-on-silicon and PZT-only resonators with the exact same lateral dimensions are summarized in Table 6.1 and 6.2.

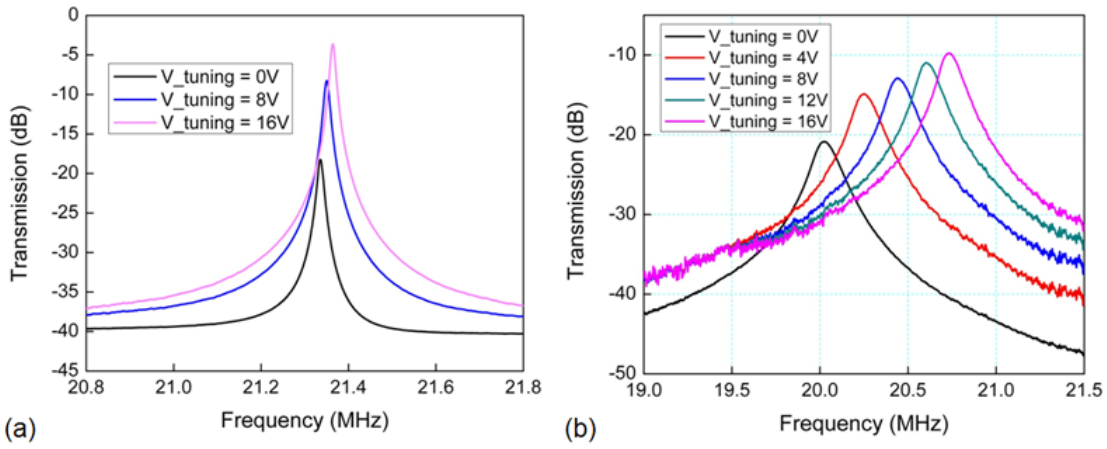

Figure 6.8: (a) Measured transmission of a 190 μm x 40 μm PZT transduced resonator on 10 μm silicon with different bias voltages in air at room temperature and pressure. 0.2% frequency tuning capability is observed due to *DC* bias dependent Young's modulus and density of PZT thin film. (b) Measured transmission of a 90 μm x 20 μm PZT-Only resonator with five different bias voltages in air at room temperature and pressure. 5.1% frequency tuning capability is observed due to *DC* bias dependent Young's modulus and density of PZT thin film.

6.4.2 DC Voltage Tuning

Wang *et al* and Cho *et al* have demonstrated that PZT has a electric field dependent Young's modulus, density and permittivity [102, 103]. As the *DC* bias increases, the transduction efficiency is improved. Therefore, by taking advantage of the electric field dependent ${k_{31}}^2$, we can reduce R_X and improve the insertion loss of the resonators. The measured transmission of a 190 μm x 40 μm PZT transduced resonator on 10 μm silicon with different bias voltages is shown in Figure 6.8 (a). A 0.2% frequency tuning capability is observed due to the *DC* bias dependent Young's modulus of PZT thin film. Since the resonant frequency is dominated by the silicon device layer, there is very little resonant frequency tuning, whereas the improvement in electromechanical coupling leads to 11x improvement in motional impedance at 16 V *DC* bias. The measured characteristics of the resonator are summarized in Table 6.3.

In contrast, the measured transmission of a 90 μm x 20 μm PZT-only resonator

Table 6.3: The measured characteristics of PZT-on-silicon resonator with different bias voltages

Tuning Voltage (V)	0	4	8	12	16
Q	2,020	2,021	2,021	2,022	2,023
f_C (MHz)	21.332	21.340	21.345	21.355	21.365
R_X (Ω)	582	223	142	83	50

Table 6.4: The measured characteristics of PZT-only resonator with different bias voltages

Tuning Voltage (V)	0	4	8	12	16
Q	125	126	136	147	148
f_C (MHz)	20.025	20.250	20.440	20.610	20.730
R_X (Ω)	1,004	453	343	253	207

with different bias voltages in air at room temperature and pressure is shown in Figure 6.8 (b). The PZT-only resonators demonstrate 5.1% DC bias dependent frequency tuning capability, the highest tuning range reported by any piezoelectrically transduced contour mode resonators to date. The measured characteristics of the resonator are summarized in Table 6.4.

6.4.3 Linearity

The immunity of the resonators to the third-order intermodulation distortion IM_3 was characterized similar to the procedure outlined in reference [80]. Two interferer signals f_1 and f_2 separated Δf away from each other are generated by the signal generators to excite the in-band IM_3 at $f_C = 2f_1$ - f_2. The PZT-only resonator exhibits the IIP_3 value of +23.3 dBm at Δf = 100 kHz. By integrating PZT

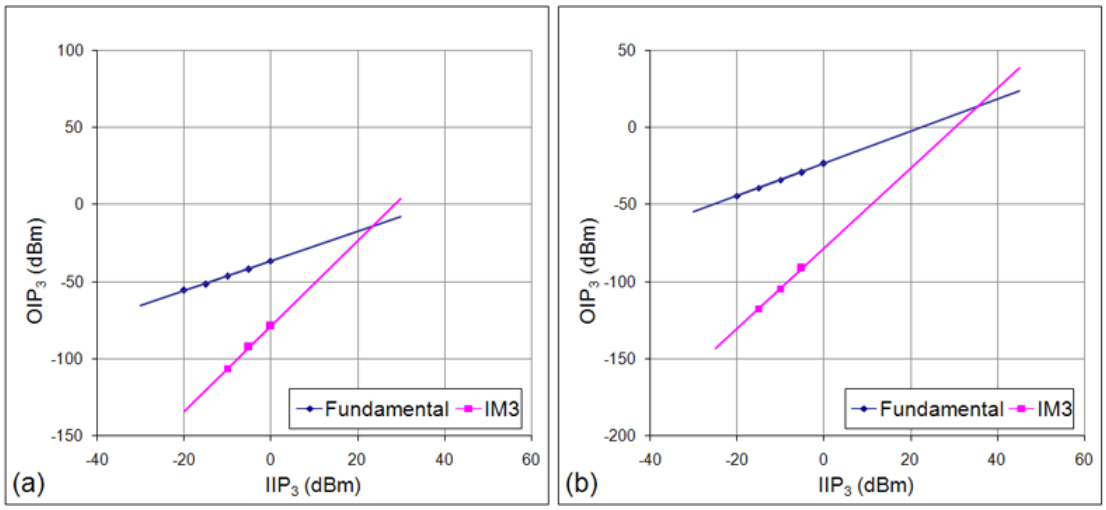

Figure 6.9: Measured IIP_3 of (a) a 90 x 20 μm^2 PZT-only, and (b) a 190 x 40 μm^2 PZT on 10 μm silicon resonator with 0 V DC bias in air at room temperature.

transduction with SCS, the nonlinear behavior of PZT can be strongly attenuated because the vibrating structure is dominated by silicon that has a superior acoustic linearity. This gives an improvement in IIP_3 to a value of +35.3 dBm, as shown in Figure 6.9.

6.4.4 Hysteresis

The hysteresis of PZT causes undesirable resonance frequency shifts in the resonator. Figure 6.10 (a) shows the dynamically varying relative permittivity ϵ_r of the PZT film caused by the influence of increasing and decreasing electric fields. This hysteresis effect is translated into a minor frequency shift, as shown in Figure 6.10 (b). This effect can be adjusted with the DC tuning.

6.5 High-overtone Width-extensional Mode Resonators

PZT transduced length-extensional mode resonators have been successfully demonstrated in the previous sections of this chapter. By varying the silicon thickness, t_{Si}

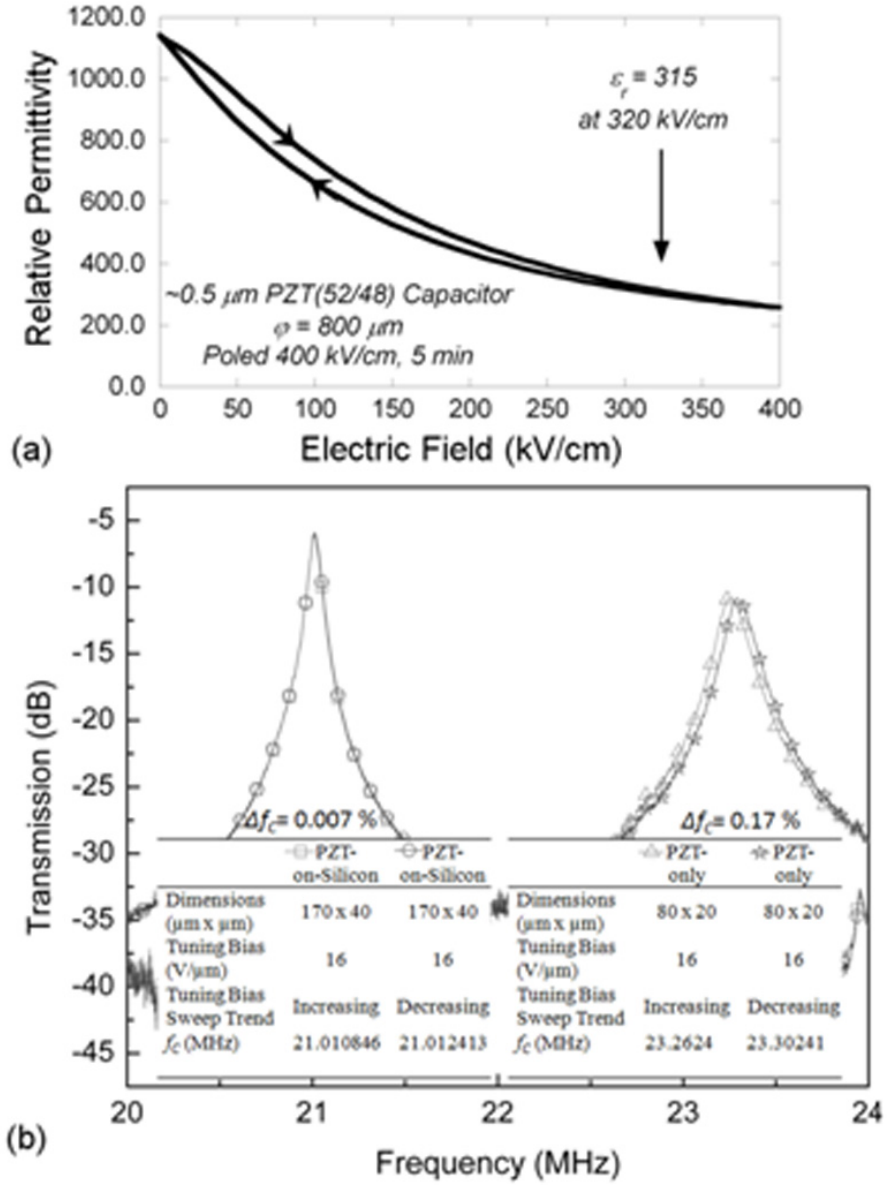

Figure 6.10: (a) Measured hysteresis effect in the relative permittivity of a PZT thin film. (b) A PZT-on-silicon resonator shows imperceptible hysteresis, while a PZT-Only resonator shows a maximum of 0.17% center frequency (f_C) shift.

(thereby the % mass of crystalline silicon in the resonator) and DC bias voltage we can define the desired Q and frequency tuning range of the resonators. However, various applications in wireless communication systems demand for higher frequency of operation. In order to reach f_C above 100 MHz using length-extensional mode of vibration, the length of PZT-on-silicon resonator has to be scaled down to less than 40 μm. The length of PZT-only resonators has to be shrunk even more due to a lower acoustic velocity. Aggressive scaling in lateral dimensions of the resonator reduces the transduction area that leads into poor motional impedances.

In order to attain a high frequency of operation, alternative modes of vibrations will be explored. Thickness shear mode resonators in Chapter 2 have demonstrated a high resonance frequency and high Q. However, since the frequency of operation is mainly defined by the device thickness, they have a very limited frequency design space. Furthermore, the packaging process for these resonators is especially challenging. High-overtone square-extensional mode resonators presented in Chapter 3 were able to reach above 500 MHz frequency of operation. In Chapter 4 the design and packaging technology for a width-extensional mode (WEM) resonators were discussed. A high-overtone width-extensional mode of vibration can be excited to reach a high resonance frequency while acquiring a large transduction area. WEM resonators are excited by patterning IDT like electrodes on top of the resonators as shown in Figure 6.11 (a) and (b). By selectively patterning the interdigitated electrodes the higher-overtone of width extensional mode is excited as demonstrated in ANSYS modal analysis in Figure 6.11 (c).

6.6 Air-bridge Fabrication Process

The device fabrication is largely based on the fabrication sequence outlined in [109] with additional improvements in the process to eliminate the pad capacitances.

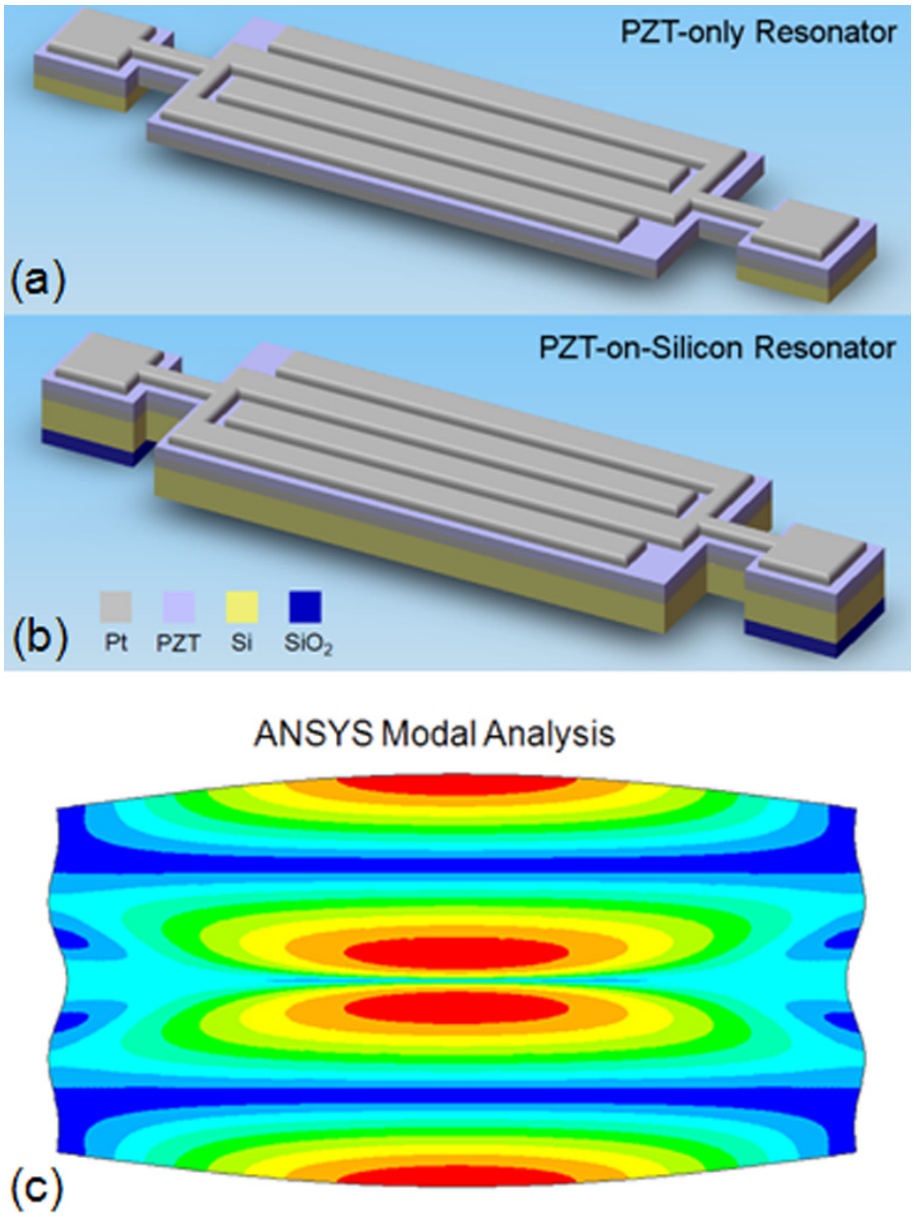

Figure 6.11: (a) Schematic of a PZT-only high-overtone width-extensional mode resonator. (b) Schematic of a PZT-on-silicon high-overtone width-extensional mode resonator. (c) ANSYS mode shape of a high-overtone width-extensional mode resonator.

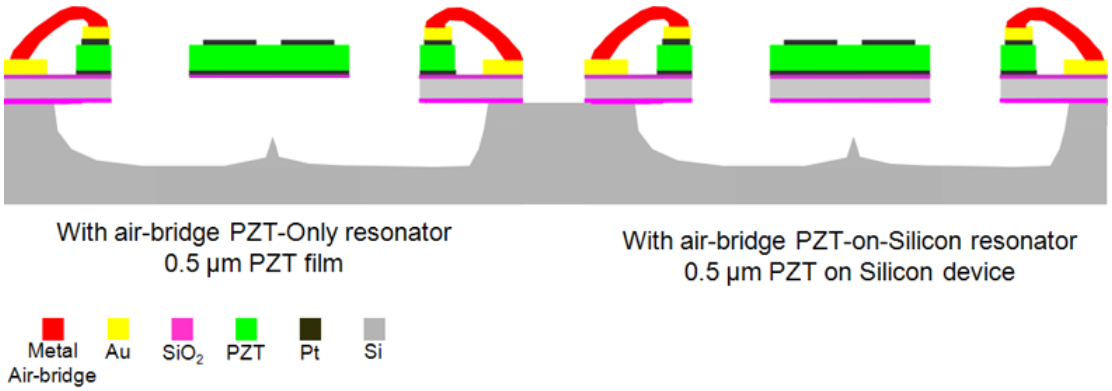

Figure 6.12: Air-bridge process cross-section of PZT-only and PZT-on-silicon high-overtone width-extensional mode resonators fabricated on the same wafer.

PZT is well known to have a large permittivity that can lead into large pad capacitances. Therefore, in this refined fabrication process, the air-bridge metal routings were implemented to carry electrical signals while avoiding large capacitances from the bond-pads. In addition, a novel fabrication technique was developed to fabricate the resonators with and without silicon layer using the same mask-set on the same wafer. A systematic study is essential to investigate the effect of silicon on quality factor (Q), resonant frequency (f_C) and motional impedance (R_X) of PZT transduced resonators at radio frequency. In this research effort, we fabricated PZT-only and PZT-on 3, 5 and 10 μm SCS high-overtone width-extensional mode resonators with identical lateral dimensions.

A thin elastic layer of SiO_2 and a PZT actuator comprised of Ti/Pt/PZT/Pt were deposited on SOI wafers with 3 μm, 5 μm and 10 μm thick device layer and 250 nm of buried oxide. The input and output terminals of the resonators are lithographically defined by patterning the top Pt electrode on top of the PZT actuator. The current configuration of the resonator uses a common bottom Pt electrode underneath of the PZT for both the input and output ports. The process cross-section of released PZT-on-silicon and PZT-only resonators is shown in Figure 6.12. To ensure survival of the SCS component of the resonators, an organic

photo-definable layer was developed to provide protection of the resonator while allowing undercutting of the handle wafer silicon using a XeF_2 etch. The PZT films were deposited using a chemical solution deposition method with a crystallization temperature of 700°C to achieve full densification and high crystallinity. At the end of device fabrication, the PZT film already possesses some degree poling as a result of the plasma processing. In order to improve the degree of poling, the resonators were subjected to electric fields of 200 kV/cm for 10 minutes prior to testing. SEM images of released PZT-on-silicon and PZT-only filters are shown in Figure 6.13.

6.7 Measurement Results

The resonators were characterized in an RF probe station in a 2-port configuration using GSG probes. Parasitics up to the probe tips were first calibrated with SOLT measurements on a standard calibration substrate. All measurements were performed in air, at room temperature and pressure. The trade-offs in Q, f_C and R_X of resonators with different silicon thicknesses were recorded. Resonators with thicker silicon layer exhibit higher Q, higher f_C and lower R_X for frequency up to about 900 MHz as shown in Figure 6.14 (a). The loss-tangent of PZT starts to dominate the insertion loss and degrade the quality factor for frequency of operation above 1 GHz. The measured characteristics of the high-overtone width-extensional mode resonators with different silicon thicknesses are summarized in Table 6.5.

The measured resonance frequency of the resonators with different silicon thicknesses are in agreement with the theoretically analyzed and simulated data. Figure 6.14 (b) plotted the calculated, simulated and measured resonance frequency of PZT transduced high-overtone WEM resonators with different silicon thicknesses (t_{Si}). By integrating PZT transduction with single-crystal silicon the figure of

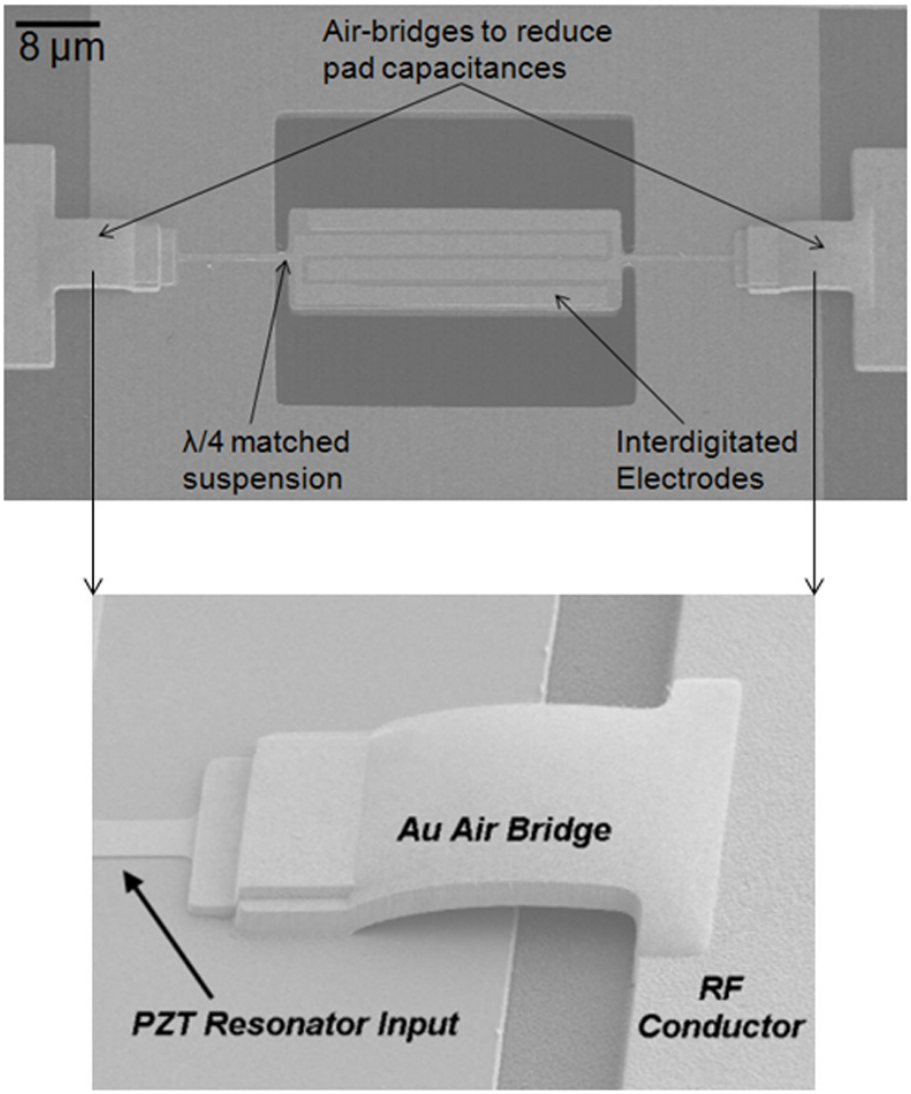

Figure 6.13: SEM of the fabricated high-overtone width-extensional mode resonator. The zoom-in picture shows the air-bridge routing that isolates the resonator from the bonding-pads.

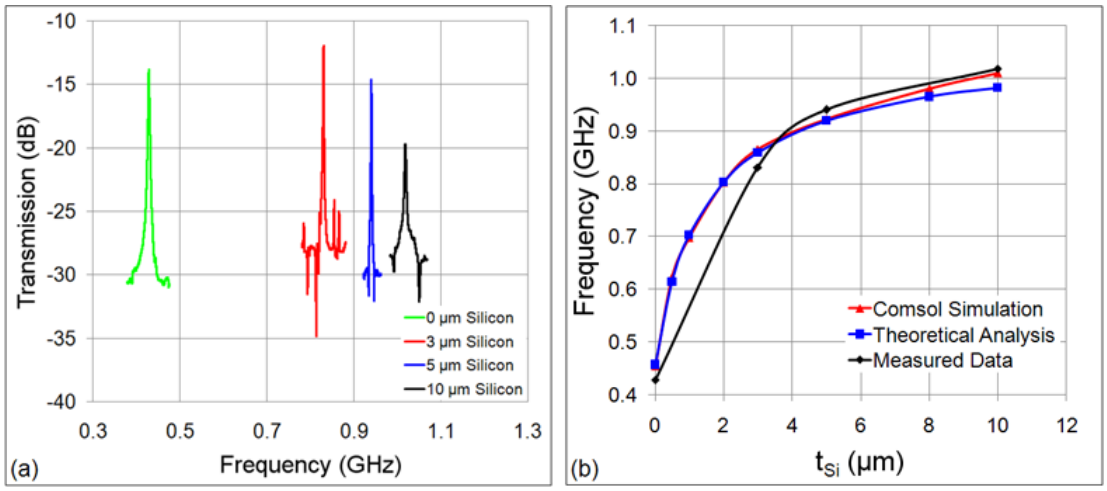

Figure 6.14: (a) Measured transmission response of PZT-only and PZT on 3 μm, 5 μm and 10 μm silicon resonators with the exact same lateral dimensions in air at room temperature and pressure. All measurements were performed using termination impedances (R_L) of 50 Ω. (b) A plot of silicon thickness (t_{Si}) vs the calculated, simulated and measured resonance frequency (f_C).

merit, f_C x Q is improved by one order of magnitude.

6.8 Conclusion

PZT transduced length-extensional mode resonators with and without silicon device layer have been theoretically modeled, designed, fabricated and characterized. By varying the silicon thickness (thereby the % mass of crystalline silicon in the resonator) and DC bias voltage we can define the desired Q and frequency tuning range of the resonators, and tradeoff between steep-walled narrow-bandwidth filters, low-Q wide-bandwidth filters, linearity and frequency agility. For the first time, electric field dependent properties of PZT are exploited to facilitate contour mode resonator design with a very large frequency tuning range.

The performances of PZT transduced high-overtone width-extensional mode resonators with various silicon thickness were systematically studied. A novel fabrication technique was developed to allow cancelation of large pad capacitances.

Table 6.5: The measured characteristics of high-overtone WEM resonators with different silicon thicknesses

t_{Si} (μm)	0	3	5	10
Q	150	314	501	458
f_C (MHz)	428	834	942	1,018
R_X (Ω)	390	296	435	700
R_L (Ω)	50	50	50	50
f_C x Q	$6.4\text{x}10^{10}$	$1.4\text{x}10^{11}$	$4.71\text{x}10^{12}$	$4.66\text{x}10^{11}$

The high-overtone excitation of the resonator is able to reach resonance frequency above 1 GHz. This technology will enable PZT transduced resonators and filters that covers up to low-band GSM frequencies.

CHAPTER 7

PZT TRANSDUCED MECHANICALLY-COUPLED FREQUENCY-AGILE FILTERS

7.1 Introduction

The forthcoming software defined radios that have compact dimensions, miniscule weight, low power demands and robustness to process and temperature variations are greatly desirable. In addition to commercial applications, the U.S. military has been actively developing the Joint Tactical Radio System (JTRS) to work in harmony with existing military and civilian radios. This radio architecture demands the existence of high performance tunable filters and filter banks to discern signals with dynamic waveforms and bandwidths. A width-extensional mode (WEM) resonator discussed in Chapter 6 is an excellent constituent resonator to realize these filter-banks because it has a high quality factor (Q) and frequency of operation that can be defined lithographically. Furthermore, higher-overtone frequency response can be excited by selectively patterning the electrodes of the filter.

Dielectrically-transduced thickness shear mode filters with analog voltage tunable center frequency and bandwidth and digitally-tunable MEMS filter using mechanically-coupled resonator array have been demonstrated in Chapter 2 and 3. However, the barriers in frequency design space, bandwidths range and processing technology have motivated the investigations for a new transducer material that has a large electromechanical coupling coefficient and frequency tuning capability. PZT is an appealing transducer material because it has been previously shown to have up to 6% frequency tuning capabilities [102]. It also exhibits a large electromechanical coupling coefficient (${k_t}^2 = 35\%$) in thickness-extensional mode (TEM) [101]. The maximum % bandwidth (BW/f_C) of the filter is determined

by the ${k_t}^2$ of the tranducer. The large ${k_t}^2$ of PZT facilitates a filter design with a large % bandwidth. In our previously reported research, we have fabricated and characterized PZT transduced contour-mode resonators that demonstrate 5.1% electric field dependent frequency tuning capability [109]. A bandpass filter with a small footprint, tunable bandwidth and center frequency agility can be realized by coupling PZT transduced contour-mode resonators mechanically.

An excellent stop-band rejection is a very desirable property in modern radio transceivers. A closely packed dense array of MEMS filters on the same chip introduces large feed-through capacitance between the drive and sense electrodes, leading to poor stop-band rejection of the filter. The fully-differential filter configuration cancels the feed-through capacitance and improves the stop-band floor of the filter [111].

7.2 PZT-only Mechanically-coupled Filters

7.2.1 Fully-differential High-overtone Width-extensional Filters

The resonant frequency of vibration for contour mode resonators and filters is defined by lithography. Therefore, contour-mode filters are preferred for realizing multi-band and multi-frequency filters on a single-chip [54]. The bulk-extensional mode resonance of a width-extensional mode resonator depends on W, with frequency of operation (f_C) given by:

$$f_C = \frac{n}{2W}\sqrt{\frac{E}{\rho}} \tag{7.1}$$

where W is the width of the resonator, E and ρ are effective elastic modulus for $2-D$ expansion and density of the resonator respectively, and n is the harmonic

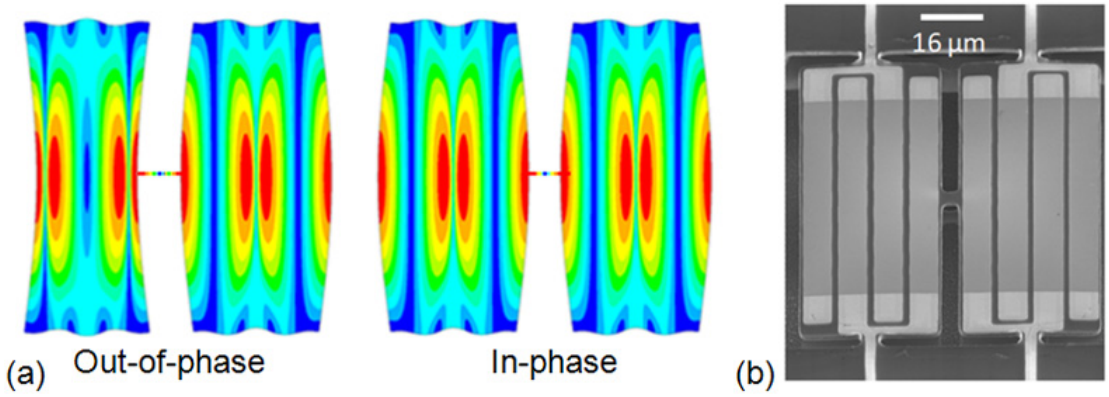

Figure 7.1: (a) ANSYS modal analysis showing in-phase and out-of-phase mode of vibrations of a mechanically-coupled high-overtone width extensional filter. (b) SEM image of a PZT transduced high-overtone mechanically-coupled width-extensional filter with differential electrodes.

order. Higher frequency overtone modes of the width-extensional mode resonators are selectively excited by patterning electrodes in differential interdigitated configuration on top of the resonator [111].

Mechanically-coupled devices demand smaller area since the coupling spring is small. Furthermore, they do not require extra device area to implement a differential configuration due to inherent mechanical inversion available through the resonators [112]. To realize a two-pole mechanically-coupled filter, two resonators are coupled using a suspension spring as shown in Figure 7.1. The length of the coupling spring is designed to be a quarter acoustic-wavelength long to minimize mass-loading of the resonators. The width of the coupling spring then defines the stiffness of the coupling spring. The bandwidth (BW) of such a mechanically-coupled filter is given by:

$$BW = \frac{f_C}{k_{ij}} \frac{k_s}{k_r} \tag{7.2}$$

where f_C is the resonant frequency, k_s and k_r are the spring stiffness of the coupling spring and resonator respectively and k_{ij} is the filter coefficient [27]. Figure 7.1(a) shows the in-phase and out-of-phase high-overtone modes of a width-

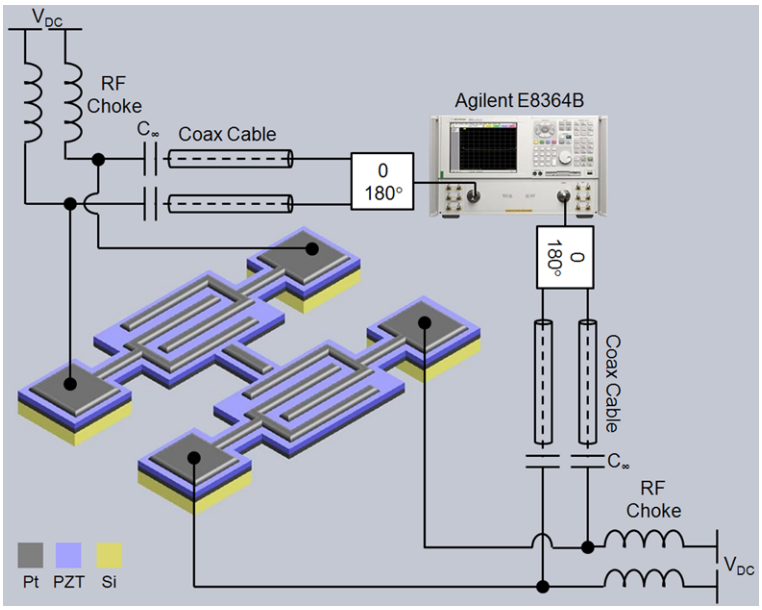

Figure 7.2: Testing configuration for a 2-pole mechanically-coupled high-overtone fully-differential filter.

extensional filter simulated in ANSYS. Device fabrication is the same as reported in reference [109]. The SEM image of a PZT transduced 2-pole fully-differential mechanically-coupled high-overtone width-extensional filter fabricated in this process is shown in Figure 7.1(b).

7.2.2 Measurement Results

Frequency Response

We characterized the 2-pole fully-differential mechanically-coupled filter using the measurement setup illustrated in Figure 7.2. The fully-differential configuration enables us to cancel feedthrough capacitances between drive and sense electrodes thereby improving the stop-band floor of the filter. The filter was characterized on a Cascade microwave probe station using GSGSG probes and a 2-port Agilent E8364B network analyzer. The *DC* bias is superimposed to the *AC* signal at both input and output ports using bias-Ts for all measurements. Figure 7.3 shows

the differential filter response as the electric field tuning biases are applied to the electrodes. The wide frequency measurement was performed and all other harmonics modes of vibrations are strongly attenuated by at least 30 dB below the designed frequency of operation. The electric field not only improves the piezoelectric coupling coefficient (via poling of the ferroelectric domains), but also increases the Young's modulus of the PZT film [109]. The increase in Young's modulus of the PZT film, increases the effective acoustic velocity of the constituent resonators, thereby increasing the center frequency of the filter. The result is up to 3% increase in filter center frequency for a 32 V/μm applied electric field, the highest tuning range reported by any piezoelectrically transduced contour-mode filters to date. In addition, the applied electric field also increases the ratio of k_s to k_r, thereby providing up to 100% bandwidth tuning capability for a 32 V/μm applied electric field. The measured transmission response of a PZT transduced 2-pole high-overtone width extensional filter with electric field tuning of 8 to 32 V/μm in 8 V/μm increment step in air at room temperature are tabulated in Table 7.1. The center frequency and bandwidth tuning features demonstrated by this class of filter could eliminate the necessity of multiple-filter and switch networks in radio architecture [113].

Linearity

The immunity of the resonators to the third-order intermodulation distortion (IM_3) was characterized by using a two-tones technique. Two interferer signals f_1 and f_2 separated Δ_f away from each other are generated by the signal generators to excite the in-band IM_3 at $f_C = 2f_1$ - f_2. Both interferer signals were excited in the bandpass region of the filter with Δ_f = 400 kHz. The filter demonstrated the third-order input intercept point (IIP_3) of +21 dBm as shown in Figure 7.4.

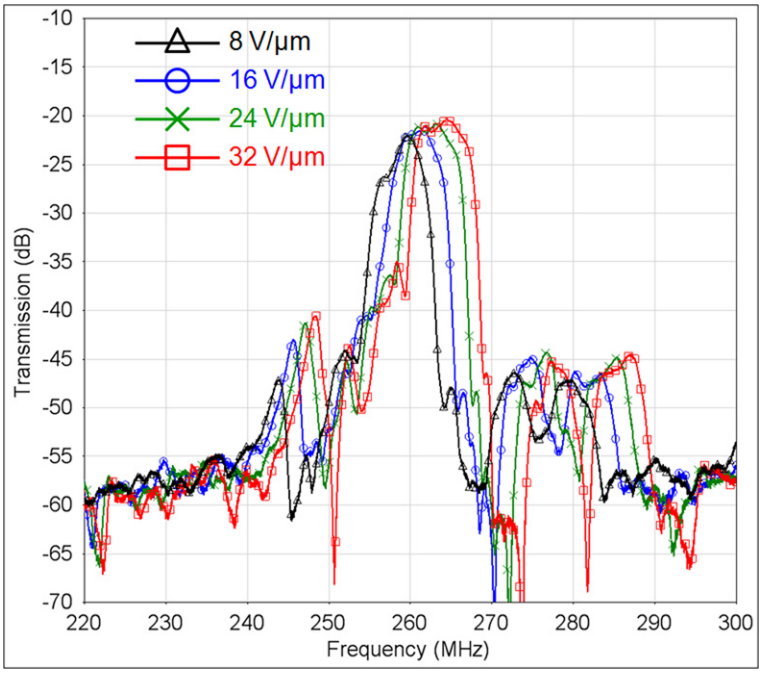

Figure 7.3: Measured transmission of a PZT transduced 2-pole high-overtone WEM filter with electric field tuning. Input and output terminals were terminated with 50 Ω termination impedances (R_L) for all measurements.

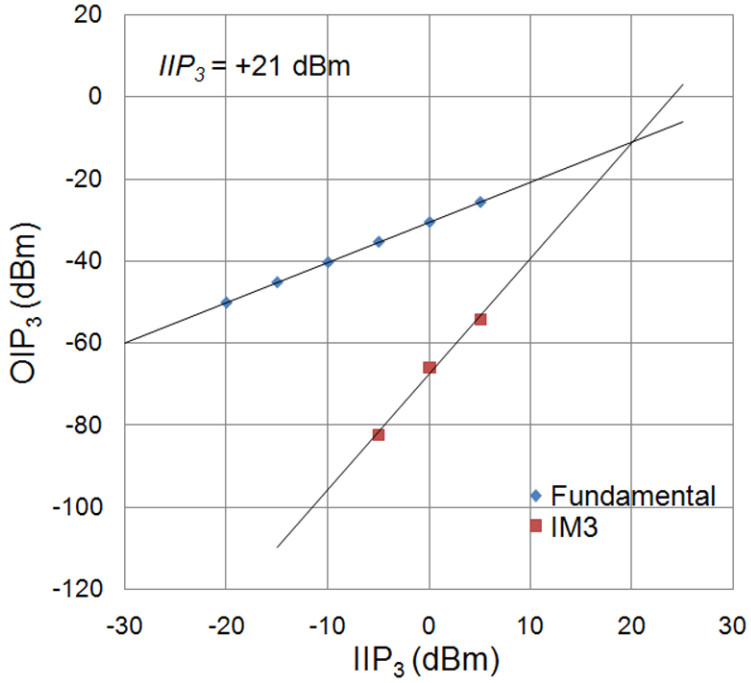

Figure 7.4: Measured third-order input intercept point ($\Delta_f = 400$ kHz) of the filter demonstrates IIP_3 of +21 dBm.

Table 7.1: The measured frequency response of a PZT transduced high-overtone WEM filter

Electric Field (V/μm)	8	16	24	32
IL (dB)	-22.4	-21.5	-21.3	-20.7
3dB BW (MHz)	3.03	3.9	5.5	6.3
f_C (MHz)	259.1	260.5	262.3	264.2
Stop-band rejection (dB)	37.6	38.5	38.7	39.3
R_L (Ω)	50	50	50	50

Hysteresis Effect

The hysteresis effect of PZT may cause the filter to experience undesirable center frequency shifts. The hysteresis effect was characterized on the filter by applying increasing and decreasing electric fields across the PZT thin film. A maximum frequency shift of 0.14% was recorded as shown in Figure 7.5.

Temperature Coefficient of Frequency (TCF)

All the measurement results demonstrated up to this point have shown the filter performances at room temperature and pressure. Several targeted applications of this filter, however, operate at environments with wide range of temperature fluctuations. Thus filters with high insensitivity to temperature variations are highly desirable. Temperature characterization was performed by placing the filter on the Cascade probe station with temperature control stage. Frequency responses were recorded while the device was cooled down to -20°C and heated up to 100°C. The filter with different DC bias voltages was characterized over the whole temperature range of operation and exhibits TCF between -22 to -25 ppm/°C.

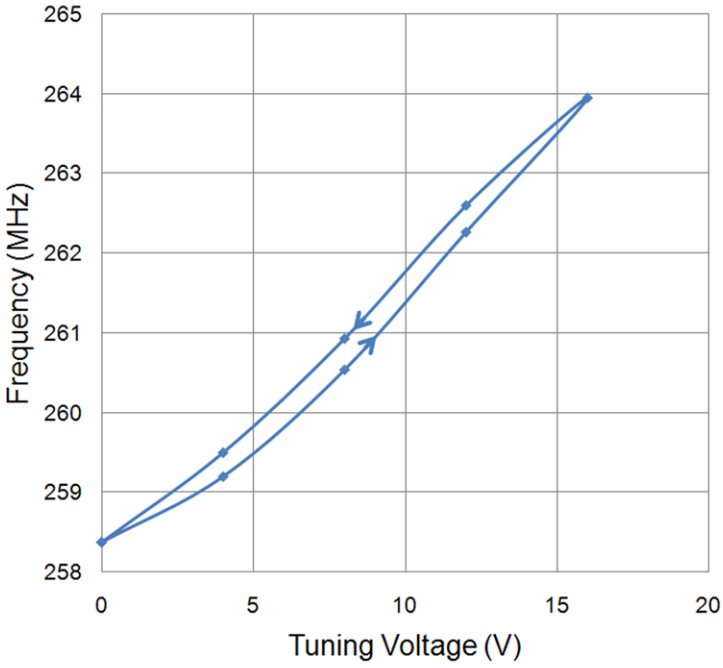

Figure 7.5: Measured frequency shifts in PZT transduced high-overtone width extensional filter due hysteresis effect in PZT. A maximum frequency shift of 0.14% was recorded.

7.3 PZT-on-silicon Mechanically-coupled Filters

PZT-only mechanically-coupled filters with fully-differential electrodes configuration have been designed, fabricated and characterized in the previous section. The filter demonstrated a wide bandwidth, large frequency and bandwidth tuning range and excellent stop-band rejection. Narrow bandwidth tunable channel-select filters that exhibit smaller than 1 MHz nominal bandwidth have been presented in Chapter 2 and 3. The PZT-only mechanically-coupled filters have shown bandwidth coverage between 3 MHz to 6 MHz. A filter design that can give bandwidth coverage between 1 MHz to 3 MHz is highly desirable to enable the analog signal processor receiver architecture introduced in Chapter 1.

In order to overcome the low quality factor of PZT-only resonators, a novel fabrication technology has been developed and presented in Chapter 6 by integrating PZT transduction with single-crystal silicon. Since the mechanical energy in

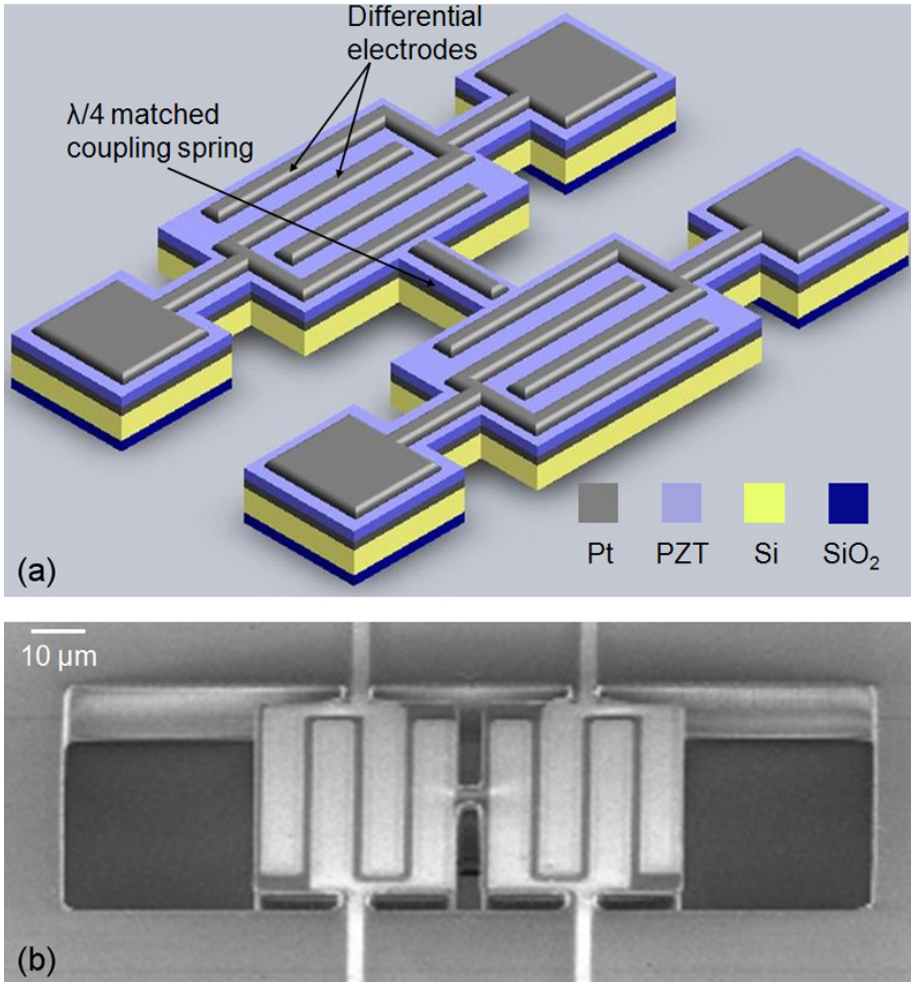

Figure 7.6: (a) Schematic of a mechanically-coupled PZT-on-silicon filter. (b) SEM image of a PZT-on-silicon high-overtone mechanically-coupled width-extensional filter with differential electrodes.

this class of resonators is retained in the single crystal silicon layer, the resonators have higher quality factors compared to PZT-only counterparts. By applying a *DC* bias across the PZT transducer, the transducer coupling coefficient and filter center frequency can be modestly tuned, enabling voltage-dependent dynamic voltage frequency tuning and trimming.

High-Q PZT-on-silicon high-overtone width-extensional-mode resonators can be mechanically-coupled to facilitate narrow-bandwidth filter design with a modest frequency tuning capability. The schematic of a mechanically-coupled PZT-on-silicon high-overtone width-extensional-mode filter is presented in Figure 7.6 (a).

Integrating PZT transduction with silicon is also a potential solution to improve the filter linearity and reduce the hysteresis effect in filter response. PZT-on-silicon filters are fabricated using the same mask-set and on the same wafer as PZT-only filters according to the fabrication process outlined in Chapter 6. The fully-differential electrodes configuration is again implemented to cancel the feed-through capacitance and improves the stop-band floor of the filter. The SEM image of the fabricated PZT-on-silicon mechanically-coupled fully-differential filter is shown in Figure 7.6 (b).

7.3.1 Measurement Results

Frequency Response

We characterized the 2-pole fully-differential mechanically-coupled PZT-on-silicon filter using the same measurement setup illustrated in Figure 7.2. The filter was characterized on a Cascade microwave probe station using GSGSG probes and a 2-port Agilent E8364B network analyzer. The *DC* bias is superimposed to the *AC* signal at both input and output ports using bias-Ts for all measurements. Figure 7.7 shows the differential filter response as the electric field tuning biases are applied to the electrodes. The wide frequency measurement was performed to make certain all other undesired harmonics modes of vibrations are significantly attenuated. The fully-differential configuration enables us to cancel feedthrough capacitances between drive and sense electrodes and demonstrated -62 dB stop-band rejection floor.

The measured transmission response of a 2-pole PZT-on-silicon high-overtone width extensional filter with electric field tuning of 8 to 32 V/μm in 8 V/μm increment step in air at room temperature are tabulated in Table 7.2. The termination impedance (R_L) of 50 Ω is used for all measurements. The filter demonstrated a

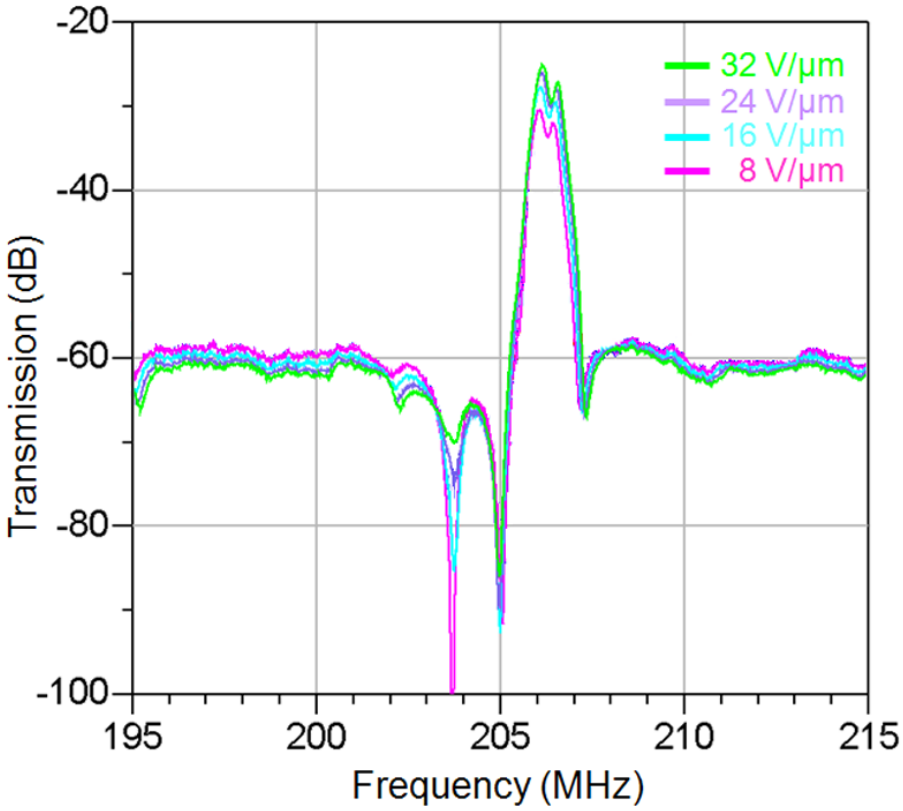

Figure 7.7: Measured transmission of a PZT-on-silicon 2-pole high-overtone WEM filter with electric field tuning. Input and output terminals were terminated with 50 Ω termination impedances (R_L) for all measurements.

Table 7.2: The measured frequency response of a PZT-on-silicon high-overtone WEM filter

Electric Field (V/μm)	8	16	24	32
IL (dB)	-30.2	-28.4	-27.2	-26.7
3dB BW (MHz)	1.24	1.26	1.31	1.35
f_C (MHz)	206.4	206.5	206.5	206.7
Stop-band rejection (dB)	29.8	31.6	32.8	33.3
R_L (Ω)	50	50	50	50

narrower nominal filter bandwidth compared to PZT-only transduced filters. However, the 10 μm thick silicon layer that dominates the structure limits the frequency tuning capability of the filter. A 0.22% center frequency tuning was recorded due to a 32 V/μm applied electric field across the PZT thickness.

Linearity

The immunity of the resonators to the third-order intermodulation distortion (IM_3) was characterized by using a two-tones technique. Two interferer signals f_1 and f_2 separated Δ_f away from each other are generated by the signal generators to excite the in-band IM_3 at $f_C = 2f_1$ - f_2. Both interferer signals were excited in the bandpass region of the filter with Δ_f = 400 kHz. By integrating PZT transduction with single-crystal silicon, the non-linear behavior of PZT can be suppressed because the vibrating structure is dominated by the thick silicon layer that has a superior acoustic linearity compared to PZT. The filter demonstrated the third-order input intercept point (IIP_3) of +29 dBm as shown in Figure 7.8.

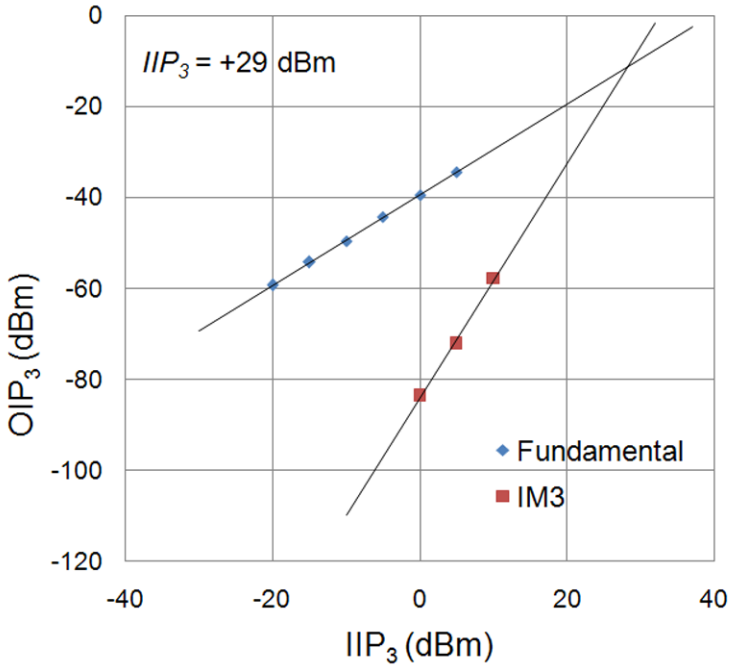

Figure 7.8: Measured third-order input intercept point ($\Delta_f = 400$ kHz) of the filter demonstrates IIP_3 of +29 dBm.

Hysteresis Effect

Hysteresis of PZT can cause an undesirable resonance frequency shifts in the filter. By integrating PZT transduction with a 10 μm thick silicon layer, the frequency shifts due to hysteresis can be significantly minimized. The hysteresis effect in PZT-on-silicon is translated into very minor frequency shifts as shown in Figure 7.9.

Temperature Coefficient of Frequency (TCF)

Temperature characterization was again performed by placing the filter on the Cascade probe station with temperature control stage. Frequency responses were recorded while the device was cooled down to -20°C and heated up to 100°C. The filter with different *DC* bias voltages was characterized over the whole temperature range of operation and exhibits TCF between −16 to −19 ppm/°C. These values

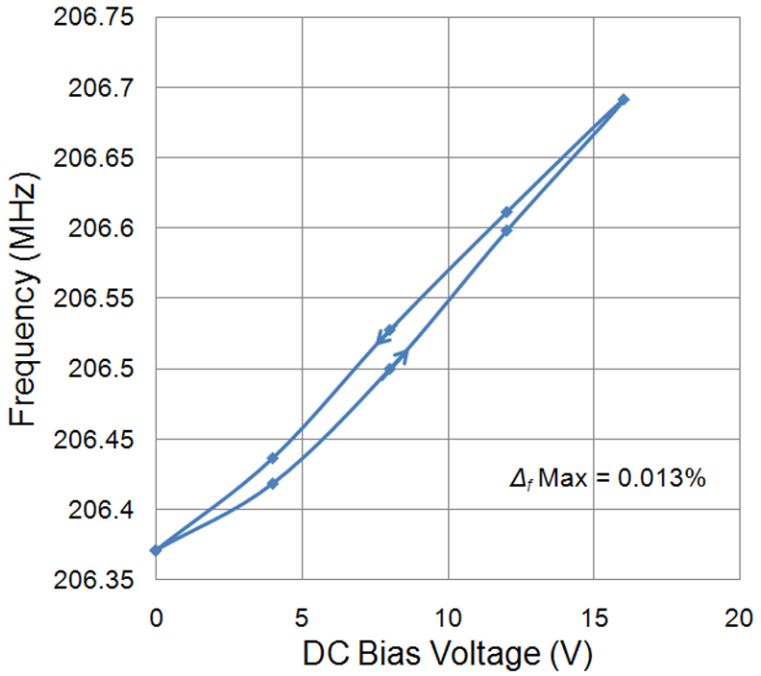

Figure 7.9: Measured frequency shifts in PZT-on-silicon high-overtone width extensional filter due hysteresis effect in PZT. An imperceptible frequency shift of 0.013% was recorded.

are comparable to AlN transduced resonators and filters and quartz crystals used in time-keeping applications for handsets [55].

7.4 Conclusion

The PZT transduced fully-differential mechanically-coupled filters have been designed, fabricated and characterized. The PZT-only filters have shown a large center frequency and bandwidth tuning range. These tuning features have never been demonstrated by any piezoelectrically transduced contour-mode filters reported to date. The fully-differential configuration eliminates the feedthrough capacitances between drive and sense electrodes, thereby improving the stop-band rejection floor of the transmission. The filter demonstrates excellent capability to overcome hysteresis effect by applying an electric field across the PZT transducer to adjust

the center frequency. These features satisfy the filter specifications in JTRS to handle multiple waveforms, eliminate out-of-channel interferers, and substantially decrease the number of filters in next-generation radios.

PZT-on-silicon fully-differential mechanically-coupled filters have been designed, fabricated and characterized. The filters demonstrated a narrower nominal filter bandwidth compared to PZT-only filters. Integrating PZT transduction with silicon also improves the filter immunity to the third-order intermodulation distortion and hysteresis effect of PZT.

CHAPTER 8

MONOLITHICALLY INTEGRATED PIEZO-MEMS SWITCHES AND CONTOUR-MODE FILTERS

8.1 Introduction

RF MEMS has been a significant area of research for well over a decade due to the promise of improved performance and integration potential in commercial and military wireless communication and radar systems. RF MEMS switches have demonstrated superior performance in terms of insertion loss, isolation, power consumption, and linearity [114]. RF MEMS filter technologies can provide insertion loss, percent bandwidth, and rejection performance similar to off-chip crystal filters and surface acoustic wave (SAW) devices with the compact integration of multiple frequencies on the same chip [54,69,115]. The integration of these two technologies has long been a goal of researchers and will enable not only more compact and lower cost systems but previously unachievable signal processing functions [116].

A number of transduction approaches have been utilized for both MEMS switch and filter operation, including electrostatic, electromagnetic, electro-thermal, and piezoelectric. Piezoelectric and or ferroelectric transduction can provide superior electro-mechanical coupling and mechanical energy densities; metrics applicable to both switch and filter operation. Piezoelectric AIN is a popular filter material due to the high acoustic velocity, high mechanical quality factor, and the ease of post-CMOS integration [54]. AIN is generally the preferred material for direct piezoelectric effect transduction due to its favorable ratio of stress constant to dielectric constant.

Ferroelectric lead zirconate titanate (PZT) has an effective piezoelectric stress constant that is an order of magnitude larger than AIN and is generally the pre-

ferred material for indirect piezoelectric effect transduction [117]. Thin films of ferroelectric PZT also permit tuning of the piezoelectric coefficients, some elastic constants, permittivity, and hence the electro-mechanical coupling factor of the material with a modest DC bias. Low-voltage (<10 V) ohmic contact series switches with high isolation and good insertion loss characteristics up through 65 GHz have been demonstrated with surface micro-machined PZT MEMS [107].

In Chapter 7, PZT-only and PZT-on-silicon contour-mode filters have been designed, fabricated and characterized. The integration of PZT thin films with high mechanical quality factor single crystal silicon features allows a tradeoff between steep-walled narrowbandwidth filters, low-Q wide-bandwidth filters, linearity and center frequency agility. Single pole dual throw (SP2T) PZT MEMS switches have also been previously demonstrated with better than 50 dB of isolation and less than 0.4 dB of insertion loss at 2 GHz [118]. These switches can be fabricated on the same wafer as PZT-only and PZT-on-silicon contour-mode filters presented in Chapter 7. The incorporation of these switches in the design facilitates the ability to cover all characteristics that have been demonstrated by both PZT-only and PZT-on-silicon contour-mode filters on a single chip. Unlike AIN, integration of high quality piezoelectric PZT films with CMOS remains a challenge for MEMS applications because of the high process temperatures. However, PZT thin films with high quality ferroelectric properties have been successfully integrated with CMOS for ferroelectric random access memory (FeRAM) [119].

Recently, Mahameed *et al.* successfully co-fabricated aluminum nitride (AIN) switches and resonators and reported cascaded S-parameter data illustrating how a switchable resonator should function [120]. In this Chapter, integration of a PZT RF MEMS single pole dual throw (SP2T) series switches with contour-mode mechanically coupled PZT-on-silicon high-Q filters and the first experimental demon-

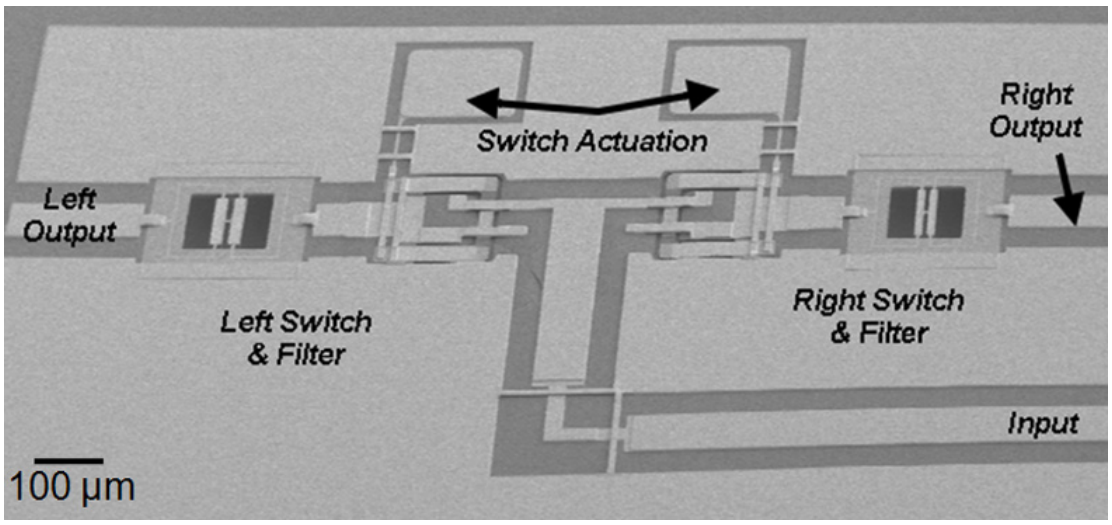

Figure 8.1: SEM image of an integrated single pole dual throw (SP2T) PZT-MEMS switch and two PZT transduced width-extensional contour-mode filters.

stration of monolithically integrated piezoelectric MEMS RF switches and filters will be presented.

8.2 Design of Integrated PZT transduced Switches and Filters

Using a single pole dual throw (SP2T) architecture similar to that reported previously [107], two normally-open, ohmic contact, series switches were used to select between two contour-mode mechanically coupled PZT-on-silicon high-Q filters as shown in Figure 8.1. As presented in Figure 8.1, a conductive pad and contacts are located on the dielectric structure mechanically coupling the two cantilevered PZT unimorph actuators. The switch resides in the gaps of the co-planar waveguide (CPW) transmission line. Unlike the cantilevered designs in [107,118], the RF gold air bridge contact structures above the switch contact pad were redesigned as clamped-clamped structures to mitigate deformation of these structures during and after fabrication. Two bias line air bridges located at the anchors of the actuators

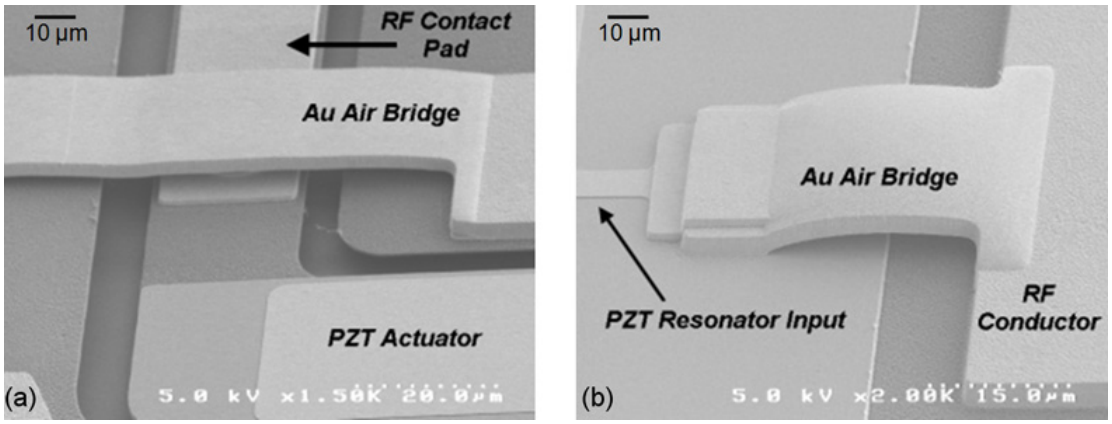

Figure 8.2: (a) SEM image of the air-bridge used for switch operation, and (b) reduced large pad capacitances in the filters.

electrically connect the top and bottom electrodes of the two actuators. To enable switch biasing with a single trace, the top electrode bias line air bridge anchors to one of the CPW ground planes and the bottom electrode bias line air bridge anchors to a single bias line. The typical switch actuator composite stress states, composition, and thicknesses are designed to provide static negative curvature in the switch to dictate the preferred initial contact gap. The application of voltage to the top and bottom electrodes provides d_{31} mode bending actuation to the switch and raises the contact pad into contact with the two clamped-clamped RF gold air bridges. These devices were designed with analytical models, ANSYS, ADS Momentum, and HFSS. The ohmic series switches and SP2T design are similar to the designs presented in [107, 118].

The filter designs in this work are based on the work presented in Chapter 7. The designs in this work feature significantly reduced parasitic shunt capacitances by reducing the top electrode contact area, not associated with the active transducer, through the use of air bridge structures available with the switch process steps as shown in Figure 8.2. The constituent resonators are fundamental width-extensional contour mode designs as shown in Figure 8.3 (a). Two of these

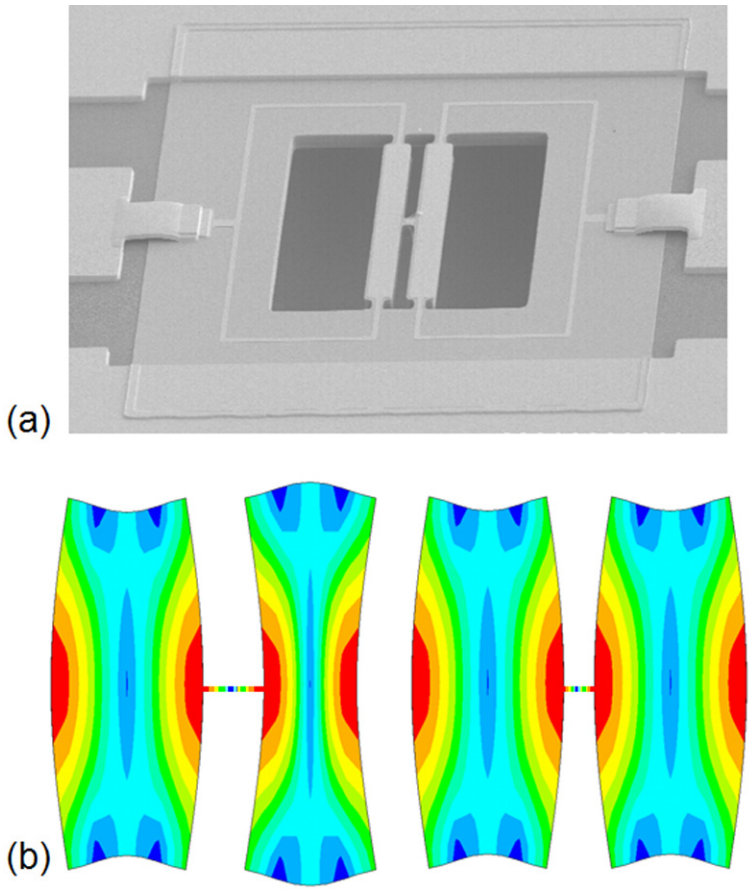

Figure 8.3: (a) SEM image of the width-extensional contour-mode filter. (b) Anti-symmetric and symmetric ANSYS mode shapes of a fundamental width-extensional mode filter.

resonators are coupled via an acoustic quarter-wave coupling spring (not simulated) to create a two-pole mechanically coupled filter as shown in Figure 8.3 (b). The filters presented in this chapter were designed as 209 MHz and 313 MHz. The fundamental resonant frequency of the width extensional mode is given by Equation 7.1. To realize a two-pole mechanically-coupled filter, two resonators are coupled using a suspension spring as shown in Figure 8.3 (a). The length of the coupling spring is designed to be a quarter acoustic-wavelength long to minimize mass-loading of the resonators. The width of the coupling spring then defines the stiffness of the coupling spring. The bandwidth (BW) of such a mechanically-coupled filter is given by Equation 7.2.

Relatively few modifications were required to integrate the two device types as most of the steps of the two individual processes were initially common. The substrate was chosen as SOI to accommodate the filters. The switch sacrificial layer features were altered to ensure proper release timing in the presence of the added passivation layer necessary to protect the device silicon features of the filter during the XeF_2 release and the release sequence was reversed to accommodate the integration.

8.3 Fabrication Process

Device fabrication was done at the Specialty Electronic Materials and Sensors Cleanroom Facility, U.S. Army Research Laboratory, Adelphi, MD. The fabrication process for the monolithically integrated piezoelectric MEMS RF switches and filters utilized a silicon-on-insulator substrate with a 5 μm thick device layer with nominal resistivity of 30 Ω-cm. A 500 nm silicon dioxide thin-film was deposited by plasma-enhanced chemical vapor deposition (PECVD) and was followed by a sputtered Ti/Pt bottom electrode layer for the PZT deposition. The 518.5 nm PZT thin films were prepared via a chemical solution derived deposition process modified from that outline in [108]. After the final PZT anneal, a 105 nm platinum thin film was sputter-deposited directly onto the PZT surface at 300°C.

The switch actuator and filter drive and sense electrode were patterned with the argon ion-milling of the top platinum layer and was followed by an additional ion-milling of the PZT and bottom electrode features. A wet-etch then opened up contact vias to the local bottom electrodes of the switches and filters. The switch structure was then further defined by patterning the silicon dioxide layer with a reactive ion etch to provide access to the silicon device layer for the eventual release etch. A titanium/gold bi-layer was then deposited with electron beam evaporation

and patterned via lift-off to define the CPW transmission line, contact structures for the switch, and anchor features required for gold air bridges. A lift-off process was then used to pattern the switch contact material. The filters were defined using a single photomask by an ion-milling of the PZT and bottom electrode, an RIE of the silicon dioxide layer, a DRIE of the device silicon layer, followed by an RIE of the buried oxide layer. A photo-resist sacrificial layer was then patterned and cured and was followed by the deposition and lift-off of 2 μm gold air-bridge features necessary for both the switches and filters. A thick photo-resist layer was then patterned to encase the silicon resonator features in resist and the buried oxide during release. The sidewalls of the switches and regions near the filters were not coated to permit a timed XeF_2 etch of the silicon device layer directly beneath the switch and the silicon handle layer beneath the filter. The release process reversed the typical release sequence utilized in [117], with the XeF_2 silicon etch preceding the oxygen plasma release of the gold air-bridge structures.

8.4 Measurement Results

8.4.1 Frequency Domain Measurement

All switch and filter measurements were completed with a network analyzer using a 50 Ω termination impedance (R_L) in air at room temperature and pressure. Individual switches exhibited isolation better than -40 dB from DC through 500 MHz as shown in Figure 8.4 (a). Switch actuation was achieved with the application of 7 V resulting in an insertion loss (IL) less than -0.4 dB from DC to 500 MHz. Processing these devices on a relatively low-resistivity SOI wafer resulted in the insertion loss being higher than the individual switches processed on silicon substrates with a resistivity greater than 10 kΩ-cm in previously reported

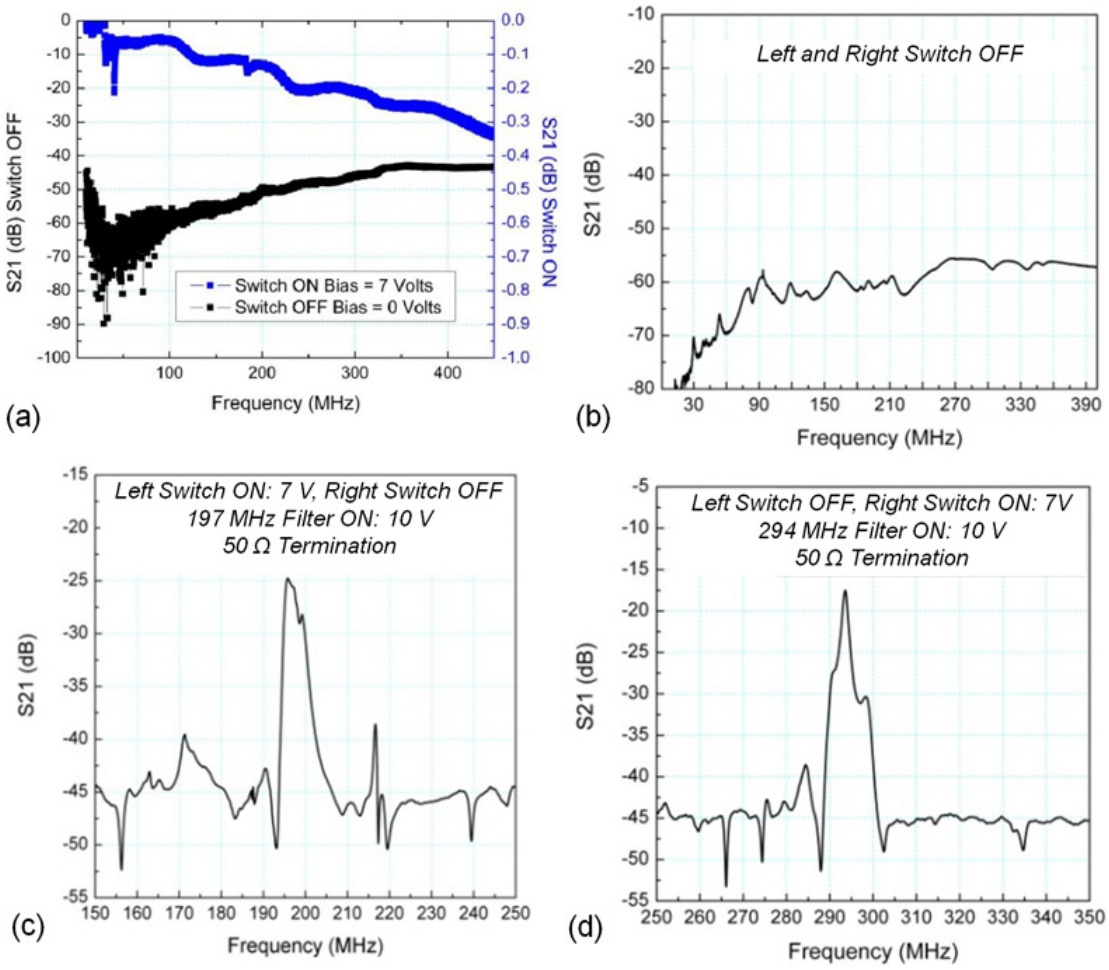

Figure 8.4: (a) S_{21} data at 0 V and 7 V for the PZT-MEMS switch co-fabricated with the PZT transduced width-extensional contour-mode filters. (b) S_{21} response of an integrated SP2T switch and filter with the switch in the Off-state (0 V), (c) S_{21} response for the left switch and filter with the switch On (7 V) and with 10 V V_{DC} applied to the filter, and (d) S_{21} response for the right switch and filter.

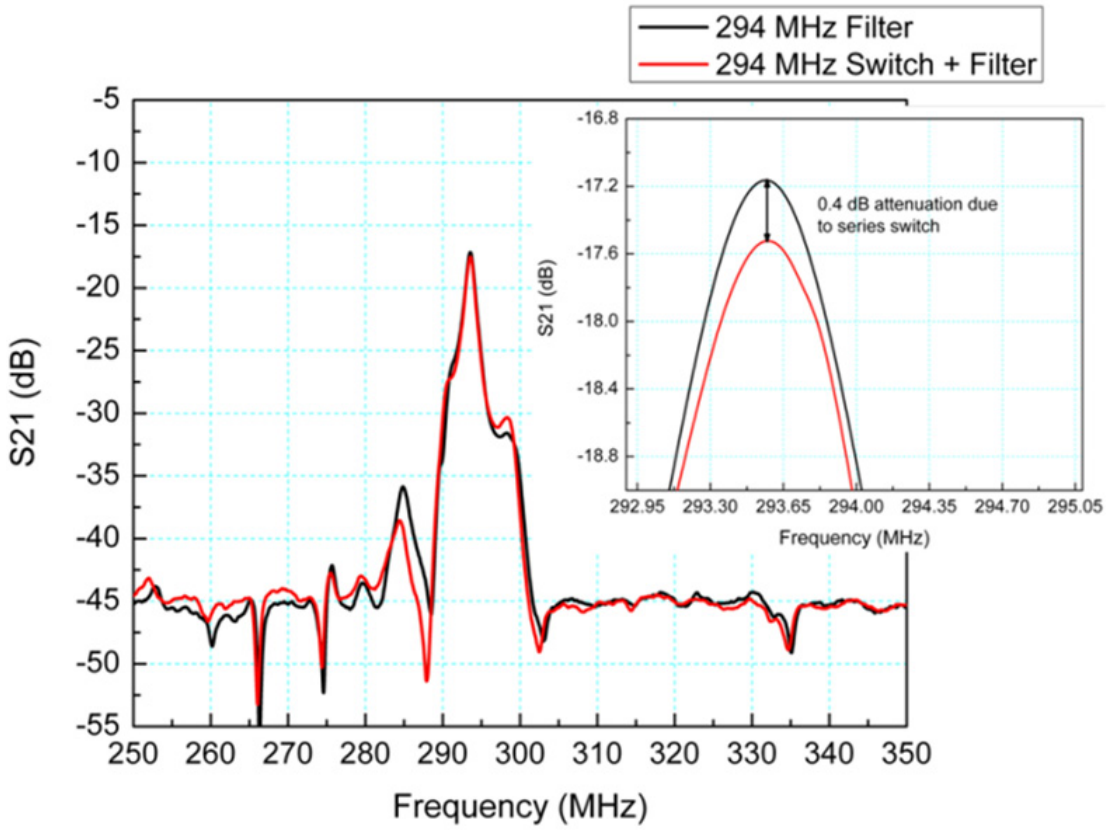

Figure 8.5: S_{21} response for a stand-alone PZT transduced contour-mode filter and an integrated PZT transduced switch + contour-mode filter with the DC bias at 10 V for both devices. The switch increases insertion loss (IL) by 0.4 dB.

research [117].

With both switches in the Off-state (i.e. 0 V applied), the output from both the left or right filters exhibited a flat S_{21} response with a magnitude of -60 dB as shown in Figure 8.4 (b). This is somewhat surprising since a simple linear cascade of S-parameters of the switch and resonator should show the filter response shifted down by the individual switch isolation as in [107]. Although this curiosity is still under investigation, we believe it is most likely due to current shunting around the open switch effectively reducing its isolation. The exclusion of air bridges at the SP2T junctions is a likely source of this reduced isolation.

As each switch was actuated at 7 V, the associated filter response was detected

at the relevant output port for each filter as recorded in Figure 8.4 (c) and (d). For both filters, an improvement in the insertion loss was observed with the application of a DC voltage applied to the RF signal through the bias-Ts of the network analyzer. The impedance tuning agrees with the previous observation of Chandrahalim *et al* [109]. The filters exhibited out-of-band rejection of nearly -30 dB and a 50 Ω terminated IL of -17 dB and -24 dB (as measured from the minimum insertion loss) with the application of a 10 V DC bias as demonstrated in Figure 8.4 (c) and (d). Similar filter responses were observed in the integrated (add 0.4 dB insertion loss) as in the standalone filters fabricated on the same wafer. The similar performances between individual filters and filters integrated with SP2T switches as shown in Figure 8.5 suggest obtaining improved device performance is a matter of updating the filter design, which is currently in progress.

8.4.2 Time Domain Measurement

A series of time domain measurements were used to examine the switching and filter characteristics as a function of switch cycling. As shown in Figure 8.6, the output response from the integrated switch and filter is ringing up with each switching pulse. It is unclear whether this is due to ring up of the filter or is influenced by the electrical time constant due to the switch contact resistance. Similar to previous PZT switches, the switch cycle lifetime is expected to last in excess of tens of millions of switch cycles and improve with more suitable contact materials, switch optimization, and integrated packaging.

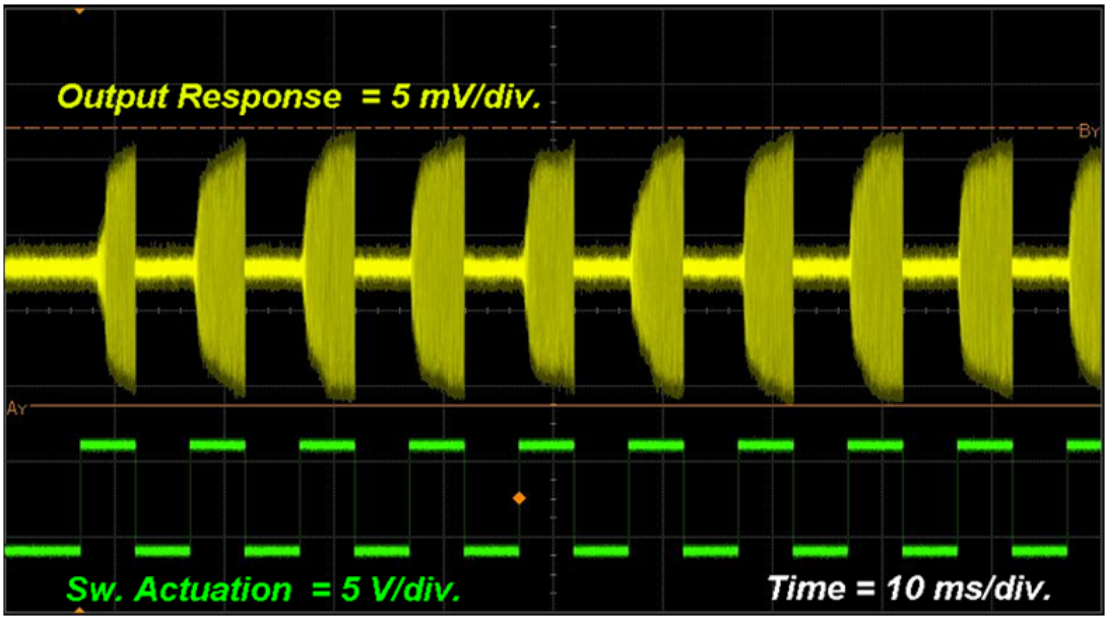

Figure 8.6: Time domain measurements of the switch + filter highlighting the 7 V switching actuation pulses and the ring-up response of the filter with the switch in the On-state.

8.5 Conclusion

For the first time, piezoelectric MEMS RF switches and contour-mode filters have been monolithically integrated and demonstrated as a switchable filter array. Lead zirconate titanate (PZT) thin films were utilized to enable both low-voltage switch operation and filter tunability. By incorporating RF switches and contour-mode filters on the same chip, all the characteristics of PZT-only and PZT-on-silicon resonators and filters can be acquired and selectively excited. On-going research is focusing on improving the loss performance of the filters, suppressing spurious modes, addressing switch lifetime, and incorporating wafer-level packaging. The low-voltage switches and voltage tunable Piezo-MEMS filter array provides a drop-in solution for frequency-agile channel selectivity.

CHAPTER 9

FUTURE RESEARCH DIRECTIONS

Voltage tunable micromechanical resonators and filters have marvelous potential to reshape the contemporary wireless communication systems. The research efforts and results presented in this dissertation provide a foundation for future investigations and developments. However, additional refinements are essential to enhance the ultimate practicality of these devices.

9.1 Solid Dielectrically Transduced Devices

9.1.1 Transduction Efficiency

A vacuum-encapsulated, silicon nitride transduced resonators were successfully designed, fabricated and characterized in Chapter 4. The performance of the epitaxial-silicon packaging is also verified to sufficiently package VHF and UHF devices. Further research to investigate dielectric materials with higher dielectric constants (κ) to improve the transduction efficiency is necessary. Figure 9.1 predicted the values of motional resistance (R_X) versus DC bias voltage for different dielectric materials in the case of contour-mode disk resonators [121].

9.1.2 On-chip Fully-differential Configuration

In order to overcome the parasitic capacitances, the vacuum-encapsulated resonator presented in Chapter 4 was characterized using a pseudo-differential measurement technique as shown in Figure 9.2 (a). This measurement requires complex setup and extra off-chip wirings. Real wireless applications will require the inherent ability of the device to exhibit mechanical resonance at the desired res-

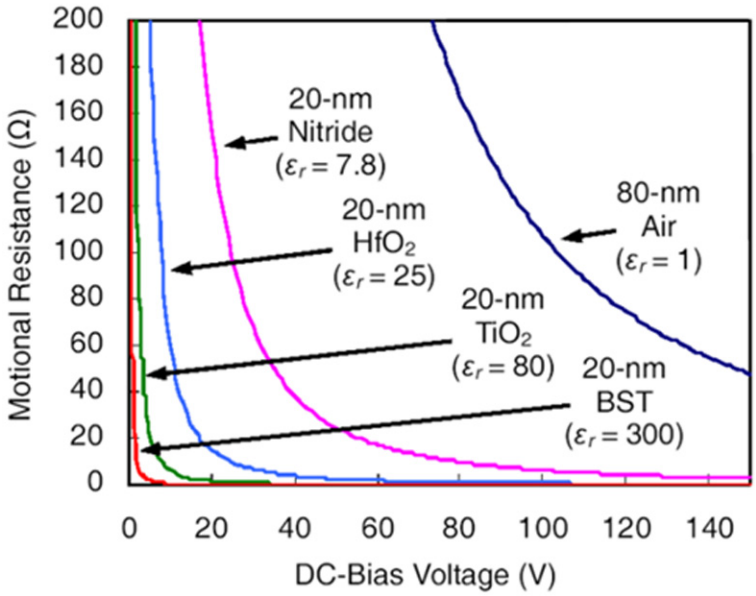

Figure 9.1: Estimated values of motional resistance (R_X) versus DC bias voltage for different dielectric materials.

onance frequency. The implementation of fully-differential devices on-chip will be greatly beneficial to reduce these parasitic capacitances. It also simplifies the characterization procedure enormously. Figure 9.2 (b) presents the design of the next generation on-chip fully-differential MEMS filter.

9.1.3 Long-term Stability

Open-loop measurement for long-term stability on a vacuum-encapsulated resonator has been performed by measuring the quality factor and resonance frequency of the resonator over four months period of time. The measured Q over time in Figure 9.3 (a) indicates that the quality factor of the resonator fluctuates between $8,450$ and $8,650$ during the measurement period. The resonance frequency of the resonator exhibits 1 MHz variation during the measurement period as shown in Figure 9.3 (b). The quality factor and frequency drifts could be due

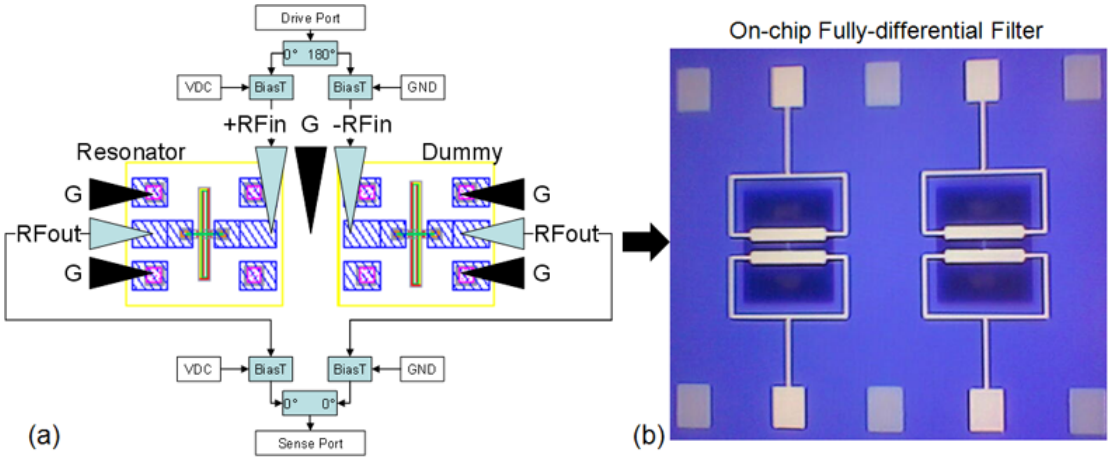

Figure 9.2: (a) Pseudo-differential measurement setup to characterize the vacuum-encapsulated resonator. (b) On-chip fully-differential configuration to eliminate parasitic capacitances.

to the Network Analyzer, the probe-tips, RF cables etc. Further investigations are necessary to pinpoint the causes of these drifts. A closed-loop oscillator circuit can be designed to perform a proper study of phase noise and Allan deviation of the device.

9.1.4 Post-MEMS CMOS Integrated Systems

Traditionally RF MEMS devices are integrated with CMOS electronics using wire-bonding technique as shown in Figure 9.4 (a) [122]. This kind of hybrid integration not only demands extra space but also introduces losses due to the wires. In Chapter 4 a successful packaging of MEMS resonators using CMOS compatible process has been demonstrated. The next step will be to develop a post-MEMS CMOS monolithically integrated system as shown in Figure 9.4 (b). The monolithically integrated system will provide low-loss interconnects between MEMS devices and CMOS integrated circuits. In addition, it facilitates devices with smaller size, lighter weight and cheaper cost.

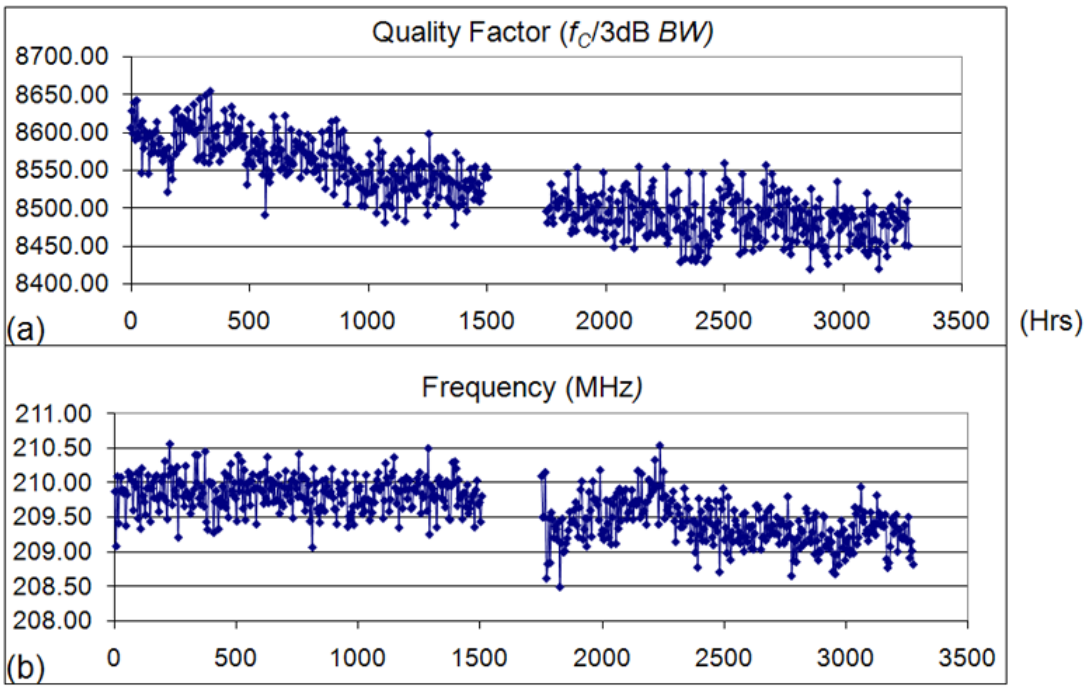

Figure 9.3: Open-loop long-term stability measurement of a silicon nitride transduced vacuum-encapsulated resonator. (a) Measured quality factor as a function of time, and (b) Measured frequency as a function of time.

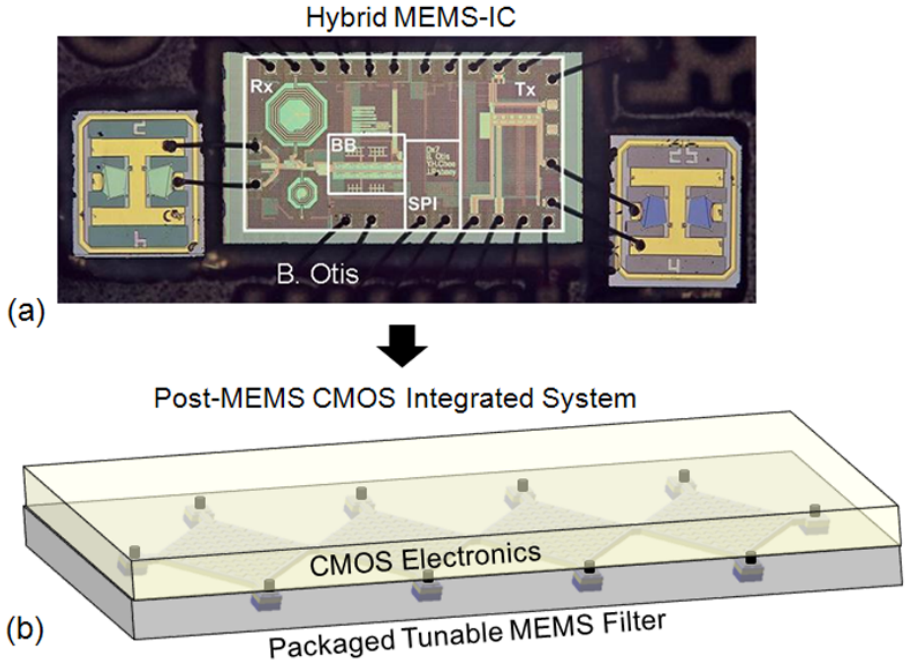

Figure 9.4: (a) Hybrid-integration of a super-regenerative CMOS-MEMS transceiver. (b) Post-MEMS CMOS monolithically integrated system.

9.2 Liquid Dielectrically Transduced Devices

Aqueous transduction is an excellent alternative to solid-dielectric transduction due to the high permittivity and low acoustic velocity of water. However, the operating frequency is limited up to 2 GHz as water has a significant loss tangent above that frequency [96]. Aqueous transduction also facilitates a large frequency tuning capability. The 3% limit of electrostatic tuning capability was mainly due to electrolysis of water and bubble formation, which suggests that using an alternate low loss-tangent liquid such as dielectric oil [99] will enable high resonant frequency operation and wide tuning range. In addition to RF applications, aqueous transduction can be used for thermal cooling and isolation, single-molecule mass detection in liquid media and frequency-domain dielectric spectroscopy.

Integration of contour-mode MEMS resonators and filters with micro-fluidic devices allows incorporation of fluid dielectric materials in the transducer gaps in a more controllable manner. Electrowetting method has been successfully demonstrated to create, transport, cut, and merge liquid droplets as shown in Figure 9.5 (a) [123]. Several research groups have been able to drive the motion of liquids on a flat solid surface using light as demonstrated in Figure 9.5 (b) [124]. The microheaters as shown in Figure 9.5 (c) have the capability to actuate liquid in a very controllable manner [125]. More recently, micro-structured surface ratchets have been fabricated to enhance the liquid droplet transport as presented in Figure 9.5 (d) [126]. These micro-fluidic devices and techniques to control liquids can be integrated with contour-mode MEMS resonators and filters to provide a more precise way to flow liquid dielectric materials into the transducer gaps.

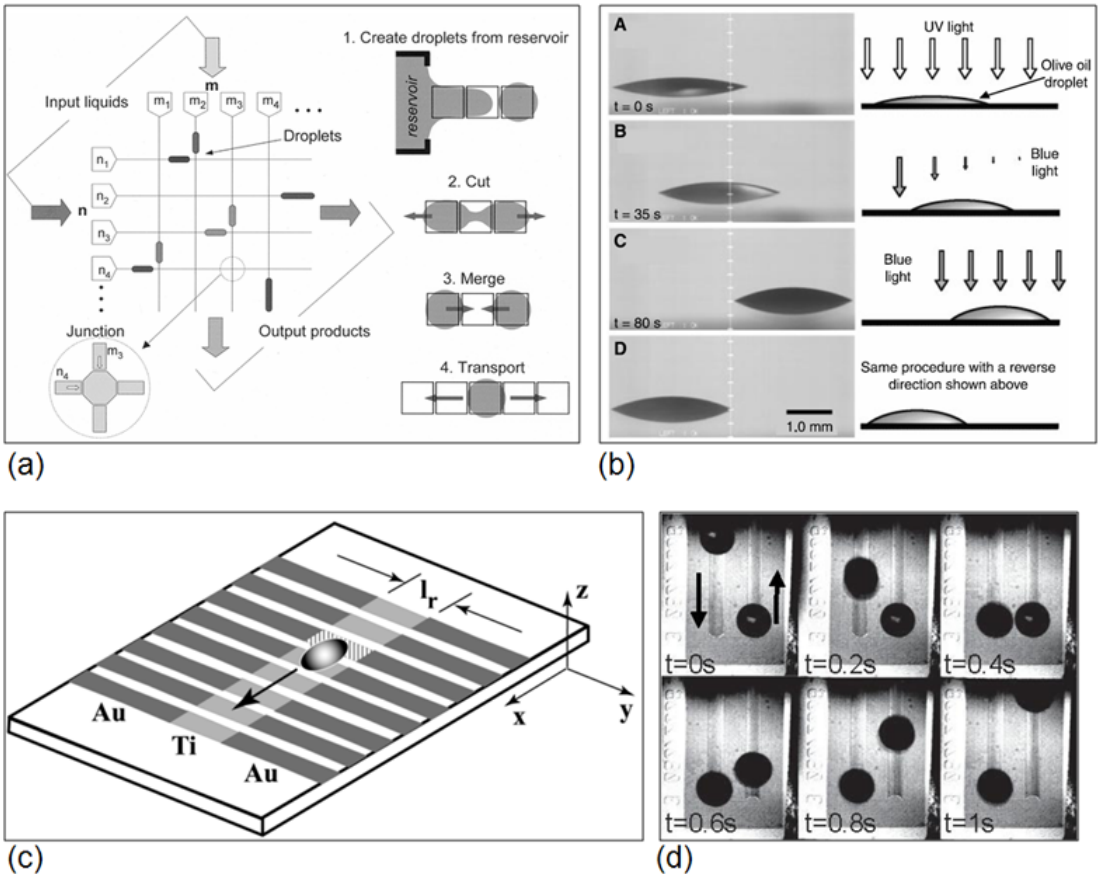

Figure 9.5: (a) Four fundamental fluidic operations considered essential to build digital microfluidic circuits, which can be used for lab-on-a-chip or micro total analysis system all by electrowetting. (b) Lateral photographs of light-driven motion of an olive oil droplet. (c) Top-view of a liquid droplet moving along a liquophilic microstripe. The array of Ti-resistors (shown in light gray) beneath the liquophilic stripes locally heat the droplet thereby modifying the surface tension and propelling the liquid toward the colder regions of the device surface. The dark gray stripes represent the leads and contacts (Au) for the heating resistors. (d) Time shots of droplets moving on ratchet-tracks.

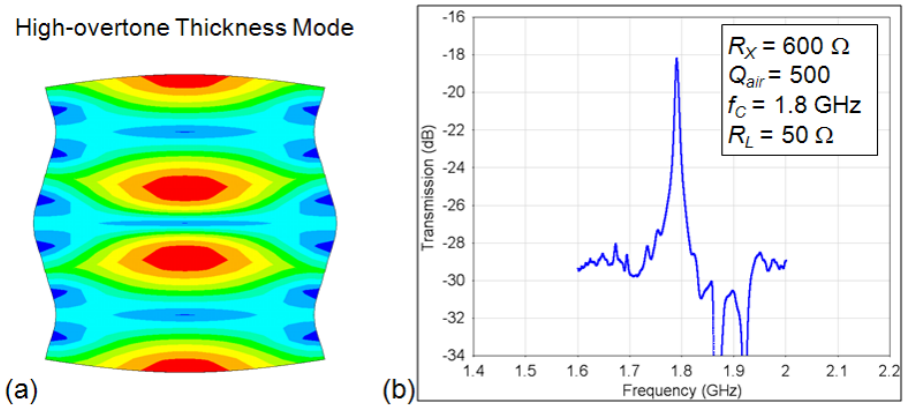

Figure 9.6: (a) ANSYS modal analysis of a high-overtone thickness-mode resonator. (b) Measured frequency response of a 50 Ω terminated PZT transduced high-overtone thickness-mode resonator in air at room temperature and pressure.

9.3 PZT Transduced Devices

9.3.1 High-Q SHF PZT Transduced Resonators

Using the latest deposited PZT film with a specifically engineered orientation we have been able to characterize the resonance of a high-overtone thickness-mode PZT-on-silicon resonator at 1.8 GHz. ANSYS mode shape and the measured frequency response of the resonator is presented in Figure 9.6. We can immediately see applications such as TV broadcast, amateur radio, mobile telephones, cordless telephones and wireless networking at this frequency range. The loss-tangent of PZT starts to dominate the loss at frequency above 2 GHz. A bulk-mode PZT transduced resonator with a particular texture design has been demonstrated at above 4 GHz resonance frequency [127]. However, the resonator exhibited Q of less than 200. Integration of textured PZT transduction with single-crystal silicon may be a potential solution to improve quality factor for super-high frequency operation.

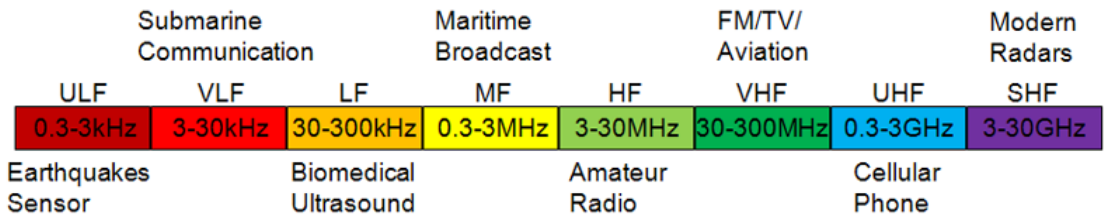

Figure 9.7: Applications within the radio frequency spectrum.

9.3.2 Monolithically-integrated PZT Based Microsystems

PZT transduction can cover a very wide range frequency of applications as shown in Figure 9.7. With our latest measured result PZT transduced resonators and filters can be used for numerous wireless applications at UHF band. We are hopeful that the high-Q textured PZT-on-silicon will be able to operate at SHF.

Our current fabrication technology has enabled us to monolithically integrate PZT transduced switches, resonators, filters, sensors and actuators on the same substrate. We can be optimistic to realize a PZT based 1 mm^3 integrated microsystem that covers multi-function applications that operate from ultra-low frequency up to super-high frequency in the near future.

APPENDIX A

FABRICATION PROCESS OF THICKNESS SHEAR RESONATORS AND FILTERS

---

1. Start with 3 micron thick device layer heavily-doped SOI wafers

n-type/Sb, <1 0 0>

Resistivity: 0.01-0.02 Ohm-cm

Run a standard MOS clean

---

2. Deposit of 30 nm hafnia thin-film on the wafer

by atomic layer deposition

---

3. Dehydrate the wafer on the hot-plate at 115 degree Celsius

for 2 minutes

---

4. Spin SPR220-3 photoresist on the wafer at 3,000 rpm

for 30 seconds to get a 3 micron thick photoresist mask

---

5. Soft-bake the wafer on the hot-plate at 130 degree Celsius

for 3 minutes

---

6. Exposure of the alignment-mark mask (Mask 1) using

GCA200 Auto Stepper for 0.6 seconds

---

7. Post-exposure bake the wafer on the hot-plate

at 130 degree Celsius for 3 minutes

---

8. Manually develop the mask using MIF300 developer
for 2.5 minutes

---

9. Bake the wafer inside convection oven at 90 degree Celsius
for 2 hours

---

10. Etch the wafer using Oxford 80 RIE etcher for 10 minutes
to pattern the alignment mark on the dielectric layer
Use standard CHF3/O2 oxide etch recipe

---

11. Continue etching the wafer using Oxford 100 RIE etcher
for 11 minutes to pattern the 1 micron thick alignment mark on
the silicon device layer
Use standard CF4 silicon etch recipe

---

12. Run oxygen plasma recipe in Oxford 80 for 15 minutes
to remove the photoresist on the wafer

---

13. Dehydrate the wafer on the hot-plate at 115 degree Celsius
for 2 minutes

---

14. Spin S1813 photoresist on the wafer at 4,000 rpm
for 30 seconds to get a 1.3 micron thick photoresist mask

---

15. Soft-bake the wafer on the hot-plate at 115 degree Celsius

for 2 minutes

---

16. Exposure of the dielectric layer mask (Mask 2)

using GCA200 Auto Stepper for 0.35 seconds

---

17. Develop the mask using Hamatech automatic developer

Use MIF300, spin at 2,500 rpm for 90 seconds

---

18. Hard-bake the wafer on the hot plate at 115 degree Celsius

for 2 minutes

---

19. Etch the wafer using Oxford 80 RIE etcher for 10 minutes

to pattern the dielectric layer

Use standard CHF3/O2 oxide etch recipe

---

20. Run oxygen plasma recipe in Oxford 80 for 15 minutes

to remove the photoresist on the wafer

---

21. Run a standard MOS clean process

---

22. LPCVD of 50 nm n+ polysilicon layer at 620 degree Celsius

for 20 minutes

---

23. Deposit 38 nm undoped oxide mask to pattern

polysilicon layer using GSI PECVD machine

Use standard undoped oxide recipe for 10 seconds

---

24. Dehydrate the wafer on the hot-plate at 115 degree Celsius
for 2 minutes

---

25. Spin S1813 photoresist on the wafer at 4,000 rpm
for 30 seconds to get a 1.3 micron thick photoresist mask

---

26. Soft-bake the wafer on the hot-plate at 115 degree Celsius
for 2 minutes

---

27. Exposure of the polysilicon mask (Mask 3)
using GCA200 Auto Stepper for 0.35 seconds

---

28. Develop the mask using Hamatech automatic developer
Use MIF300, spin at 2,500 rpm for 90 seconds

---

29. Hard-bake the wafer on the hot plate at 115 degree Celsius
for 2 minutes

---

30. Use Oxford 80 RIE etcher to pattern the Oxide mask layer
Use standard CHF3/O2 oxide etch recipe

---

31. Run oxygen plasma recipe in Oxford 80 for 15 minutes
to remove the photoresist on the wafer

---

32. Etch the wafer using Plasma Thermal 770 etcher

for 50 seconds to pattern the polysilicon layer

Use the standard Chlorine gas etch recipe

---

33. Dip the wafer in BOE (Buffered Oxide Etchant) 30:1

for 1 minute to remove the oxide hard-mask

---

34. Spin SPR220-7 photoresist on the wafer at 3,000 rpm

for 30 seconds to get a 7 micron thick photoresist mask

---

35. Soft-bake the wafer on the hot-plate at 130 degree Celsius

for 3 minutes

---

36. Exposure of the silicon mask (Mask 4)

using GCA200 Auto Stepper for 0.57 seconds

---

37. Manually develop the mask using MIF300 developer

for 3.5 minutes

---

38. Bake the wafer inside convection oven at 90 degree Celsius

for 2 hours

---

39. Etch the wafer using Oxford 80 RIE etcher for 10 minutes

to pattern the dielectric layer

Use standard CHF3/O2 oxide etch recipe

---

40. Continue etching the wafer using Unaxis 770 DRIE etcher

for 10 cycles to pattern the the silicon device layer

---

41. Use Branson Barrel asher for 40 minutes

to remove the photoresist from the wafer

---

42. Dice the wafer using KS7000 dicing saw

---

43. Release the structures in 49% Hydrofluoric acid

for 57 seconds

---

44. Run a standard critical point dry process

APPENDIX B

CALIBRATION AND DE-EMBEDDING TECHNIQUES

The resonators and filters are characterized in a Cascade RF probe station in a 2-port configuration using high-performance RF coaxial wires, GSG probes and bias-Ts. In order to characterize the 4-pole filters, additional in-phase and out-of-phase power-splitters are necessary. Parasitics up to the probe tips are first cancelled with Short-Open-Load-Thru (SOLT) RF measurements on a standard calibration substrate. De-embedding is then performed with Cascade WinCal software, using Short-Open-Thru (SOT) structures fabricated on-chip, but separate from the resonators [81]. All RF components such as bias-Ts and power-splitters are included in the de-embedding procedure. This de-embedding allows for the cancellation of the large pad capacitance and sheet resistance without canceling out any parasitics inherent to the resonators and filters, including the suspension beam routing and intrinsic capacitance between the transduction electrodes and the device body. Figure B.1 illustrates the SOT de-embedding procedure that is performed prior to every device characterization for all applied DC bias. The $OPEN$ structure cancels parasitic capacitances in parallel to device under test (DUT). The $SHORT$ structure removes parasitic elements in series to DUT. Finally, the $THRU$ structure is used to eliminate sheet resistances associated with bond pads of the device.

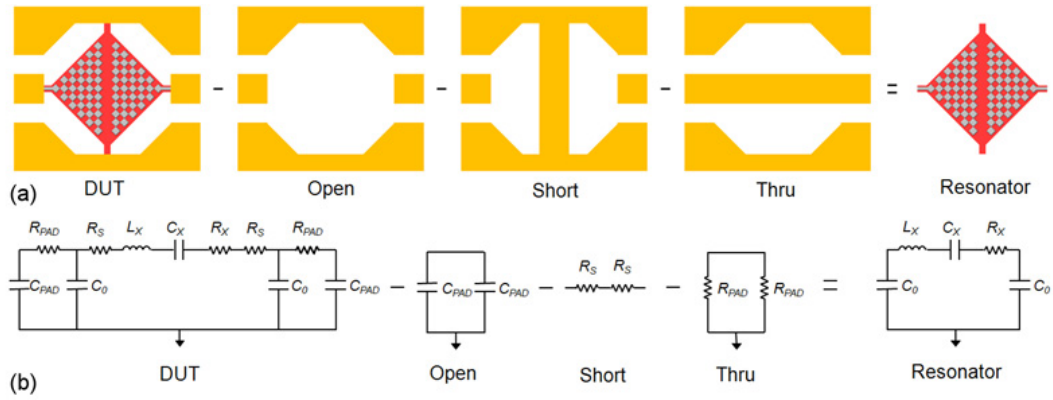

Figure B.1: SOT de-embedding (a) schematic (b) equivalent circuit to cancel pad capacitance and sheet resistance without canceling out any parasitic elements inherent to the resonators and filters.

BIBLIOGRAPHY

[1] A. A. Abidi, "Direct-conversion radio transceivers for digital communications," *IEEE Journal of Solid-State Circuits* **30**(12), pp. 1399 – 1410, 1995.

[2] J. Crols and M. Steyaert, "A Single-chip 900 MHz CMOS receiver front-end with a high performance low-IF topology," *IEEE Journal of Solid-State Circuits* **30**(12), pp. 1483 – 1492, 1995.

[3] J. C. Rudell, J. J. Ou, T. B. Cho, G. Chien, F. Brianti, J. A. Weldon, and P. R. Gray, "A 1.9-GHz wide-band IF double conversion CMOS receiver for cordless telephone applications," *IEEE Journal of Solid-State Circuits* **32**(12), pp. 2071–2088, 1997.

[4] D. H. Shen, C. M. Hwang, B. B. Lusignan, and B. A. Wooley, "A 900-MHz RF front-end with integrated discrete-time filtering," *IEEE Journal of Solid-State Circuits* **31**(12), pp. 1945 – 1954, 1996.

[5] T. Stetzler, I. Post, J. Havens, and M. Koyama, "A 2.7V-4.7V single chip GSM transceiver RF integrated circuit," *IEEE Journal of Solid-State Circuits* **30**(12), pp. 1421 – 1429, 1995.

[6] W. H. Ko, M.-. H. Bao, and Y.-. D. Hong, "A high-sensitivity integrated-circuit capacitive pressure transducer," *IEEE Transactions on Electron Devices* **29**(1), pp. 48 – 56, 1982.

[7] R. T. Howe and R. S. Muller, "Resonant-microbridge vapor sensor," *IEEE Transactions on Electron Devices* **33**(4), pp. 499 – 506, 1986.

[8] K. Petersen, P. Barth, J. Poydock, J. Brown, J. Mallon, J., and J. Bryzek, "Silicon fusion bonding for pressure sensors," *Hilton Head '88. Solid-State Sensor and Actuator Workshop. Digest of Technical Papers* **1**, pp. 144 – 147, (Hilton Head Island, SC, USA), 1988.

[9] W. Yun, R. T. Howe, and P. R. Gray, "Surface micromachined, digitally force-balanced accelerometer with integrated cmos detection circuitry," *Hilton Head '92. Solid-State Sensor and Actuator Workshop. Digest of Technical Papers* **1**, pp. 126 – 131, (Hilton Head Island, SC, USA), 1992.

[10] H. C. Nathanson and R. A. Wickstrom, "A resonant-gate silicon surface transistor with high-Q band-pass properties," *Applied Physics Letters* **7**(4), pp. 84–86, 1965.

[11] H. C. Nathanson, W. E. Newell, R. A. Wickstrom, and J. Davis, J. R., "The resonant gate transistor," *IEEE Transactions on Electron Devices* **14**(3), pp. 117 – 133, 1967.

[12] K. E. Petersen, "Silicon as a mechanical material," *Proceedings of the IEEE* **70**(5), pp. 420 – 457, 1982.

[13] W. C. Tang, T. C. H. Nguyen, and R. T. Howe, "Laterally driven polysilicon resonant microstructures," *Sensors and Actuators* **20**(1-2), pp. 25 – 32, 1989.

[14] L. Lin, R. T. Howe, and A. P. Pisano, "Microelectromechanical filters for signal processing," *Journal of Microelectromechanical Systems* **7**(3), pp. 286 – 294, 1998.

[15] C. T. C. Nguyen and R. T. Howe, "An integrated CMOS micromechanical resonator high-Q oscillator," *IEEE Journal of Solid-State Circuits* **34**(4), pp. 440 – 455, 1999.

[16] R. Ruby and P. Merchant, "Micromachined thin film bulk acoustic resonators," *Proceedings of the 48th IEEE International Frequency Control Symposium* , pp. 135 – 138, (Boston, MA, USA), 1994.

[17] S. Pourkamali and F. Ayazi, "SOI-based HF and VHF single-crystal silicon resonators with sub-100 nanometer vertical capacitive gaps," *The 12th International Conference on TRANSDUCERS, Solid-State Sensors, Actuators and Microsystems* , pp. 837 – 840, (Boston, MA, USA), 2003.

[18] T. Mattila, J. Kiihamaki, T. Lamminmaki, O. Jaakkola, P. Rantakari, A. Oja, H. Seppa, H. Kattelus, and I. Tittonen, "A 12 MHz micromechanical bulk acoustic mode oscillator," *Sensors and Actuators, A: Physical* **101**(1-2), pp. 1 – 9, 2002.

[19] J. Wang, Z. Ren, and C.-C. Nguyen, "1.156-GHz self-aligned vibrating micromechanical disk resonator," *IEEE Transactions on Ultrasonics, Ferroelectrics and Frequency Control* **51**(12), pp. 1607 – 1628, 2004.

[20] G. Piazza, *Piezoelectric Aluminum Nitride Vibrating RF MEMS for Radio Front-End Technology*. PhD thesis, University of California at Berkeley, 2005.

[21] P. J. Stephanou, *Piezoelectric Aluminum Nitride MEMS Resonators for RF Signal Processing*. PhD thesis, University of California at Berkeley, 2006.

[22] R. G. Kinsman, *Crystal Filters: Design, Manufacture, and Application*, John Wiley & Sons, New York, 1987.

[23] R. A. Johnson, *Mechanical Filters in Electronics*, John Wiley & Sons, New York, 1983.

[24] W. G. Cady, "Piezo-electric resonator," *Proceedings of the Institute of Radio Engineers* **10**(2), pp. 83 – 114, 1922.

[25] C. T.-C. Nguyen, *Micromechanical Signal Processors*. PhD thesis, University of California at Berkeley, 1994.

[26] E. A. Gerber, *Precision Frequency Control, Volume 2: Oscillators and Standards*, Academic Press, Inc., New York, 1985.

[27] A. I. Zverev, *Handbook of Filter Synthesis*, John Wiley & Sons, New York, 1967.

[28] J. W. S. Rayleigh, "On waves propagating along the plane surface of an elastic solid," *Proceedings of the London Mathematical Society* **17**, pp. 4 – 11, 1887.

[29] R. M. White and F. W. Voltmer, "Direct piezoelectric coupling to surface elastic waves," *Applied Physics Letters* **7**(12), pp. 314 – 316, 1965.

[30] T. Matsuda, H. Uchishiba, O. Ikata, T. Nishihara, and V. Satoh, "L and S band low-loss filters using SAW resonators," *Proceedings of the IEEE Ultrasonics Symposium* , pp. 163 – 167, (Cannes, France), 1994.

[31] M. Ueda, J. Tsutsumi, S. Inoue, T. Matsuda, O. Ikata, and Y. Satoh, "Ultra-miniaturized and high performance PCS SAW duplexer with steep cut-off filters," *IEEE MTT-S International Microwave Symposium Digest* , pp. 913 – 916, (Fort Worth, TX, USA), 2004.

[32] R. Ruby, P. Bradley, J. D. Larson III, Y. Oshmyansky, and D. Figueredo, "Ultra-miniature high-Q filters and duplexers using fbar technology," *2001 IEEE International Solid-State Circuits Conference. Digest of Technical Papers. ISSCC* , pp. 120 – 1, (San Francisco, CA, USA), 2001.

[33] R. Aigner, J. Ella, H. J. Timme, L. Elbrecht, W. Nessler, and S. Marksteiner, "Advancement of MEMS into RF-filter applications," *IEEE International Electron Devices Meeting* , pp. 897 – 900, (San Francisco, CA, USA), 2002.

[34] R. Aigner, J. Kaitila, J. Ella, L. Elbrecht, W. Nessler, M. Handtmann, T. R. Herzog, and S. Marksteiner, "Bulk-acoustic-wave filters: performance optimization and volume manufacturing," *IEEE MTT-S International Microwave Symposium Digest* , pp. 2001 – 2004, (Philadelphia, PA, USA), 2003.

[35] R. Aigner, S. Marksteiner, L. Elbrecht, and W. Nessler, "Rf-filters in mobile phone applications," *The 12th International Conference on TRANSDUCERS, Solid-State Sensors, Actuators and Microsystems* , pp. 891 – 894, (Boston, MA, USA), 2003.

[36] R. Aigner, "High performance RF-filters suitable for above IC integration: film bulk-acoustic- resonators (FBAR) on silicon," *Proceedings of the IEEE 2003 Custom Integrated Circuits Conference* , pp. 141 – 146, (San Jose, CA, USA), 2003.

[37] S. Marksteiner, M. Handtmann, H. J. Timme, R. Aigner, R. Welzer, J. Portmann, and U. Bauernschmitt, "A miniature BAW duplexer using flip-chip on LTCC," *Proceedings of the IEEE Ultrasonics Symposium* , pp. 1794 – 1797, (Honolulu, HI, USA), 2003.

[38] R. Aigner, "MEMS in RF-filter applications: thin film bulk-acoustic-wave technology," *The 13th International Conference on TRANSDUCERS, Solid-State Sensors, Actuators and Microsystems* , pp. 5 – 8, (Seoul, Korea), 2005.

[39] R. Aigner, "SAW and BAW technologies for RF filter applications: A review of the relative strengths and weaknesses," *Proceedings of the IEEE Ultrasonics Symposium* , pp. 582 – 589, (Beijing, China), 2008.

[40] R. Ruby, P. Bradley, J. D. Larson III, and Y. Oshmyansky, "PCS 1900 MHz duplexer using thin film bulk acoustic resonators (FBARs)," *Electronics Letters* **35**, pp. 794 – 795, 1999.

[41] R. C. Ruby, P. Bradley, Y. Oshmyansky, A. Chien, and J. D. Larson III, "Thin film bulk wave acoustic resonators (FBAR) for wireless applications," *Proceedings of the IEEE Ultrasonics Symposium* , pp. 813 – 821, (Atlanta, GA, USA), 2001.

[42] P. Bradley, R. Ruby, J. D. Larson III, Y. Oshmyansky, and D. Figueredo, "A film bulk acoustic resonator (FBAR) duplexer for USPCS handset applications," *2001 IEEE MTT-S International Microwave Symposium Digest* **vol.1**, pp. 367 – 70, (Phoenix, AZ, USA), 2001.

[43] W. Pang, H. Zhang, H. Yu, C.-Y. Lee, and E. S. Kim, "Electrical frequency tuning of film bulk acoustic resonator," *Journal of Microelectromechanical Systems* **16**(6), pp. 1303 – 13, 2007.

[44] W. T. Hsu, J. R. Clark, and C. T.-C. Nguyen, "A sub-micron capacitive gap process for multiple-metal-electrode lateral micromechanical resonators," *Technical Digest. MEMS 2001. 14th IEEE International Conference on Micro Electro Mechanical Systems* , pp. 349 – 52, (Interlaken, Switzerland), 2001.

[45] J. R. Clark, W. T. Hsu, M. A. Abdelmoneum, and C. T. C. Nguyen, "High-Q UHF micromechanical radial-contour mode disk resonators," *Journal of Microelectromechanical Systems* **14**(6), pp. 1298 – 310, 2005.

[46] S.-S. Li, Y.-W. Lin, Y. Xie, Z. Ren, and C. T. C. Nguyen, "Micromechanical "hollow-disk" ring resonators," *17th IEEE International Conference on Micro Electro Mechanical Systems. Maastricht MEMS 2004 Technical Digest* , pp. 821 – 4, (Maastricht, The Netherlands), 2004.

[47] Y. Xie, S.-S. Li, Y.-W. Lin, Z. Ren, and C. T. C. Nguyen, "1.52-GHz micromechanical extensional wine-glass mode ring resonators," *IEEE Transactions on Ultrasonics, Ferroelectrics and Frequency Control* **55**(4), pp. 890 – 907, 2008.

[48] J. Wang, J. E. Butler, T. Feygelson, and C. T. C. Nguyen, "1.51-GHz nanocrystalline diamond micromechanical disk resonator with material-mismatched isolating support," *17th IEEE International Conference on Micro Electro Mechanical Systems. Maastricht MEMS 2004 Technical Digest* , pp. 641 – 4, (Maastricht, The Netherlands), 2004.

[49] V. Kaajakari, T. Mattila, A. Oja, J. Kiihamaki, H. Kattelus, M. Koskenvuori, P. Rantakari, I. Tittonen, and H. Seppa, "Square-extensional mode single-crystal silicon micromechanical RF-resonator," *TRANSDUCERS '03. 12th International Conference on Solid-State Sensors, Actuators and Microsystems. Digest of Technical Papers* **vol.2**, pp. 951 – 4, (Boston, MA, USA), 2003.

[50] H. Takeuchi, E. Quevy, S. A. Bhave, T.-J. King, and R. T. Howe, "Ge-blade damascene process for post-CMOS integration of nano-mechanical resonators," *IEEE Electron Device Letters* **25**(8), pp. 529 – 31, 2004.

[51] T. Mattila, A. Oja, H. Seppa, O. Jaakkola, J. Kiihamaki, H. Kattelus, M. Koskenvuori, P. Rantakari, and I. Tittonen, "Micromechanical bulk acous-

tic wave resonator," *Proceedings of the IEEE Ultrasonics Symposium* **1**, pp. 945 – 948, (Munich, Germany), 2002.

[52] S. Humad, R. Abdolvand, G. K. Ho, G. Piazza, and F. Ayazi, "High frequency micromechanical piezo-on-silicon block resonators," *Technical Digest - International Electron Devices Meeting* , pp. 957 – 960, (Washington, DC, United states), 2003.

[53] G. Piazza, P. J. Stephanou, J. M. Porter, M. B. J. Wijesundara, and A. P. Pisano, "Low motional resistance ring-shaped contour-mode aluminum nitride piezoelectric micromechanical resonators for UHF applications," *18th IEEE International Conference on Micro Electro Mechanical Systems* , pp. 20 – 3, (Miami, FL, USA), 2005.

[54] G. Piazza, P. J. Stephanou, and A. P. Pisano, "Single-chip multiple-frequency AlN MEMS filters based on contour-mode piezoelectric resonators," *Journal of Microelectromechanical Systems* **16**(2), pp. 319 – 328, 2007.

[55] G. Piazza, P. J. Stephanou, and A. P. Pisano, "Piezoelectric aluminum nitride vibrating contour-mode MEMS resonators," *Journal of Microelectromechanical Systems* **15**(6), pp. 1406 – 1418, 2006.

[56] G. K. Ho, R. Abdolvand, A. Sivapurapu, S. Humad, and F. Ayazi, "Piezoelectric-on-silicon lateral bulk acoustic wave micromechanical resonators," *Journal of Microelectromechanical Systems* **17**(2), pp. 512 – 520, 2008.

[57] R. Abdolvand, G. K. Ho, J. Butler, and F. Ayazi, "ZnO-on-nanocrystalline diamond lateral bulk acoustic resonators," *2007 20th IEEE International Conference on Micro Electro Mechanical Systems - MEMS '07* , pp. 795 – 8, (Kobe, Japan), 2007.

[58] R. H. Olsson, C. M. Washburn, J. E. Stevens, M. R. Tuck, and C. D. Nordquist, "VHF and UHF mechanically coupled aluminum nitride MEMS filters," *2008 IEEE International Frequency Control Symposium* , pp. 634 – 9, (Waikiki, HI, USA), 2008.

[59] M. Rinaldi, C. Zuniga, and G. Piazza, "5-10 GHz AlN contour-mode nanoelectromechanical resonators," *Proceedings of the IEEE International Conference on Micro Electro Mechanical Systems (MEMS)* , pp. 916 – 919, 2009.

[60] S. A. Bhave and R. T. Howe, "Silicon nitride-on-silicon bar resonator using

internal electrostatic transduction," *Digest of Technical Papers - International Conference on Solid State Sensors and Actuators and Microsystems, TRANSDUCERS '05* **2**, pp. 2139 – 2142, (Seoul, Republic of Korea), 2005.

[61] S. A. Bhave and R. T. Howe, "Internal electrostatic transduction for bulk-mode MEMS resonators," *Hilton Head '04. Solid-State Sensor and Actuator Workshop. Digest of Technical Papers* **1**, pp. 59 – 60, (Hilton Head Island, SC, USA), 2004.

[62] S. Pourkamali, G. K. Ho, and F. Ayazi, "Vertical capacitive SiBARs," *18th IEEE International Conference on Micro Electro Mechanical Systems* , pp. 211 – 14, (Miami Beach, FL, United states), 2005.

[63] Y.-W. Lin, S.-S. Li, Y. Xie, Z. Ren, and C. T. C. Nguyen, "Vibrating micromechanical resonators with solid dielectric capacitive transducer gaps," *Proceedings of the IEEE International Frequency Control Symposium and Exposition* **2005**, pp. 128 – 134, (Vancouver, BC, Canada), 2005.

[64] L. F. Cheow, H. Chandrahalim, and S. A. Bhave, "MEMS filter with voltage-tunable center frequency and bandwidth," *Hilton Head '06. Solid-State Sensor and Actuator Workshop. Digest of Technical Papers* , pp. 304–307, (Hilton Head Island, SC, USA), 2006.

[65] F. P. Stratton, D. T. Chang, D. J. Kirby, R. J. Joyce, T.-Y. Hsu, R. L. Kubena, and Y.-K. Yong, "A MEMS-based quartz resonator technology for GHz applications," *Proceedings of the IEEE International Frequency Control Symposium and Exposition* , pp. 27 – 34, (Montreal, Canada), 2005.

[66] R. Blevins, *Formulas for Natural Frequency & Mode Shape*, Krieger Publishing Co., Florida, 1979.

[67] S. Pourkamali, R. Abdolvand, G. K. Ho, and F. Ayazi, "Electrostatically coupled micromechanical beam filters," *17th IEEE International Conference on Micro Electro Mechanical Systems. Maastricht MEMS 2004 Technical Digest* , pp. 584 – 587, (Maastricht, The Netherlands), 2004.

[68] D. Galayko, A. Kaiser, B. Legrand, L. Buchaillot, D. Collard, and C. Combi, "Tunable passband T-filter with electrostatically-driven polysilicon micromechanical resonators," *Sensors and Actuators, A: Physical* **117**(1), pp. 115 – 120, 2005.

[69] H. Chandrahalim, D. Weinstein, L. F. Cheow, and S. A. Bhave, "High-κ

dielectrically transduced MEMS thickness shear mode resonators and tunable channel-select RF filters," *Sensors and Actuators, A: Physical* **136**(2), pp. 527 – 539, 2007.

[70] K.-L. Chen, H. Chandrahalim, A. B. Graham, S. A. Bhave, R. T. Howe, and T. W. Kenny, "Epitaxial silicon microshell vacuum-encapsulated CMOS-compatible 200 MHz bulk-mode resonator," *Proceedings of the IEEE International Conference on Micro Electro Mechanical Systems (MEMS)* , pp. 23 – 26, 2009.

[71] D. Weinstein, H. Chandrahalim, L. F. Cheow, and S. A. Bhave, "Dielectrically transduced single-ended to differential MEMS filter," *Digest of Technical Papers - IEEE International Solid-State Circuits Conference* , pp. 318 – 319, (San Francisco, CA, United states), 2006.

[72] S. Pourkamali, G. K. Ho, and F. Ayazi, "Low-impedance VHF and UHF capacitive silicon bulk acoustic-wave resonators - Part II: Measurement and characterization," *IEEE Transactions on Electron Devices* **54**(8), pp. 2024 – 2030, 2007.

[73] H. Chandrahalim, S. A. Bhave, E. P. Quevy, and R. T. Howe, "Aqueous transduction of poly-sige disk resonators," *TRANSDUCERS and EUROSENSORS '07 - 4th International Conference on Solid-State Sensors, Actuators and Microsystems* , pp. 313 – 316, (Lyon, France), 2007.

[74] S.-S. Li, Y.-W. Lin, Z. Ren, and C. T. C. Nguyen, "A micromechanical parallel-class disk-array filter," *Proceedings of the IEEE International Frequency Control Symposium and Exposition* , pp. 1356 – 1361, (Geneva, Switzerland), 2007.

[75] V. Kaajakari, T. Mattila, A. Oja, and H. Seppa, "Nonlinear limits for single-crystal silicon microresonators," *Journal of Microelectromechanical Systems* **13**(5), pp. 715 – 724, 2004.

[76] L. Khine and M. Palaniapan, "Effect of structural thickness, anchor length and number of anchors on performance of micromechanical bulk-mode resonators," *Electronics Letters* **45**(1), pp. 37 – 39, 2009.

[77] M. U. Demirci and C. T. C. Nguyen, "Mechanically corner-coupled square microresonator array for reduced series motional resistance," *Journal of Microelectromechanical Systems* **15**(6), pp. 1419 – 1436, 2006.

[78] J. A. Judge, B. H. Houston, D. M. Photiadis, and P. C. Herdic, "Effects of disorder in one- and two-dimensional micromechanical resonator arrays for filtering," *Journal of Sound and Vibration* **290**(3-5), pp. 1119 – 1140, 2006.

[79] H. Chandrahalim and S. A. Bhave, "Digitally-tunable MEMS filter using mechanically-coupled resonator array," *Proceedings of the IEEE International Conference on Micro Electro Mechanical Systems (MEMS)* , pp. 1020 – 1023, (Tucson, AZ, United states), 2008.

[80] C. Zuo, N. Sinha, M. B. Pisani, C. R. Perez, R. Mahameed, and G. Piazza, "Channel-select RF MEMS filters based on self-coupled AlN contour-mode piezoelectric resonators," *Proceedings - IEEE Ultrasonics Symposium* , pp. 1156 – 1159, 2007.

[81] M.-H. Cho, G.-W. Huang, C.-S. Chiu, K.-M. Chen, A.-S. Peng, and Y.-M. Teng, "A cascade open-short-thru (COST) de-embedding method for microwave on-wafer characterization and automatic measurement," *IEICE Transactions on Electronics* **E88-C**(5), pp. 845 – 849, 2005.

[82] S.-S. Li, *Medium-scale Integrated Micromechanical Filters for Wireless Communications*. PhD thesis, University of Michigan, 2007.

[83] Y.-W. Lin, S. Lee, S.-S. Li, Y. Xie, Z. Ren, and C. T. C. Nguyen, "60-MHz wine-glass micromechanical-disk reference oscillator," *Digest of Technical Papers - IEEE International Solid-State Circuits Conference* **47**, pp. 322 – 323, (San Francisco, CA., United states), 2003.

[84] R. N. Candler, W.-T. Park, H. Li, G. Yama, A. Partridge, M. Lutz, and T. W. Kenny, "Single wafer encapsulation of MEMS devices," *IEEE Transactions on Advanced Packaging* **26**(3), pp. 227 – 232, 2003.

[85] B. Kim, R. N. Candler, M. A. Hopcroft, M. Agarwal, W.-T. Park, and T. W. Kenny, "Frequency stability of wafer-scale film encapsulated silicon based MEMS resonators," *Sensors and Actuators, A: Physical* **136**(1), pp. 125 – 131, 2007.

[86] R. Melamud, B. Kim, S. A. Chandorkar, M. A. Hopcroft, M. Agarwal, C. M. Jha, and T. W. Kenny, "Temperature-compensated high-stability silicon resonators," *Applied Physics Letters* **90**(24), 2007.

[87] W.-T. Park, A. Partridge, R. N. Candler, V. Ayanoor-Vitikkate, G. Yama, M. Lutz, and T. W. Kenny, "Encapsulated submillimeter piezoresistive ac-

celerometers," *Journal of Microelectromechanical Systems* **15**(3), pp. 507 – 514, 2006.

[88] K.-L. Chen, J. Salvia, R. Potter, R. T. Howe, and T. W. Kenny, "Performance evaluation and equivalent model of silicon interconnects for fully-encapsulated RF MEMS devices," *IEEE Transactions on Advanced Packaging* **32**(2), pp. 402 – 409, 2009.

[89] K. L. Ekinci, Y. T. Yang, X. M. H. Huang, and M. L. Rouke, "Balanced electronic detection of displacement in nanoelectromechanical systems," *Applied Physics Letters* **81**(12), pp. 2253 – 2253, 2002.

[90] P. Rantakari, J. Kiihamaki, M. Koskenvuori, T. Lamminmaki, and I. Tittonen, "Reducing the effect of parasitic capacitance on mems measurements," *TRANSDUCERS '01. EUROSENSORS XV. 11th International Conference on Solid-State Sensors and Actuators. Digest of Technical Papers* **vol.2**, pp. 1556 – 9, (Berlin, Germany), 2001.

[91] S.-S. Li, Y.-W. Lin, Z. Ren, and C. T. C. Nguyen, "Disk-array design for suppression of unwanted modes in mlcromechanical composite-array filters," *Proceedings of the IEEE International Conference on Micro Electro Mechanical Systems (MEMS)* **2006**, pp. 866 – 869, (Istanbul, Turkey), 2006.

[92] T. L. Sounart and T. A. Michalske, "Electrostatic actuation without electrolysis in microfluidic MEMS," *TRANSDUCERS '03. 12th International Conference on Solid-State Sensors, Actuators and Microsystems. Digest of Technical Papers* **1**, pp. 615 – 618, (Boston, MA, USA), 2003.

[93] V. Mukundan and B. L. Pruitt, "Experimental characterization of frequency dependent electrostatic actuator for aqueous media," *Hilton Head '06. Solid-State Sensor and Actuator Workshop. Digest of Technical Papers* , pp. 167 – 170, (Hilton Head Island, SC, USA), 2006.

[94] R. L. Borwick, P. A. Stupar, and J. F. DeNatale, "Wide dynamic range microelectromechanical viscocity sensor," *Hilton Head '06. Solid-State Sensor and Actuator Workshop. Digest of Technical Papers* , pp. 340 – 343, (Hilton Head Island, SC, USA), 2006.

[95] E. P. Quevy, A. San Paulo, E. Basol, R. T. Howe, T.-J. King, and J. Bokor, "Back-end-of-line poly-SiGe disk resonators," *Proceedings of the IEEE International Conference on Micro Electro Mechanical Systems (MEMS)* **2006**, pp. 234 – 237, (Istanbul, Turkey), 2006.

[96] R. Buchner, J. Barthel, and J. Stauber, "The dielectric relaxation of water between 0°C and 35°C," *Chemical Physics Letters* **306**(1 - 2), pp. 57 – 63, 1999.

[97] J. R. Clark, *Micromechanical disk resonators for wireless communications*. PhD thesis, University of Michigan, 2003.

[98] S. Pourkamali and A. Ayazi, "High frequency low impedance capacitive silicon bar structures," *Hilton Head '06. Solid-State Sensor and Actuator Workshop. Digest of Technical Papers* , pp. 284 – 287, (Hilton Head Island, SC, USA), 2006.

[99] D. T. McCormick, Z. Li, and N. C. Tien, "Silicon mems tunable capacitors operating in dielectric fluid," *TRANSDUCERS '03. 12th International Conference on Solid-State Sensors, Actuators and Microsystems. Digest of Technical Papers* **1**, pp. 871 – 874, (Boston, MA, USA), 2003.

[100] R. C. Ruby, A. Barfknecht, C. Han, Y. Desai, F. Geefay, G. Gan, M. Gat, and T. Verhoeven, "High-Q FBAR filters in a wafer-level chip-scale package," *Digest of Technical Papers - IEEE International Solid-State Circuits Conference* , pp. 184 – 185, (San Francisco, CA, United states), 2002.

[101] J. D. Larson III, S. R. Gilbert, and B. Xu, "PZT Material properties at UHF and microwave frequencies derived from FBAR measurements," *Proceedings - IEEE Ultrasonics Symposium* **1**, pp. 173 – 177, (Montreal, Que., Canada), 2004.

[102] Q.-M. Wang, T. Zhang, Q. Chen, and X.-H. Du, "Effect of DC bias field on the complex materials coefficients of piezoelectric resonators," *Sensors and Actuators, A: Physical* **109**(1-2), pp. 149 – 155, 2003.

[103] J. Cho, M. Anderson, R. Richards, D. Bahr, and C. Richards, "Optimization of electromechanical coupling for a thin-film PZT membrane: II. Experiment," *Journal of Micromechanics and Microengineering* **15**(10), pp. 1804 – 1809, 2005.

[104] B. Piekarski, D. DeVoe, M. Dubey, R. Kaul, and J. Conrad, "Surface micromachined piezoelectric resonant beam filters," *Sensors and Actuators, A: Physical* **91**(3), pp. 313 – 320, 2001.

[105] B. Antkowiak, J. P. Gorman, M. Varghese, D. J. D. Carter, and A. E. Duwel, "Design of a high-Q, low-impedance, GHz-range piezoelectric MEMS resonator," *TRANSDUCERS '03. 12th International Conference on Solid-State*

Sensors, Actuators and Microsystems. Digest of Technical Papers **1**, pp. 841 – 846, (Boston, MA, USA), 2003.

[106] A. Jaakkola, P. Rosenberg, A. Nurmela, T. Pensala, T. Riekkinen, J. Dekker, T. Mattila, and A. Alastalo, "Piezotransduced single-crystal silicon BAW resonators," *Proceedings - IEEE Ultrasonics Symposium* , pp. 1653 – 1656, (New York, NY, United states), 2007.

[107] R. G. Polcawich, J. S. Pulskamp, D. Judy, P. Ranade, S. Trolier-McKinstry, and M. Dubey, "Surface micromachined microelectromechanical ohmic series switch using thin-film piezoelectric actuators," *IEEE Transactions on Microwave Theory and Techniques* **55**(12), pp. 2642 – 2654, 2007.

[108] K. D. Budd, S. K. Dey, and D. A. Payne, "SOL-GEL processing of $PbTiO_3$, $PbZrO_3$, PZT, and PLZT thin films," *British Ceramic Proceedings* (36), pp. 107 – 121, (London, Engl), 1985.

[109] H. Chandrahalim, S. A. Bhave, R. Polcawich, J. Pulskamp, D. Judy, R. Kaul, and M. Dubey, "Performance comparison of $Pb(Zr_{0.52}Ti_{0.48})O_3$-only and $Pb(Zr_{0.52}Ti_{0.48})O_3$-on-silicon resonators," *Applied Physics Letters* **93**(23), p. 233504, 2008.

[110] G. K. Ho, R. Abdolvand, and F. Ayazi, "High-order composite bulk acoustic resonators," *Proceedings of the IEEE International Conference on Micro Electro Mechanical Systems (MEMS)* , pp. 791 – 794, (Kobe, Japan), 2007.

[111] H. Chandrahalim, S. A. Bhave, R. G. Polcawich, J. S. Pulskamp, and D. Judy, "Fully-differential mechanically-coupled PZT-on-silicon filters," *Proceedings - IEEE Ultrasonics Symposium* , pp. 713 – 716, 2008.

[112] S. A. Bhave, D. Gao, R. Maboudian, and R. T. Howe, "Fully-differential poly-SiC Lame-mode resonator and checkerboard filter," *Proceedings of the IEEE International Conference on Micro Electro Mechanical Systems (MEMS)* , pp. 223 – 226, (Miami Beach, FL, United states), 2005.

[113] G. Piazza, P. J. Stephanou, and A. P. Pisano, "One and two port piezoelectric higher order contour-mode MEMS resonators for mechanical signal processing," *Solid-State Electronics* **51**(11-12), pp. 1596 – 1608, 2007.

[114] G. M. Rebeiz, *RF MEMS: Theory, Design, and Technology*, Wiley-Interscience, Hoboken, NJ, 2003.

[115] F. D. Bannon, J. R. Clark, and C. T. C. Nguyen, "High-Q HF microelectromechanical filters," *IEEE Journal of Solid-State Circuits* **35**(4), pp. 512 – 26, 2000.

[116] C. T. C. Nguyen, "Integrated micromechanical radio front-ends," *International Symposium on VLSI Technology, Systems, and Applications, Proceedings* , pp. 3 – 4, (Hsinchu, Taiwan), 2008.

[117] P. Muralt, "PZT thin films for microsensors and actuators: Where do we stand?," *IEEE Transactions on Ultrasonics, Ferroelectrics, and Frequency Control* **47**(4), pp. 903 – 915, 2000.

[118] D. J. Chung, R. G. Polcawich, D. Judy, J. Pulskamp, and J. Papapolymerou, "A SP2T and a SP4T switch using low loss piezoelectric MEMS," *IEEE MTT-S International Microwave Symposium Digest* , pp. 21 – 24, (Atlanta, GA, United states), 2008.

[119] Y. Arimoto and H. Ishiwara, "Current status of ferroelectric random-access memory," *MRS Bulletin* **29**(11), pp. 823 – 8, 2004.

[120] R. Mahameed, N. Sinha, M. B. Pisani, and G. Piazza, "Dual-beam actuation of piezoelectric AlN RF MEMS switches monolithically integrated with AlN contour-mode resonators," *Journal of Micromechanics and Microengineering* **18**(10), 2008.

[121] Y.-W. Lin, *Low Phase Noise Micromechanical Reference Oscillators for Wireless Communications*. PhD thesis, University of Michigan, 2007.

[122] B. Otis, S. Gambini, R. Shah, D. Steingart, E. Quevy, J. Rabaey, A. Sangiovanni-Vincentelli, and P. Wright, "Modelling and simulation techniques for highly integrated, low-power wireless sensor networks," *IET Computers and Digital Techniques* **1**(5), pp. 528 – 536, 2007.

[123] S. K. Cho, H. Moon, and C.-J. Kim, "Creating, transporting, cutting, and merging liquid droplets by electrowetting-based actuation for digital microfluidic circuits," *Journal of Microelectromechanical Systems* **12**(1), pp. 70 – 80, 2003.

[124] K. Ichimura, S.-K. Oh, and M. Nakagawa, "Light-Driven Motion of Liquids on a Photoresponsive Surface," *Science* **288**(5471), pp. 1624–1626, 2000.

[125] A. A. Darhuber, J. P. Valentino, S. M. Troian, and S. Wagner, "Ther-

mocapillary actuation of droplets on chemically patterned surfaces by programmable microheater arrays," *Journal of Microelectromechanical Systems* **12**(6), pp. 873 – 879, 2003.

[126] A. Shastry, D. Taylor, and K. F. Bohringer, "Micro-structured surface ratchets for droplet transport," *TRANSDUCERS and EUROSENSORS '07 - 4th International Conference on Solid-State Sensors, Actuators and Microsystems* , pp. 1353 – 1356, (Lyon, France), 2007.

[127] N. Yamauchi, T. Shirai, T. Yoshihara, Y. Hayasaki, T. Matsushima, I. Kanno, and K. Wasa, "Development of 4 GHz bulk acoustic wave resonators by sputtered $Pb(Mn, Nb)O_3 - Pb(Zr, Ti)O_3$ thin films," *Proceedings - IEEE Ultrasonics Symposium* , pp. 1920 – 1923, 2008.